

Cover Page



Universiteit Leiden



The handle <http://hdl.handle.net/1887/74366> holds various files of this Leiden University dissertation.

**Author:** Bastiaansen, R.

**Title:** Lines in the sand : behaviour of self-organised vegetation patterns in dryland ecosystems

**Issue Date:** 2019-06-27

# lines in the sand

Behaviour of self-organised vegetation  
patterns in dryland ecosystems



Robbin Bastiaansen



# **Lines in the Sand**

Behaviour of self-organised vegetation patterns  
in dryland ecosystems

Proefschrift

ter verkrijging van  
de graad van Doctor aan de Universiteit Leiden,  
op gezag van Rector Magnificus prof. mr. C.J.J.M. Stolker,  
volgens besluit van het College voor Promoties  
te verdedigen op donderdag 27 juni 2019  
klokke 13:45 uur

door

**Robbin Bastiaansen**

geboren te Bergen op Zoom  
in 1991



Promotores:            prof. dr. Arjen Doelman            (Leiden University)  
                              prof. dr. Max Rietkerk            (Utrecht University)  
Copromotor:            dr. Martina Chirilus-Bruckner    (Leiden University)

Promotiecommissie:  prof. dr. Aad van der Vaart        (Leiden University)  
                              prof. dr. Roeland Merks            (Leiden University)  
                              dr. Maarten Eppinga                (University of Zurich)  
                              prof. dr. Jens Rademacher         (Bremen University)  
                              prof. dr. Mary Silber                (University of Chicago)

©2019 Robbin Bastiaansen  
Printed by Ipskamp printing

This research was funded by a joint grant to Arjen Doelman and Max Rietkerk within the Mathematics of Planet Earth program of the Netherlands Organization of Scientific Research (NWO).

*Laat ons een bloem en wat gras dat nog groen is  
Laat ons een boom en het zicht op de zee  
Vergeet voor één keer hoeveel geld een miljoen is  
De wereld die moet nog een eeuwigheid mee*  
— *Louis Neefs, Laat ons een bloem*

*Leave them a flower, some grass and a hedgerow  
A hill and a valley, a view to the sea  
These things are not yours to destroy as you want to  
A gift given once for eternity*  
— *Wally Whyton, Leave them a flower*



# Table of Contents

<b>1</b>	<b>Introduction</b>	<b>9</b>
<b>2</b>	<b>Multistability of model and real dryland ecosystems through spatial self-organization</b>	<b>21</b>
2.1	Introduction . . . . .	21
2.2	Theory . . . . .	23
2.2.1	Model description . . . . .	23
2.2.2	Theoretical outcomes . . . . .	23
2.2.3	Testable predictions . . . . .	26
2.3	Data acquisition & processing . . . . .	26
2.4	Results . . . . .	27
2.5	Discussion . . . . .	29
	<b>Appendices</b>	
2.A	Dimensional extended-Klausmeier . . . . .	31
2.B	Description of study sites . . . . .	31
2.C	Data sets . . . . .	32
2.C.1	Topographical data . . . . .	32
2.C.2	Biomass measurements . . . . .	32
2.C.3	Optical data . . . . .	33
2.D	Data processing . . . . .	33
2.D.1	Spectral analysis, direction of anisotropy and wavelength . . . . .	33
2.D.2	Pattern classification . . . . .	34
2.D.3	Cross-spectral analysis and migration speed . . . . .	35
2.D.4	Assessment of uncertainty in calculations of slope gradient and aspect from topographical data . . . . .	35
2.D.5	Assessment of uncertainty in estimation of pattern frequency from optical imagery . . . . .	36
<b>3</b>	<b>The dynamics of disappearing pulses in a singularly perturbed reaction-diffusion system with parameters that vary in time and space</b>	<b>41</b>
3.1	Introduction . . . . .	41
3.1.1	Size assumptions . . . . .	48
3.2	PDE to ODE reduction . . . . .	50
3.2.1	The inner regions . . . . .	51
3.2.2	The outer regions . . . . .	53
3.2.3	Pulse location ODE under assumption (A3) . . . . .	54
3.2.4	Pulse location ODE under assumption (A3') . . . . .	57
3.3	Linear Stability . . . . .	59

3.3.1	Stability of homoclinic pulses on $\mathbb{R}$ . . . . .	60
3.3.2	Stability of $N$ -pulse solutions . . . . .	66
3.4	Numerical Simulations . . . . .	70
3.4.1	Flat terrains . . . . .	71
3.4.2	The effect of sloped terrains . . . . .	77
3.5	Discussion and Outlook . . . . .	84
<b>Appendices</b>		
3.A	The movement of water on a varying terrain . . . . .	87
3.B	Fixed Points of the pulse-location ODE - Proofs . . . . .	88
3.B.1	Properties of $R_{\pm}$ . . . . .	89
3.B.2	Unbounded domains . . . . .	90
3.B.3	Bounded domains with periodic boundaries . . . . .	90
3.B.4	Bounded domains with Neumann boundary conditions . . . . .	93
<b>4</b>	<b>Pulse solutions for an extended Klausmeier model with spatially varying coefficients</b> . . . . .	<b>95</b>
4.1	Introduction . . . . .	95
4.1.1	Assumptions . . . . .	100
4.2	Analysis of stationary pulse solutions . . . . .	101
4.2.1	Stationary pulse solutions for $f = 0$ and $g = 0$ . . . . .	102
4.2.2	Stationary pulse solutions for varying $f$ and $g$ . . . . .	105
4.2.3	Some basic results from the theory of exponential dichotomies . . . . .	110
4.2.4	Dynamics on $\mathcal{M}$ (Proof of Proposition 4.2.9) . . . . .	112
4.2.5	Existence results . . . . .	115
4.2.6	Proof of existence results . . . . .	118
4.3	Linear stability analysis . . . . .	118
4.3.1	Qualitative description of the point spectrum location (Proof of Theorem 4.3.2) . . . . .	120
4.3.2	Small eigenvalue close to $\lambda = 0$ (Proof of Theorem 4.3.5) . . . . .	130
4.4	The effect of the small eigenvalue: movement of pulse . . . . .	136
4.4.1	Formal derivation of pulse location ODE . . . . .	137
4.4.2	Stability of fixed points of pulse location ODE (4.4.1) . . . . .	138
4.4.3	Small eigenvalue in case of small spatially varying coefficients . . . . .	139
4.4.4	Examples of stationary single-pulse solutions . . . . .	141
4.4.5	Stationary multi-pulse solutions . . . . .	145
4.5	Discussion . . . . .	148
<b>5</b>	<b>Stable planar vegetation stripe patterns on sloped terrain in dryland ecosystems</b> . . . . .	<b>151</b>
5.1	Introduction . . . . .	151
5.2	Slow-fast analysis of traveling wave equation . . . . .	157
5.2.1	Critical manifolds . . . . .	157
5.2.2	Layer fronts . . . . .	160
5.2.3	Slow flow . . . . .	163
5.2.4	Singular orbits . . . . .	163
5.2.5	Main existence results . . . . .	168
5.3	Persistence of solutions for $0 < \varepsilon \ll 1$ . . . . .	169
5.3.1	Transversality along singular orbits . . . . .	169
5.3.2	Proof of existence results . . . . .	171
5.4	Stability . . . . .	172

5.4.1	Essential spectrum . . . . .	173
5.4.2	Point spectrum . . . . .	175
5.4.3	Formal computation of small eigenvalues . . . . .	175
5.4.4	Main stability results . . . . .	178
5.5	Rigorous proof for stability theorems . . . . .	181
5.5.1	Exponential dichotomies/trichotomies . . . . .	181
5.5.2	Reduction to region of bounded $ \ell $ . . . . .	182
5.5.3	The region $(\tilde{\lambda}(\ell), \ell) \in R_3(M) \times [-L_M, L_M]$ . . . . .	184
5.5.4	Setup for the region $(\tilde{\lambda}(\ell), \ell) \in R_1(\delta) \cup R_2(\delta, M) \times [-L_M, L_M]$ . . . . .	184
5.5.5	The region $(\tilde{\lambda}(\ell), \ell) \in R_1(\delta) \times [-L_M, L_M]$ . . . . .	187
5.5.6	The region $(\tilde{\lambda}(\ell), \ell) \in R_2(\delta, M) \times [-L_M, L_M]$ . . . . .	195
5.5.7	Proof of Theorem 5.4.3 . . . . .	196
5.6	Defects and curved vegetation pattern solutions . . . . .	197
5.7	Numerics . . . . .	198
5.7.1	Continuation of traveling stripes and gaps . . . . .	199
5.7.2	Direct simulations . . . . .	200
5.8	Discussion . . . . .	200
<b>Appendices</b>		
5.A	Stability of steady states . . . . .	206
5.B	Absence of point spectrum in $R_2(\delta, M)$ . . . . .	206
<b>References</b>		<b>209</b>
<b>Dutch Summary</b>		<b>221</b>
<b>Curriculum Vitae</b>		<b>223</b>



# 1 Introduction

The world around us is – and has been – changing constantly. In the past, there have been large fluctuations in, for instance, solar activity [168], the concentration of carbon dioxide in the earth’s atmosphere [2] and the global average temperature [74, 75] – to name a few. These changes in climate have huge impacts on ecosystems; whole groups of organisms can become extinct if these changes are severe [37, 82] – or, perhaps even more crucially, if they happen at a rapid rate [37, 146, 157]. In these cases, nature has too little leeway to adapt to the new status quo in a slow, minor way and instead large, often more destructive changes occur [97, 157, 177] – such as the extinction of a species. The prototypical example is the sudden mass extinction that occurred roughly 66 million years ago in which the dinosaurs died out (marking the end of the Mesozoic Era and the beginning of the Cenozoic Era) [18, 61]. Nowadays, climate change is again a (literal) hot topic. Since the start of the industrial revolution, changes in climate have been both severe and unprecedentedly rapid. Undeniably, this already has a large impact on life on earth, and also in the future will continue to change earth [37, 88, 92, 96, 177]. To compensate the impact of these changes in climate, deep knowledge of nature’s systems is necessary; a feat that can be achieved with the use of mathematical analysis.

In this thesis, the focus is on ecosystem models that describe the dynamics in dryland ecosystems, and the process of desertification that occurs in these areas (as a consequence of climate change). Loosely speaking, desertification is the process in which a relatively dry semi-arid region loses its vegetation – typically as an effect of increased grazing activity, ongoing drought and/or global climate change [93, 114, 124, 139, 176]. At the end of the process, all vegetation is gone. Since water and nutrients are better preserved in the soil when vegetation is present, their absence causes the soil to deteriorate: it becomes hard and even less suitable for plants [145]. Therefore, it is very hard to recolonize bare soil [145]. Hence, the desertification process needs to be stopped before it has become irreversible. Not least since the areas in danger grow in size every year, and even house a large portion of the world’s population [118]. Since the people in these regions rely heavily on livestock and crops made within these regions, preservation of these areas is vital to their livelihood. This is a difficult task, and one that also poses many important socioeconomic dilemmas that need to be resolved [118, 167]. Nevertheless, a thorough understanding of the desertification process is required to effectively combat it.

Vegetation patterns in semi-arid ecosystems have been the topic of research for many decades. This interest started around the 1940s when aerial photographs – up to that point mainly used for military operations – became (somewhat) more openly



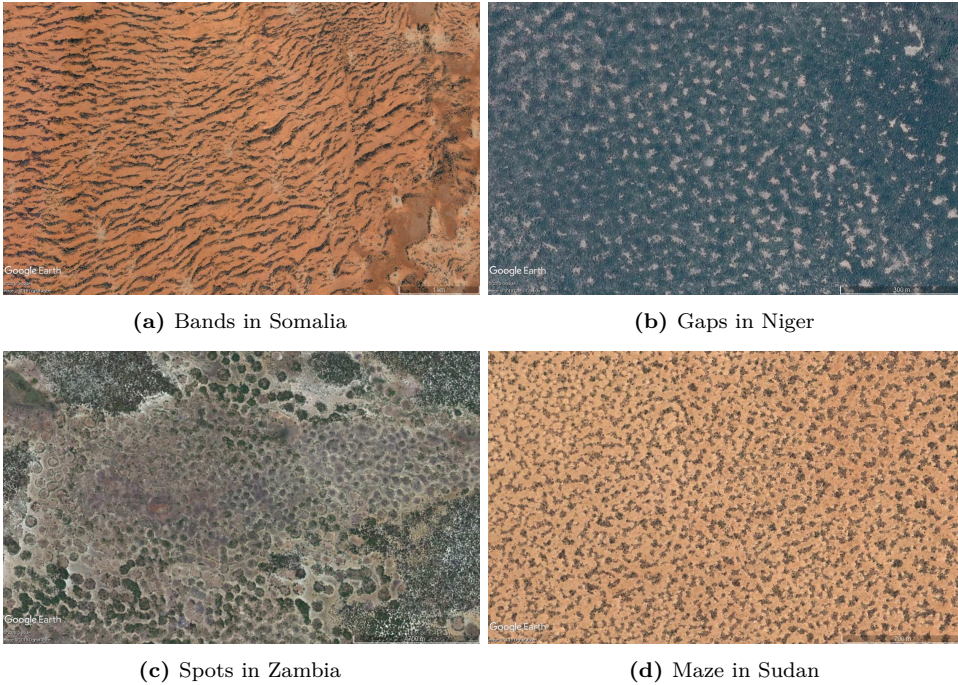


**Figure 1.1** – Google Earth satellite images of several different vegetation patterns in semi-arid climates. (a) Banded vegetation in Somalia ( $8^{\circ}5'N$ ;  $47^{\circ}27'E$ ); (b) Gapped vegetation in Niger ( $12^{\circ}22'N$ ;  $2^{\circ}24'E$ ); (c) Spotted vegetation patterns in Zambia ( $15^{\circ}38'S$ ;  $22^{\circ}46'E$ ); (d) Maze pattern in Sudan ( $11^{\circ}8'N$ ;  $27^{\circ}50'E$ ).

available. In 1950, this led Macfadyen to publish a report on the vegetation patterns in ‘British Somaliland’ [112]. Since then, vegetation patterns have been observed in many other semi-arid areas [57, 81, 119, 181]. Depending on the precise environment, the reported patterns include gaps, bands, mazes and patches [42, 57, 64, 81, 112, 119, 136, 176, 181] – see Figure 1.1 for some examples. Currently, the existence of these patterns is attributed to a combination of water scarcity in these systems and the effect of vegetation on the soil’s permeability [136]. Through these two effects, vegetation arranges itself in the observed patterns – that is, these are self-organized patterns that are not caused by external inhomogeneities.

Over the years, numerous amounts of conceptual mathematical models have been postulated that aim to capture the dynamics of these dryland ecosystems [67, 95, 136, 163, 176]. The most predominant models are of reaction-diffusion type. They describe the interplay between vegetation and the little amount of water in these areas. In general, most of these models can be captured heuristically as

$$\left\{ \begin{array}{l} \text{change in surface water} = \text{movement} + \text{precipitation} - \text{infiltration in soil;} \\ \text{change in soil water} = \text{movement} + \text{infiltration} - \text{deep infiltration} - \text{uptake;} \\ \text{change in vegetation} = \text{movement} - \text{mortality} + \text{growth through uptake.} \end{array} \right. \quad (1.1)$$

Examples of these models include those by Rietkerk et al [136] and by Gilad et al [67]. They differ in the degree of complexity and realism that is used to model aforementioned effects. None of the models, however, are completely based on first principles (although parts of them are – such as the movement of water that is typically modeled

as diffusion). Moreover, most of these effects have never been measured accurately and/or are very hard to measure for a given ecosystem (such as water movement in the soil or vegetation growth through water uptake). Therefore, it is difficult to validate models and to compare model output with observations on real ecosystems in a meaningful way. Because of this, it is important to find the qualitative and universal behavior of these models and compare that to reality.

These insights can be provided through numerical studies – as has been done extensively in recent times [53, 152, 155, 158, 170, etc.]. However, it is hard to classify and understand all possible model responses, for all parameter combinations, from direct numerics alone. Therefore, to complement the numerical studies, it is typically insightful to analyze the model mathematically as well – as such mathematical analyses are better suited to, for example, pinpoint bifurcation/tipping points. To facilitate these mathematical methods, in practice it is often unavoidable to make specific choices for model and/or parameters – as will be done throughout this thesis as well. Here, it is important to distinguish between generic and model-specific properties; the precise, quantitative response is often model-specific, whereas the qualitative response is usually more universal. The challenge lies in finding those minimal models that (still) capture the essential dynamics, but are also simple enough to study mathematically.

The general model (1.1) is already relatively complicated because it is a three-component model (surface water, soil water, vegetation). Therefore, an inherently simpler two-component model is usually used in mathematical studies. Those two-component models only take into account one water component (and the vegetation component). This can be achieved for instance by lumping together soil and surface water in (1.1) or by ignoring the surface water component – the latter is a good approximation when infiltration in the soil is fast. In words, these simpler models have the form

$$\begin{cases} \text{change in water} & = & \text{movement} + \text{precipitation} - \text{deep infiltration} - \text{uptake}; \\ \text{change in vegetation} & = & \text{movement} - \text{mortality} + \text{growth through uptake}. \end{cases} \quad (1.2)$$

This still leaves room for many models to coexist; there are still dozens of ways to model each effect [163]. In this thesis, a few of those two component models are explored in detail. Here, the models are often restricted to one spatial dimension to further simplify them mathematically.

However, there are also similarities between models. For example, the vegetation’s positive effect on the soil’s permeability is modeled in some way or another as this is needed for patterns to emerge – as has been discussed before. Moreover, another important feature of all models is the difference in movement/migration speed of water and vegetation; water moves on much faster scales than vegetation. It is because of the presence of such a ‘scale separation’ that patterns can emerge (this is true in general and not only for dryland ecosystems [98, 138, 165]).

Whether, and which, patterns actually emerge depends on the water availability, which is usually characterized by the amount of precipitation. For decreasing amount of rainfall, in turn the following happens (see Figure 1.2 for a model run). Initially, there is enough water available to sustain vegetation everywhere. Slowly, the density of vegetation decreases, until, for some critical rainfall value, there is not enough water to sustain vegetation everywhere and patterns emerge [165]. At first, these patterns are small deviations from the uniform covered state<sup>1</sup>, but they will get more pronounced as water becomes more scarce, until vegetation is only present at a few, localized

---

<sup>1</sup>These so-called ‘close-to-equilibrium’ patterns can be studied analytically using for instance amplitude equations; see for instance [35, 173]. This is, however, not the focus of this thesis.

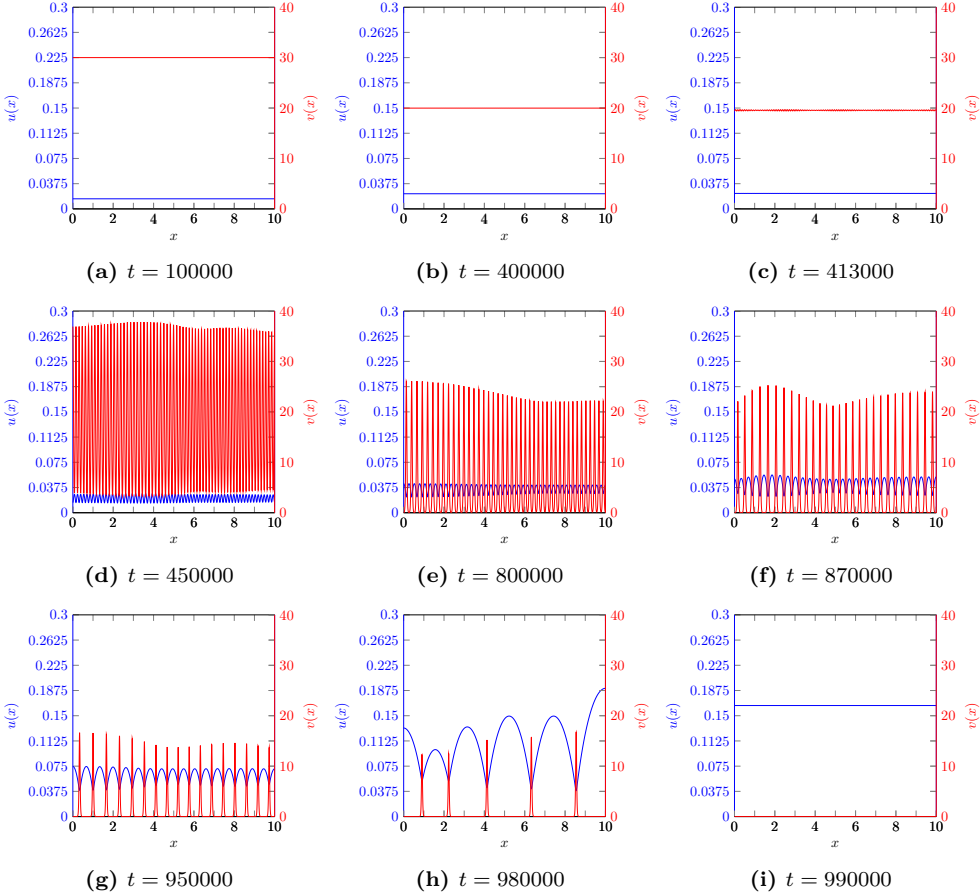


**Figure 1.2** – Snapshots of direct simulation of a dryland ecosystem model (with one spatial dimension) in which the precipitation was slowly decreased. Here,  $U(x)$  denotes the water in the system and  $V(x)$  the amount of vegetation. The on-set of patterns from a uniform configuration can be seen (small fluctuations are present in c), as well as the typical pattern changes that subsequently occur when the amount of rainfall decreases, until – for low precipitation – no vegetation can be sustained and all vegetation has disappeared from the system. The model used is the extended-Klausmeier model with parameters  $m = 0.45$ ,  $D = 0.01$ ,  $a(t) = 15(1 - 10^{-6}t)$  – see also chapter 3.

positions. Then, these localized patterns slowly change and vegetation continues to disappear at more and more locations. Finally, for some critical precipitation value, there is not enough water available to sustain any vegetation and the system is trapped in a desert state – with no vegetation anywhere.

In this thesis, the focus is on the localized patterns that emerge when water scarcity is high. These patterns exhibit vegetation only at some localized positions; elsewhere there are no plants and the soil is bare. The aforementioned gaps, bands, mazes and patches are all examples of this category of patterns (as are those in Figure 1.1). These localized structures form the last resort for vegetation in dryland ecosystems; once they cannot be maintained any longer, it is not possible for vegetation to exist there any more.

These patterns, however, are not fixed in time and space. Instead, the localized vegetation structures are in competition for resources (mainly water); each tries to optimize their own water uptake, which simultaneously changes the water distribution in the system. It is through this mechanism that the localized structures interact with each other. As a consequence of these interactions, the vegetation migrates over the landscape, moving towards water – and thus typically improving their (own) sustainability. Moreover, when resource scarcity is too high, these interactions can prevent a total desertification by losing only some of the localized structures. All in all, these patterns are thus highly self-structured and adaptive; They are able to adjust to changes in climate. The way in which these adaptations occur, is not predetermined though; it depends heavily on the severity and rate of the imposed (climate) change [157, 158].

This thesis aims to improve the knowledge of this desertification process. For this, it is necessary to determine the type of patterns that can emerge under which conditions, to describe the interactions between localized structures and to understand the possible adaptive responses of these systems. Luckily, since dryland ecosystems have a natural separation of scales, this opens the way for advanced mathematical techniques that can be used to answer these questions.

## Mathematical Tools

Most of the mathematical analysis in this thesis utilizes perturbation arguments to exploit the scale separations present in the models. In these problems there is a small parameter (typically denoted by  $0 < \varepsilon \ll 1$ ). Solutions to the full problem are then related in one way or another to solutions for the  $\varepsilon = 0$  case. In particular, the theory of geometric singular perturbations and regular expansions are used for this. In this thesis, these techniques will be used to study existence, stability and dynamics of localized solutions to the ecosystem models. To illustrate the basics of both, in this section they are applied to a simple example system.

### Geometric arguments

Consider the following differential equation

$$\begin{cases} \frac{du}{d\xi} = \varepsilon(v - u), \\ \frac{dv}{d\xi} = \frac{v^2}{2u} - v, \end{cases} \quad \boxed{\text{fast system}} \quad (1.3)$$

where  $0 < \varepsilon \ll 1$  is a small parameter and  $\xi$  is a so-called fast coordinate<sup>2</sup>. There is also a slow coordinate<sup>2</sup>  $x = \varepsilon\xi$ , and with a coordinate transformation the system can also be written as

$$\begin{cases} \frac{du}{dx} = v - u, \\ \varepsilon \frac{dv}{dx} = \frac{v^2}{2u} - v. \end{cases} \quad \boxed{\text{slow system}} \quad (1.4)$$

Both systems are equivalent as long as  $\varepsilon \neq 0$ ; when  $\varepsilon = 0$  they have different dynamics. However, by combining the dynamics for both  $\varepsilon = 0$  cases the behavior for the  $\varepsilon \neq 0$  system can be understood. First, by setting  $\varepsilon = 0$  in the fast system the following fast

---

<sup>2</sup>For spatial coordinates, perhaps the terms ‘elongated’ and ‘shortened’ feel more suitable; however, the terminology of ‘fast’ and ‘slow’ coordinates is typically used even for non-temporal coordinates.

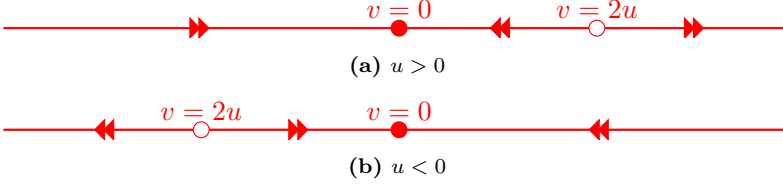


**Figure 1.3** – Flow of  $\frac{dv}{d\xi} = \frac{v^2}{2u} - v$  for fixed  $u > 0$  (a) and  $u < 0$  (b).

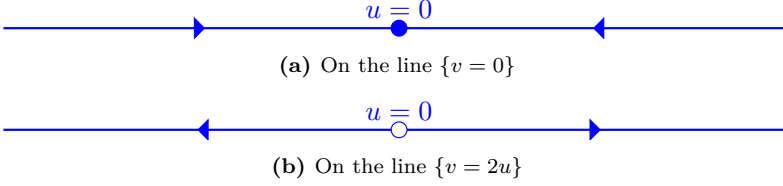


**Figure 1.4** – Flow of the slow reduced system on the lines  $\{v = 0\}$ (a) and  $\{v = 2u\}$ (b).

reduced system is found

$$\begin{cases} \frac{du}{d\xi} = 0, \\ \frac{dv}{d\xi} = \frac{v^2}{2u} - v. \end{cases} \quad \boxed{\text{fast reduced system}} \quad (1.5)$$

Clearly,  $u$  is constant in this system. For given  $u \neq 0$ , the differential equation  $\dot{v} = v^2/(2u) - v$  has (hyperbolic) fixed points at  $v = 0$  and  $v = 2u$ . In all cases flow is directed away from  $v = 2u$  and towards  $v = 0$  (see Figure 1.3).

On the other hand, setting  $\varepsilon = 0$  in the slow system results in a slow reduced system given by:

$$\begin{cases} \frac{du}{dx} = v - u, \\ 0 = \frac{v^2}{2u} - v. \end{cases} \quad \boxed{\text{slow reduced system}} \quad (1.6)$$

The algebraic condition  $0 = v^2/(2u) - v$  stipulates  $v = 0$  or  $v = 2u$  (not coincidentally the fixed points of the fast reduced problem). So two separate cases are revealed. On the line  $\{v = 0\}$ , the slow reduced system becomes

$$\frac{du}{dx} = -u, \quad \boxed{\text{slow reduced system on } \{v = 0\}} \quad (1.7)$$

which has a stable fixed point at  $u = 0$  (see Figure 1.4); on the line  $\{v = 2u\}$  the system becomes

$$\frac{du}{dx} = u, \quad \boxed{\text{slow reduced system for } \{v = 2u\}} \quad (1.8)$$

which has an unstable fixed point at  $u = 0$  (see Figure 1.4).

Information from the reduced systems can then be combined. Graphically, the flow is summarized in Figure 1.5. From this, one can heuristically deduce that a homoclinic connection to the point  $(0, 0)$  can be constructed as follows: starting from  $(0, 0)$  flow

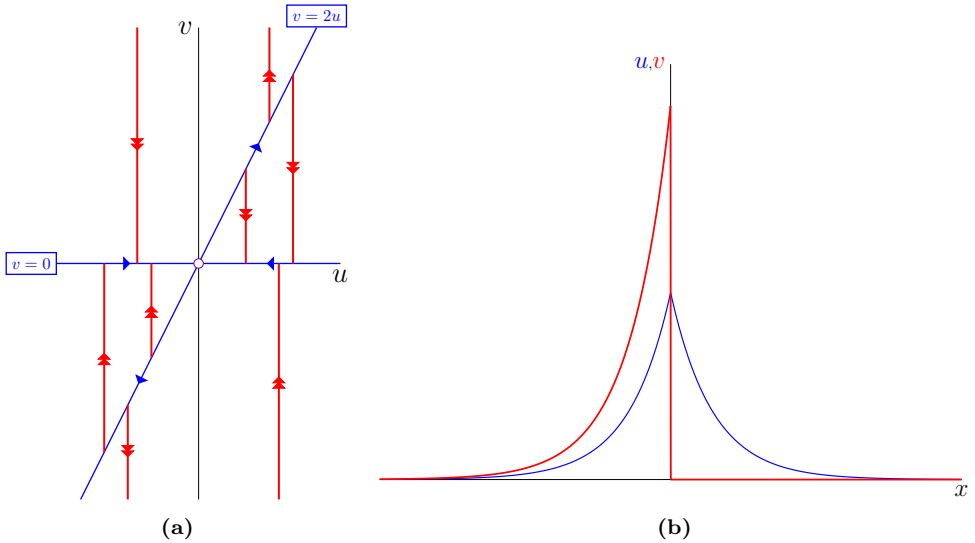


**Figure 1.5** – Flow of the system (1.3) as indicated by the reduced systems (a) and a first order approximation of a homoclinic solution to this system with  $\varepsilon = 0.01$  (b).

can be followed along the line  $\{v = 2u\}$ , and at some moment a so-called fast jump occurs from the line  $\{v = 2u\}$  to the line  $\{v = 0\}$ , which is subsequently followed back to the point  $(0, 0)$ .

This construction is only based on the information from the reduced systems and does not immediately guarantee the found solutions (a family of homoclinic connections) also exist for the  $\varepsilon \neq 0$  system. For that, it is necessary to verify that the structure of the system persists for  $\varepsilon > 0$ . This can be achieved using for instance geometric singular perturbation theory [62]. Without going into the details here, in this case this theory indicates that the fast jumps from the line  $\{v = 2u\}$  to the line  $\{v = 0\}$  persist in the system with  $\varepsilon > 0$  and subsequently proves existence of the found family of homoclinic orbits connecting  $(u, v) = (0, 0)$  to itself. Details on how to use geometric singular perturbation theory to prove these assertions can be found in one of the many excellent review articles on this topic – see for example [80, 86, 89].

## Regular expansion

The above explained technique is useful to get a grip on the qualitative behavior of the system. However, it is often also necessary to obtain approximations for these solutions (e.g. for proofs using geometric singular perturbations these often come in handy). To derive these estimates, regular expansions are used to expand  $u$  and  $v$  in powers of  $0 < \varepsilon \ll 1$ . Specifically, one sets

$$\begin{pmatrix} u \\ v \end{pmatrix} = \begin{pmatrix} u_0 \\ v_0 \end{pmatrix} + \varepsilon \begin{pmatrix} u_1 \\ v_1 \end{pmatrix} + \mathcal{O}(\varepsilon^2) \quad (1.9)$$

and solves the system per order of  $\varepsilon$ . In practice, for most cases it is sufficient to determine only the leading or next to leading order terms.

In the rest of this section, a leading order approximation for the homoclinic orbits is derived. Here, for each building block of the homoclinic orbit another expansion

is needed. For notational clarity, it is assumed that the fast jump occurs close to  $x = 0$ , in a region denoted by  $I_f$ . The region to the left of the jump is denoted by  $I_s^-$  and the solution in that region by  $(u_s^-, v_s^-)^T$ ; similarly to the right of the jump the region is called  $I_s^+$  and the solution  $(u_s^+, v_s^+)^T$ ; in region  $I_f$  the solution is denoted by  $(u_f, v_f)^T$ . The three regions are inspected one by one, and only the leading order terms are computed in each region.

In  $I_s^-$ , the solution follows the dynamics of the slow system (1.4). To leading order the system is given by

$$\begin{cases} \frac{d}{dx} u_s^- &= v_s^- - u_s^-, \\ 0 &= \frac{(v_s^-)^2}{2u_s^-} - v_s^-. \end{cases} \quad (1.10)$$

From the previously determined geometrical structure of the solutions, it is known that  $v_s^- = 2u_s^-$ . Thus,

$$\frac{du_s^-}{dx} = u_s^-, \quad (1.11)$$

which yields the family of solutions

$$u_s^-(x) = C_s^- e^x, \quad v_s^-(x) = 2C_s^- e^x, \quad (C_s^- \in \mathbb{R}). \quad (1.12)$$

In  $I_s^+$ , the same reasoning can be repeated. In this region,  $v_s^+ = 0$  and thus the dynamics of  $u_s^+$  is governed by

$$\frac{du_s^+}{dx} = -u_s^+, \quad (1.13)$$

which results in the family of solutions given by

$$u_s^+(x) = C_s^+ e^{-x}, \quad v_s^+(x) = 0, \quad (C_s^+ \in \mathbb{R}). \quad (1.14)$$

During the jump (when  $x \in I_f$ ), the dynamics are governed by the fast system (1.3). To leading order it is given by

$$\begin{cases} \frac{du_f}{d\xi} &= 0; \\ \frac{dv_f}{d\xi} &= \frac{v_f^2}{2u_f} - v_f. \end{cases} \quad (1.15)$$

Solving this system gives

$$u_f(\xi) = C_f, \quad v_f(\xi) = C_f (1 - \tanh(\xi/2)), \quad (C_f \in \mathbb{R}). \quad (1.16)$$

The derived expressions still have undetermined constants. These can be related to each other by requiring continuity at the edges of the different regions (typically called ‘matching of solutions’). In practice, this can often be achieved by equating the expressions  $(u_s^-(0), v_s^-(0))^T = \lim_{\xi \rightarrow -\infty} (u_f(\xi), v_f(\xi))^T$  and  $(u_s^+(0), v_s^+(0))^T = \lim_{\xi \rightarrow \infty} (u_f(\xi), v_f(\xi))^T$ . For this problem that leads to  $C_s^- = C_f = C_s^+$ .

To summarize, the leading order approximation of a homoclinic orbit of (1.4) is

$$u_0(x) = \begin{cases} Ue^x, & x \in I_s^-; \\ U, & x \in I_f; \\ Ue^{-x}, & x \in I_s^+; \end{cases} \quad v_0(x) = \begin{cases} 2Ue^x, & x \in I_s^-; \\ U(1 - \tanh(\frac{x}{2\varepsilon})), & x \in I_f; \\ 0, & x \in I_s^+, \end{cases} \quad (1.17)$$

where  $U$  is a free constant, since a family of homoclinic connections exists in the system. A plot of the found approximation is given in Figure 1.5.

---

## Contents of this thesis

The research presented in this thesis aims to improve the (mathematical) knowledge about (localized) patterns in dryland ecosystems. The various chapters focus on different aspects and effects. The general idea, however, is the same in all chapters: an (ecological) phenomenon is studied using an explicit ecosystem model that is deliberately chosen to be as simple as possible, so that explicit mathematical analysis and computations can be done – while making sure the desired behavior of the real system is still present. In this way, the underlying structure is more transparent and qualitative conclusions can typically be extrapolated to more realistic models. Ultimately, this leads to theoretical predictions for the real system, which can (and should) be tested using data from real vegetation patterns – part of which is also done in this thesis.

### Multistability of patterns

Chapter 2, titled ‘*Multistability of model and real dryland ecosystems through spatial self-organization*’<sup>3</sup>, explores the properties of patterns that generically emerge in reaction-diffusion models, and compares these theoretical insights with data from observations on vegetation patterns in Somalia. In the models, typically a lot of different patterns can be found – with differences in both their type (e.g. bands, gaps) and their size (characterized for example by the band-interband period and wavenumber). Importantly, these different patterns can even co-exist for the same parameter values – that is, the models show multistability. The precise set of patterns that are stable solutions to the model (for a given set of parameters) can be captured in a so-called Busse balloon. For dryland ecosystems, this reveals that, for a given set of environmental conditions, an ecosystem can sustain a set of patterns, whose wavenumber is contained in a continuous range of substantial spread. In chapter 2, this theoretical insight is confronted by data of vegetation patterns in Somalia, which indeed corroborate the theories of multistability of patterned vegetation states.

This property has important consequences for the way in which vegetation patterns indicate ecosystem resilience and mediate responses to environmental change. In contrast to models with monostability – the typical assumption in ecological frameworks [137, 144] – the multistable models do not possess a single tipping point, but a cascade of destabilization; when environmental changes push a pattern outside of the region of stable patterns (outside of the Busse balloon), a wavenumber adaptation happens, in which typically only few patches are lost (and the remaining ones grow in size). The precise extent of these adaptations depends on both the severity and the rate of the change. In this way, vegetation is highly adaptive and self-organizing; moreover, it shows that the adaptability of a pattern might be a better indicator for ecosystem resilience than the shape of the pattern itself.

Despite these important conclusions, comparisons of model results have mainly been limited to visual inspection. Therefore, in chapter 2 a systematic comparison is performed using data on wavenumber, biomass and migration speed of banded vegetation patterns in Somalia. In agreement with reaction-diffusion models, a wide distribution of regular pattern wavenumbers was found in the data. This highlights the potential for extrapolating predictions of those models to real ecosystems, including

---

<sup>3</sup>Joint work with Olfa Jaïbi, Vincent Deblauwe, Maarten B. Eppinga, Koen Siteur, Stéphane Mermoz, Alexandre Bouvet, Arjen Doelman and Max Rietkerk; has appeared as publication in *PNAS* [9].



those that elucidate how spatial self-organization of vegetation enhances ecosystem resilience.

## Dynamics of disappearing pulses

The localized vegetation patterns in dryland ecosystems are not fixed in time and space; instead, the vegetation is constantly changing and adapting to each other and to variations in environmental conditions. This behavior is the topic of chapter 3, ‘*The dynamics of disappearing pulses in a singularly perturbed reaction-diffusion system with parameters that vary in time and space*’<sup>4</sup>. Here, topic of study is the evolution of patterns with multiple (vegetation) pulses under changing climatological circumstances. In particular, focus is given to the migration and disappearance of vegetation in a simple ecosystem model.

In this chapter, a hybrid asymptotic-numerical method is used to get a grip on the dynamics of the full model. First, the full dynamics are reduced to a simpler dynamical system that describes the movement of the vegetation pulses. Next, the stability of specific pulse configurations is studied. Here, not only the moment of destabilization is studied, but also the pattern adaptation that then occurs. With the aid of numerous simulations, the coarsening dynamics of pulses is then inspected in a wide variety of situations.

It is found that vegetation migrates towards places with more water. Since the presence of vegetation itself influences the distribution of water, ultimately vegetation slowly evolves towards a regular, spatially periodic, pattern. Moreover, a difference between pattern adaptations of regular and irregular patterns is revealed. In the case of irregular patterns, pulses are typically lost one by one, whereas regular patterns undergo catastrophic transitions in which either half or all pulses disappear.

## Topographical effects

Most ecosystem models consider only specific, idealized topographies, in which the terrain is often taken to be perfectly flat, or constantly sloped – typically modeled by reaction-(advection)-diffusion equations with constant coefficients. Such idealized landscapes are of course not very realistic. Moreover, small variations in topography can have large impacts on the distribution of water over the landscape, which in turn impacts the migration of vegetation. Therefore, some behavior of the real system is lost when those idealized terrains are used. To comprehend this more involved behavior, in chapter 4, titled ‘*Pulse solutions for an extended Klausmeier model with spatially varying coefficients*’<sup>5</sup>, a simple ecosystem model is extended to allow for more complex topographies.

The inclusion of more generic terrains leads to behavior that cannot be found in the simpler models. For instance, on constantly sloped terrains, models predict that vegetation always migrates uphill, while on generic terrains, both uphill and downhill movement is possible – challenging the assertion that movement of patterns can be used as a mechanism to confirm or reject the presence of a specific pattern formation mechanism [57]. Additionally, in chapter 4 the distinction between uphill and downhill movement is linked to the terrain’s curvature.

---

<sup>4</sup>Joint work with Arjen Doelman; has appeared as publication in *Physica D* [8].

<sup>5</sup>Joint work with Martina Chirilus-Bruckner and Arjen Doelman; has been submitted for publication [7].

---

From a mathematical perspective, the inclusion of generic topographies means spatially varying terms need to be added to the model. These ecosystem models are normally studied using geometric singular perturbation theory. The typical proofs rely heavily on the presence of explicitly solvable (sub)systems – these are not present for generic terrains. In chapter 4 this lack is compensated for by explicit bounds derived from the theory of exponential dichotomies. In this way, existence of stationary pulse solutions is established rigorously and their spectral stability is studied. It is found that, due to the break-down of translation invariance, the presence of spatially varying coefficients can stabilize or destabilize pulse solutions. In particular, a pitchfork bifurcation is found and existence of stationary multi-pulse solutions is shown.

## Stable planar bands

Observations have indicated that depending on the topography different kind of patterns are found; on flat grounds, reported patterns are gaps, mazes and spots, while on sloped terrain, (curved) banded patterns form [42, 64, 136, 176]. It has been shown (mathematically) that bands are unstable against lateral perturbations when movement of water is diffusion dominant (as is the case for flat terrains) [148]. Moreover, numerical analysis revealed 2D stable bands when movement is advection dominant (that is, for large slopes) [155]. In chapter 5, ‘*Stable planar vegetation stripe patterns on sloped terrain in dryland ecosystems*’<sup>6</sup>, the limit case is analyzed, in which the movement of water is purely due to downhill movement.

Here, vegetation bands, stripes and fronts are constructed rigorously in a simple ecosystem model. Mathematically, these solutions consist of (two) fast heteroclinic connections, instead of (one) homoclinic connection that normally is found in the diffusion dominant case. As a consequence, these patterns are now all stable in 2D – aligning with the aforementioned observations. This fact also implies that curved banded patterns can occur, which are typically oriented convex uphill. These provide a possible explanation for the observed vegetation arcs – even in the absence of topographic mechanisms.

## Impact in mathematics beyond ecology

Despite the fact that the mathematical models studied in this thesis were initially designed to understand vegetation patterns in dryland ecosystems, the mathematical results extend beyond this one specific application in ecology. The research in this thesis can easily be adapted to other (singularly perturbed) systems – that can be used to model a wide diversity of systems [10, 13, 15, 113, 115, 178, etc.]. In this regard, chapter 3 contributes to the development of a general coarsening theory of interacting pulses. Chapter 4 develops a method to rigorously study reaction-diffusion equations with spatially varying coefficients by blending the theories of geometric singular perturbations and exponential dichotomies. Finally, the research in chapter 5 explores the stabilizing effect that strong advection has on (stripe) patterns.

---

<sup>6</sup>Joint work with Paul Carter and Arjen Doelman; is set to appear in *Nonlinearity* [6].

## Lines in the Sand

In this thesis, various aspects of the desertification process are analyzed. Here, the focus is on the localized vegetation patterns that arise when water scarcity is high, and in particular on banded vegetation – *Lines in the Sand* (see Figure 1.1) – because these vegetation bands are the easiest to capture mathematically. In the process of desertification these localized vegetation patterns are the last resort; when water scarcity becomes even higher, the ecosystem can no longer sustain any vegetation. Since water and nutrients are better preserved in the soil when vegetation is present, their absence causes the soil to deteriorate: it becomes hard and even less suitable for plants, and as a consequence cracks in the soil – *Lines in the Sand* – appear (see cover image). At this point, it has become very hard to recolonize the soil, and therefore it is said that the desertification process has become (virtually) irreversible. The moment when this happens is sometimes called a tipping point, or more informally a line in the sand. However, as the research in this thesis demonstrates, dryland ecosystems do not possess a single tipping point, but, instead, a cascade of destabilizations – that is, multiple *Lines in the Sand*.

# 2 | Multistability of model and real dryland ecosystems through spatial self-organization

Spatial self-organization of dryland vegetation constitutes one of the most promising indicators for an ecosystem's proximity to desertification. This insight is based on studies of reaction-diffusion models that reproduce visual characteristics of vegetation patterns observed on aerial photographs. However, until now, the development of reliable early warning systems has been hampered by the lack of more in-depth comparisons between model predictions and real ecosystem patterns. In this paper, we combined topographical data, (remotely sensed) optical data and in-situ biomass measurements from two sites in Somalia to generate a multi-level description of dryland vegetation patterns. We performed an in-depth comparison between these observed vegetation pattern characteristics and predictions made by the extended-Klausmeier model for dryland vegetation patterning. Consistent with model predictions, we found that for a given topography, there is multi-stability of ecosystem states with different pattern wavenumbers. Furthermore, observations corroborated model predictions regarding the relationships between pattern wavenumber, total biomass and maximum biomass. In contrast, model predictions regarding the role of slope angles were not corroborated by the empirical data, suggesting that inclusion of small-scale topographical heterogeneity is a promising avenue for future model development. Our findings suggest that patterned dryland ecosystems may be more resilient to environmental change than previously anticipated, but this enhanced resilience crucially depends on the adaptive capacity of vegetation patterns.

## 2.1 Introduction

A key aim of ecological modeling is to generate an understanding of the mechanisms driving observed patterns [110]. A significant challenge in this pursuit, however, is that multiple alternative processes may generate the same emergent outcome [59, 71, 110, 169], a phenomenon also referred to as equifinality [106, 107]. As a result, modeling efforts may reveal that a particular ecological pattern can be explained by a suite of alternative driver mechanisms. Therefore, a match between a pattern simulated with a mechanistic model and a pattern observed in a real ecosystem may only constitute limited support for the modeled mechanism being its true driver [71, 106, 107].

Pattern-oriented modeling [70, 71] aims to address the challenge of equifinality of alternative model formulations. In this approach, model assessment is based on the degree to which the output corresponds to observed patterns. A distinction is made between strong and weak patterns. Strong patterns are the dominant emergent features a model should reproduce, such as the cycles within predator and prey population

sizes, or a spatial distribution of vegetation patches [70, 107]. Weak patterns are typically qualitative relationships, such as the existence of a population over a specific timespan, or a positive association between one state variable and another [70, 107]. Rather than comparing model output to a single strong pattern, additional comparisons to multiple weak patterns, at different scales or levels of organization, provide more power to model validation and selection procedures [70, 71, 107].

A specific type of ecological patterns that has received considerable attention is regular spatial patterning of sessile biota [138]. On flat terrain, the reported patterns are gaps, labyrinths, and spots [136, 176]. On sloping grounds banded patterns form, their regular spacing enabling a description of the characteristic band-inter-band period and wavenumber. Evidence is accumulating that these patterns are self-organized, meaning that the larger-scale patterning is driven by internal ecosystem processes operating at smaller scales [137, 138]. The crucial component in this self-organization process is a long-range negative effect of biota on itself, either directly or through modulation of resource availability. In cases where this long-range negative feedback is coupled to a locally positive feedback, the mechanism creating pattern formation may be linked to the existence of alternative stable states, as well as the possibility of so-called catastrophic shifts between these states [137]. This phenomenon has been most prominently studied in (semi-)arid ecosystems, where decreases in resource availability or increases in grazing pressure may trigger catastrophic shifts from vegetated states to desert states without vegetation [114, 124, 139]. In this context, the formation of regular spatial vegetation patterns may indicate proximity to a threshold of catastrophic change [137].

There is a long tradition in the scientific literature of explaining regular spatial patterning with reaction-diffusion models [35, 129, 165]. In line with this work, a variety of reaction-diffusion models has been applied to investigate self-organization in (semi-)arid ecosystems [67, 95, 136, 176]. Despite the broad support for the findings obtained with these models and their implications for (semi-)arid ecosystem functioning, comparisons of model results with empirical data have mainly been limited to comparison of a single strong pattern, namely the spatial distribution of vegetation patches. Until now, the few studies considering additional weak patterns have shown that reaction-diffusion model simulations successfully reproduce associations between pattern shape and aridity, and associations between pattern shape and slope of the terrain [42]. In addition, models that account for sloped terrain also seem to capture the observed migration of the location of banded patterns in uphill direction [41]. Despite these promising agreements between model results and empirical data, a more systematic comparison between model results and data, based on multiple patterns at different levels of organization [70, 71], was still lacking.

Advanced model analyses that have recently been applied to ecological models have yielded a number of findings which, when confronted with high quality remote sensing products, makes a more systematic comparison possible. More specifically, recent theoretical studies have shown that for a given environmental condition (i.e. a given parameter combination), not a single ecosystem state, but multiple ecosystem states with patterns spanning a range of wavenumbers may be stable, hence observable [155, 158, 170]. The range of observable patterns, across a range of environmental conditions forms a bounded region in (parameter,wavenumber)-space. This region is referred to as the Busse balloon, after F.H. Busse, who studied similar phenomena in the field of fluid dynamics [19]. Although the patterned ecosystem states in the Busse balloon are defined by their wavenumber, other properties, like migration speed and

spatially averaged biomass, have also been studied [150] and are suggested to depend on the position of a system within the Busse balloon. These theoretical findings provide multiple additional weak patterns that can be compared to empirical data, providing opportunities for more powerful tests of the validity of the developed reaction-diffusion models to describe dryland ecosystems.

The aim of this study was to confront theoretical findings regarding pattern wavenumber, biomass and migration speed with the same pattern properties derived from aerial imagery and remote sensing products of banded vegetation patterns in the Horn of Africa, a location with prominent undisturbed presence of vegetation pattern formation. Hence, a multi-level comparison between theory and data in line with the pattern-oriented modeling approach was conducted [70, 71, 107].

## 2.2 Theory

### 2.2.1 Model description

Multiple reaction-diffusion models of dryland vegetation dynamics include a mechanism in which vegetation acts as an ecosystem engineer, locally increasing the influx of available water [67, 95, 136, 176]. Despite the different nuances between these models, a number of predictions can be robustly derived from these frameworks. One of the simplest of these ecosystem models – and the archetype considered in this article – is an extended version of the dryland ecosystem model by Klausmeier [95, 170], which we will refer to as the extended-Klausmeier model. This model describes the interaction between water,  $w$ , and plant biomass,  $n$ . A non-dimensional version of this model is used for the purposes of this article. A dimensional version of the model and the physical meaning of its parameters can be found in appendix 2.A. The model is given by the following equations

$$\begin{cases} \frac{\partial w}{\partial t} &= e \frac{\partial^2 w}{\partial x^2} + \frac{\partial(vw)}{\partial x} + a - w - wn^2, \\ \frac{\partial n}{\partial t} &= \frac{\partial^2 n}{\partial x^2} - mn + wn^2. \end{cases} \quad (2.2.1)$$

The reaction terms model the change in water as a combined effect of rainfall ( $+a$ ), evaporation ( $-w$ ) and uptake by plants ( $-wn^2$ ). The change of plant biomass comes from mortality ( $-mn$ ) and plant growth ( $+wn^2$ ). Dispersion by plants is modeled as diffusion and the movement of water as a combined effect of diffusion and advection. The latter is due to gradients in the terrain, which are proportional to the slope parameter  $v$ .

### 2.2.2 Theoretical outcomes

#### Multi-stability of patterned states

Reaction-advection-diffusion equations in general – and the extended-Klausmeier model in particular – exhibit a vast variety of spatial patterns [109, 127]. However, not all feasible patterns are stable solutions of these models. Which patterned states are stable (hence, observable) depends on the combination of the model parameters. For regular patterns, the concept of the Busse balloon can help to illustrate this dependency [19]. A Busse balloon is a model dependent shape in the (parameter,wavenumber)-space that indicates all combinations of parameter and wavenumber that represent stable solutions of the model. If, for a given set of model parameters, a wavenumber  $k$  lies

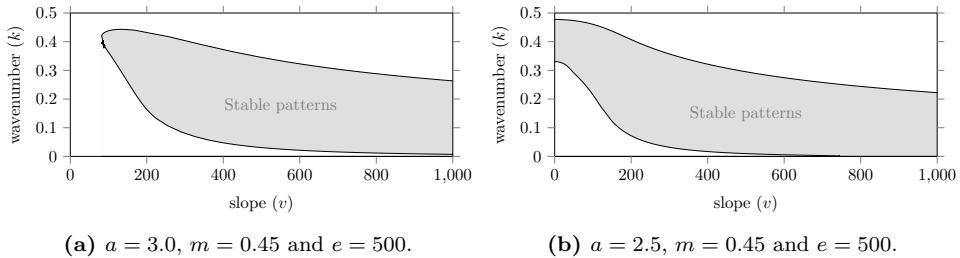


**Figure 2.1** – (*slope, wavenumber*)-Busse balloon slices for the extended-Klausmeier model for two different values of the rainfall parameter  $a$ . A banded pattern solution to the extended-Klausmeier model with slope  $v$  and wavenumber  $k$  is stable if the  $(v, k)$ -combination lies inside the Busse balloon. This indicates that a wide spread of  $(v, k)$ -combinations yields stable banded patterns. The latter are therefore expected for a broad range of wavenumbers – and not for specific  $(v, k)$ -choices only. The shape of a Busse balloon can change between models and between parameter values. This is illustrated in the figures which were computed for different  $a$ -values.

within the Busse balloon, then regular patterns with wavenumber  $k$  are observable. So, in measurements, all (non-transient) patterns are expected to be present in the Busse balloon.

Typically, the Busse balloon is a high-dimensional structure due to the number of parameters in a system. Therefore, usually, only one parameter is varied when a Busse balloon is visualized. This produces a 2D-slice of the full Busse balloon. In the context of desertification research, the straightforward choice would be to vary the rainfall [158]. However, mean annual rainfall was relatively constant in our study sites during the observation period considered. Instead, topography (i.e. the slope gradient) comprised the main source of environmental variation within our study areas. Thus, relevant theoretical predictions for our study sites can be generated by varying the slope parameter  $v$  (while keeping rainfall constant). Here, we present two of such 2D-Busse balloon slices for the extended-Klausmeier model (Figure 2.1), which were constructed by tracking the boundary of the Busse balloon using numerical continuation methods [133, 154, 155, 158]. The shaded region in these figures indicates the combinations of pattern wavenumber  $k$  and slope  $v$  for which stable solutions exist. Thus, the model shows multi-stability; a given slope  $v$  can sustain a continuous range of wavenumbers  $k$ . That is, knowing all current parameter values of a system is not enough to predict the pattern, but only gives a range of possible wavenumbers – as indicated by the Busse balloon. For patterns with wavenumbers above this range, there are too few resources to sustain all bands; below this range, there is an abundance of resources that leads to the formation of additional vegetation bands.

It is in general not possible to predict which of these wavenumbers is selected at a specific location; small changes in the (entire) history of environmental changes can have large impacts on the wavenumber that is currently selected [150, 153]. To understand these hysteretic dynamics, it is vital to acknowledge that model patterns do not change their wavenumber unless they have to [154, 158]: if an environmental change forces the system outside of the Busse balloon, the current pattern has become unstable, and will need to adapt into a new pattern that is again stable – thus part of the Busse balloon. During this (fast) adaption, only part of the vegetation bands are lost, while the remaining bands increase in volume; these adaptations thus have

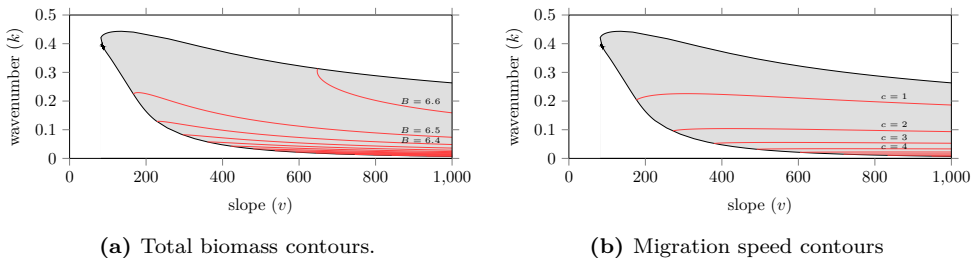


**Figure 2.2** –  $(slope, wavenumber)$ -Busse balloon slices for the extended Klausmeier model that include contours for the total biomass (per area)  $B$  (a) and the migration speed  $c$  (b). Biomass (per area) is positively correlated with both wavenumber  $k$  and slope  $v$ ; the migration speed is negatively correlated with the wavenumber  $k$ . Model parameters used:  $a = 3$ ,  $m = 0.45$ ,  $e = 500$ .

limited effect on the total biomass in the system [158]. Hence, multiple wavenumber adaptations are expected to occur after each other that will, gradually, lead to a complete desertification of the system [158]. Both the moment of a destabilization and the then occurring wavenumber adaption can be vastly different depending on (historical) environmental conditions [8, 150, 153]. Thus, indeed, precisely which wavenumber  $k$  gets selected at each of these destabilizations is difficult to predict.

Numerical simulations help to get an insight in the kind of wavenumber distribution one ought to expect in observations. To illustrate the typical spread in wavenumber, a total of 200 simulations on a flat terrain ( $v = 0$ ) were run, where the rainfall parameter was slowly decreased from  $a = 3$  to  $a = 0.5$ . The initial configurations for these runs were chosen randomly, but close to the equilibrium state of uniform biomass before the onset of patterns (between 90% and 110% of the uniform vegetated equilibrium state). At the end of each simulation – after several pattern selections – the wavenumber of the remaining pattern was measured. This gives a snapshot of the wavenumber distribution, similar to the snapshots acquired from observations. Note that a similar experiment was done before, albeit on a much smaller scale [154]. The histogram of the resulting wavenumbers is shown in Figure 2.3. It shows a substantial spread, which goes from a wavenumber of 0.08 to 0.16 (a difference of 100%).

### Biomass & migration speed

Besides a wavenumber, each ecosystem state also has a specific biomass and a specific pattern migration speed. The biomass of regular patterned states has been studied using numerical simulations [158] and more general formulas have been derived for patterns with small wavenumber [8]. Both indicate that the biomass (per unit area) is positively correlated with both the wavenumber  $k$  of the pattern and the slope parameter  $v$  [158]; see also Figure 2.2a. This has a physical interpretation: both steeper slopes and higher wavenumbers (lower wavelengths) reduce the time it takes for water to reach vegetation bands, and thereby reduce water losses during the transportation process. As a result, the vegetation will be able to harvest water from the uphill inter-bands more effectively. The biomass per wavelength is also of interest. The same studies indicate that the band biomass (per wavelength) is increased when the wavenumber  $k$  is decreased and when the slope  $v$  is increased. Hence, vegetation bands are expected to have more biomass when other vegetation is farther away, because of



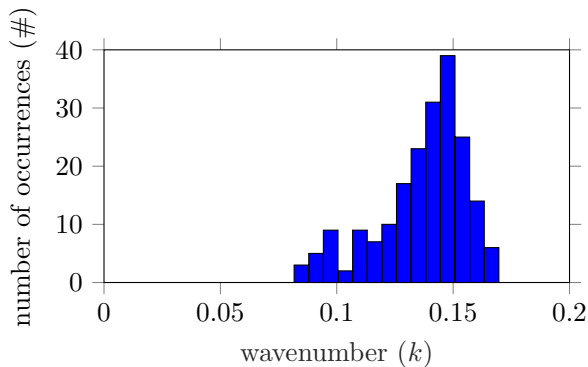


**Figure 2.3** – Histogram demonstrating a spread in wavenumber ( $k$ ) at the end of 200 simulations of the extended-Klausmeier model on a flat terrain ( $v = 0$ ) with model parameters  $e = 500$  and  $m = 0.45$ . These simulations had a random initial configuration close to a stable fully vegetated state. A climate change was simulated by decreasing the rainfall parameter  $a$  linearly from 3 to 0.5 over the course of  $10^5$  time unit, causing several pattern selections and corresponding changes in wavenumber.

the larger (upslope) inter-band area water can be collected from.

The theoretical predictions for migration speed (of a pattern’s location) are a bit more subtle. For terrains with a constant slope, numerical simulations have been done [149, 151] and general formulas have been determined for patterns with small wavenumber [8, 148]. In these idealized limit cases, migration speed is negatively correlated with wavenumber  $k$  and positively correlated with slope  $v$ . However, beyond these idealizations, numerical computations show the contour lines are slightly humped, see Figure 2.2b. This indicates a (slightly) negative correlation between speed and slope  $v$  for large slopes.

### 2.2.3 Testable predictions

The theoretical findings in this section lead to predictions that can be confronted with the field data. First of all, the model possesses a Busse balloon, which should lead to a wide spread in observable pattern wavenumbers (Figures 2.1 and 2.3). Moreover, biomass and migration speed are affected by pattern wavenumber. The biomass (per unit area) is expected to be positively correlated with both the wavenumber and the slope of the terrain (Figure 2.2a). Migration speed is expected to decrease as a function of pattern wavenumber; the effect of slope on the migration speed is context-specific, as it can be either positive or negative depending on the specific topographical and environmental conditions (Figure 2.2b).

## 2.3 Data acquisition & processing

For this comparison study, two sites were selected in Somalia. The first one ( $8^{\circ}0'14''$  to  $8^{\circ}15'11''$ N;  $47^{\circ}11'54''$  to  $47^{\circ}31'4''$ E) is located in the Haud pastoral region, which will be referred to as the ‘Haud’ site. The other site ( $9^{\circ}18'49''$  to  $9^{\circ}34'34''$ N;  $48^{\circ}8'15''$  to  $48^{\circ}43'15''$ E) is located in the Sool-Plateau pastoral area and will be called the ‘Sool’ site. Both sites mainly exhibit banded vegetation and have ground slopes ranging from

0% to 1%. Vegetation mainly constitutes of perennial grasses, which typically have an average lifetime of 1-7 years [20, 108, 182]. A more detailed description of these sites can be found in appendix 2.B; a map with the location of these sites along with the mean annual rainfall in these areas is shown in Figure 2.7.

To study the pattern properties in these study areas, each site was divided into square windows (of size  $750m \times 750m$  for the Haud site and of size  $1010m \times 1010m$  for the Sool site). As has been done in previous studies, the type of pattern (e.g. bare soil, banded vegetation), along with its wavenumber, was determined using spectral analysis [4, 33, 42, 128]. Only those windows were kept that exhibited banded vegetation with a wavenumber that could be determined with enough certainty (i.e. between 0.4 and 2.5 cycles per  $100m$ ). Moreover, windows with a too large curvature were ignored, because the theoretical predictions only apply to terrains with a constant slope. To obtain data on the migration speed of the banded vegetation, a cross-spectral analysis was performed, along the lines of previous studies [5, 41, 68]. A more in-depth explanation of the processing steps can be found in appendix 2.D.

The topographical data used in this article were derived from the Advanced Land Observation Satellite (ALOS) World 3D (AW3D) digital raster elevation model; biomass data for the Haud site have been retrieved from a recently made map on (above-ground) biomass of African savannahs and woodlands [14] (no reliable data for the Sool site was available). Finally, optical data was acquired from various sources: three multi-spectral WorldView-2 images were mosaicked and used as reference for the Haud site; a panchromatic Ikonos 'Geo' Imagery was acquired for the same site. For the Sool site, six WorldView-2 images were used and a panchromatic Satellite Pour l'Observation de la Terre (SPOT) 4 image preprocessed to level 2A was used as reference layer (©Cnes 2004 – Spot Image distribution). Moreover, two  $7\mu m$  digitized panchromatic declassified Corona spy satellite image, national intelligence reconnaissance system, available from the US Geological Survey, were obtained for the Haud and the Sool sites. More information about these data sets can be found in appendix 2.C.

## 2.4 Results

### Empirical Busse balloon

The most prominent pattern property studied in this article is the pattern wavenumber, which was derived from aerial imagery. The resulting distribution of wavenumbers is reported in Figure 2.4 (a map with the spatial distribution of wavenumbers over the study sites is shown in Figure 2.8). These figures show the number of windows that have a particular slope-wavenumber combination. Also given is the relative frequency that indicates the spread of wavenumbers across all windows. The data display banded vegetation with wavenumbers roughly between 0.4 and 2.0 cycles per  $100m$ . Importantly, this large spread is present for all of the ground slope values which had a representative sample size and could not be explained by present heterogeneities in elevation or rainfall. This shows that for a given environmental condition not a single wavenumber pattern, but rather multiple patterns spanning a sizable range of wavenumbers are observable. Additionally, measurements used to determine the migration speed show barely any changes in wavenumber over the scope of 39 years (consistent with [68]), indicating that these patterns are in fact quite stable. Therefore, the observations are in agreement with the existence of a Busse balloon in the real ecosystem.

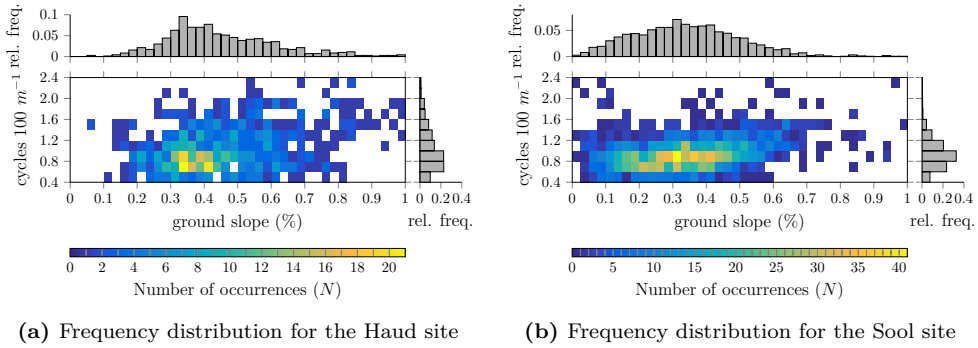


**Figure 2.4** – Frequency distribution of banded patterns as function of ground slope and wavenumber (number of cycles per 100m) for the Haud site (a) and Sool site (b). The distribution on the right indicates the relative frequency of banded vegetation with corresponding wavenumber. The color gradient indicates the amount of windows ( $N$ ).

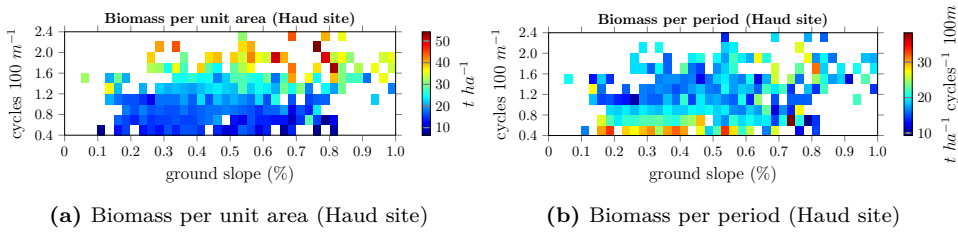


**Figure 2.5** – Biomass distribution per area (a) and per period (b) as a function of ground slope and wavenumber (cycles per 100m) for the Haud site. The color gradient indicates the amount of biomass measured for a particular (*slope*, *wavenumber*)-combination.

## Biomass and migration speed

The processed biomass data for the Haud site is shown in Figure 2.5. In Figure 2.5a the relation between biomass per area (in  $t\ ha^{-1}$ ) is plotted against the ground slope and the wavenumber. From the same data the biomass per period is computed – which is biomass per area divided by the window’s wavenumber. The resulting plot is given in Figure 2.5b. The measurements of biomass show agreement with theoretical predictions of model studies; in both, the total biomass increases (all slopes:  $r^2 = 0.64$ ,  $n = 714$ ,  $P < 0.001$ ; linear regression) and the biomass per period decreases when the wavenumber increases (all slopes:  $r^2 = 0.09$ ,  $n = 714$ ,  $P < 0.001$ ; linear regression). However, a more in-depth inspection reveals disagreements. For one, the effect of ground slope is not strongly present in the data, though its effect is clear in the extended-Klausmeier model (Figure 2.2a). Additionally, the more refined details of wavenumber dependence also differ (it is concave in the theoretical model and convex in the real-life data).

The migration speed is plotted in Figure 2.6 for both the Haud and the Sool sites. These measurements show an increase in speed when the wavenumber decreases (Haud:  $r^2 = 0.43$ ,  $n = 104$ ,  $P < 0.001$ ; Sool:  $r^2 = 0.45$ ,  $n = 79$ ,  $P < 0.001$ ; linear regression), corroborating theoretical predictions (see Figure 2.2b).

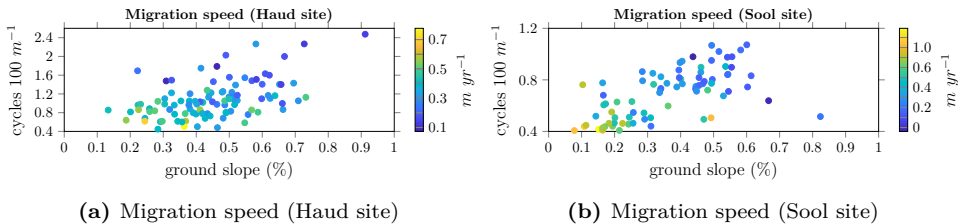


**Figure 2.6** – Observed (average) migration speed of vegetation bands in the Haud (a) and the Sool (b) sites over the course of 39 years as a function of ground slope and wavenumber (cycles per  $100m$ ). The color gradient indicates the migration speed for a particular (*slope*, *wavenumber*)-combination. The sign indicates the direction of migration relative to the slope, with positive and negative values indicating upslope and downslope migration respectively.

## 2.5 Discussion

Leading ecological frameworks emphasize the potential role of regular spatial vegetation patterns as indicators for proximity to catastrophic ecosystem shifts [137, 144]. In these frameworks, however, mono-stability of patterns is implicitly assumed, suggesting that for a given environmental condition there is only one stable vegetated state, i.e. a single pattern with a specific wavelength [137, 144]. Subsequent theoretical insights have challenged this view, highlighting the possibility of multi-stability of patterns, bounded by the so-called Busse balloon. In this study, we provide empirical evidence corroborating the existence of a Busse balloon for stable vegetation patterns in dryland ecosystems. Specifically, our two study sites in Somalia revealed the sustained (i.e. over a 39 year period) co-occurrence of banded vegetation with wavenumbers varying over a substantial range. Our findings have major implications for the way in which vegetation patterns indicate ecosystem resilience and mediate ecosystem responses to environmental change.

Specifically, the existence of a Busse balloon implies that an ecosystem’s resilience can no longer merely be defined by the magnitude of environmental change it can cope with [82]. In these systems there is not one tipping point, but a cascade of destabilizations – indicated by the boundary of the Busse balloon. When environmental changes push a patterned ecosystem beyond the boundary of the Busse balloon, a wavelength adaptation occurs, and typically part of the vegetation patches are lost, while the remaining patches grow in size. The extent of these adaptations depends on the rate of environmental change [150, 156, 157, 158]. Moreover, human activities or natural variations can cause local disturbances, diminishing the regularity of ecosystem patterns. The recovery process from such disturbances may involve a rearrangement of patches in the landscape [8, 158]. Again, the extent to which such recovery is possible depends on the rate of environmental change that the ecosystem is exposed to [157]. Hence, the existence of a Busse balloon of stable dryland vegetation patterns suggests that adaptability of patches to changing environmental conditions provides a more comprehensive indicator for the ecosystem’s resilience than the shape of the pattern itself, as suggested in current leading frameworks [137, 144]. To fully comprehend the consequences of this, it is necessary to provide a more thorough understanding of what determines the spatial rearrangement of vegetation patches resulting from disturbances, environmental changes, and spatial heterogeneities in the landscape.

The pattern-oriented modeling approach was mainly developed to aid model development and design, but the approach can also be used to evaluate the success of existing models to explain multiple strong and weak patterns observed [70]. This so-called ‘reverse pattern-oriented modeling’ approach [70] was used in the current study. Such systematic comparisons between model predictions and empirical data can be part of an iterative process toward further model improvement [106, 107]. In this context, it is interesting to note the discrepancy that we observed between model predictions and field measurements of the influence of the ground slope on pattern migration speeds. Because topography critically changes the distribution of water within ecosystems, it also alters the migration speed of patterns. Therefore, it is of interest to determine the effects of more complex topographies for dryland ecosystem dynamics.

Moreover, the available empirical data aligns with theoretical predictions on both strong and weak patterns. However, environmental conditions were characterized by differences in slope gradient only. Although, indeed, the topography comprised the main source of environmental variation, other less pronounced heterogeneities are present and can cause spreads in wavenumber. The observed spread could not be attributed to variation in rainfall or elevation, but the role of other heterogeneities (e.g. soil composition and grazing activity) could not be fully determined for lack of precise and accurate data sets. When these become more readily available, further research might infer to which extent the observed wavenumber spread is explained by these environmental drivers.

Since their appearance on aerial photographs in the 1950s [111], the origin of regular vegetation patterns in dryland ecosystems has been a topic of fascination within the scientific community. The study of these patterns through reaction-diffusion modeling subsequently highlighted the importance of these patterns for the functioning of dryland ecosystems, and their response to environmental change. The recent increase in the availability of optical and topographical data provides unprecedented opportunities to confront model predictions with empirical data [107, 153]. In this study, we combined these data sources with in-situ measurements of biomass, enabling the comparison of multiple pattern characteristics of Somalia drylands with predictions derived from reaction-diffusion modeling. The empirical evidence corroborates theories of multi-stability of patterned vegetation states, improving our understanding of these systems’ resilience to environmental changes. In addition, our results call for more detailed investigations of the role of small-scale topographic variability in pattern formation and migration.

## Acknowledgments

We thank Lotte Sewalt for help with the initiation of this study. This study was financially supported by a joint grant of Arjen Doelman and Max Rietkerk within the Mathematics of Planet Earth program of the Netherlands Organization of Scientific Research (NWO). Koen Siteur was supported by the National Key Research and Development Program of China (2017YFC0506001), the National Natural Science Foundation of China (41676084) and the EU Horizon 2020 project Marine Ecosystem Restoration in European Seas (MERCES) (689518).

## Appendices

### 2.A Dimensional extended-Klausmeier

The dimensional extended-Klausmeier model is given by (2.A.1). The model used throughout the paper, equation (2.2.1), can be obtained from the dimensional version by the right set of scaling. Following [158, Appendix A], the required scaling is given in (2.A.2) for the variables and in (2.A.3) for the parameters of the model.

$$\begin{cases} \frac{\partial W}{\partial T} &= E \frac{\partial^2 W}{\partial X^2} + \frac{\partial(VW)}{\partial X} + A - LW - RWN^2 \\ \frac{\partial N}{\partial T} &= D \frac{\partial^2 N}{\partial X^2} + RJWN^2 - MN \end{cases} \quad (2.A.1)$$

$$w = \frac{\sqrt{RJ}}{\sqrt{L}}W \quad n = \frac{\sqrt{R}}{\sqrt{L}}N \quad x = \frac{\sqrt{L}}{\sqrt{D}}X \quad t = LT \quad (2.A.2)$$

$$a = \frac{\sqrt{RJ}}{L\sqrt{L}}A \quad m = \frac{1}{L}M \quad v = \frac{1}{\sqrt{LD}}V \quad e = \frac{E}{D} \quad (2.A.3)$$

In these equations, water is supplied to the system at a rate  $+A$ , modeling uniform rainfall. Because of evaporation, water is lost at a rate  $-LW$ ; water is also lost through uptake by plants, at rate  $-RWN^2$ . The parameter  $J$  models the increase of biomass per unit of water consumed, which results in the reproduction of plants at rate  $+RJWN^2$ . Plant mortality is modeled as  $-MN$ . The parameter  $V$  is the speed at which water flows downhill; this is proportional to the slope gradient. Finally,  $E$  is the diffusion coefficient of water;  $D$  is the diffusion coefficient of vegetation, modeling the dispersal of biomass. See also [95].

### 2.B Description of study sites

For this study, two sites in Somalia were selected that exhibit mostly banded vegetation. The Haud site is a  $35km$  by  $28km$  study area ( $8^\circ 0'14''$  to  $8^\circ 15'11''N$ ;  $47^\circ 11'54''$  to  $47^\circ 31'4''E$ ) at  $650-750m$  elevation in the Haud pastoral region – see also Figure 2.7. Here, banded vegetation dominates the landscape with some minor occurrences of gapped vegetation on flat ground on the summits of rolling hills. Bands display a broad range of wavelengths (from  $60m$  to  $200m$ ). Ground slope ranges from 0 to 1%. Mean annual precipitation, ranging from  $210mm$  to  $270mm$ , is distributed in two rainy seasons around spring (April–May) and fall (September–November) separated by two dry seasons. Rainfall data was extracted from Climate Hazards Group InfraRed Precipitation with Stations [63]. Estimates were provided by [43].

In the north-eastern corner of this area near Kalabaydh city, the soils of the bands and inter-bands are very similar [81]. Moreover, the large perennial tussock grass *Andropogon kelleri* dominates the core of the band along with some scattered small trees and bushes [81]. Characteristically, plants are sparsely distributed on the downslope side of the bands. Along this edge and below it, in the bare inter-band, dead trees of all of the species found within the bands were present. Along the bands' upslope side, some initial colonization by two perennial grass species, tussock-forming *Chrysopogon aucheri* var. *quinqueplumis* and stoloniferous *Dactyloctenium scindicum*, was observed [81]. Although the lifespan of perennial grasses is highly variable, ranging from less than a year to multiple decades [108], the average lifespan of perennial

grasses in arid and semi-arid environments is typically 1-7 years [20, 108, 182]. Upon inspection of satellite imageries taken 39 years apart, an upslope migration speed of  $0.3m\ yr^{-1}$  was observed [41].

The Sool site is an approximately  $77km$  by  $29km$  study site, located  $190km$  to the NE of the Haud site ( $9^{\circ}18'49''$  to  $9^{\circ}34'34''N$ ;  $48^{\circ}8'15''$  to  $48^{\circ}43'15''E$ ); it is located in the Sool-Plateau pastoral area, which has more arid conditions ( $100mm$ - $140mm$ ) and higher elevations ( $900m$ - $1000m$ ) – see also Figure 2.7. Here, the ground slope ranges from 0 to 1%, and ground is either bare or covered with banded vegetation which sometimes displays a dashed physiognomy. To the authors knowledge, there is no published record of the composition of these vegetated bands and associated soils. Remote sensing analysis of vegetation dynamic in this area over the last decades have shown a continuous upslope migration of the bands as well as a change in band width. However, no change in wavelength has been observed [41, 68].

## 2.C Data sets

### 2.C.1 Topographical data

For both sites, topographical data was retrieved from the ALOS World 3D  $30m$  (AW3D30, v. 2.1) digital raster elevation model. This model describes the height above sea level (in  $m$ , rounded to the nearest integer), at a ground resolution of approximately  $30m$  at the equator. The elevation data was preprocessed for the removal of artifacts by applying a global soft-thresholding on its dual tree complex wavelet transform. Specifically, we set a threshold of 0.9 on the first five dual-tree complex wavelet transform levels. From the preprocessed data, we calculated the slope gradient (in %) and slope aspect (in degrees). We first extracted square DEM windows of  $33$  by  $33$  cells (i.e. approximately  $990m \times 990m$ ), centered on the image windows. We then applied a least squares fitting procedure of an unconstrained quadratic surface on the unweighted elevation values. From the first derivatives of this fitted surface, evaluated at the focal cell, we could then calculate slope gradient and aspect analytically, following [158]. Complex topographic features were discarded from subsequent analysis by ignoring windows (see below) with quadratic fit RMSE above  $1m$  or a total curvature (as defined by [147]) above  $10^{-10}$  radians per  $m^2$ .

### 2.C.2 Biomass measurements

Recently, a map has been made with data on (above-ground) biomass of African savannahs and woodlands at a resolution of  $25m$  [14], which provides the biomass data of the patterns studied in this article. This map is built from 2010 L-band PALSAR mosaic produced by JAXA following a method adapted from [116], while the perturbing sources that affect the SAR data have been minimized: the environmental effects (soil and vegetation moisture) were reduced by stratifying the African continent into wet/dry season areas, and the speckle noise inherent to SAR data acquisitions was decreased by applying a multi-image filter developed by [17] that preserves the spatial resolution of the images. Then, the sensitivity of the radar backscatter to AGB was analyzed to develop a direct model relating the PALSAR backscatter to AGB, calibrated with the help of in-situ and ancillary data. The in-situ data were composed of 144 selected field plots, located in 8 countries (Cameroon, Burkina Faso,

Malawi, Mali, Ghana, Mozambique, Botswana and South Africa), with plot size larger than  $0.25ha$  and a mean plot size of  $0.89ha$ .

### 2.C.3 Optical data

Three multispectral WorldView-2 images, acquired on December 25th 2011, January 21st 2012 and July 21st 2012, were mosaicked and used as reference orthoimage for the Haud site. For the diachronic study, a panchromatic Ikonos “Geo” imagery, with a  $1m$  nominal ground resolution, was used as the reference layer. It was acquired on January 7th 2006. Orthorectification was performed using a rational polynomial coefficient (RPC) camera model block adjustment without ground control points [72].

A mosaic of six WorldView-2 images, acquired between February 3rd 2011 and September 12th 2013, was used for the Sool sites. For the diachronic study, a panchromatic SPOT4 image preprocessed to level 2A, with a  $10m$  nominal ground resolution, was used as reference layer (©Cnes 2004 – Spot Image distribution). It was acquired on February 18th 2004.

Two  $7\mu m$  digitized panchromatic declassified Corona spy satellite image, national intelligence reconnaissance system, available from the USGS, were acquired on February 28th 1967 (KH-4A, mission 1039, AFT camera) and December 12th 1967 (KH-4B, mission 1102, FWD camera), respectively for the Haud and the Sool. The images were co-registered with the orthorectified reference imagery. Co-registration was performed using a third-order polynomial adjustment using landmarks such as geological features, crossroads, isolated trees, or large termite nests. We obtained an RMS adjustment error below the KH-4A ground resolution, which is  $3m$  for this area. The resolution of the imagery was then lowered through pixel averaging to match the coarsest image pair.

The analysis of pattern wavelength was performed over the full area of the study sites. However, for the diachronic study, a subset of each of the sites covered by the historic and reference image was selected. Projection and datum for all data sets were WGS 1984, UTM Zone 38N and 39N respectively for the Haud and the Sool sites.

## 2.D Data processing

### 2.D.1 Spectral analysis, direction of anisotropy and wavelength

On visible light digital images over drylands, bright pixels correspond to bare soil, intermediate gray-scale levels to closed grass cover, and darker pixels to woody vegetation. As a first approximation, gray-scale levels can thus be considered as a monotonically decreasing function of the aboveground biomass [34]. This approximation allows us to analyze the spatiotemporal dynamics of biomass organization through image analysis techniques.

We used a Fourier windowing technique equivalent to short time Fourier transforms to obtain spatial maps of dominant pattern wavelength  $\lambda$  and orientation  $\theta$  from the satellite images as previously used for banded vegetation systems [4, 33, 42, 128]. We applied a two-dimensional (2D) Fourier transform to obtain the power spectrum within square, non-overlapping moving windows. In order to maintain resolution and signal-to-noise ratio a boxcar windowing function to signal was applied. This choice is, in this case, reasonable as only one periodic component is expected to be present in the vegetation. The technique provides information about the local wave-vector



$k = k_x\hat{x} + k_y\hat{y}$ . The two-dimensional (2D) fast Fourier transform  $\tilde{f}(k_x, k_y)$  of the pattern of biomass  $f(x, y)$  was obtained for each window  $\tilde{f}(k)$  of size  $L \times L$ . As  $L$  increases, the spatial resolution, i.e. localization in space of frequency or orientation change, is reduced. Conversely, as  $L$  decreases, the frequency resolution is decreased, i.e. the likelihood of separating frequency components close together in Fourier space. To optimize both,  $L$  was chosen to be at least  $3\lambda$ , i.e.  $750m$  and  $1010m$  respectively for the Haud and the Sool sites.

To separate the characteristics of the signal that are meaningful for this study, each  $k$ , of frequency  $2\pi/\lambda$  (wavenumber), was decomposed into its orientation  $\theta$  and its magnitude. For each window, the power spectrum  $S(k) = |\tilde{f}(k)|^2$  was computed. The power spectrum measures how the variation, or power, of the pattern is distributed over the wavevectors  $k$ , of different frequencies and spatial directions. To identify the dominant  $k$  in each window,  $S(k)$  was binned into annular rings of unit width [135]. The resulting radial spectrum thus quantifies the contribution of successive ranges of spatial frequencies to the image variance across all orientations.

To deconvolve the natural  $1/k$  scaling of the power spectrum, the total power within each annular ring,  $S(k)$ , was computed instead of the mean power. The location peak of this total power is used to define the most energetic wavenumber,  $k_1$ . To compensate for the discrete  $k$ -resolution in Fourier space, the location of the weighted average  $k_1 := (\sum_k kS(k)) / (\sum_k S(k))$  was computed over all rings that formed part of the peak and contained more than 70% of the peak power.

The patterns were characterized in terms of level and orientation of anisotropy (i.e. direction orthogonal to the long axis of the bands) following [42]. The average pattern orientation was studied using the circular mean direction weighted by the power spectrum values,  $\bar{\theta} := \frac{1}{2}\arctan2(S, C)$ , where

$$S := \left( \sum_k 2k_{x,y} \sin \theta_{x,y} \right) / \left( \sum_k k \right)$$

and

$$C := \left( \sum_k 2k_{x,y} \cos \theta_{x,y} \right) / \left( \sum_k k \right).$$

The norm of the resultant vector,  $\bar{R} := \sqrt{S^2 + C^2} / (\sum_k k)$ , was used as an index of pattern anisotropy. The division by the sum of periodogram amplitudes ensures bounding between zero (perfect isotropy) and one (all variance concentrated in one direction, i.e. perfect bands). Pattern orientation features were extracted from the power spectrum, within the frequency ring characterizing periodic vegetation patterns, i.e. between 0.4 and 2.5 cycles  $100m^{-1}$  for both the Haud and the Sool site, to exclude anisotropy sources resulting from large scale gradients or small scale (anthropogenic) features.

## 2.D.2 Pattern classification

The vegetation cover of each window was quantified by converting the gray-scale intensity image to a binary image using the Otsu thresholding method [125]. Windows with less than 15% vegetation cover were considered as bare soil and discarded. Windows with dominant patterns within the acceptable range (i.e. between 0.4 and 2.5 cycles

$100m^{-1}$  for both sites) and with anisotropy index above 0.2 were considered as banded patterns.

### 2.D.3 Cross-spectral analysis and migration speed

Scale specific comparisons between pairs of periodic 2D signals – in this case, images taken at different dates – can be performed through 2D Fourier cross-spectral analysis. In principle, this means identifying the frequencies and orientations of patterns dominating in any two images as well as possible shifts among them. Correction of radiometric variability between dates is not required since Fourier coefficients are invariant to linear rescaling of gray-scale levels. A detailed mathematical development of the analysis can be found in [5]. The procedure can be summarized as follows [41, 68].

To assess band migration distance for each temporal pair of image windows, a coherency spectrum and a phase spectrum were computed. The coherency spectrum expresses the correlation between the frequency components of the Fourier spectra of the pair of windows. For each spatial frequency, the coherency value is interpreted in a similar way to the classical Pearson’s coefficient but in absolute values, because the sign of the correlation is expressed by the phase spectrum. For each window pair, the maximum value of coherency and its associated frequency were recorded along the direction of maximal anisotropy computed for the first acquisition date. Window pairs with a maximum coherency below 0.9 were rejected from the analysis, because this indicates that pattern characteristics (wavelength and orientation) changed between the dates. Rejected windows often corresponded to man-made perturbations or ephemeral patterns, which are not the subject of this study. The obtained frequency value therefore corresponds to a pattern of constant scale and orientations dominating at both acquisition dates. The corresponding phase-spectrum value provides the phase difference, i.e., the angular distance, between the selected frequency components at both dates in the maximal anisotropy direction. This value is defined between  $-180$  and  $180$  degrees, with the sign representing the forward (+) vs. backward (–) displacement, with the direction of reference as the upslope direction. Angular distances were then converted into meters by multiplying the phase difference by the wavelength, which in turn were converted to an average migration speed for the time period. This conversion allows for inter-site comparisons independent of varying time intervals. An inherent limitation to this procedure is that only migration distances not exceeding half the wavelength will be correctly estimated (phase saturation). This condition was verified by visual inspection prior to image analysis.

### 2.D.4 Assessment of uncertainty in calculations of slope gradient and aspect from topographical data

As the digital raster elevation model contains errors, these will propagate into derived estimates of slope gradient and aspect. Ideally, one would use ground observations (e.g. using differential global navigation satellite systems) to assess the magnitude of these errors (e.g. [131]). Since such observations are not available for our study areas, we used a simulation method to evaluate the propagation of error from the elevation data to the estimates of slope gradient and aspect. Specifically, we created artificial elevation grids with a fixed (from here referred to as ‘true’) slope and aspect, and added to these grids (normally distributed) random errors with a similar standard deviation as observed in the AW3D30 dataset. The resulting elevation values were rounded to the nearest integers, as this is also done in the AW3D30 dataset. Then,

utilizing the same procedures as described above (see section 2.C2.C.1), we derived slope gradients and aspects from these simulated grids. Comparison of this ‘observed’ slope and aspect and the ‘true’ slope and aspect of the grid yielded insight in the propagation of errors from the elevation model to the calculated metrics. Seven fixed slope levels were considered: 0; 0.025; 0.05; 0.1; 0.2; 0.3 and 0.4%. For each level, we simulated 10,000 replicate grids of errors that were added to the fixed slope level. For each replicate, the aspect was a randomly assigned value between 0 and 360 degrees.

Following the above procedure, we found that the distributions of errors in the calculated slope gradients and aspects were relatively small, for all slope levels considered (Figure 2.9). Because the estimated slope is bounded between zero and positive infinity, a small positive bias was observed for slopes less than 0.1%. For slopes of 0.025% and higher, the RMSE is 0.010% and 95% of the observed errors for slopes of 0.1% or higher are within  $\pm 0.016\%$  (5<sup>th</sup> and 95<sup>th</sup> percentiles). For aspect, the magnitude of errors was inversely proportional to the magnitude of the slopes (abscissa; Figure 2.9). For slopes of 0.2% and higher, the RMSE is 2.9 degrees or lower, and 95% of the observed errors are within  $\pm 4.8$  degrees (5<sup>th</sup> and 95<sup>th</sup> percentiles). These results show that the errors in calculated slopes and aspects were relatively small compared to the observed range in the dataset. Hence, it is unlikely that correlations between pattern metrics and slope gradients, as observed in the main text, are strongly affected by the errors originating from the underlying topographical database.

Moreover, it should be noted that the above procedure may even be overestimating the errors associated with the AW3D30 dataset (from here referred to as the 30m elevation dataset). To generate the simulated errors, we used the global average standard deviation of the difference between the original AW3D 5m elevation dataset (from here referred to as the 5m dataset), from which the 30m dataset has been derived, and a reference LiDAR dataset. This standard deviation is 1.73m for gently sloping terrain (below 17.6%) [162]. However, as the 30m elevation dataset was produced by averaging non-overlapping windows of 7 by 7 pixels of the 5m elevation dataset, the resulting standard deviation will be lower [161]. Additionally, the ground slope in our study areas is at the lower end of the 0-17.6% range, namely below 1.5%, and therefore likely to suffer from smaller errors than reported for the whole range. Finally, the Somali area we are studying displays relatively small errors in elevation measurements compared to other areas of the world [162].

## 2.D.5 Assessment of uncertainty in estimation of pattern frequency from optical imagery

The estimation of the dominant pattern frequency using a Fourier windowing technique introduces an unknown uncertainty in these estimations. This uncertainty stems from the decomposition of the signal into a discrete set of frequencies and from the noise in the analyzed (non-stationary) signal. To assess the model’s uncertainty in the wavenumber estimations, we have used a simulation method. Specifically, we simulated 200 synthetic images, representing a two-dimensional sinusoid of each frequency class between 0.4 and 2.4 cycles  $100m^{-1}$ , with step size of 0.2. The directions of the sinusoidal waves were selected randomly and the signal was standardized to have zero mean and standard deviation of one. To mimic real images of vegetation patterns, we have added red noise with zero mean and standard deviation of 0.5 to each simulated signal. Red noise is a self-similar, or fractal, random spatial structure; this is a desirable property here because these are common in nature and especially in natural

landscapes [94]. The noise was created using the Fourier synthesis technique with an energy spectrum exponent of 0.5 [44]. Finally, in order to account for the fact that reflectance values are constant over the width of both vegetated and bare bands, the signal was converted to binomial values; that is, values between 0 and 1 were rounded to the nearest integer value. Several examples of simulated bands are presented in Figure 2.11.

Using the characteristics of the optical image windows of the Haud site (cell-size of  $2.36m$  and windows 317 by 317 cells), the root-mean-square error of the estimated frequency was  $0.082 \text{ cycles } 100m^{-1}$ . For the Sool (cell-size of  $2.36m$  and windows 425 by 425 cells), the root-mean-square error was  $0.044 \text{ cycles } 100m^{-1}$ . The magnitude of this error is significantly less than the observed variability in frequency in both sites (for every slope bin of Figure 3 in the main text, Levene's test,  $P < 0.001$ ), showing significance of the observed wavenumber spread in both study sites.

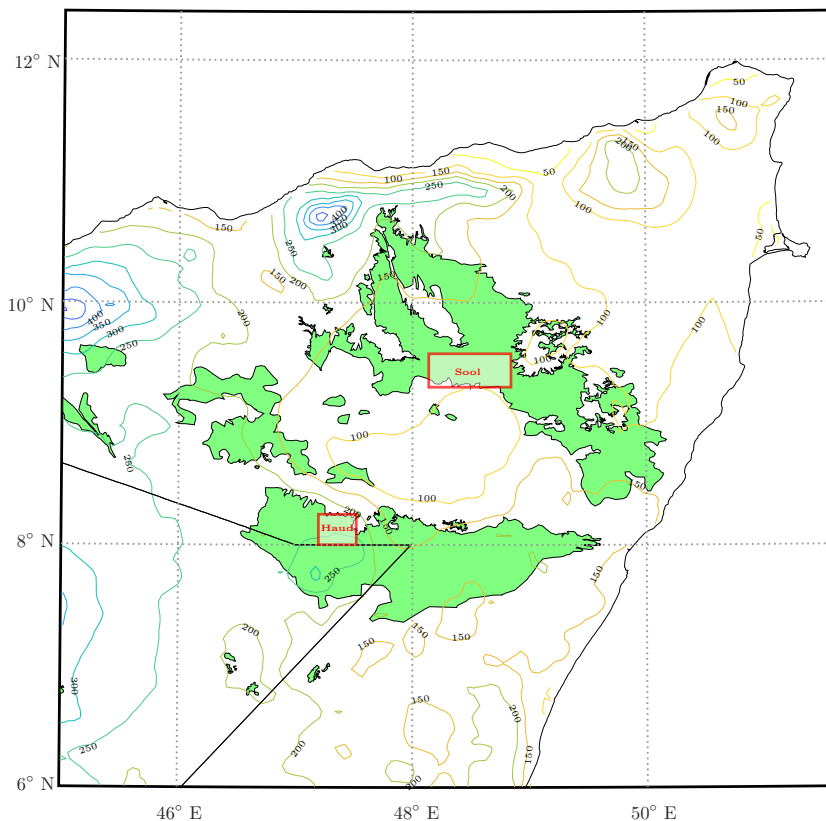


**Figure 2.7** – Locations of the study sites and rainfall gradient in the Horn of Africa. The ‘Haud’ site ( $8^{\circ}0'14''$  to  $8^{\circ}15'11''N$ ;  $47^{\circ}11'54''$  to  $47^{\circ}31'4''E$ ) has a mean annual rainfall of  $210\text{--}270mm \text{ yr}^{-1}$  whilst the ‘Sool’ site ( $9^{\circ}18'49''$  to  $9^{\circ}34'34''N$ ;  $48^{\circ}8'15''$  to  $48^{\circ}43'15''E$ ) has a mean annual rainfall of  $100\text{--}140mm \text{ yr}^{-1}$ . The distribution of periodic vegetation pattern shown in green is adapted from [40]. Precipitation data was extracted from Climate Hazards Group InfraRed Precipitation with Stations [63] and is averaged over the years 1981–2013.

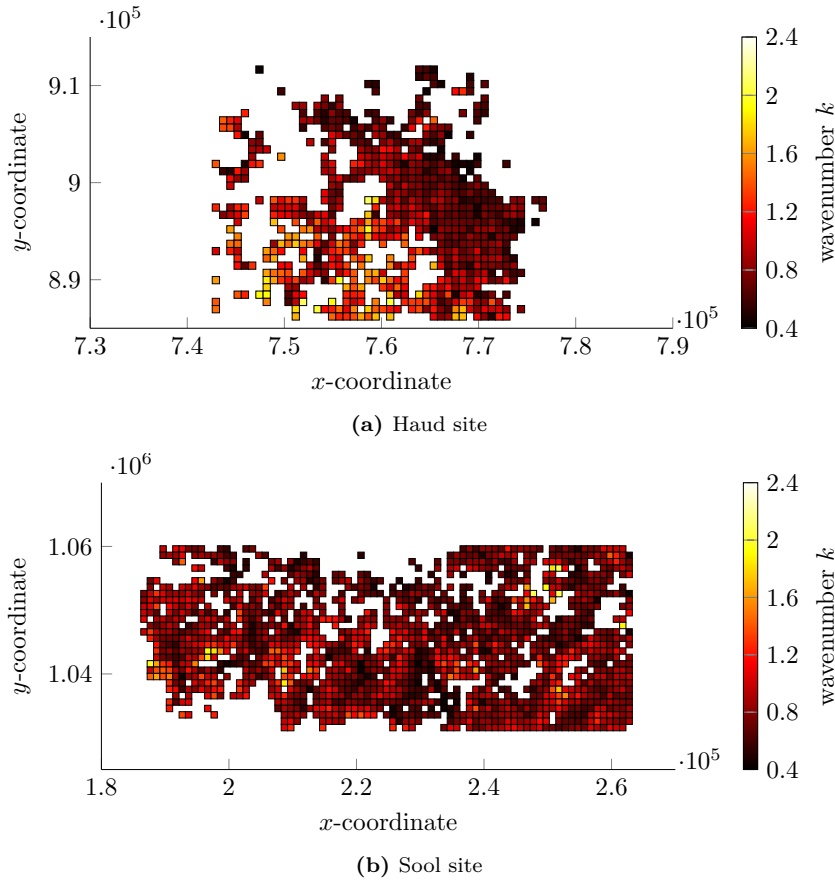


**Figure 2.8** – The distribution of the measured banded pattern’s wavenumber over the Haud site (a) and the Sool site (b). Here, darker red indicates a lower wavenumber and lighter yellow a higher wavenumber. On the  $x$ - and  $y$ -axes the UTM coordinates of the locations are given.

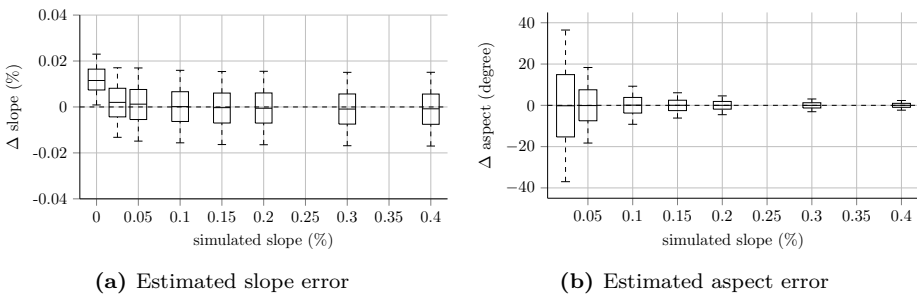


**Figure 2.9** – Slope (a) and aspect (b) estimation error from simulated topographical surfaces. Median errors are shown as horizontal bars with 25<sup>th</sup>–75<sup>th</sup> percentile ranges (boxes) and 5<sup>th</sup> and 95<sup>th</sup> percentile outlier cutoffs (whiskers). Note that aspect error could range from  $-180$  to  $+180$  degrees but has been cropped to largest measured error for visual purpose.

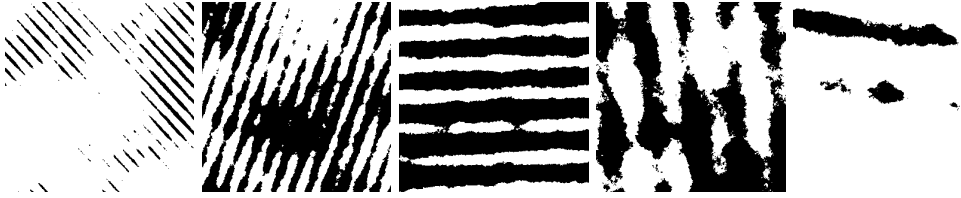


**Figure 2.10** – Examples of simulated vegetation patterns with frequency decreasing from left ( $2.4 \text{ cycles } 100\text{m}^{-1}$ ) to right ( $0.4 \text{ cycles } 100\text{m}^{-1}$ ).

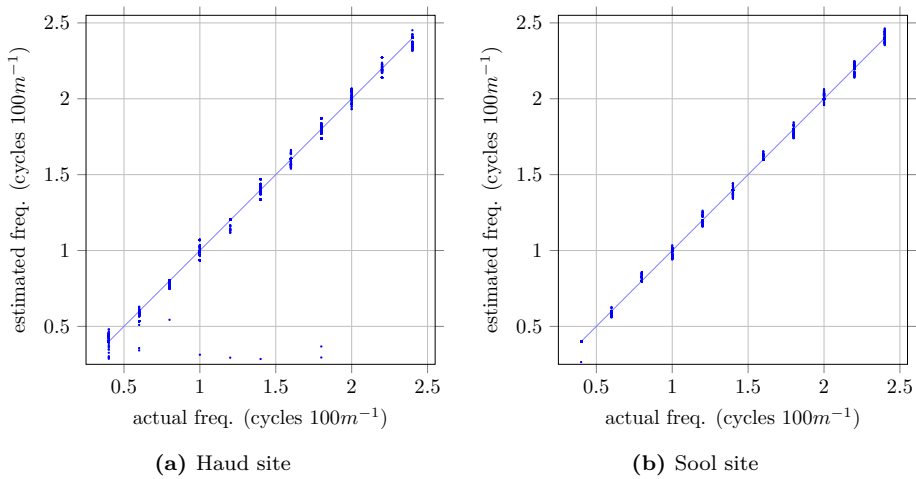


**Figure 2.11** – Pattern frequency estimation error for the Haud (a) and the Sool (b) sites. Actual frequency of the simulated patterns and the corresponding estimation of these frequencies is shown by the blue dots. The straight line represents the perfect estimation line.



# 3

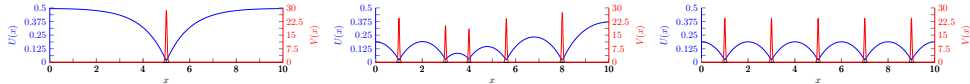
## The dynamics of disappearing pulses in a singularly perturbed reaction-diffusion system with parameters that vary in time and space

We consider the evolution of multi-pulse patterns in an extended Klausmeier equation with parameters that change in time and/or space. We formally show that the full PDE dynamics of a  $N$ -pulse configuration can be reduced to a  $N$ -dimensional dynamical system describing the dynamics on a  $N$ -dimensional manifold  $\mathcal{M}_N$ . Next, we determine the local stability of  $\mathcal{M}_N$  via the quasi-steady spectrum associated to evolving  $N$ -pulse patterns, which provides explicit information on the boundary  $\partial\mathcal{M}_N$ . Following the dynamics on  $\mathcal{M}_N$ , a  $N$ -pulse pattern may move through  $\partial\mathcal{M}_N$  and ‘fall off’  $\mathcal{M}_N$ . A direct nonlinear extrapolation of our linear analysis predicts the subsequent fast PDE dynamics as the pattern ‘jumps’ to another invariant manifold  $\mathcal{M}_M$ , and specifically predicts the number  $N - M$  of pulses that disappear. Combining the asymptotic analysis with numerical simulations of the dynamics on the various invariant manifolds yields a hybrid asymptotic-numerical method describing the full process that starts with a  $N$ -pulse pattern and typically ends in the trivial homogeneous state without pulses. We extensively test this method against PDE simulations and deduce general conjectures on the nature of pulse interactions with disappearing pulses. We especially consider the differences between the evolution of irregular and regular patterns. In the former case, the disappearing process is gradual: irregular patterns lose their pulses one by one. In contrast, regular, spatially periodic, patterns undergo catastrophic transitions in which either half or all pulses disappear. However, making a precise distinction between these two drastically different processes is quite subtle, since irregular  $N$ -pulse patterns that do not cross  $\partial\mathcal{M}_N$  typically evolve towards regularity.

### 3.1 Introduction

The far from equilibrium dynamics of solutions to systems of reaction-diffusion equations – patterns – often has the character of interacting localised structures. This is especially the case when the diffusion coefficients of different components – species – in the system vary significantly in magnitude. This property makes the system *singularly perturbed*. Such systems appear naturally in ecological models; in fact, the presence of processes that vary on widely different spatial scales is regarded as a fundamental mechanism driving pattern formation in spatially extended ecological systems [138]. Moreover, while exhibiting behaviour of a richness comparable to general – non singularly perturbed – systems, the multi-scale nature of singularly perturbed systems provides a framework by which this behaviour can be studied and (partly) understood mathematically.





(a) A homoclinic 1-pulse solution. (b) An irregular 5-pulse solution. (c) A regular 5-pulse solution.

**Figure 3.1** – Snapshots of several (multi-)pulse solutions of system (3.1.1) with  $a = 0.5$ ,  $m = 0.45$ ,  $h(x) \equiv 0$  and  $D = 0.01$ .

In this paper, we consider the interactions of singular pulses in an extended Klausmeier model [150, 153, 155, 158],

$$\begin{cases} U_t &= U_{xx} + h_x U_x + h_{xx} U + a - U - UV^2, \\ V_t &= D^2 V_{xx} - mV + UV^2, \end{cases} \quad (3.1.1)$$

sometimes also called the generalised Klausmeier-Gray-Scott system [148, 170]. This model is a generalization of the original ecological model by Klausmeier on the interplay between vegetation and water in semi-arid regions [95] – which was proposed to describe the appearance of vegetation patterns as crucial intermediate step in the desertification process that begins with a homogeneously vegetated terrain and ends with the non-vegetated bare soil state: the desert – see [41, 117, 137] and the references therein for observations of these patterns and their relevance for the desertification process. In (3.1.1),  $U(x, t)$  represents (the concentration of) water and  $V(x, t)$  vegetation; for simplicity – and as in [148, 150, 153, 158, 170] – we consider the system in a 1-dimensional unbounded domain, i.e.  $x \in \mathbb{R}$ ; parameter  $a$  models the rainfall and  $m$  the mortality of the vegetation. Since the diffusion of water occurs on a much faster scale than the diffusion – spread – of vegetation, the system is indeed – and in a natural way – singularly perturbed: the diffusion coefficient of water is scaled to 1 in (3.1.1), so that the diffusion coefficient of the vegetation  $D$  can be assumed to be small, i.e.  $0 < D \ll 1$ . The topography of the terrain is captured by the function  $h : \mathbb{R} \rightarrow \mathbb{R}$ . The derivative  $h_x$  is a measure of the slope in (3.1.1) – see Appendix 3.A for a derivation of this effect. Unlike in [95], we allow (some of) the parameters of (3.1.1) to *vary in time or space*: we consider topography functions  $h$  that may vary in  $x$ , and – most importantly – we study the impact of slow variations – typically decrease – in time of the rainfall parameter  $a$ : by considering  $a = a(t)$  we incorporate the effect of changing environmental – climatological – conditions into the model. It is crucial for all analysis in this work that if  $a(t)$  varies with  $t$  it *decreases*, i.e. that the external conditions worsen – see also [150, 153, 155, 158].

The pulse patterns studied in this paper – see Figure 3.1 for some examples – correspond directly to localised vegetation ‘patches’; trivially extending them in a  $y$ -direction leads to stripe patterns, the dominant structures exhibited by patchy vegetation covers on sloped terrains [41, 95, 155]. The central questions that motivated the research presented in this paper have their direct origins in ecological questions. Nevertheless, this paper focuses on fundamental issues in the dynamics of pulses in singularly perturbed reaction-diffusion systems with varying parameters. The ecological relevance of the insights obtained in the present work are subject of ongoing research. In that sense, the (alternative) name of generalised Klausmeier-Gray-Scott model [148, 170] perhaps is a more suitable name for model (3.1.1) in the setting of the present paper: by setting  $h(x) \equiv 0$  – i.e. in the ecological context of homogeneously

flat terrains – it reduces to the Gray-Scott model [127] that has served as paradigmatic model system for the development of our present day mathematical ‘machinery’ by which pulses in singularly perturbed reaction-diffusion equations can be studied – see [28, 45, 46, 47, 99, 101] for research on pulse patterns in the Gray-Scott model and [39, 48, 49, 102, 175] for generalizations.

$N$ -pulse patterns are solutions  $(U(x, t), V(x, t))$  to (3.1.1), characterised by  $V$ - components that are exponentially small everywhere except for  $N$  narrow regions in which they ‘peak’: the  $N$  pulses – see Figure 3.1 and notice that the heights of the pulses typically varies. In the setting of singularly perturbed reaction-diffusion models with constant coefficients, the evolution of  $N$ -pulse patterns can be regarded – and studied – as the *semi-strong interaction* [49] of  $N$  pulses. Under certain conditions – see below – the full infinite-dimensional PDE-dynamics can be reduced to an  $N$ -dimensional system describing the dynamics of the pulse locations  $P_1(t) < P_2(t) < \dots < P_N(t)$  – see [12, 28, 49] and the references therein for different (but equivalent) methods for the explicit derivation of this system. Note that the heights of the pulses also vary in time, however, the pulse amplitudes are ‘slaved’ to their (relative) locations. As starting point of our research, we show that this semi-strong pulse interaction reduction method can be – straightforwardly – generalised to systems like (3.1.1) in which coefficients vary in time or space. We do so by following the matched asymptotics approach developed by Michael Ward and co-workers – see [28, 29, 99, 100, 101, 102] and the references therein – which also means that we apply – when necessary – the hybrid asymptotic-numerical approach of [29] in which the asymptotic analysis is sometimes ‘assisted’ by numerical methods – for instance when the ‘algebra’ gets too involved or when a reduced equation cannot be solved (easily) ‘by hand’.

This semi-strong interactions reduction mechanism has been rigorously validated – by a renormalization group approach based on [130] – for several specific systems [12, 50, 172]. It is established by the approach of [12, 50, 172] – and for the systems considered in these papers – that there indeed is an approximate  $N$ -dimensional manifold  $\mathcal{M}_N$  (within an appropriately chosen function space in which the full PDE-dynamics takes place) that is attractive and nonlinearly stable and that the flow on  $\mathcal{M}_N$  is (at leading order) governed by the equations for the pulse locations  $P_j(t)$ ,  $j = 1, \dots, N$ . However, this validity result only holds if the *quasi-steady spectrum* – see Figure 3.2c – associated to the  $N$ -pulse pattern can be controlled. The quasi-steady spectrum is defined as the *approximate* spectrum associated to a ‘frozen’  $N$ -pulse pattern. Due to the slow evolution of the pattern – and the singularly perturbed nature of the problem – this spectrum can be approximated explicitly (by methods based on the literature on stationary pulse patterns, see [28, 175] and the references therein). By considering (slow) time as a parameter, the elements of the quasi-steady spectrum trace orbits through the complex plane, driven by the pulse locations  $P_j(t)$  and, in the case of (3.1.1), by the slowly changing value of  $a(t)$ . The manifold  $\mathcal{M}_N$  is attractive only when this spectrum is in the left half of the complex plane: the proof of the validity result breaks down when there is no spectral gap of sufficient width between the quasi-steady spectrum and the imaginary axis. Thus, the quasi-steady spectrum – approximately – determines a boundary of  $\mathcal{M}_N$ .

The boundary  $\partial\mathcal{M}_N$  in general does not act as a threshold for the flow on  $\mathcal{M}_N$ ; on the contrary, *an evolving  $N$ -pulse pattern may evolve towards – and subsequently through – the boundary  $\partial\mathcal{M}_N$*  – as elements of the quasi-steady spectrum travel towards the imaginary axis. Or equivalently, in the case of parameters that vary in time,

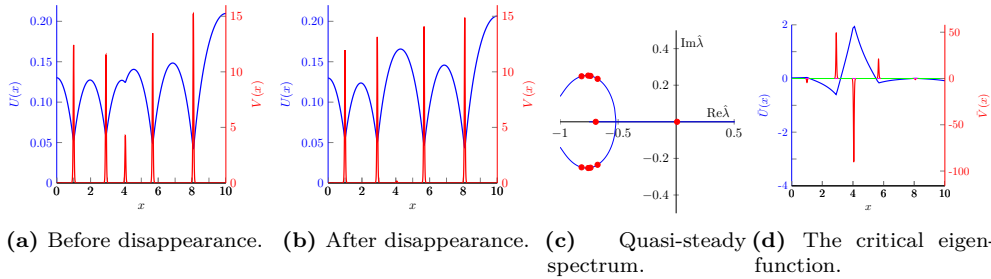


**Figure 3.2** – (a), (b): Simulations of (3.1.1) with  $a(t) = 0.5 - 5 \cdot 10^{-4} t$ ,  $m = 0.45$ ,  $H = 0$ ,  $L = 10$ ,  $P(0) = (1, 3, 4, 5.6, 8)^T$ ,  $D = 0.01$ , just before and after the 3rd pulse disappears (at  $a(t) \approx 0.28$ ). (c): The red dots – that must travel over the blue ‘skeleton structure’ (section 3.3) – indicate the analytically determined quasi-steady spectrum associated to the pattern in (a). (d): The (analytically determined) eigenfunction associated to the critical (quasi-steady) eigenvalue in (c).

the boundary  $\partial\mathcal{M}_N$  may evolve towards the pulse pattern.

In this paper, we do *not* consider the issue of the rigorous validation of the semi-strong reduction method – although we do remark that the methods of [12] a priori seem sufficiently flexible to provide validity results for  $N$ -pulse dynamics in (3.1.1) with non-homogeneous parameters (in fact, the results of [12] already cover specific parameter combinations in (3.1.1) – with  $a$  constant and  $h(x) \equiv 0$  – see Figure 3.5b). Here, we explore – in as much (formal) analytic detail as possible – the dynamics of  $N$ -pulse patterns near *and beyond* the (stability) boundary of the (approximate) invariant manifold  $\mathcal{M}_N$ . In other words, we intentionally consider situations in which we know that the rigorous theory cannot hold. As noted above, this is partly motivated by ecological issues: the final steps in the process of desertification are – conceptually – governed by interacting pulses – vegetation patches. Under worsening climatological circumstances, these patches may either ‘disappear’ in a gradual fashion – patches wither and turn to bare soil *one by one* – or catastrophically – all patches in a large region disappear *simultaneously* – see [11, 78, 137, 158] and the references therein. These types of transitions correspond to  $N$ -pulse patterns crossing through different components of the boundary  $\partial\mathcal{M}_N$  of  $\mathcal{M}_N$ : the nature of these components of  $\partial\mathcal{M}_N$  – and especially the associated dynamics of pulse patterns crossing through the component – clearly varies significantly. This leads us directly to the mathematical themes we explore here,

*Is it possible to analytically follow an  $N$ -pulse pattern as it crosses the stability boundary of a manifold  $\mathcal{M}_N$ ? Can we predict the  $M$ -pulse pattern that emerges as the pattern ‘settles’ on a lower dimensional manifold  $\mathcal{M}_M$  – and especially the value  $M < N$ ? More specifically, can we distinguish between  $N$ -pulse patterns for which  $M = 0$  (a catastrophic regime shift),  $M = N/2$  (a period doubling) and  $M = N - 1$  (a gradual decline)?*

The essence of our approach is represented by Figure 3.2. In Figures 3.2a and 3.2b two snapshots of a (full) PDE simulation of a (originally) 5-pulse pattern is shown, just before and just after the 3rd pulse has disappeared, i.e. before it ‘falls off’  $\mathcal{M}_5$  and after it ‘lands’ on  $\mathcal{M}_4$ . In Figure 3.2c, the quasi-steady spectrum associated to the

5-pulse pattern of Figure 3.2a – i.e. the pattern close to the boundary of is  $\mathcal{M}_5$  – is shown: as expected, a quasi-steady eigenvalue has approached the imaginary axis. The spectral configuration of Figure 3.2c is determined by asymptotic analysis, an analysis that simultaneously provides the (leading order) structure of the (critical) eigenfunction associated to the critical eigenvalue – see section 3.3. This eigenfunction is given in Figure 3.2d. By construction, it describes the leading order structure of the (linearly) ‘most unstable perturbation’ that starts to grow as the pattern passes through  $\partial\mathcal{M}_5$ . The eigenfunction is clearly localised around the – disappearing – 3rd pulse: the analytically obtained structure indicates that the unstable perturbation will mainly affect the 3rd pulse. By *formally* extrapolating this observation based on the *linear* asymptotic analysis – i.e. the information exhibited by Figures 3.2c and 3.2d that is based on the state of the 5-pulse pattern before it falls off  $\mathcal{M}_5$  – we are inclined to draw the *nonlinear* conclusion that the destabilised 3rd pulse will ‘disappear’ as  $\partial\mathcal{M}_5$  is crossed, while the other 4 pulses persist:  $M = 4 = N - 1$ . The PDE-simulation of Figure 3.2b shows that this linear extrapolation indeed correctly predicts the full dynamics of (3.1.1).

We develop a hybrid asymptotic-numerical method that describes the evolution of an  $N$ -pulse pattern by the reduced  $N$ -dimensional system for the pulse locations  $P_j(t)$  as long as the pulse pattern is in the interior of (approximate) invariant manifold  $\mathcal{M}_N$ . With the pulse locations as input, we (analytically) determine the associated (evolving) quasi-steady spectrum, and thus know whether the pulse configuration indeed is in this interior, i.e. bounded away from  $\partial\mathcal{M}_N$ . As elements of the quasi-steady spectrum approach the imaginary axis – i.e. as the pattern approaches  $\partial\mathcal{M}_N$  – the method follows the above described – relatively simple – extrapolation procedure: based on the (approximate) structure of the critical eigenfunction(s) corresponding to the critical element(s) of the quasi-steady eigenvalues that end up on the imaginary axis, it is – automatically – decided which pulse(s) are eliminated and thus what is the value of  $M < N$ . Next, the process is continued by following the dynamics of the  $M$ -pulse configuration on  $\mathcal{M}_M$ , that has the locations of the  $M$  remaining pulses as  $\partial\mathcal{M}_N$  is crossed as initial conditions. Thus, this method provides a formal way to follow the PDE dynamics of an evolving  $N$ -pulse pattern throughout the ‘desertification’ process of disappearing pulses, or – equivalently – as the pulse pattern falls off and subsequently lands on a sequence of invariant manifolds  $\mathcal{M}_{N_i}$  of decreasing dimension  $N_i$ .

A priori, one would guess that this method cannot work – even if there would be rigorous validation results on the reduced dynamical systems on the finite-dimensional manifolds  $\mathcal{M}_{N_i}$ . First, one can in principle not expect that the structure of the most critical eigenfunction always is as clear-cut as in Figure 3.2d: a priori one expects that the ‘automatic’ decision on which pulse(s) to eliminate – and thus how many – must be incorrect in many situations. Moreover, it is not at all clear that the (fast) nonlinear dynamics that takes the pattern from  $\mathcal{M}_N$  to  $\mathcal{M}_M$  indeed only eliminates these ‘most vulnerable pulses’. For instance, if the destabilization is induced by a pair of complex conjugate (quasi-steady) eigenvalues, our method automatically assumes that the associated ‘quasi-steady Hopf bifurcation’ is *subcritical* – i.e. that there is no (stable) periodic oscillating pulse behaviour beyond the bifurcation; in fact, even if the bifurcation is subcritical, our method implicitly assumes that the oscillating process by which the affected pulse disappears is so fast, that it does not influence the other pulses and thus can be completely neglected.

Nevertheless, we found that this method is remarkably successful. Figure 3.3a

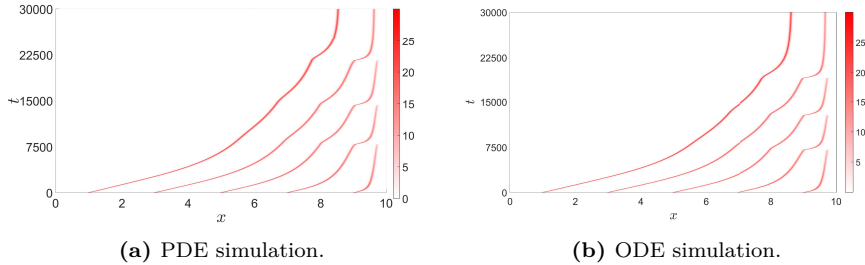


**Figure 3.3** – The evolution of a 5-pulse pattern in the extended Klausmeier model (3.1.1) represented by the locations of the pulses (with  $a = 0.5$ ,  $m = 0.45$ ,  $h(x) = x$ ,  $D = 0.01$ ,  $L = 10$ ). (a) A full PDE simulation. (b) The hybrid asymptotic-numerical ODE method developed in this work.

shows a full PDE simulation of a 5-pulse configuration ‘moving uphill’, i.e. extended Klausmeier model (3.1.1) in the (Klausmeier) setting of a constant slope,  $h(x) = x$ , on a bounded domain (with homogeneous Neumann boundary conditions). One by one, 3 pulses disappear from the system, eventually leading to a stationary stable 2-pulse pattern. Figure 3.3b shows the evolution of the same 5-pulse configuration (at  $t = 0$ ) as described by our – finite-dimensional – method: the pulse configuration ‘jumps’ from  $\mathcal{M}_5$  to  $\mathcal{M}_4$  and  $\mathcal{M}_3$ , eventually settling down in a stable critical point of the 2-dimensional dynamical system that governs the flow on  $\mathcal{M}_2$ . This is quite a slow – and nontrivial – process and it takes quite a long time before the system reaches equilibrium, nevertheless, the ODE reduction method not only provides a qualitatively correct picture, it is remarkably accurate in a quantitative sense.

This latter observation is even more remarkable, since our approach is via an asymptotic analysis and thus based on the assumption that a certain parameter – or parameter combination – is ‘sufficiently small’. Nevertheless our methods remain valid for ‘relatively large values’ of the ‘asymptotically small parameter’. This is not atypical for asymptotically derived insights. It yields another motivation to indeed set out to obtain rigorous results on the dynamics of systems like (3.1.1): in practice, such results are expected to be relevant way beyond the necessary ‘for  $\varepsilon$  sufficiently small’ caveat.

The end-goal of the numerical simulations we present – see section 3.4 – is to test our method, both to get a (formal) insight in its limitations, as well as to isolate typical behaviour of pulse configurations that may be formulated as conjectures – i.e. as challenges for the development of the theory. As an example, we mention the ‘generalised Ni conjecture’ [52, 121] of section 3.4.1 (for systems with  $h(x) \equiv 0$ ): *When a multi-pulse pattern is sufficiently irregular, the localised  $V$ -pulse with the lowest maximum is the most unstable pulse, and thus the one to disappear first.* In fact, one could claim that at a formal level, the evolution of sufficiently irregular  $N$ -pulse patterns can be understood by (successive applications of) this conjecture – and thus be described accurately by our reduction method. However, even when the initial conditions form an irregular  $N$ -pulse pattern, the situation becomes more complex than that, since the reduced  $N$ -dimensional dynamics typically evolve towards a critical point on  $\mathcal{M}_N$ . In fact, our study indicates that  $N$ -pulse patterns (on bounded domains) always evolve to one specific configuration – in the Gray-Scott setting of flat

terrains, i.e.  $h(x) \equiv 0$ , this is a regularly spaced (spatially periodic)  $N$ -pulse pattern. The final pattern is less regular if  $h(x) \not\equiv 0$  – see the stable 2-pulse pattern of Figure 3.3.

The evolution towards spatially periodic patterns induces a mechanism that challenges our method. For irregular patterns, the elements of the quasi-steady spectrum typically ‘spread out’ (over a certain skeleton structure, see Figure 3.2c and section 3.3). However, these elements might cluster together as the pattern becomes more and more regular (which agrees with the spectral analysis of spatially periodic patterns in Gray-Scott/Klausmeier type models, see [47, 148]). Therefore, it gets harder to isolate the critical (quasi-steady) eigenvalue that induces the destabilization. Moreover, the structure of the associated eigenfunctions also changes significantly: in the irregular setting these have a structure that is centered around one well-defined pulse location (as in Figure 3.2d) – which makes them very suitable for the application of our method; in the periodic case, the eigenfunctions have a more global structure. Nevertheless, as the regularised  $N$ -pulse pattern approaches the boundary of  $\mathcal{M}_N$ , two most critical quasi-steady eigenvalues can be distinguished – i.e. there typically are two (quasi-steady) eigenvalues that may cause the destabilization. The associated two critical eigenfunctions are also (almost) periodic, either with the same period of the underlying pattern, or with twice that period – which is in agreement with analytical insights in the destabilization mechanisms of ‘perfect’ spatially periodic patterns [38, 52, 53] (see also the two conjectures in section 3.4.1). These critical eigenfunctions are plotted in Figure 3.4 for a stationary regular 2-pulse pattern for  $h(x) \equiv 0$  and  $a$  fixed near its bifurcation value – i.e. in the classical constant coefficients setting of (3.1.1). The eigenfunction in Figure 3.4a has the same periodicity as the underlying pattern, it represents the catastrophic ‘full collapse’ scenario in which all pulse disappear simultaneously. Of course, this statement is once again a fully nonlinear extrapolation of completely linear insight, but it is – once again – backed up by our numerical simulations: also in the regular case, the linear mechanisms are good predictors for the fast transitions between invariant manifolds.

This nonlinear extrapolation of a linear mechanism also works for the other critical eigenfunction represented by Figure 3.4b, which induces a period doubling bifurcation in which half of the pulses of an  $N$  pulse pattern disappear. However, in this case – that is quite dominant in simulations of desertification scenarios [155, 158] – our method faces an intrinsic problem, that gets harder the more regular the pattern becomes: if the number of pulses  $N$  is odd, our method predicts that ‘half of the pulses’ disappear, but it cannot decide whether the  $N$ -pulse configuration jumps from  $\mathcal{M}_N$  to  $\mathcal{M}_{(N+1)/2}$  – in which all  $(N-1)/2$  even numbered pulses disappear – or from  $\mathcal{M}_N$  to  $\mathcal{M}_{(N-1)/2}$  – in which the even numbered pulses are the surviving ones. A similar problem occurs in the jump from  $\mathcal{M}_N$  to  $\mathcal{M}_{N/2}$  for  $N$  even: our method cannot predict whether the even or the odd numbered pulses survive. Nevertheless, also in this case our method is doing better than could be expected; moreover, also in direct PDE simulations, the resolution of this parity issue seems extremely sensitive on initial conditions.

The set-up of this paper is as follows. In section 3.2, we first perform the PDE to ODE reduction for  $N$ -pulse patterns in (3.1.1) with – in its most general setting –  $a = a(t)$  varying in time and  $h = h(x)$  varying in space (on unbounded domains and on bounded domains with various kinds of boundary conditions). As a result we obtain explicit expressions for the  $N$ -dimensional – or  $N-1$ -dimensional<sup>1</sup> – systems that

<sup>1</sup>On unbounded domains or domains with periodic boundary conditions it is essentially  $N-1$ -dimensional, as only the distances between pulses is relevant, thus reducing the dimension by 1.

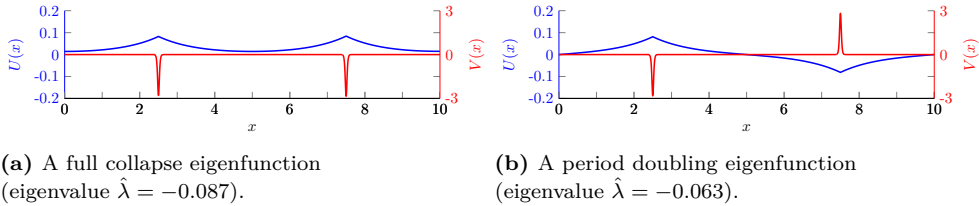


**Figure 3.4** – The 2 critical eigenfunctions of a regular 2-pulse pattern of extended Klausmeier model (3.1.1) on a domain with periodic boundaries with  $a \approx 0.19187$  (near bifurcation),  $m = 0.45$ ,  $h(x) \equiv 0$  and  $D = 0.01$ .

describe the evolution of the pulse locations  $P_j(t)$ , and thus of the  $N$ -pulse pattern on  $\mathcal{M}_N$ . Subsequently, the flow on  $\mathcal{M}_N$  is studied – the critical points and their characters are determined analytically; as a consequence, the special role of the spatially periodic patterns – as attractive fixed points – can be identified. These results need to be supplemented with an analysis of the stability of the manifold  $\mathcal{M}_N$ , especially since the analysis of section 3.2 is not equipped to distinguish the boundaries of  $\mathcal{M}_N$  – i.e. it ignores the process of pulse patterns falling off  $\mathcal{M}_N$ . This is the topic of section 3.3 in which  $N$ -pulse solutions are frozen and their quasi-steady spectrum – and thus the boundary of  $\mathcal{M}_N$  – is determined. A central part of the analysis is dedicated to determining the skeleton structure on – or better: near – which the quasi-steady eigenvalues must lie (see Figure 3.2c). Moreover, the (linearised) nature of the bifurcations that occur when specific components of  $\partial\mathcal{M}_N$  are crossed is studied. Next, in section 3.4, we first numerically check the validity of our asymptotic analysis, then set up our hybrid asymptotic-numerical method – based on the analysis of sections 3.2 and 3.3 – and subsequently extensively test its ‘predictions’ against full PDE-simulations. We find that the asymptotic analysis is correct for parameter values beyond the reaches of current rigorous theory. Moreover, we observe that our method – that is based on direct extrapolations of linear insights – works better than a priori could be expected, but also couple this to a search for the limitations of this approach. Based on these tests and simulations, we formulate general conjectures on the nature of multi-pulse dynamics generated by models as (3.1.1). Finally, we briefly discuss the implications of our findings and indicate future lines of research in the concluding section 3.5.

### 3.1.1 Size assumptions

The asymptotic analysis presented in this paper does not hold for all magnitudes of the parameters  $a$ ,  $m$ ,  $D$  and all height functions  $h$ . We therefore need to make several assumptions on the (relative) magnitudes of the parameters in (3.1.1). These assumptions are listed here, together with the type of bifurcation that occurs when these assumptions are violated.

- (A1)  $\frac{a^2}{m^2} \ll 1$  [Pulse Splitting bifurcation]
- (A2)  $\frac{Da^2}{m\sqrt{m}} \ll 1$  [Travelling Wave bifurcation]
- (A3)  $\frac{m\sqrt{m}D}{a^2} \ll 1$  [Saddle-Node bifurcation]
- (A4)  $\frac{m^2D}{a^2} \ll 1$  [Hopf bifurcation]

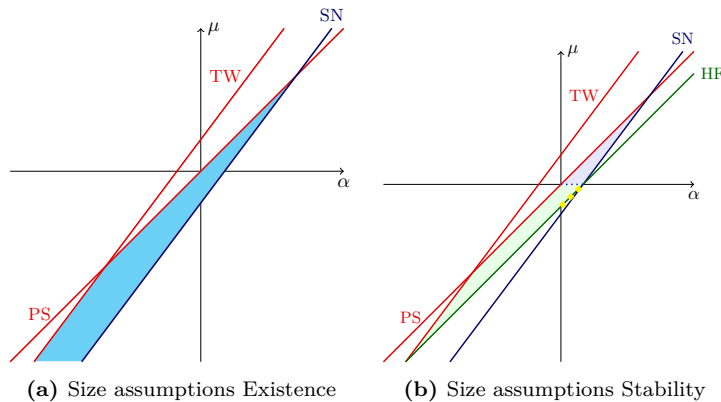


**Figure 3.5** – Graphical summary of size assumptions (A1)-(A3) in (a) and assumptions (A1)-(A4) in (b). Here  $\mu$  and  $\alpha$  denote the size of  $m$  respectively  $a$  in order of magnitude of  $0 < D \ll 1$ . That is,  $m = \mathcal{O}(D^\mu)$  and  $a = \mathcal{O}(D^\alpha)$ . This positions the pulse splitting bifurcation (PS) on the line  $\mu = \alpha$ , the Travelling-Wave bifurcation (TW) on  $\mu = \frac{2}{3}(1 + 2\alpha)$ , the Saddle-Node bifurcation (SN) on  $\mu = \frac{2}{3}(2\alpha - 1)$  and the Hopf bifurcation (HF) on  $\mu = \alpha - \frac{1}{2}$ . The coloured-in region in (a) indicate the region in which pulse solutions exist (under the additional assumptions (A5)). The coloured-in regions in (b) indicate the region in which stable pulse solutions exist (under the additional assumptions (A5),(A6)). We have also plotted the line  $\mu = 0$ , which indicates the boundary between the cases  $m \gg 1$  and  $m \ll 1$  which becomes relevant in the distinction between coupled and decoupled stability problem in our linear stability study in section 3.3. The dashed yellow line (on the Hopf line) indicates the scaling regime for which validity of the ODE reduction has been proven [12].

$$(A5) \quad \frac{Dm\sqrt{m}}{a^2} h_x(x) \ll 1 \quad \text{and} \quad \frac{a^2}{m^2} \left( \frac{Dm\sqrt{m}}{a^2} \right)^2 h_{xx}(x) \ll 1 \quad \text{for all } x \in \mathbb{R} \quad [\text{Saddle-Node bifurcation}]$$

$$(A6) \quad \frac{m^2 D}{a^2} h_x(x) \ll 1 \quad \text{for all } x \in \mathbb{R} \quad [\text{Hopf bifurcation}].$$

Previous studies of the Gray-Scott system indicate the necessity of three size assumptions to ensure the existence of (one-)pulse solutions [28, 46, 148]. The assumptions found in those previous studies can be directly linked<sup>2</sup> to our assumptions (A1)-(A3). In Figure 3.5a we have visualised the assumptions on parameters  $a$  and  $m$  that follow from (A1)-(A3). Asymptotic stability analysis has shown that a pulse solution is stable if it satisfies an additional fourth size assumption, which corresponds to our assumption (A4). We have also visualised the assumptions on  $a$  and  $m$  that follow from the assumptions (A1)-(A4) in Figure 3.5b. Finally, the assumptions on the height function  $h$  in assumptions (A5) and (A6) are new, and include the case studied in [148] (but are more general). These guarantee that the height function  $h$  does not change too rapidly, i.e.  $h$  changes on a slower scale than the  $V$ -pulse does. This ensures that the standard ‘flat-terrain’ (i.e.  $h(x) \equiv 0$ ) existence theory can be reproduced almost directly.

In principle assumptions (A3) and (A4) can be extended to include the  $\mathcal{O}(1)$  cases (i.e.  $\mathcal{O}(1)$  with respect to  $\frac{a}{m} \ll 1$ ). In fact, to study the bifurcations that occur when

<sup>2</sup>A handy conversion table between different scalings of the Gray-Scott model can be found in [148, section 2.2].



the rainfall  $a$  is decreased, it is necessary to include these cases. This leads to the alternative assumptions (A3') and (A4') which are stated below.

$$(A3') \quad \frac{m\sqrt{m}D}{a^2} \leq \mathcal{O}(1)$$

$$(A4') \quad \frac{m^2D}{a^2} \leq \mathcal{O}(1)$$

**Remark 3.1.1.** *Assumption (A3) corresponds to the so-called ‘intermediate feed-rate regime’ and  $\frac{m\sqrt{m}D}{a^2} = \mathcal{O}(1)$  to the ‘low feed-rate regime’ in [100, 160]. Thus assumption (A3') includes both regimes and (A3) can be seen as a further approximation of (A3').*

## 3.2 PDE to ODE reduction

In this section we study the dynamical movement of a  $N$ -pulse solution to the scaled extended Klausmeier model (3.1.1). We assume that there are  $N$  localised vegetation  $V$ -pulses at positions  $P_1(t) < P_2(t) < \dots < P_N(t)$ , as depicted in Figure 3.6. Depending on the domain of our problem we may put additional requirements on the first and last positions (e.g.  $0 < P_1(t)$  and  $P_N(t) < L$  on the bounded domain  $[0, L]$ ). The positions of the  $N$  pulses are not fixed in time. In fact, the  $j$ -th pulse turns out to move with a time-dependent movement speed  $\hat{c}_j(t) = \frac{dP_j(t)}{dt}$  so that its location is given by  $P_j(t) = \int_0^t \hat{c}_j(s)ds + P_j(0)$ . Our goal is to derive an ODE that describes the evolution of the locations of these pulses, that is, to find expressions for the speeds  $\hat{c}_j(t)$ . To do so, we first need to find the approximate form of a  $N$ -pulse solution to (3.1.1). For this, we divide the domain in several regions: near each pulse we have an inner region and between pulses we have outer regions. Note that in the context of geometric singular perturbation theory these regions are called fast (the inner regions) respectively slow (the outer regions).

We follow the asymptotic approach developed by Michael Ward and co-workers – see [28, 29, 99, 100, 101, 102] and references therein – to find approximate solutions in the  $N$  inner regions and in the  $N + 1$  outer regions. In the outer regions we find  $V = 0$  and in the inner regions we find  $U$  to be constant (both to leading order). A combination of a Fredholm condition and the matching of the inner and outer solution at the pulse locations then gives us the speed of the  $j$ -th pulse as a function of the solution  $U$  in the outer regions [28]. The latter is, in the end, determined by  $N + 1$  linear ODEs that are coupled via internal boundary conditions at all the pulse locations. Therefore we find a pulse-location ODE that depends only on the (current) positions of the pulses. Hence this ODE-description is a reduction of the infinite-dimensional flow of the PDE to a finite-dimensional flow on a  $N$ -dimensional<sup>3</sup> manifold  $\mathcal{M}_N$  on which  $N$ -pulses live.

After we have found this ODE description, we study the dynamics of generic  $N$ -pulse configurations in section 3.2.3 and section 3.2.4. Here the difference between assumption (A3) and (A3') and the need for a hybrid asymptotic-numerics approach becomes apparent: in the former case analytical results can be found, whereas numerics are necessary to study the possibilities in the latter case. Note that assumptions (A4) and (A6) are not needed for the analysis in this section.

---

<sup>3</sup>On unbounded domains or domains with periodic boundary conditions this manifold is essentially  $N - 1$ -dimensional, as only the distances between pulses matters, thus reducing the dimension of the manifold by 1.

### 3.2.1 The inner regions

We start inspecting the inner regions of the  $N$ -pulse solution. To zoom in to the  $j$ -th inner region, close to  $x = P_j(t)$ , we introduce the stretched traveling wave coordinate centered around  $P_j(t)$

$$\xi_j = \frac{\sqrt{m}}{D}(x - P_j(t)) = \frac{\sqrt{m}}{D} \left( x - P_j(0) - \int_0^t \hat{c}_j(s) ds \right). \quad (3.2.1)$$

Note that by assumptions (A3) and (A1) this is a stretched coordinate since  $\frac{D}{\sqrt{m}} \leq \frac{a^2}{m^2} \ll 1$ . We will denote this  $j$ -th inner region by  $I_j^{in}$ . As is common practice in geometric singular perturbation theory, we explicitly define  $I_j^{in}$  by assuming that  $\xi_j \in [-\frac{1}{\sqrt{\varepsilon}}, \frac{1}{\sqrt{\varepsilon}}]$ , with  $\varepsilon = \frac{a}{m}$ .

Following the scalings introduced in [28, 46, 155] we set  $\hat{c}_j(t) = \frac{Da^2}{m\sqrt{m}}c_j(t)$  where  $c_j(t) = \mathcal{O}(1)$ . By assumption (A2) we thus have  $\hat{c}_j(t) \ll 1$ , i.e. pulses move only slowly in time. We can thus use a quasi-steady approximation and treat  $t$  as a parameter in our analysis (cf. [28, 45, 46, 160]). At the pulse location we also need to scale  $U$  and  $V$ . Again following the previously mentioned scalings [28, 46, 155], it turns out we need to scale these in the inner regions as

$$U = \frac{m\sqrt{m}D}{a}u; \quad V = \frac{a}{\sqrt{m}D}v. \quad (3.2.2)$$

Putting in these scalings in (3.1.1) gives us the following problem for the inner region at the  $j$ -th pulse:

$$\begin{cases} -\frac{a^2}{m^2} \frac{Dm\sqrt{m}}{a^2} \frac{Da^2}{m\sqrt{m}} c_j(t) u_j' & = u_j'' - \frac{a^2}{m^2} u_j v_j^2 + \frac{a^4}{m^4} \frac{Dm\sqrt{m}}{a^2} - \frac{a^4}{m^4} \left( \frac{Dm\sqrt{m}}{a^2} \right)^2 u_j \\ & + \frac{a^2}{m^2} \frac{Dm\sqrt{m}}{a^2} h_x \left( P_j + \frac{D}{\sqrt{m}} \xi_j \right) u_j' \\ & + \frac{a^4}{m^4} \left( \frac{Dm\sqrt{m}}{a^2} \right)^2 h_{xx} \left( P_j + \frac{D}{\sqrt{m}} \xi_j \right) u_j \\ -\frac{a^2}{m^2} c_j(t) v_j' & = v_j'' - v_j + u_j v_j^2, \end{cases} \quad (3.2.3)$$

where the prime denotes derivatives with respect to  $\xi_j$  and the subscript  $j$  is here to remind us that we are looking for a solution in the  $j$ -th inner region. To find solutions in the inner region, we use regular expansions for  $u$  and  $v$ . The equations (3.2.3) suggest that the main small parameter is  $\frac{a^2}{m^2}$  – which is small by assumption (A1). Hence we look for solutions of the form

$$\begin{cases} u_j & = u_{0j} + \frac{a^2}{m^2} u_{1j} + \dots \\ v_j & = v_{0j} + \frac{a^2}{m^2} v_{1j} + \dots \end{cases} \quad (3.2.4)$$

The leading order problem in the  $j$ -th inner region is then given by the following set of equations. This system is usually called the fast-reduced system in the context of geometric singular perturbation theory.

$$\begin{cases} 0 & = u_{0j}'', \\ 0 & = v_{0j}'' - v_{0j} + u_{0j} v_{0j}^2. \end{cases} \quad (3.2.5)$$

Hence we find  $u_{0j}$  to be constant and

$$v_{0j}(\xi) = \frac{3}{2} \frac{1}{u_{0j}} \operatorname{sech}^2(\xi/2). \quad (3.2.6)$$

Thus, all  $V$ -pulses are at leading order given by the same sech-function. However, their amplitudes vary, as these are determined by the values of  $u_{0j}$ , which are, so far, unknown. Later on, we will see that the values of  $u_{0j}$  will be determined by (all) the pulse locations  $P_1(t), \dots, P_N(t)$ . Note that the pulses thus influence each other (only) through this mechanism. By assumptions (A1)-(A3) and (A5) we notice that the next order problem is given by

$$\begin{cases} u''_{1j} & = u_{0j}v_{0j}^2, \\ v''_{1j} - v_{1j} + 2u_{0j}v_{0j}v_{1j} & = -c_j(t)v'_{0j} - v_{0j}^2u_{1j}, \end{cases} \quad (3.2.7)$$

Unlike the  $u$ -equation, it is not clear a priori whether the  $v$ -equation is solvable. We define the self-adjoint operator  $\mathcal{L} := \partial_\xi^2 - 1 + 2u_{0j}v_{0j}$ .  $\mathcal{L}$  has a non-empty kernel, since  $\mathcal{L}v'_{0j} = 0$ . Hence the inhomogeneous equation  $\mathcal{L}v_{1j} = -c_j(t)v'_{0j} - v_{0j}^2u_{1j}$  might not be solvable and we need to impose a Fredholm solvability condition

$$\int_{I_j^{in}} c_j(t)v'_{0j}(\eta)^2 d\eta = \int_{I_j^{in}} -v_{0j}(\eta)^2 u_{1j}(\eta)v'_{0j}(\eta) d\eta. \quad (3.2.8)$$

Applying integration by parts twice to the right-hand side yields

$$\begin{aligned} & \int_{I_j^{in}} u_{1j}(\eta)v_{0j}(\eta)^2 v'_{0j}(\eta) d\eta = \frac{1}{3} \int_{I_j^{in}} u_{1j}(\eta) \frac{d}{d\eta} [v_{0j}(\eta)^3] d\eta \\ & = \frac{1}{3} [v_{0j}(\eta)^3 u_{1j}(\eta)]_{\eta=-\frac{1}{\sqrt{\varepsilon}}}^{\eta=\frac{1}{\sqrt{\varepsilon}}} - \frac{1}{3} \int_{I_j^{in}} u'_{1j}(\eta)v_{0j}(\eta)^3 d\eta \\ & = -\frac{1}{3} \left[ u'_{1j}(\eta) \int_0^\eta v_{0j}(y)^3 dy \right]_{\eta=-\frac{1}{\sqrt{\varepsilon}}}^{\eta=\frac{1}{\sqrt{\varepsilon}}} + \frac{1}{3} \int_{I_j^{in}} u''_{1j}(\eta) \int_0^\eta v_{0j}(y)^3 dy d\eta + h.o.t. \end{aligned}$$

To get from the second to the third line, we have used that  $v_{0j}$  gets exponentially small near the boundaries of  $I_j^{in}$  and that  $u_{1j}$  does not get exponentially large there. We note that  $v_{0j}$  is an even function. Therefore  $u''_{1j}$  is an even function and  $\eta \mapsto \int_0^\eta v_{0j}(y)^3 dy$  is an odd function. So the last integral over the inner region vanishes. Finally, because  $v_{0j}^3$  is even, we can reformulate the solvability condition and obtain

$$c_j(t) \int_{I_j^{in}} v'_{0j}(\eta)^2 d\eta = \frac{1}{6} \left[ u'_{1j} \left( \frac{1}{\sqrt{\varepsilon}} \right) + u'_{1j} \left( -\frac{1}{\sqrt{\varepsilon}} \right) \right] \int_{I_j^{in}} v_{0j}(\eta)^3 d\eta. \quad (3.2.9)$$

The integrals over the inner region can be approximated by integrals over  $\mathbb{R}$ , because  $v_{0j}$  is exponentially small outside  $I_j^{in}$ . As we know the function  $v_{0j}$  explicitly, it is possible to evaluate the integrals in this Fredholm condition explicitly. This gives us an expression for the (scaled) speed of the  $j$ -th pulse as

$$c_j(t) = \frac{1}{u_{0j}} \left[ u'_{1j} \left( \frac{1}{\sqrt{\varepsilon}} \right) + u'_{1j} \left( -\frac{1}{\sqrt{\varepsilon}} \right) \right]. \quad (3.2.10)$$

It follows from the  $u$ -equation in (3.2.7) that,

$$\begin{aligned} u'_{1j} \left( \frac{1}{\sqrt{\varepsilon}} \right) - u'_{1j} \left( -\frac{1}{\sqrt{\varepsilon}} \right) & = \int_{I_j^{in}} u''_{1j}(\eta) d\eta = \int_{I_j^{in}} u_{0j}v_{0j}(\eta)^2 d\eta \\ & = \int_{-\infty}^{\infty} u_{0j}v_{0j}(\eta)^2 d\eta + h.o.t. = \frac{6}{u_{0j}} + h.o.t. \end{aligned} \quad (3.2.11)$$

Combining this with (3.2.10), we conclude

$$\begin{aligned} c_j(t) &= \frac{1}{6} \left[ u'_{1j} \left( \frac{1}{\sqrt{\varepsilon}} \right) + u'_{1j} \left( -\frac{1}{\sqrt{\varepsilon}} \right) \right] \left[ u'_{1j} \left( \frac{1}{\sqrt{\varepsilon}} \right) - u'_{1j} \left( -\frac{1}{\sqrt{\varepsilon}} \right) \right] \\ &= \frac{1}{6} \left[ u'_{1j} \left( \frac{1}{\sqrt{\varepsilon}} \right)^2 - u'_{1j} \left( -\frac{1}{\sqrt{\varepsilon}} \right)^2 \right]. \end{aligned} \quad (3.2.12)$$

The values  $u'_{1j}(\pm 1/\sqrt{\varepsilon})$  can be found by matching this inner solution to the outer solutions for  $U$ . Note that the speed of the  $j$ -th pulse does not seem to depend explicitly on the other pulses. However, the values of  $u'_{1j}$  are not yet determined and we will find that these *do* depend on the location of (all) other pulses.

### 3.2.2 The outer regions

In the outer regions, the  $V$ -component should be exponentially small, since  $v_{0j}$  gets exponentially small near the boundaries of the inner regions. Since the  $V$ -equation is automatically solved by  $V = 0$ , we can set  $V = 0$  in the outer regions to acquire a leading order approximation and we thus only need to deal with the  $U$ -equation. In each of the outer regions, equation (3.1.1) reduces to the ODE

$$0 = U_{xx} + h_x U_x + h_{xx} U + a - U. \quad (3.2.13)$$

Since the pulses only travel asymptotically slow, the solutions of these equations are expected to be of order  $\mathcal{O}(a)$  because of the forcing term. Therefore we rescale  $U$  as  $U = a\tilde{U}$ , so that

$$0 = \tilde{U}_{xx} + h_x \tilde{U}_x + h_{xx} \tilde{U} + 1 - \tilde{U}. \quad (3.2.14)$$

Without explicitly solving these equations, we can already match the outer solutions to the inner solutions. For this we need to recall the scalings in equations (3.2.1) and (3.2.2). Careful bookkeeping then reveals that

$$\begin{aligned} \tilde{U}(P_j) &= \frac{m\sqrt{m}D}{a^2} u_{0j} + h.o.t. \\ \tilde{U}_x(P_j^\pm) &= \frac{m\sqrt{m}D}{a^2} \frac{\sqrt{m}}{D} \frac{a^2}{m^2} u'_{1j} \left( \pm \frac{1}{\sqrt{\varepsilon}} \right) + h.o.t. = u'_{1j} \left( \pm \frac{1}{\sqrt{\varepsilon}} \right) + h.o.t. \end{aligned}$$

where  $P_j^+$  denotes taking the limit from above (from the right), and  $P_j^-$  the limit from below (from the left). Thus at this moment we have reduced the full PDE problem to a ODE problem with (undetermined) internal boundary conditions. We thus need to find a function  $\tilde{U}$  and constants  $u_{0j}$  that simultaneously satisfy the ODE

$$0 = \tilde{U}_{xx} + h_x \tilde{U}_x + h_{xx} \tilde{U} + 1 - \tilde{U}; \quad \tilde{U}(P_j) = \frac{m\sqrt{m}D}{a^2} u_{0j}. \quad (3.2.15)$$

and, by (3.2.11), the jump conditions

$$\tilde{U}_x(P_j^+) - \tilde{U}_x(P_j^-) = \frac{6}{u_{0j}}, \quad (3.2.16)$$

This set of an ODE coupled with an algebraic equation is often referred to as a differential-algebraic equation (DAE) and was first identified in the Gierer-Meinhardt model [85].

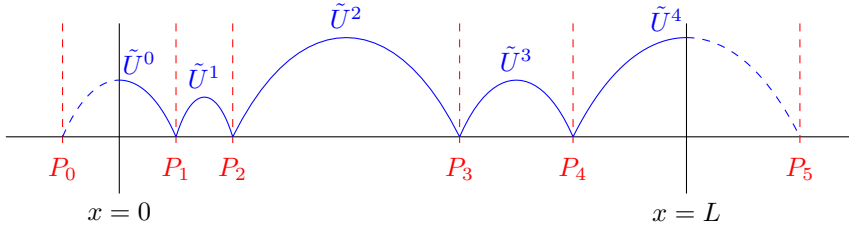


**Figure 3.6** – Sketch of the outer regions and the solutions  $\tilde{U}^k$  in the corresponding  $k$ -th outer region.

Note that the ODE should also be accompanied by two boundary conditions, which – of course – depend on the type of domain we are interested in. Moreover, the expression (3.2.12) for the speed  $c_j(t)$  can be rewritten to

$$c_j(t) = \frac{1}{6} \left[ \tilde{U}_x(P_j^+)^2 - \tilde{U}_x(P_j^-)^2 \right]. \quad (3.2.17)$$

Thus the speed of the  $j$ -th pulse is determined by the (differences of the) squares of the derivative of  $\tilde{U}$  at the pulse location. Since we are interested in this pulse movement, our next task is to actually solve the problem given by (3.2.15)-(3.2.16). We separate this problem into two different cases: (i) the case of assumption (A3) and (ii) the case of assumption (A3'), in particular when  $\frac{m\sqrt{m}D}{a^2} = \mathcal{O}(1)$ . The former case will be significantly simpler as the internal boundaries are approximately zero.

### 3.2.3 Pulse location ODE under assumption (A3)

Under assumption (A3), the internal boundary conditions are approximated as  $\tilde{U}(P_j) = 0$  so that  $\tilde{U}$  is independent of  $u_{0j}$  at leading order,

$$0 = \tilde{U}_{xx} + h_x \tilde{U}_x + h_{xx} \tilde{U} + 1 - \tilde{U}; \quad \tilde{U}(P_j) = 0. \quad (j = 1, \dots, N) \quad (3.2.18)$$

This immensely reduces the complexity of the problem, as  $\tilde{U}$  in the  $k$ -th outer region now only depends on the positions  $P_{k-1}(t)$  and  $P_k(t)$  – and not on any of the others. It is therefore relatively easy to analytically approximate these expressions – and the pulse location ODE – if we know the explicit solutions to the ODE. For general  $h = h(x)$  it is, however, in general not possible to find explicit solutions (in closed form) of this ODE. This does not obstruct the fact that also in this case the PDE can be reduced to a finite dimensional system of ODEs. However, to explicitly evaluate the ODE dynamics, we need to turn to numerical boundary value problem solvers. Note that although the value of  $u_{0j}$  does not play a leading order role in the outer region expressions  $\tilde{U}$ , it does play a leading order role in the linear stability analysis – therefore it is important to (also) still find a leading order expression of  $u_{0j}$ .

**Terrain with constant slope, i.e.  $h(x) = Hx$**

When we consider a terrain with a constant slope, we do have access to explicit solutions for the outer region ODE (3.2.18). Equation (3.2.18) then becomes

$$0 = \tilde{U}_{xx} + H\tilde{U}_x + 1 - \tilde{U}; \quad \tilde{U}(P_j) = 0. \quad (j = 1, \dots, N) \quad (3.2.19)$$

The general solution is

$$\tilde{U}(x) = 1 + C_1 e^{D_1 x} + C_2 e^{D_2 x},$$

where

$$D_{1,2} := \frac{1}{2} \left( -H \pm \sqrt{H^2 + 4} \right).$$

We denote the solution in the  $k$ -th outer region by  $\tilde{U}^k$  (see Figure 3.6). All, but the first and last, satisfy two internal boundary conditions  $\tilde{U}^k(P_k) = 0$  and  $\tilde{U}^k(P_{k+1}) = 0$ , and are then given by

$$\tilde{U}^k(x) = 1 + \frac{(1 - e^{D_2 \Delta P_k}) e^{D_1(x-P_k)} + (e^{D_1 \Delta P_k} - 1) e^{D_2(x-P_k)}}{e^{D_2 \Delta P_k} - e^{D_1 \Delta P_k}}, \quad (k = 1, \dots, N-1) \quad (3.2.20)$$

where  $\Delta P_k := P_{k+1} - P_k$  is the distance between the two consecutive pulses. To derive an expression for the pulse-location ODE, it is necessary to find  $\tilde{U}_x^k(P_k)$  and  $\tilde{U}_x^k(P_{k+1})$ . Direct computation of these derivatives yields after some algebra:

$$\begin{aligned} \lim_{x \downarrow P_k} \tilde{U}_x^k(x) &= \frac{D_1 (1 - e^{D_2 \Delta P_k}) + D_2 (e^{D_1 \Delta P_k} - 1)}{e^{D_2 \Delta P_k} - e^{D_1 \Delta P_k}} \\ &= \frac{H}{2} - \frac{\sqrt{H^2 + 4} e^{H \Delta P_k / 2} - \cosh(\sqrt{H^2 + 4} \Delta P_k / 2)}{2 \sinh(\sqrt{H^2 + 4} \Delta P_k / 2)}, \\ \lim_{x \uparrow P_{k+1}} \tilde{U}_x^k(x) &= \frac{D_1 (1 - e^{D_2 \Delta P_k}) e^{D_1 \Delta P_k} + D_2 (e^{D_1 \Delta P_k} - 1) e^{D_2 \Delta P_k}}{e^{D_2 \Delta P_k} - e^{D_1 \Delta P_k}} \\ &= \frac{H}{2} + \frac{\sqrt{H^2 + 4} e^{-H \Delta P_k / 2} - \cosh(\sqrt{H^2 + 4} \Delta P_k / 2)}{2 \sinh(\sqrt{H^2 + 4} \Delta P_k / 2)}. \end{aligned} \quad (3.2.21)$$

Substitution of these expression in equation (3.2.17) gives the movement of pulses on a terrain given by  $h(x) = Hx$  as

$$\begin{aligned} \frac{dP_j}{dt} &= \frac{Da^2}{m\sqrt{m}} \frac{1}{6} \left[ \left( \frac{H}{2} - \frac{\sqrt{H^2 + 4} e^{H \Delta P_j / 2} - \cosh(\sqrt{H^2 + 4} \Delta P_j / 2)}{2 \sinh(\sqrt{H^2 + 4} \Delta P_j / 2)} \right)^2 \right. \\ &\quad \left. - \left( \frac{H}{2} + \frac{\sqrt{H^2 + 4} e^{-H \Delta P_{j-1} / 2} - \cosh(\sqrt{H^2 + 4} \Delta P_{j-1} / 2)}{2 \sinh(\sqrt{H^2 + 4} \Delta P_{j-1} / 2)} \right)^2 \right]. \end{aligned} \quad (3.2.22)$$

For completely flat terrains we have a slope  $H = 0$  so that the ODE reduces to

$$\frac{dP_j}{dt} = \frac{Da^2}{m\sqrt{m}} \frac{1}{6} [\tanh(\Delta P_j / 2)^2 - \tanh(\Delta P_{j-1} / 2)^2], \quad (j = 2, \dots, N-1) \quad (3.2.23)$$

which is in agreement with [28, Equation (2.28)]. The values for  $u_{0j}$  are obtained by combining the expressions in (3.2.21) with equation (3.2.16). We obtain

$$\begin{aligned} \frac{6}{u_{0j}} &= - \frac{\sqrt{H^2 + 4}}{2} \left[ \frac{e^{H \Delta P_j / 2} - \cosh(\sqrt{H^2 + 4} \Delta P_j / 2)}{\sinh(\sqrt{H^2 + 4} \Delta P_j / 2)} \right. \\ &\quad \left. + \frac{e^{-H \Delta P_{j-1} / 2} - \cosh(\sqrt{H^2 + 4} \Delta P_{j-1} / 2)}{\sinh(\sqrt{H^2 + 4} \Delta P_{j-1} / 2)} \right]. \end{aligned} \quad (j = 2, \dots, N-1) \quad (3.2.24)$$

For  $H = 0$  this expression reduces to

$$\frac{6}{u_{0j}} = \tanh(\Delta P_j/2) + \tanh(\Delta P_{j-1}/2). \quad (j = 2, \dots, N-1). \quad (3.2.25)$$

Note that in principle these expressions (3.2.22)-(3.2.25) do not hold for  $j = 1$  and  $j = N$  as these pulses do not have two neighbours. In fact, the solutions  $\tilde{U}$  in the first and last outer region do not satisfy the same boundary conditions as the solution in the other regions. One should therefore recompute  $\tilde{U}_x^1(P_1)$  and  $\tilde{U}^{N+1}(P_N)$  for each type of domain. However, it is possible to introduce the two auxiliary locations  $P_0$  and  $P_{N+1}$  in such a way that expressions (3.2.22) and (3.2.23) still holds true for  $j = 1$  and  $j = N$  (see Figure 3.6). Below we inspect several type of domains and explain this reasoning further.

**Unbounded domains** On unbounded domains, we only have the requirement that solutions stay bounded as  $|x| \rightarrow \infty$ . So  $\tilde{U}^1$  should satisfy this boundedness requirement, the ODE and the boundary condition  $\tilde{U}(P_1) = 0$ . From this it follows that  $\tilde{U}_x^1(P_1) = \frac{H}{2} - \frac{\sqrt{H^2+4}}{2}$ . Similarly,  $\tilde{U}_x^{N+1}(P_N) = \frac{H}{2} + \frac{\sqrt{H^2+4}}{2}$ . When we introduce  $P_0 \rightarrow -\infty$  and  $P_{N+1} \rightarrow \infty$  in equation (3.2.22) we see that the pulse location ODE is given by (3.2.22), even for  $j = 1$  and  $j = N$ .

**Bounded domains with periodic boundary conditions** When we consider the bounded domain  $[0, L]$  with periodic boundary conditions, we set  $\tilde{U}(0) = \tilde{U}(L)$ . That is, the first pulse has the last pulse as a neighbour. Therefore expression (3.2.22) is directly applicable when we set  $\Delta P_0 = \Delta P_N = L - P_N + P_1$  or – equivalently –  $P_0 := P_N - L$  and  $P_{N+1} := L + P_1$ .

**Domains with Neumann boundary conditions** When the domain  $[0, L]$  has Neumann boundary conditions, we impose the boundary conditions  $\tilde{U}_x(0) = 0$  and  $\tilde{U}_x(L) = 0$ . A similar and straightforward computation then yields

$$\lim_{x \uparrow P_1} \tilde{U}_x^0(x) = \frac{-2 \sinh(\sqrt{H^2+4}P_1/2)}{H \sinh(\sqrt{H^2+4}P_1/2) + \sqrt{H^2+4} \cosh(\sqrt{H^2+4}P_1/2)},$$

$$\lim_{x \downarrow P_N} \tilde{U}_x^N(x) = \frac{2 \sinh(\sqrt{H^2+4}P_N/2)}{H \sinh(\sqrt{H^2+4}P_N/2) + \sqrt{H^2+4} \cosh(\sqrt{H^2+4}P_N/2)}.$$

The positions of the auxiliary locations  $P_0 < 0$  respectively  $P_{N+1} > L$  are determined as the negative zero of  $\tilde{U}^0$  extended below  $x = 0$  respectively the second zero of  $\tilde{U}^N$  extended beyond  $x = L$ . However, for general  $H$  there is no simple expression (in closed form) for  $P_0$  and  $P_{N+1}$ , though we find that  $\Delta P_0 = P_1 - P_0$  decreases as  $P_0$  decreases and  $\Delta P_N = P_{N+1} - P_N$  decreases as  $L - P_N$  decreases (i.e. as  $P_N$  increases). In the specific case  $H = 0$  we do find explicit expressions:  $P_0 = -P_1$  and  $P_{N+1} = 2L - P_N$ .

### Fixed points of the pulse-location ODE

It is natural to study the fixed points of the pulse-location ODE (3.2.22). Whether this ODE has any fixed points depends on the type of domain and boundary conditions. Below we summarise the results we acquired for bounded domains with Neumann boundary conditions, for bounded domains with periodic boundary conditions and

for unbounded domains. The proofs of these statements rely on the fact that the derivatives  $\Delta\tilde{U}(P_k^\pm)$  strictly increase/decrease as a function of the distance to the neighbouring pulse. The (mostly technical) details of the proofs can be found in appendix 3.B.

Note that the results in this section only consider the behaviour of the pulse-location ODE (3.2.22) in itself and do *not* take the behaviour of the full PDE into account. Specifically we do not take the stability of the  $N$ -pulse manifold  $\mathcal{M}_N$  into account. It can happen that a fixed point of the ODE is stable under the flow of the ODE, but not under the flow of the complete PDE (as we will see in section 3.4, e.g. Figure 3.20).

**Bounded domains with Neumann boundary conditions** For these domains the pulse location ODE (3.2.22) has precisely one fixed point. This fixed point is (locally) stable under the flow of the ODE. An example of this is given in Figure 3.20.

**Bounded domain with periodic boundary conditions** On these domains the ODE does not have any fixed points, unless  $H = 0$ , for which there is a continuous family of fixed points. All of these fixed points are regularly spaced configurations, i.e.  $\Delta P_j = L/N$  for all  $j$ . This family of fixed points is (globally) stable under the flow of the ODE.

Moreover, on bounded domains with periodic boundary conditions, the pulse-location ODE (3.2.22) has a continuous family of uniformly traveling solutions in which all pulses move with the same speed and the distance between two consecutive pulses is  $\Delta P_j = L/N$  for all  $j$ , i.e. the pulses are regularly spaced. This family of solutions is stable under the flow of the ODE.

**Unbounded domains** In this situation the ODE (3.2.22) does not have any fixed points and there does not exist any uniformly traveling solution either, unless  $N = 1$ . In fact, the distance between the first and last pulse,  $P_N - P_0$ , is ever increasing.

### 3.2.4 Pulse location ODE under assumption (A3')

When  $\frac{m\sqrt{m}D}{a^2} = \mathcal{O}(1)$ , equation (3.2.15) can no longer be simplified to (3.2.18). Thus we do need to determine the values of  $u_{0j}$  directly and we do need to make sure these lead to a solution  $\tilde{U}$  that satisfies the jump conditions in equation (3.2.16). More concretely, for a given  $\vec{u}_0 := (u_{01}, \dots, u_{0N})^T$ , a vector of the values of the internal boundary conditions, the boundary value problem (3.2.15) is well-posed and has a (uniquely determined) solution  $\tilde{U}$  on all subdomains. With this  $\tilde{U}$  we can validate the jump conditions (3.2.16). The following quantity defines a way to measure how well the internal boundary conditions  $\vec{u}_0$  satisfy the jump conditions

$$\vec{F}(\vec{u}_0) := \begin{pmatrix} \tilde{U}_x(P_1^+; \vec{u}_0) - \tilde{U}_x(P_1^-; \vec{u}_0) - \frac{6}{u_{01}} \\ \vdots \\ \tilde{U}_x(P_N^+; \vec{u}_0) - \tilde{U}_x(P_N^-; \vec{u}_0) - \frac{6}{u_{0N}} \end{pmatrix}.$$

The correct internal boundary conditions  $\vec{u}_0^*$  should satisfy  $\vec{F}(\vec{u}_0^*) = \vec{0}$ . If (3.2.15) has closed-form solutions, the function  $\vec{F}(\vec{u}_0^*)$  can be constructed explicitly. However, in general one needs a numerical root-finding scheme to solve  $\vec{F}(\vec{u}_0^*) = \vec{0}$ . We have used



the standard Newton scheme for this. Note that  $\vec{F}(\vec{u}_0) = \vec{0}$  does not necessarily have any solution and if it has, those solutions are – in general – not unique. Some cases for which we can find the roots explicitly are studied below. For notational convenience we define  $\delta := \frac{m\sqrt{m}D}{a^2}$ .

**Terrain with constant slope, i.e.  $h(x) = Hx$**

The reasoning in section 3.2.3 leading to the pulse-location ODE (3.2.22) in the case of  $\delta \ll 1$ , can be repeated here. The only difference is the addition of non-zero internal boundary conditions. The derivatives  $\tilde{U}_x^k(P_k)$  and  $\tilde{U}_x^k(P_{k+1})$  can be computed in a similar way as before. This time – when  $\delta = \mathcal{O}(1)$  – we find

$$\begin{aligned} \lim_{x \downarrow P_k} \tilde{U}_x^k(x) &= (1 - \delta u_{0,k}) \frac{H}{2} \\ &\quad - \frac{\sqrt{H^2 + 4} (1 - \delta u_{0,k+1}) e^{H\Delta P_k/2} - (1 - \delta u_{0,k}) \cosh(\sqrt{H^2 + 4}\Delta P_k/2)}{2 \sinh(\sqrt{H^2 + 4}\Delta P_k/2)}, \\ \lim_{x \uparrow P_{k+1}} \tilde{U}_x^k(x) &= (1 - \delta u_{0,k+1}) \frac{H}{2} \\ &\quad + \frac{\sqrt{H^2 + 4} (1 - \delta u_{0,k}) e^{-H\Delta P_k/2} - (1 - \delta u_{0,k+1}) \cosh(\sqrt{H^2 + 4}\Delta P_k/2)}{2 \sinh(\sqrt{H^2 + 4}\Delta P_k/2)} \end{aligned} \quad (k = 1, \dots, N-1)$$

Substitution of these expressions in equation (3.2.17) gives the movement of the pulses as

$$\begin{aligned} \frac{dP_j}{dt} &= \frac{Da^2}{m\sqrt{m}} \frac{1}{6} \left[ \left( \kappa_k \frac{H}{2} - \frac{\sqrt{H^2 + 4} \kappa_{k+1} e^{H\Delta P_j/2} - \kappa_k \cosh\left(\frac{H^2+4}{2}\Delta P_j\right)}{\sinh(\sqrt{H^2 + 4}\Delta P_j/2)} \right)^2 \right. \\ &\quad \left. - \left( \kappa_k \frac{H}{2} + \frac{\sqrt{H^2 + 4} \kappa_{k-1} e^{-H\Delta P_{j-1}/2} - \kappa_k \cosh\left(\frac{H^2+4}{2}\Delta P_j\right)}{\sinh(\sqrt{H^2 + 4}\Delta P_{j-1}/2)} \right)^2 \right], \end{aligned} \quad (3.2.26)$$

where  $\kappa_j := 1 - \delta u_{0j}$ . However, the  $u_{0j}$ -values are still unknown at this moment. To obtain these we need to solve  $\vec{F}(\vec{u}_0) = \vec{0}$ . With the explicit expressions for the derivatives  $\tilde{U}_x^k(P_k)$  and  $\tilde{U}_x^k(P_{k+1})$  at hand we can express the components of this function explicitly

$$\begin{aligned} F^k(\vec{u}_0) &= - \frac{\sqrt{H^2 + 4}}{2} \left[ \frac{\kappa_{k+1} e^{H\Delta P_k/2} - \kappa_k \cosh(\sqrt{H^2 + 4}\Delta P_k/2)}{\sinh(\sqrt{H^2 + 4}\Delta P_k/2)} \right. \\ &\quad \left. + \frac{\kappa_{k-1} e^{-H\Delta P_{k-1}/2} - \kappa_k \cosh(\sqrt{H^2 + 4}\Delta P_{k-1}/2)}{\sinh(\sqrt{H^2 + 4}\Delta P_{k-1}/2)} \right] - \frac{6}{u_{0k}}. \end{aligned} \quad (3.2.27)$$

As before equations (3.2.26) and (3.2.27) do not hold true for  $j = 1$  and  $j = N$  because these do not have two neighbour pulses. Again it is possible to derive expressions for  $\tilde{U}_x^1(P_1)$  and  $\tilde{U}_x^{N+1}(P_N)$  as we did in section 3.2.3 when  $\delta \ll 1$ . As the procedure is so similar, we refrain from doing that here. In general, one cannot expect to be able to determine the roots of (3.2.27) explicitly. Therefore we only consider the upcoming one-pulse example explicitly. We refrain from studying the pulse-location ODE analytically and use a numerical root-solving algorithm in section 3.4.

### A one-pulse on $\mathbb{R}$

The simplest, explicitly solvable, case is a 1-pulse on  $\mathbb{R}$ . The solution of ODE (3.2.15) is for all  $u_{01}$  and given by

$$\tilde{U}^0(x) = 1 + (\delta u_{01} - 1) e^{D_1(x-P_1)}, \quad \tilde{U}^1(x) = 1 + (\delta u_{01} - 1) e^{D_2(x-P_1)}.$$

Thus the function  $F$  is given by

$$F(u_{01}) = \sqrt{H^2 + 4} (1 - \delta u_{01}) - \frac{6}{u_{01}}.$$

so that  $F(u_{01}) = 0$  is solved by

$$(u_{01})_{\pm} = \frac{1}{2} \frac{1 \pm \sqrt{1 - 24\delta/\sqrt{H^2 + 4}}}{\delta}. \quad (3.2.28)$$

This expression agrees with the expressions found in the literature [45, 148]. It is also clear from this expression that there are two solutions as long as  $\delta < \delta_c := \frac{1}{24}\sqrt{H^2 + 4}$ . So for  $H = 0$  we find  $\delta_c = \frac{1}{12}$ , again in correspondence with the literature [45, page 8]. When  $\delta = \delta_c$  a saddle-node bifurcation occurs where the two solutions coincide and for  $\delta > \delta_c$  solutions no longer exist. The pulse-location ODE for this situation is given by

$$\frac{dP_1}{dt} = \frac{Da^2}{m\sqrt{m}} H \sqrt{H^2 + 4} (1 - \delta u_{01})^2. \quad (3.2.29)$$

In the asymptotic limit  $\delta \ll 1$ , equation (3.2.28) yields two solutions, given to leading order by

$$(u_{01})_+ = \frac{1}{\delta} + \mathcal{O}(1), \quad (u_{01})_- = \frac{6}{\sqrt{H^2 + 4}} + \mathcal{O}(\delta).$$

In section 3.2.3, in equation (3.2.24) we found only one value for  $u_{0j}$ . Carefully taking the limit  $\Delta P_0 \rightarrow -\infty$  and  $\Delta P_1 \rightarrow \infty$  of (3.2.24) reveals that only  $(u_{01})_-$  is found. This is because  $(u_{01})_+ \gg 1$  in this asymptotic limit and it therefore does not satisfy the (implicit) assumption that  $u_{01} = \mathcal{O}(1)$ . This focus on  $(u_{01})_-$  is justified; if one were to study the other possibility, i.e. pulses that have the internal boundary condition  $(u_{01})_+$ , one would quickly find out that these pulses are always unstable [47].

## 3.3 Linear Stability

In this section, we look at perturbations of  $N$ -pulse solutions and study the associated quasi-steady spectrum. For this we freeze the  $N$ -pulse solution and (at leading order) its time-dependent movement on the manifold  $\mathcal{M}_N$ . We then linearise around this  $N$ -pulse configuration to obtain a quasi-steady eigenvalue problem, which can be solved along the very same lines as the existence problem. This gives us quasi-steady eigenvalues and eigenfunctions. We can compute these for any given time  $t$  and as such these quasi-steady eigenvalues and eigenfunctions are parametrised by time  $t$  (via the pulse locations  $P_j(t)$ ) – see also [12, 50, 172]). Although our approach in principle works in a general setting – thus for instance with a general topography  $h(x)$  – both its interpretation and its presentation are significantly facilitated when we restrict ourselves to pulse-solutions of the extended Klausmeier model (3.1.1) for

terrains with constant slope, i.e.  $h(x) = Hx$ . For other kind of terrains the PDE has space-dependent coefficients and explicit expressions are not present in general. Here other techniques need to be used [7].

We start with the classical case of a single pulse (i.e.  $N = 1$ ) on  $\mathbb{R}$  in section 3.3.1. This illustrates the concepts and shows how it generalises to other boundaries or multiple pulses, which we will study subsequently in section 3.3.2. In both sections we find essential differences between the asymptotic cases  $m \gg 1 + H^2/4$  and  $m \ll 1 + H^2/4$ . In the former case ( $m \gg +H^2/4$ ) we find Hopf bifurcations. Moreover, we find that pulses in the stability problem are far apart such that the eigenfunctions decouple and can be studied per pulse. In the latter case ( $m \ll 1 + H^2/4$ ) we find saddle-node bifurcations. However, in this situation the eigenfunctions are coupled, which leads to a more involved eigenvalue problem and more involved eigenfunctions [28].

The first step in the stability analysis consists of linearizing the extended Klausmeier model around a (frozen)  $N$ -pulse solution. We denote the  $N$ -pulse configuration of this equation by  $(U_p^N, V_p^N)$  and set  $(U, V) = (U_p^N, V_p^N) + e^{\lambda t}(\bar{U}, \bar{V})$  to study its linear stability. Following the scalings in [28, 46] we scale the eigenvalue as  $\lambda = m\hat{\lambda}$  to study the so-called large eigenvalues that correspond to perturbations non-tangent to the manifold  $\mathcal{M}_N$  of  $N$ -pulse solutions. Thus we obtain the quasi-steady eigenvalue problem

$$\begin{cases} 0 &= \bar{U}_{xx} + H\bar{U}_x - (1 + m\hat{\lambda} + (V_p^N)^2)\bar{U} - 2U_p^N V_p^N \bar{V} \\ 0 &= D^2\bar{V}_{xx} + (2U_p^N V_p^N - m - m\hat{\lambda})\bar{V} + (V_p^N)^2\bar{U}. \end{cases} \quad (3.3.1)$$

Our aim is to find the values  $\hat{\lambda}$  for which we can solve this eigenvalue problem. To find these eigenvalues  $\hat{\lambda}$  we can exploit the inner and outer regions of our previously obtained  $N$ -pulse solution. Because  $V_p^N$  is localised near the pulse locations, we see that in the outer regions this problem reduces in leading order to

$$\begin{cases} 0 &= \bar{U}_{xx} + H\bar{U}_x - (1 + m\hat{\lambda})\bar{U} \\ 0 &= -(m + m\hat{\lambda})\bar{V}. \end{cases} \quad (3.3.2)$$

Hence  $\bar{V} = 0$  in the outer regions;  $\bar{V}$  is also concentrated around the pulse locations in the stability problem.

Our approach now essentially boils down to the following. We first solve the  $\bar{U}$ -equation in the outer regions for general  $\hat{\lambda}$ . We then need to glue these solutions together at the pulse locations. For this we require continuity of  $\bar{U}$  and we additionally obtain a  $\hat{\lambda}$ -dependent jump condition for  $\bar{U}_x$  at each pulse location, which is imposed by the solution in the inner regions. The correct eigenvalues  $\hat{\lambda}$  are then those values that allow solutions  $\bar{U}$  which satisfy the boundary conditions at both ends of the domain. This method thus also immediately gives us the form of the eigenfunction as well.

### 3.3.1 Stability of homoclinic pulses on $\mathbb{R}$

We first consider the case of a homoclinic pulse on  $\mathbb{R}$  that is located at  $x = P_1$ . In this setting we have one inner region,  $I_1^{in}$ , and two outer regions,  $I_{1,2}^{out}$ . Since we are working on  $\mathbb{R}$  we do not have boundary conditions, but only require solutions in the outer regions to be bounded. Solving the homogeneous ODE (3.3.2) in the outer regions gives the solutions  $\bar{U}_1$  in the first outer field and  $\bar{U}_2$  in the second outer region

as

$$\begin{aligned}\bar{U}_1(x) &= C_1 e^{\frac{1}{2}[-H + \sqrt{H^2 + 4(1+m\hat{\lambda})}](x-P_1)}, \\ \bar{U}_2(x) &= C_2 e^{\frac{1}{2}[-H - \sqrt{H^2 + 4(1+m\hat{\lambda})}](x-P_1)},\end{aligned}$$

where  $C_1$  and  $C_2$  are some constants. To satisfy the continuity condition on  $\bar{U}$ , we set  $C_1 = C_2 = \rho_1$ . With respect to the outer regions the jump in  $\bar{U}_x$  is given by

$$\Delta_{out}\bar{U}_x(P_1) := \bar{U}_x(P_1^+) - \bar{U}_x(P_1^-) = -\rho_1 \sqrt{H^2 + 4(1+m\hat{\lambda})}. \quad (3.3.3)$$

In the inner region the system is given by

$$\begin{cases} 0 &= \frac{m}{D^2}\bar{U}'' + \frac{\sqrt{m}}{D}\bar{U}' - (1+m\hat{\lambda})\bar{U} - 2U_p^N V_p^N \bar{V} - (V_p^N)^2 \bar{U}; \\ 0 &= m\bar{V}'' - (m+m\hat{\lambda})\bar{V} + 2U_p^N V_p^N \bar{v} + (V_p^N)^2 \bar{U}, \end{cases} \quad (3.3.4)$$

where primes again denote derivatives with respect to the stretched coordinate  $\xi_1$ . From equation (3.2.6) and the scalings of (3.2.2) we know the approximate form of  $V_p^1$  and  $U_p^1$  in the inner region. For notational convenience we write  $\omega(\xi) := \frac{3}{2} \operatorname{sech}(\xi/2)^2$ . Moreover we note that  $\bar{U} \approx \rho_1$  in the inner region by matching with the solutions in the outer region. Upon scaling  $\bar{V}$  as

$$\bar{V} = -\frac{a^2}{m^2} \frac{1}{D^2} \frac{\rho_1}{u_{01}^2} V_{in}, \quad (3.3.5)$$

the stability problem in the inner region reduces to

$$\bar{U}'' + \frac{a^2}{m^2} \frac{Dm\sqrt{m}H}{a^2} \bar{U}' - \frac{a^4}{m^4} \left( \frac{Dm\sqrt{m}}{a^2} \right)^2 (1+m\hat{\lambda})\bar{U} - \frac{a^2}{m^2} (2\omega V_{in} - \omega^2) = 0, \quad (3.3.6)$$

where  $V_{in}$  satisfies

$$\left( \mathcal{L}_f(\zeta) - \hat{\lambda} \right) V_{in} := V_{in}'' - (1 + \hat{\lambda})V_{in} + 2\omega V_{in} = \omega^2. \quad (3.3.7)$$

Because of assumptions (A1), (A3) and (A5) we find the leading order change of  $\bar{U}'$  in the inner region to be

$$\Delta_{in}\bar{U}'_1 := \int_{I_1^{in}} \bar{U}''(\zeta) d\zeta = \frac{a^2}{m^2} \frac{\rho_1}{u_{01}^2} \int_{-\infty}^{\infty} (\omega^2 - 2\omega V_{in}) d\zeta + h.o.t. \quad (3.3.8)$$

For notational simplicity we write

$$\hat{C}(\hat{\lambda}) := \int_{-\infty}^{\infty} (\omega(\zeta)^2 - 2\omega(\zeta)V_{in}(\zeta; \hat{\lambda})) d\zeta. \quad (3.3.9)$$

Because  $\bar{U}_x = \frac{\sqrt{m}}{D}\bar{U}'$ , we find the total jump in  $\bar{U}_x$  over  $I_1^{in}$ ,

$$\Delta_{in}\bar{U}_x(P_1) = \frac{a^2}{m\sqrt{m}D} \frac{\rho_1}{u_{01}^2} \hat{C}(\hat{\lambda}). \quad (3.3.10)$$

Combining the outer and inner approximations of  $\Delta\bar{U}_x$  in equations (3.3.3) and (3.3.10) yields

$$\frac{a^2}{m\sqrt{m}D} \frac{\rho_1}{u_{01}^2} \hat{C}(\hat{\lambda}) = -\sqrt{H^2 + 4(1+m\hat{\lambda})}\rho_1. \quad (3.3.11)$$

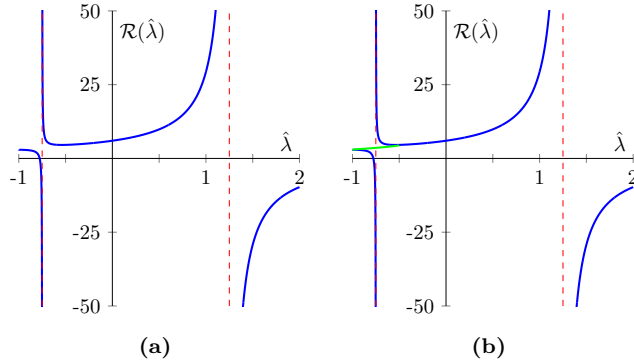


**Figure 3.7** – The function  $\mathcal{R}(\hat{\lambda})$ . In (a) we show the form of  $\mathcal{R}(\hat{\lambda})$  only for real-valued  $\hat{\lambda}$ , whereas in (b) we also show the complex values of  $\hat{\lambda}$  that lead to  $\mathcal{R}(\hat{\lambda})$  that do not have an imaginary part (shown in green). In both figures the poles at  $\hat{\lambda} = -3/4$  and  $\hat{\lambda} = 5/4$  are indicated with dashed red lines.

Since  $\rho_1 = 0$  corresponds to ‘small eigenvalue’ solutions of (3.3.1) – which are already captured by the pulse-location ODE (3.2.17) – we take  $\rho_1 \neq 0$  and find the eigenvalue condition

$$m^2 D \frac{u_{01}^2}{a^2} = \frac{\int_{-\infty}^{\infty} \omega V_{in} d\zeta - 3}{\sqrt{\hat{\lambda} + \frac{H^2 + 4}{4m}}} \quad (3.3.12)$$

where we have used (3.3.9) and  $\int_{-\infty}^{\infty} \omega(\zeta)^2 d\zeta = 6$ . We can only get a detailed understanding of the eigenvalues  $\hat{\lambda}$  of this problem, once we understand the form of the right-hand side of (3.3.12), which boils down to studying the integral

$$\mathcal{R}(\hat{\lambda}) := \int_{-\infty}^{\infty} \omega(\zeta) V_{in}(\zeta; \hat{\lambda}) d\zeta, \quad (3.3.13)$$

where  $V_{in}(\zeta; \hat{\lambda})$  is a bounded function that solves (3.3.7).

### Properties of the integral $\mathcal{R}(\hat{\lambda})$

To get a detailed understanding of  $\mathcal{R}(\hat{\lambda})$ , we need to solve (3.3.7). It is possible to transform this differential equation to a hypergeometric differential equation. The details of this procedure can be found in [47, section 5] and [48, section 5.2] – see Figure 3.7 for evaluations of  $\mathcal{R}(\hat{\lambda})$  based on this procedure. For several specific values of  $\hat{\lambda}$  it is possible to get a direct grip on  $\mathcal{R}(\hat{\lambda})$ . Foremost,  $V_{in}$  is only uniquely defined for  $\hat{\lambda}$  that are not eigenvalues of the operator  $\mathcal{L}_f$ . When  $\hat{\lambda}$  is an eigenvalue of  $\mathcal{L}_f$ , the solution  $V_{in}$  is either not defined or not uniquely defined. When  $V_{in}(\xi; \hat{\lambda})$  does not exist, the function  $\mathcal{R}(\hat{\lambda})$  has a pole for this value of  $\hat{\lambda}$ . When  $V_{in}(\xi; \hat{\lambda})$  is not uniquely defined for an eigenvalue  $\hat{\lambda}$  of  $\mathcal{L}_f$ , the value of  $\mathcal{R}(\hat{\lambda})$  is still uniquely defined [48].

The operator  $\mathcal{L}_f$  is well-studied. The eigenvalues are known to be  $\hat{\lambda} = \frac{5}{4}$ ,  $\hat{\lambda} = 0$  and  $\hat{\lambda} = -\frac{3}{4}$  and the essential spectrum is  $(-\infty, -1)$  [54]. It turns out that  $\mathcal{R}(\hat{\lambda})$  has poles for  $\hat{\lambda} = \frac{5}{4}$  and for  $\hat{\lambda} = -\frac{3}{4}$ . For  $\hat{\lambda} = 0$  one can verify that  $V_{in}$  is given by

$V_{in}(\xi; 0) = C\omega'(\xi) + \omega(\xi)$ , where  $C$  is a constant. Direct substitution in (3.3.13) shows that this constant  $C$  drops out and we obtain

$$\mathcal{R}(0) = 6. \quad (3.3.14)$$

The derivative of  $\mathcal{R}$  at  $\hat{\lambda} = 0$  can also be determined. For this, we first observe that  $\mathcal{R}'(\hat{\lambda}) = \int_{-\infty}^{\infty} \omega(\xi) \partial_{\hat{\lambda}} V_{in}(\xi; \hat{\lambda}) d\xi$ , where  $\partial_{\hat{\lambda}} V_{in}(\xi; \hat{\lambda})$  satisfies

$$\mathcal{L}_f \left( \partial_{\hat{\lambda}} V_{in}(\xi; \hat{\lambda}) \right) = V_{in}(\xi; \hat{\lambda}). \quad (3.3.15)$$

Thus we must solve  $\mathcal{L}_f \left( \partial_{\hat{\lambda}} V_{in}(x; 0) \right) = \omega$ . This yields  $\partial_{\hat{\lambda}} V_{in}(\xi; 0) = C\omega'(\xi) + \omega(\xi) + \frac{1}{2}\xi\omega'(\xi)$  and hence

$$\mathcal{R}'(0) = \frac{9}{2}. \quad (3.3.16)$$

Finally, at  $\hat{\lambda} = -1$ , the boundary of the essential spectrum, the differential equation for  $V_{in}(\xi; -1)$  has a family of bounded solutions given as

$$V_{in}(\xi; -1) = \omega(\xi) - \frac{1}{2} + C \left( 2 \tanh(\xi/2) + \frac{10}{3} \omega'(\xi) \right) \quad (3.3.17)$$

and thus

$$\mathcal{R}(-1) = 3. \quad (3.3.18)$$

The above properties are the most important properties of  $\mathcal{R}$  for the analysis in this article. A more extensive study of the properties of  $\mathcal{R}$  is presented in [54, section 4.1] and [48, section 5]<sup>4</sup>.

### Finding eigenvalues

There is also a square root on the right-hand side of (3.3.12). Thus, real solutions are only possible when  $\hat{\lambda} > \hat{\lambda}^H := \frac{H^2+4}{4m}$ . Moreover, this term can create an additional pole at  $\hat{\lambda} = \hat{\lambda}^H$ . Depending on the value of  $\hat{\lambda}^H$  one of three things can happen.

- $\hat{\lambda}^H \leq -1$ : The new pole falls in the essential spectrum and the whole form of  $\mathcal{R}(\hat{\lambda})$  is visible.
- $-1 < \hat{\lambda}^H < -\frac{3}{4}$ : The new pole is seen, in addition to the two poles of  $\mathcal{R}(\hat{\lambda})$ .
- $-\frac{3}{4} \leq \hat{\lambda}^H$ : The new pole at  $\hat{\lambda} = \hat{\lambda}^H$  ‘replaces’ the pole of  $\mathcal{R}(\hat{\lambda})$  that is located at  $\hat{\lambda} = -\frac{3}{4}$ .

All three cases lead to different forms for the right-hand side of (3.3.12) – see Figure 3.8.

Now that we understand the right-hand side, we can determine the eigenvalues for our problem with a simple procedure. For this we compute the (current) value of the left-hand side of (3.3.12) and then we see which values of  $\hat{\lambda}$  lead to the same value on the right-hand side. Note that the value for  $u_{01}$  is thus crucial in our stability problem. In section 3.2.3 and section 3.2.4 we determined  $u_{01}$  and thus how it changes in time. When we let the rainfall parameter  $a$  decrease over time, we typically see that  $\frac{u_{01}}{a}$  increases. From this observation it is natural to study what happens to the eigenvalues when the left-hand side of (3.3.12) increases.

<sup>4</sup>Be aware though, that the  $\mathcal{R}$  in this article has a different factor in front of it and is defined in terms of  $\hat{\lambda}$ , whereas the cited articles define it as function of  $P := 2\sqrt{1 + \hat{\lambda}}$ .

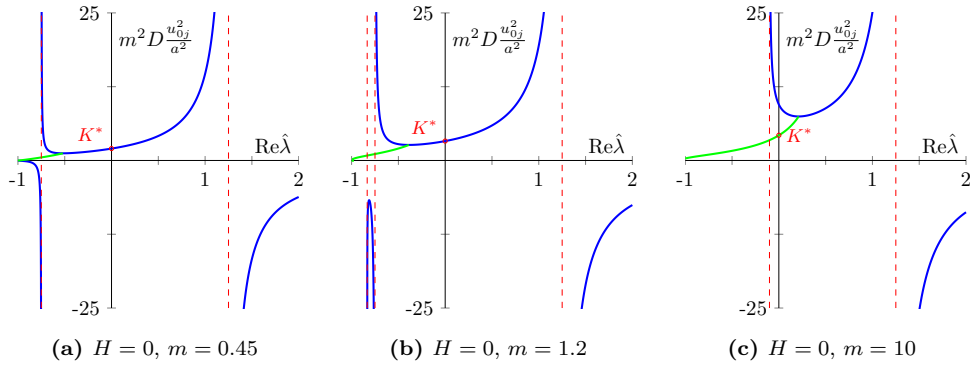


**Figure 3.8** – The right-hand side of (3.3.12) for different possible values of  $\hat{\lambda}^H$ : in (a)  $\hat{\lambda}^H = -20/9 < -1$ , in (b)  $\hat{\lambda}^H = -5/6 \in (-1, -3/4)$  and in (c)  $\hat{\lambda}^H = -1/10 > -3/4$ . The location of the poles are indicated with dashed red lines. Additionally we show the complex  $\hat{\lambda}$  that lead to real values in green and the value of  $K^*(m, H)$ , see (3.3.20).

The left-hand side of (3.3.12) is always real-valued and positive. Therefore the right-hand side needs to be as well. Thus for given  $H$  and  $m$  only a specific set of  $\hat{\lambda}$  are possible eigenvalues of the eigenvalue problem (3.3.12) – precisely those  $\hat{\lambda}$  that lead to a real-valued and positive right-hand side in (3.3.12). This leads to a skeleton in  $\mathbb{C}$  on which all eigenvalues necessarily lie. These skeletons come in three qualitatively different forms, which we show in Figure 3.9. The difference between those skeletons is the place where the complex eigenvalues land on the real axis. For a critical value  $m_c(H)$  they land precisely on  $\hat{\lambda} = 0$ . For  $m > m_c(H)$  they land to the right of the imaginary axis and for  $m < m_c(H)$  they land to the left of it.

The point where the complex eigenvalues land on the real axis, needs to be a local minimum<sup>5</sup> of the right-hand side of (3.3.12). Therefore the critical value  $m_c(H)$  must be such that this minimum is attained at  $\hat{\lambda} = 0$ . Differentiating (3.3.12) and setting the result to zero then indicates that  $m_c(H)$  must satisfy

$$2\mathcal{R}'(0) \frac{H^2 + 4}{4m_c(H)} - \mathcal{R}(0) + 3 = 0.$$

Substitution of (3.3.14) and (3.3.16) then yields the critical value

$$m_c(H) = 3 \left( 1 + \frac{H^2}{4} \right). \quad (3.3.19)$$

The eigenvalues of (3.3.12) can now simple be read of, and depend on the value of the left-hand side. For small values the eigenvalues approach the points  $A_{1,2}$  in Figure 3.9. When the left-hand side is increased, we follow the skeletons and see that the pair of complex eigenvalues changes into two real eigenvalues, points  $B_{1,2}$  in Figure 3.9. Increasing the value even further we end up close to the poles, points  $C_{1,2}$  in Figure 3.9.

Somewhere along this trajectory a bifurcation has occurred, when an eigenvalue  $\hat{\lambda}$  gets a positive real part. For  $m < m_c(H)$  this happens for one eigenvalue that has no imaginary part. Thus here we find a saddle-node bifurcation; the corresponding

<sup>5</sup>Otherwise there is a range of left-hand side values that have four eigenvalues, which is impossible as indicated by a winding number argument.

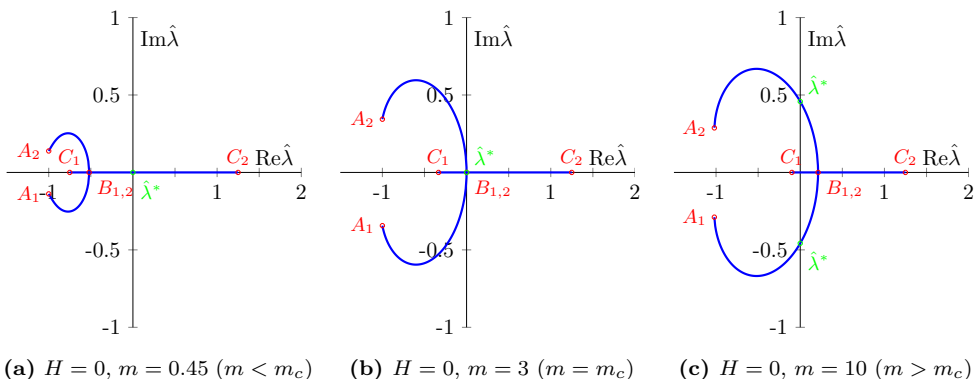


**Figure 3.9** – Plots of the skeletons on which eigenvalues of (3.3.12) necessarily lie. In (a)  $H = 0, m = 0.45$  ( $m < m_c$ ), in (b)  $H = 0, m = 3$  ( $m = m_c$ ) and in (c)  $H = 0, m = 10$  ( $m > m_c$ ). When the right-hand side of (3.3.12) is small – e.g. for a high rainfall parameter  $a$  – the eigenvalues are located at  $A_{1,2}$  and when the right-hand side is big – e.g. for a low rainfall parameter  $a$  – the eigenvalues are located at  $C_{1,2}$ . In between they follow the pictured skeleton, changing from a pair of complex eigenvalues to two real eigenvalues at  $B_{1,2}$ . The critical, destabilizing eigenvalue  $\hat{\lambda}^*$  is also depicted in these figures. Note that in (a) eigenvalues cross the imaginary axis by a saddle-node bifurcation and in (c) by a Hopf bifurcation; (b) corresponds to a Bogdanov-Takens bifurcation.

eigenfunction is shown in Figure 3.10a. For  $m > m_C(H)$  a pair of complex eigenvalues enters the right-half plane and we thus have a Hopf bifurcation; the corresponding eigenfunction is shown in Figure 3.10b. Finally for  $m = m_C(H)$  a codimension 2 Bogdanov-Takens bifurcation occurs. In all of these situations we find that there is a critical value  $K^*(m, H)$  of the right-hand side. For values below  $K^*(m, H)$  the pulse is stable and for values above it the pulse is unstable. This critical value is given by

$$K^*(m, H) := \frac{\mathcal{R}(\hat{\lambda}^*) - 3}{\sqrt{\hat{\lambda}^* + \frac{H^2+4}{4m}}}. \quad (3.3.20)$$

For  $m \leq m_C(H)$  the critical eigenvalue is  $\hat{\lambda}^* = 0$  and therefore  $K^*(m, H) = 6\sqrt{\frac{m}{H^2+4}}$ . Also note that  $K^*(m_C(H), H) = 3\sqrt{3}$ . For  $m > m_C(H)$  there is no explicit expression, but for given parameters  $m$  and  $H$  it is not hard to obtain it by numerical evaluation. Note that this value necessarily needs to be smaller than  $6\sqrt{\frac{m}{H^2+4}}$ .

### Asymptotic considerations

Although we now understand the eigenvalue problem (3.3.12) completely for any set of parameters, it is useful to still study the asymptotic cases. There are two parameter regimes that will play a role in the analysis of multi-pulse solutions, (1)  $\frac{H^2+4}{4m} \gg 1$  (i.e.  $m \ll 1 + H^2/4$ ) and (2)  $\frac{H^2+4}{4m} \ll 1$  (i.e.  $m \gg 1 + H^2/4$ ).



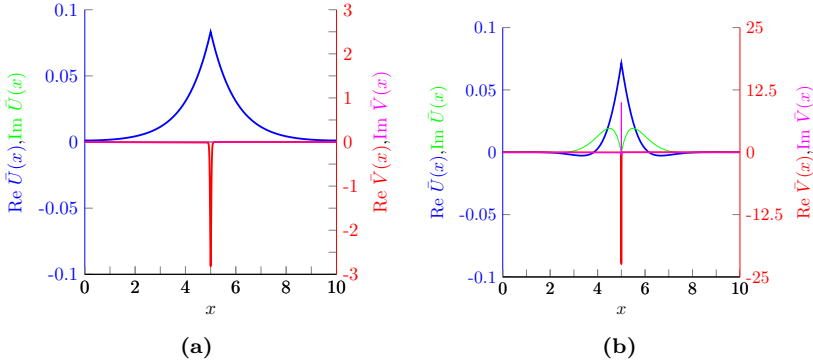


**Figure 3.10** – Approximation of an analytically obtained eigenfunction of a (single) pulse when we encounter a saddle-node bifurcation (a) or a Hopf bifurcation (b). The real part of the  $U$ -value is given in blue, the imaginary part in green, the real part of the  $V$ -pulse in red and its imaginary part in pink. Parameter values  $H = 0$ ,  $D = 0.01$ ,  $L = 10$  and  $m = 0.45$ ,  $a = 0.19032$  (in a) and  $m = 10$ ,  $a = 2.1065$  (in b).

- (1) In the first case, we see that (3.3.12) reduces to

$$\frac{m^2 D}{a^2} u_{01}^2 = \frac{\mathcal{R}(\hat{\lambda}) - 3}{\sqrt{\frac{H^2 + 4}{4m}}}.$$

Rewriting this gives the condition

$$\sqrt{1 + H^2/4} \frac{m\sqrt{mD}}{a^2} u_{01}^2 = \mathcal{R}(\hat{\lambda}) - 3.$$

From our previous analysis we know that the eigenvalues  $\hat{\lambda}$  have negative real parts, when the left-hand side is small enough. Thus assumptions (A3) and (A5) now guarantee that the left-hand side is (asymptotically) small and therefore that the pulse solution is stable. Only when these size assumptions are violated is it possible for the pulse to become unstable, in this regime. Moreover, destabilisation happens through a saddle-node bifurcation in this regime.

- (2) In the second case, equation (3.3.12) reduces to

$$\frac{m^2 D}{a^2} u_{01}^2 = \frac{\mathcal{R}(\hat{\lambda}) - 3}{\sqrt{\hat{\lambda}}}.$$

This time we see that assumptions (A4) and (A6) indicate that the left-hand side is (asymptotically) small and therefore that the pulse is stable. When these size assumptions are violated the pulse may become unstable, via a Hopf bifurcation.

### 3.3.2 Stability of $N$ -pulse solutions

This section is devoted to the stability of multi-pulse solutions and pulse-solutions on bounded domains. The pulses in these solutions interact with each other and the

boundary and are therefore moving in space, see section 3.2. In the stability problem these interactions can show up as well, leading to a more involved stability problem than in the previous section. We consider  $N$ -pulse solutions, with pulses located at  $P_1(t) < \dots < P_N(t)$ . Similar to the existence problem of these solutions, we again have an inner region,  $I_j^{in}$ , near each pulse and outer regions  $I_j^{out}$  between each pulses and between the first/last pulse and the boundary.

The stability problem in the outer region is again described by equation (3.3.2). Here we again see an important distinction between the  $m \gg 1 + H^2/4$  and the  $m \ll 1 + H^2/4$  situations. In the former case the eigenvalue  $\hat{\lambda}$  has a leading order role in the outer problem, whereas in the latter case it only has a higher order role. Moreover, in the situation with  $m \gg 1 + H^2/4$  the pulses are far apart in the stability problem. As a result the background state  $(\bar{U}, \bar{V}) = (0, 0)$  is approached in between pulses (to leading order). Therefore there is no direct interaction between the pulses in the stability problem in this regime. This leads to a decoupled stability problem in which we can treat the stability of each pulse separately. In the other situations, when  $m \leq \mathcal{O}(1 + H^2/4)$ , this effect does not occur and the stability problem of all pulses is coupled. We will consider these situations separately.

### $m \gg 1 + H^2/4$ - decoupled stability problem

Solving the homogeneous ODE in the outer regions, equation (3.3.2), for  $\tilde{U}$  gives the following solution in the outer region between the  $j$ -th and the  $j + 1$ -th pulse as

$$\bar{U}_j(x) = S_{1j} e^{\frac{1}{2}[-H - \sqrt{H^2 + 4(1+m\hat{\lambda})}](x-P_j)} + S_{2j} e^{\frac{1}{2}[-H + \sqrt{H^2 + 4(1+m\hat{\lambda})}](x-P_{j+1})}, \quad (3.3.21)$$

where  $S_1$  and  $S_2$  are constants. We can also define the solution in the outer regions with  $x < P_1$  and  $x > P_N$  in a consistent manner with the definition of  $P_0$  and  $P_{N+1}$  as described in section 3.2.3. Since  $m \gg 1 + H^2/4$ , we see that  $-H \pm \sqrt{H^2 + 4(1+m\hat{\lambda})} \gg 1$ , regardless of the size of  $H$  compared to  $m$ . Therefore  $\bar{U}_j(P_j) = S_{1j}$  and  $\bar{U}_j(P_{j+1}) = S_{2j}$  to leading order. Thus we can approximate the outer solutions by setting the constants  $S_{1j}$  and  $S_{2j}$  as follows:

$$S_{1j} = \rho_j; \quad S_{2j} = \rho_{j+1}; \quad S_{10} = 0; \quad S_{2N} = 0, \quad (3.3.22)$$

where  $\rho_j$  is (an approximation of) the value  $\bar{U}_j(P_j)$ . Note that the thus constructed outer solution  $\bar{U}$  automatically is continuous in each pulse location, again to leading order. Similar to the 1-pulse case, we need to impose jump conditions on the derivative  $\bar{U}_x$  at each pulse location. In the outer regions this jump is approximated by

$$\Delta_{out} \bar{U}_x(P_j) := \bar{U}_x(P_j^+) - \bar{U}_x(P_j^-) = -\rho_j \sqrt{H^2 + 4(1+m\hat{\lambda})}. \quad (3.3.23)$$

Note the similarities with equation (3.3.3). The jump in the inner region can be computed at each pulse. This computation is identical as for the homoclinic pulse in section 3.3.1. Hence we obtain (see equation (3.3.10)):

$$\Delta_{in} \bar{U}_x(P_j) = \frac{a^2}{m\sqrt{m}D} \frac{\rho_j}{u_{0j}^2} \hat{C}(\hat{\lambda}). \quad (3.3.24)$$

where  $C(\hat{\lambda})$  is defined in equation (3.3.9). Equating both descriptions of the jump gives us  $N$  equations that a solution of the stability problem should satisfy:

$$\frac{a^2}{m\sqrt{mD}} \frac{\rho_j}{u_{0j}^2} \hat{C}(\hat{\lambda}) = -\rho_j \sqrt{H^2 + 4(1 + m\hat{\lambda})}. \quad (3.3.25)$$

This condition is immediately satisfied when  $\rho_j = 0$ . After division by  $\rho_j$  it is clear that the left-hand side depends on the pulse number  $j$ , whereas the right side does not. Therefore, we know the eigenfunctions of the linear stability problem generically have one  $n \in \{1, \dots, N\}$  such that  $\rho_n \neq 0$  and  $\rho_j = 0$  for all  $j \neq n$ . Thus the pulses are decoupled in the stability problem and eigenfunctions are always localised near a single pulse. A solution with  $\rho_n \neq 0$  is only a solution to the stability problem if the jump condition is satisfied, i.e. if it satisfies

$$\frac{a^2}{m\sqrt{mD}} \frac{1}{u_{0n}^2} \int_{-\infty}^{\infty} (\omega^2 - 2\omega V_{in}) ds = -\sqrt{H^2 + 4(1 + m\hat{\lambda})}. \quad (3.3.26)$$

Note that this is precisely the same condition as we found for the stability of a homoclinic pulse in equation (3.3.11). Thus we can use the conclusions from that case here. That is, eigenvalues necessarily need to lie on the skeleton given in Figure 3.9c. Moreover, the  $n$ -th eigenfunction has an eigenvalue with positive real part when  $K_n := \frac{m^2 D}{a^2} u_{0n}^2 > K^*(m, H)$ . Therefore when  $K_j < K^*(m, H)$  for all  $j \in \{1, \dots, N\}$  we know that the solution is stable. However, if  $K_k > K^*(m, H)$  for some  $k$ , we know that the  $N$ -pulse solution is unstable. More specifically we know that the corresponding eigenfunction has  $\rho_k \neq 0$  and consists of a localised pulse, located at  $x = P_k$ . This linear reasoning now suggests that, as the pattern is destabilised, the  $k$ -th pulse should disappear.

In degenerate cases, it is possible that multiple pulses have the same  $K_j$ -value, say the value  $\bar{K}$ . If that happens, then there exist eigenfunctions that have more than one non-zero  $\rho_j$ -value. That is, the eigenspace corresponding to the corresponding eigenvalue  $\hat{\lambda}$  is multidimensional. To really get a grip on what's happening at a bifurcation in these cases, we need to zoom in on the corresponding eigenvalues  $\hat{\lambda}$ , where the stability problem becomes a coupled stability problem once again. This has already been done in the case of spatially periodic pulse configurations [53], where Floquet theory has been used to find the form of the possible eigenfunctions. From this we know that in these situations – when there are multiple pulses with the same  $K_j$ -value – the eigenvalues are asymptotically close together, though still separated. Moreover, the eigenfunctions become combinations of the single-pulse eigenfunctions that we have already encountered. In fact, in [53], it is found that the most unstable eigenfunction will always be a period-doubling Hopf bifurcation (when  $\gamma = -1$ ) or a full desertification bifurcation (when  $\gamma = 1$ ). At present, it is not clear how we get from the simple, one-pulse eigenfunctions to these more involved (periodic) eigenfunctions as patterns evolve towards regularity. These two types of destabilisations are intertwined in an involved way, which is explained by the appearance of ‘Hopf dances’ [52, 53]. We refrain from going in the details here.

### $m \leq \mathcal{O}(1 + H^2/4)$ - coupled stability problem

As before, we can use the outer solution (3.3.21). However, we can no longer use the approximations in (3.3.22), which leads to more involved eigenfunctions that have localised structures at all pulse locations. To find eigenfunctions, we need to understand

when a function is an eigenfunction of this (now) coupled stability problem. Foremost, we need to have continuity of  $\bar{U}$  at each pulse location, i.e.  $\bar{U}_j(P_j) = \bar{U}_{j-1}(P_j)$ . Secondly at each pulse location there will be – as before – a jump in the derivative  $\bar{U}_x$ , of size  $\Delta_{in}\bar{U}_x(P_j) = \frac{a^2}{m\sqrt{mD}} \frac{\rho_j}{u_{0j}^2} \hat{C}(\hat{\lambda})$ , where  $\rho_j := \bar{U}(P_j)$  and  $\hat{C}$  as in (3.3.9).

With these two conditions it is possible to find the value for the constants  $S_{1j+1}$  and  $S_{2j+1}$  when we are given the values of  $S_{1j}$  and  $S_{2j}$  and the eigenvalue  $\hat{\lambda}$ . Thus, when given the value  $S_{10}$  and  $S_{20}$  that satisfy the left boundary condition, it is possible to deduce the constants  $S_{1N}$  and  $S_{2N}$  by using the algebraic relations coming from the continuity of  $\bar{U}$  and the jump in  $\bar{U}_x$  at each pulse location. The concept of finding the eigenfunctions is now simple: the eigenvalues  $\hat{\lambda}$  are precisely those values that lead to constants  $S_{1N}$  and  $S_{2N}$  that satisfy the right boundary conditions. Note that when we are using periodic boundary conditions things get a bit more involved. In this case we can only fix either  $S_{10}$  or  $S_{20}$ . Say we have fixed  $S_{10}$ . This time we must then find a *combination* of  $S_{20}$  and  $\hat{\lambda}$  that lead to  $S_{1N}$  and  $S_{2N}$  that are identical to  $S_{10}$  and  $S_{20}$  respectively.

We recall that  $V_{in}$  can be found explicitly, as function of  $\hat{\lambda}$  with the use of hypergeometric functions [47, 48], as we have seen before in section 3.3.1. Therefore it is possible to find good approximations of the eigenfunctions – and the corresponding eigenvalues – using this outlined method. Depending on the precise configuration of the  $N$  pulses and the parameters of the model, the form of the eigenfunctions changes. Because these eigenfunctions have localised structures at all of the pulse locations – unlike in the case  $m \gg 1 + H^2/4$  – it is in general hard to draw strong conclusions about the dynamics of the pattern beyond the linear destabilisation, i.e. what happens when an eigenvalue crosses the imaginary axis and the solution ‘falls’ off the manifold  $\mathcal{M}_N$ . In section 3.4 we will see that there essentially are two distinct possibilities: when pulses are irregularly arranged and when the pulses form a regular pattern.

### Eigenvalues when $m \ll 1 + H^2/4$

Even for the most simple  $N$ -pulse configurations it is hard to find the correct values for  $S_{1j}$  and  $S_{2j}$  by hand. It is, however, possible to say something about the *eigenvalues* in the asymptotic case  $m \ll 1 + H^2/4$ . When  $m \ll 1 + H^2/4$  we see that the exponents in (3.3.21) become independent of  $\hat{\lambda}$ . To be more precise we find  $\bar{U}_j$  is given up to exponentially small errors by

$$\bar{U}_j(x) = S_{1j} e^{\frac{1}{2}[-H + \sqrt{H^2 + 4}]} + S_{2j} e^{\frac{1}{2}[-H - \sqrt{H^2 + 4}]}.$$

Therefore the jump of the derivative  $\bar{U}_x$  at each pulse location, as dictated by the stability problem in the outer regions, becomes independent of  $\hat{\lambda}$  as well:

$$\begin{aligned} \Delta_{out}\bar{U}_x(P_j) &= \frac{1}{2} \left( H(S_{2j-1} - S_{1j}) - \sqrt{H^2 + 4}(S_{1j} + S_{2j-1}) \right) \\ &+ \frac{1}{2} H \left( S_{1j-1} e^{\frac{1}{2}[-H - \sqrt{H^2 + 4}]\Delta P_{j-1}} - S_{2j} e^{-\frac{1}{2}[-H + \sqrt{H^2 + 4}]\Delta P_j} \right) \\ &+ \frac{1}{2} \sqrt{H^2 + 4} \left( S_{1j-1} e^{\frac{1}{2}[-H - \sqrt{H^2 + 4}]\Delta P_{j-1}} + S_{2j} e^{-\frac{1}{2}[-H + \sqrt{H^2 + 4}]\Delta P_j} \right). \end{aligned}$$

As always we need this jump to be equal to the jump as indicated by the fast, inner regions. That is, we need to have

$$\Delta_{out}\bar{U}_x(P_j) = \Delta_{in}\bar{U}_x(P_j) = \frac{a^2}{m\sqrt{mD}} \frac{\rho_j}{u_{0j}^2} \hat{C}(\hat{\lambda}),$$

where – as before in (3.3.22) –  $\rho_j = \bar{U}(P_j)$ ; however this time  $\rho_j$  does not (implicitly) depend on  $\hat{\lambda}$ . Note that the only place where  $\hat{\lambda}$  comes into play is in the term  $\hat{C}(\hat{\lambda})$ . This enables us to rearrange the terms such that we find the eigenvalue condition

$$\frac{m\sqrt{mD}}{a^2} \frac{u_{0j}^2}{\rho_j} \Delta_{out} \bar{U}_x(P_j) = \hat{C}(\hat{\lambda}).$$

Now we note that the right-hand side of this expression does depend only on  $\hat{\lambda}$  and not on the pulse  $j$  and the left-hand side does only depend on the pulse  $j$  and not on  $\hat{\lambda}$ . Since we have a similar jump condition at all of the pulse locations, we know that the constants  $S_{1j}$  and  $S_{2j}$  of an eigenfunction must be chosen such that the left-hand side of this equation is the same for all  $N$  pulses. That is, we can define

$$\hat{C}^* = \frac{u_{0j}^2}{\rho_j} \Delta_{out} \bar{U}_x(P_j). \quad (3.3.27)$$

An eigenvalue must now satisfy the equation

$$-\frac{m\sqrt{mD}}{a^2} \frac{\hat{C}^*}{2} = \mathcal{R}(\hat{\lambda}) - 3. \quad (3.3.28)$$

The right-hand side of this equation is similar to the condition (3.3.12) that we studied for the stability of homoclinic pulses in the limit  $m \ll 1 + H^2/4$ . Therefore the right-hand side of (3.3.28) is represented by Figure 3.8a up to a multiplicative constant and eigenvalues necessarily need to lie on a skeleton, see Figure 3.9a. The reasoning of said section can be applied here immediately as well: if  $-\frac{m\sqrt{mD}}{a^2} \frac{\hat{C}^*}{2}$  is small enough the pulse configuration is stable and when it is too big the configuration becomes unstable. The destabilisation now occurs via a saddle-node bifurcation.

Finally we notice that the left-hand side of (3.3.28) is of order  $\mathcal{O}\left(\frac{m\sqrt{mD}}{a^2}\right)$ . Therefore if  $\frac{m\sqrt{mD}}{a^2} \ll 1$  we know that the configuration necessarily is stable and if  $\frac{m\sqrt{mD}}{a^2} \gg 1$  it is unstable. When  $\frac{m\sqrt{mD}}{a^2} = \mathcal{O}(1)$  the stability can change and a (saddle-node) bifurcation occurs. A precise computation of the value  $C^*$  is necessary to establish stability.

## 3.4 Numerical Simulations

In this section, we study the behaviour of pulse solutions using the methods developed in the previous sections. We employ our method – in the form of a Matlab code – to determine the dynamics of pulses via the ODE as explained in section 3.2.4 – note that this thus does *not* assume  $U(P_j) = 0$ . Simultaneously, we determine the evolution of the quasi-steady spectrum associated to the evolving multi-pulse configuration. Thus we check whether the pulse configuration approaches the boundary of the  $N$ -pulse manifold  $\mathcal{M}_N$  beyond which it is no longer attracting in the PDE flow – see section 3.3. When this happens, we deduce from the eigenfunction analysis which specific pulse – or pulses – of the multi-pulse configuration destabilises and in our method we then simply cut out these pulses. This essentially means that we have to assume that the associated quasi-steady bifurcation is subcritical, and thus that the pulse/pulses annihilate at a fast time scale. Note that this is based on numerical observation in all literature on pulse dynamics in Gray-Scott and Gierer-Meinhardt type models, see [174] for

a mathematical analysis of this bifurcation in the homoclinic 1-pulse context (that establishes the subcritical nature of the bifurcation in the Gierer-Meinhardt setting) and [174, 175] for a more thorough discussion and examples of systems that do not satisfy this condition.

In our code, the determination of the quasi-steady spectrum can be done in two different ways:

- (DSP) We treat the quasi-steady spectral problem as if it were a decoupled stability problem, see section 3.3.2;
- (CSP) We treat the quasi-steady spectral problem as if it were a coupled stability problem, see section 3.3.2.

There are pros and cons to both methods. The main benefit of (DSP) is that is easy to determine which pulse disappears when a bifurcation happens. On the other hand, this simplification is only valid in the asymptotic region in which  $m \gg 1 + H^2/4$  (and when pulses are distinguishable, see section 3.3.2). However, we will see in this section that it also provides useful information when  $m \leq \mathcal{O}(1 + H^2/4)$ . The other method, (CSP), does hold true for all  $m$  (and all configurations). However, the eigenfunctions are no longer restricted to a single pulse and can become quite involved. This makes it significantly harder to determine which – and especially how many – pulses annihilate as we will see later in this section. Moreover, the (CSP) approach becomes unreliable when the eigenfunctions get large spikes at one pulse location (i.e. for  $m \gg 1 + H^2/4$ ) and when eigenvalues are close, as the underlying root-finding Newton scheme cannot easily distinguish these closely packed eigenvalues.

In our numerical studies in this section we employ our aforementioned approach and test it against direct simulations of the full PDE. We will show that our method is in general good – even in situations for which our analysis should normally not hold – but we will also point out its limitations. The outcome of these endeavours will be captured in several conjectures throughout the text. Our numerical study starts with pulse solutions on flat terrains ( $h(x) \equiv 0$ ) in section 3.4.1. We focus here on the difference between irregular and regular configurations. Subsequently, in section 3.4.2, we investigate the effect of topography. Here we encounter downhill movement – which a priori is counter intuitive from the ecological point of view – and we study the infiltration of vegetation into bare soil among other things.

In all of our simulations – both the simulations using our method and the simulations of the full PDE – we found Hopf bifurcations when  $m$  was large and saddle-node bifurcations when  $m$  was small. In cases of a Hopf bifurcation, the PDE simulations show a (fast) vibration of the pulses height. In cases of saddle-node bifurcation this vibration was absent. Moreover, the computation of the  $u_{0j}$ -values, as explained in section 3.2.4 was slower. This indicates that the Jacobian determinant is very small, which happens near a (existence) bifurcation – precisely as expected with a saddle-node bifurcation.

### 3.4.1 Flat terrains

On flat terrains on a bounded domain  $[0, L]$  our asymptotic analysis in section 3.2.3 – valid for  $\frac{m\sqrt{mD}}{a^2} \ll 1$  – indicates that a regularly spaced configuration is a stable fixed point of the pulse-location ODE (3.2.17). Both the direct PDE simulation as simulations using our method suggest that these regular patterns are still fixed points and that, typically,  $N$ -pulse solutions evolve to these regular configurations – even

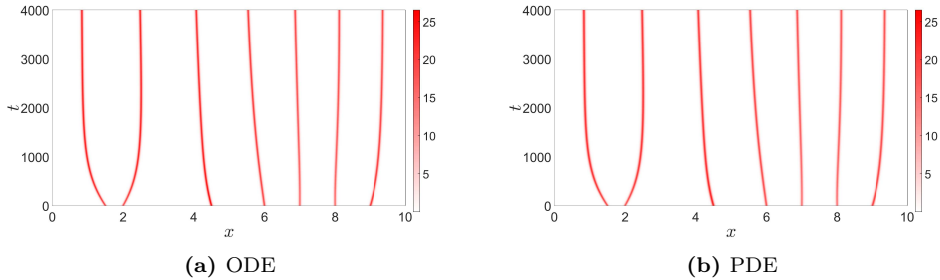


**Figure 3.11** – Plot of the vegetation  $V$  obtained from simulations using the pulse-location ODE (in a) and the full PDE (in b). In these plots the shade of red indicates the concentration of vegetation, with darker meaning more vegetation is located at that position. In both simulations we have used a constant height function  $h(x) \equiv 0$  and parameters  $m = 0.45$  and  $a = 0.5$ ,  $D = 0.01$  and  $L = 10$  (ecological relevant parameter values [95, 158]), and the starting configurations are the same. From these plots it is clear that the ODE and the PDE simulation agree to a great extent, and that the seven pulses evolve to a equally distributed seven pulse solution.

when  $\frac{m\sqrt{m}D}{a^2} = \mathcal{O}(1)$  – see however the results and simulations of [103]. In Figure 3.11 we give an example of this for the situation of a 7-pulse solution starting from an irregular configuration. So the dynamical movement drives pulse solutions to a regularly spaced configuration (on flat terrains). At the same moment, the flow of the PDE determines the boundaries of the manifold  $\mathcal{M}_N$ , where  $N$ -pulse solutions stop to exist and pulses may disappear. We want to understand the bifurcations that occur when a pulse configuration becomes unstable. For this we took the rainfall parameter  $a$  as our main bifurcation parameter. In our simulations we let the rainfall parameter decrease slowly<sup>6</sup> such that a bifurcation occurs<sup>7</sup>. Our study shows a significant difference between destabilisations of irregular patterns and regular patterns.

### Irregular patterns - irregularly arranged pulses

Two typical configurations with irregularly placed pulses are shown in Figures 3.12a and 3.13a. In these configurations we see that the  $V$ -pulses have varying heights. Consequently the values for  $u_{0j}$  differ, with the highest  $V$ -pulses having the lowest values  $u_{0j}$ . We have determined the eigenfunction near the bifurcation point for these situations, using the (CSP) method. In all our studies of similar irregular configurations, we have found that the eigenfunctions always look the same (see Figures 3.12b and 3.13b): there is a big  $\bar{V}$ -peak at the location of the pulse with the highest  $u_{0j}$ -value and the neighbouring pulses have a smaller  $\bar{V}$ -pulse in the opposite direction. If we – for a moment – assume that the pulses are not coupled (like was the case in section 3.3.2), it is clear that the pulse with the highest  $u_{0j}$ -value is the most unstable one. Indeed, this pulse has the highest value  $K_j = m^2 D \frac{u_{0j}^2}{a^2}$ , indicating that it is the most unstable one. The corresponding eigenfunction has a single  $\bar{V}$ -pulse located at this pulse's

<sup>6</sup>When  $a(t)$  changes with time, delayed bifurcation effects can occur, which fall outside the scope of this article. We refer the interested reader to [30, 141, 166] for analysis of these effects in related systems.

<sup>7</sup>For irregular patterns we need to make sure that the bifurcation occurs fast enough that the pulses have not moved to form a regular pattern yet.

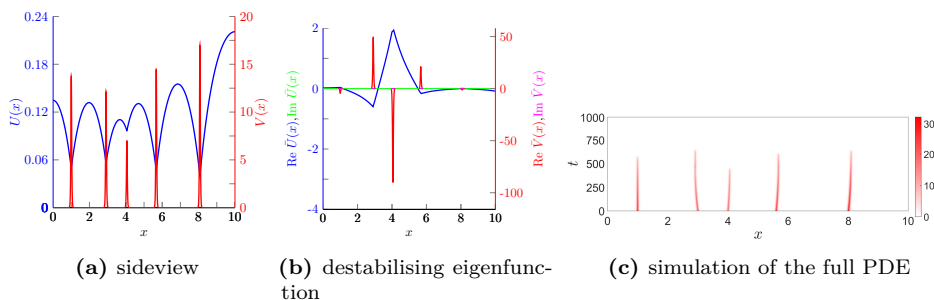


**Figure 3.12** – Sideview (a) of a 5-pulse configuration near a bifurcation and the destabilising eigenfunction (b) for this bifurcation (on a bounded domain with Neumann boundary conditions) and a simulation of the full PDE (c) with  $m = 0.45$ ,  $h(x) \equiv 0$ ,  $D = 0.01$ ,  $L = 10$  and  $a_{bif} = 0.296$ . The analytically determined quasi-steady eigenvalue is  $\hat{\lambda} \approx 0$ , suggesting a saddle-node bifurcation (in agreement with our theory for  $m < m_c(H)$ , see (3.3.19) and the surrounding text). Here we can clearly see that the most unstable pulse is the pulse with the lowest  $V$ -peak. This is also found in the eigenfunction plot where this pulse has the highest peak. In the simulation of the PDE we see that our prediction was correct: the third pulse is the first to become unstable. In the PDE simulation we let the rainfall parameter  $a$  decrease starting from  $a = 0.5$ .

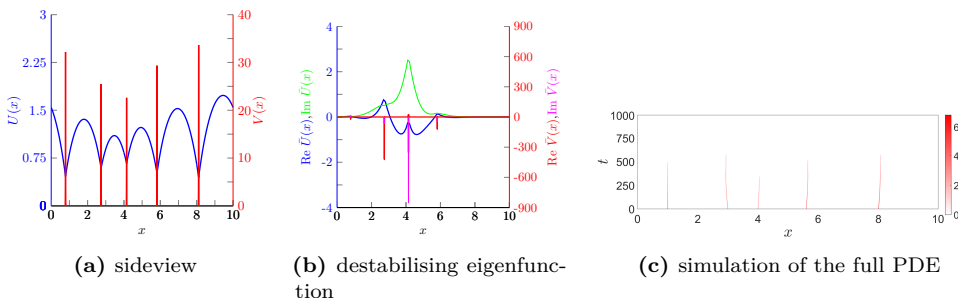


**Figure 3.13** – Sideview (a) of a 5-pulse configuration near a bifurcation and the destabilising eigenfunction (b) for this bifurcation (on a bounded domain with Neumann boundary conditions) and a simulation of the full PDE (c) with  $m = 10$ ,  $H = 0$ ,  $D = 0.01$ ,  $L = 10$  and  $a_{bif} = 2.96$ . The quasi-steady eigenvalue here is  $\hat{\lambda} \approx 0.018 \pm 0.472i$ , suggesting a Hopf bifurcation (in agreement with our theory for  $m > m_c(H)$ , see (3.3.19) and the surrounding text). Here we again see that the most unstable pulse is the pulse with the lowest  $V$ -peak, as is also shown in the eigenfunction plot where this pulse has the highest peak. The simulation of the full PDE shows that the third pulse is indeed the first one to become unstable, as was predicted by the linear stability analysis. In the PDE simulation we let the rainfall parameter  $a$  decrease starting from  $a = 5$ .

location. When the pulses in the stability problem are coupled, they are relatively close-packed. Consequently, we find (relatively small)  $\bar{V}$ -pulses for the neighbouring pulses as well. Nevertheless this suggests that such kind of eigenfunctions leads to the death of the pulse with the highest  $u_{0j}$ -value. Note that linear stability theory does not guarantee this (at all): a priori it cannot be excluded that the neighbouring pulses (also) disappear.



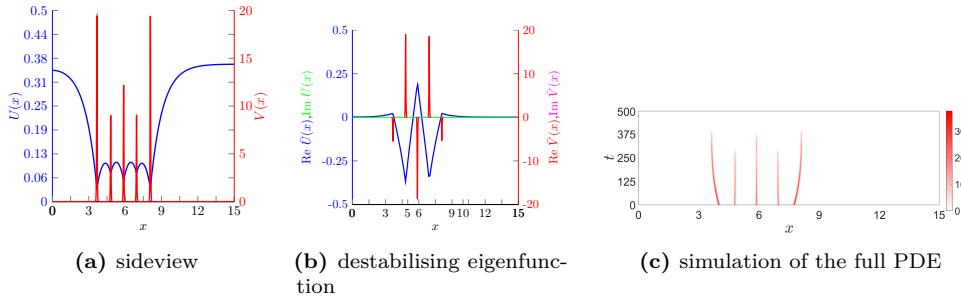


**Figure 3.14** – Sideview (a) of a specifically constructed 5-pulse configuration near a bifurcation and the corresponding destabilising eigenfunction (b) for this bifurcation (on a bounded domain with Neumann boundary conditions) and a simulation of the full PDE (c) with  $m = 0.45$ ,  $h(x) \equiv 0$ ,  $D = 0.01$ ,  $L = 15$  and  $a_{bif} = 0.36$ . The quasi-steady eigenvalue is  $\hat{\lambda} \approx 0$ , suggesting a saddle-node bifurcation. Here we can see that the most unstable pulse is still the pulse with the lowest  $V$ -peak (pulse 2), although this cannot be seen easily from the eigenfunction here. In the PDE simulation we let the rainfall parameter  $a$  decrease starting from  $a = 0.75$ . Note that another bifurcation, in which pulse 4 dies follows quickly after the disappearing of pulse 2 in the PDE simulation (which can be hard to see in the figures, but is clear from the raw data).

In numerous PDE simulations we have only ever seen the pulses disappear that have the highest  $u_{0j}$ -values (i.e. lowest  $V$ ). We have tried to find situations for which this reasoning does not hold, but were unable to find those. Interestingly enough this rule of thumb is good, even when the destabilising eigenfunction does not have an easily recognisable biggest peak. In Figure 3.14 we encounter such a case. Here one could think from the eigenfunction that pulse 3 should annihilate. However pulse 2 – the one with the lowest peak in  $V$  – is the one to disappear (and pulse 4 quickly follows).

This all give rise to the following conjecture on the stability of (irregular)  $N$ -pulse configurations.

**Conjecture/Observation 3.4.1** (Generalised Ni). *When a multi-pulse pattern is sufficiently irregular, the localised  $V$ -pulse with the lowest maximum (highest  $u_{0j}$ -value) is the most unstable pulse, and thus the one to disappear first.*

This conjecture can be seen as a generalisation of Ni’s conjecture [121]. The value of  $u_{0j}$  is determined through the distance between pulses. When pulses are far apart the value of  $u_{0j}$  decreases. Consequently the homoclinic pulse, the solitary  $V$ -pulse, is furthest away from any other pulses and has the lowest  $u_{0j}$ -value. It should therefore be the most stable configuration, as stated by Ni [52, 53, 121].

This conjecture also helps in the search for the most stable  $N$ -pulse configuration. Judging from our conjecture, the quasi-steady stability (in the PDE sense) of a  $N$ -pulse configuration is determined by the maximum of all  $u_{0j}$ -values, i.e. by  $\max_{j \in \{1, \dots, N\}} u_{0j}$ . Therefore the most stable  $N$ -pulse configuration is the configuration in which all pulses have the same value for  $u_{0j}$ . Put differently, as long as the manifold  $\mathcal{M}_N$  exist, it contains the regularly spaced configuration – which only becomes unstable under the PDE flow the moment that  $\mathcal{M}_N$  is no longer a hyperbolic invariant manifold.

## Regular patterns - regularly spaced pulses

Understanding the stability and bifurcations of these regular patterns (see Figure 3.15a) is more difficult. In these configurations all  $V$ -pulses have the same height and also the values for  $u_{0j}$  are equal. Therefore we can no longer speak of the most unstable pulse. We have determined the eigenfunctions and found two different cases depending on the value of  $m$ . A precise distinction between these two cases – similar to the critical value  $m_c(H)$  in the homoclinic pulse stability study in section 3.3.1 – could not be found; it seems this critical value of  $m$  might even depend on the number and precise location of all pulses. However, in the asymptotic cases  $m \ll 1 + H^2/4$  and  $m \gg 1 + H^2/4$ , the parameter  $m$  definitely is ‘small’ respectively ‘large’.

### $m$ small

When  $m$  is small, we only found critical eigenfunctions with alternating one pulse upwards and one pulse downwards<sup>8</sup>, like the example depicted in Figure 3.15b. This type of eigenfunctions suggests that adjacent pulses evolve differently when the configuration becomes unstable: one of the pulses grows and the other shrinks. PDE simulations back this idea in general. However it is not clear at all from the eigenfunction *which* pulses disappear: the odd ones or the even ones. PDE simulations indicate that both possibilities can happen; it seems to be very sensitive to the initial conditions.

Moreover, it can happen that a (naive) PDE simulation does not follow the critical destabilising eigenfunction but the next most unstable one, see Figure 3.15d. This has to do with the symmetry breaking that is necessary to follow the most unstable eigenfunction. Since the PDE (simulation) preserves symmetry, it only follows eigenfunctions that satisfy the same symmetry – though that eigenfunction still does resemble a period doubling as much as possible. This issue is easily solved when we apply a non-symmetric perturbation to the initial condition of the PDE.

We also observed that the eigenvalues, corresponding to these destabilizing eigenfunctions, always have  $\lambda \approx 0$  (i.e. no imaginary part). This would suggest a saddle-node bifurcation. It was proven in [148] that there are two periodic  $N$ -pulse solutions in the Gray-Scott system. One of these is stable and the other unstable, which underpins the possibility of a saddle-node bifurcation [148]. Moreover, studies of similar models indicates that such kind of saddle-node bifurcations generally are preceded by a period-doubling bifurcation or a sideband bifurcation [38, 134]. Our numerical observations are thus in agreement with these recent discoveries.

This gives rise to another conjecture

**Conjecture/Observation 3.4.2** (Regular Patterns I). *When vegetation  $V$ -pulses form a regular pattern and  $m$  is sufficiently small, destabilisation happens via a period doubling bifurcation and the critical eigenvalue crosses  $\lambda = 0$ .*

### $m$ large

When  $m$  is large, we have encountered two sorts of eigenfunctions in our numerical simulations. Both are Hopf bifurcations; one of them suggests a period doubling bifurcation and the second a full collapsing bifurcation (an example of the latter is shown in

<sup>8</sup>Or a configuration that is closest to this: for instance with an odd number of pulses and periodic boundary conditions there necessarily are two pulses pointing in the same direction next to each other.

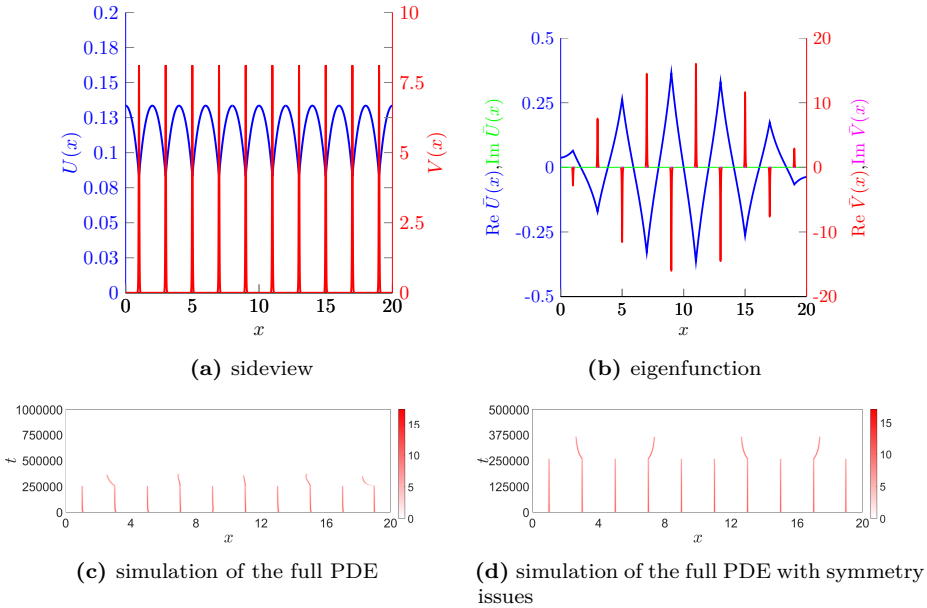


**Figure 3.15** – Sideview (a) of a 10-pulse configuration near a bifurcation and the destabilising eigenfunction (b) for this bifurcation (on a bounded domain with Neumann boundary conditions) for parameters  $m = 0.45$ ,  $H = 0$ ,  $L = 20$ ,  $D = 0.01$  and  $a_{bif} = 0.226$ . The eigenvalue here is  $\hat{\lambda} \approx 0$ , suggesting a saddle-node bifurcation. The PDE simulations (c-d) ran with  $a$  decreasing from  $a = 0.3$  to  $a = 0$ , but the initial condition was chosen to be perfectly symmetric in (d). The PDE simulation in (d) does not follow the destabilising eigenfunction from (b), because the solution maintains its symmetry. Therefore the regular 10-pulse configuration persists for longer time (lower  $a$ ) as well.

Figure 3.16b). As stated in section 3.3.2, this backs the idea of Hopf dances near the tip of the Busse Balloon [52, 53]. However in this situation our linear predictions have only limited value. When the eigenfunction point to a period doubling, it is possible that the PDE simulation shows a full collapse and vice versa. The faster we decrease our bifurcation parameter, the more likely it is that this happens – see Figure 3.16 for an example. Recalling the asymptotic analysis in section 3.3.2, this can be understood as follows: when  $m \gg 1 + H^2/4$  the eigenvalues for the period doubling and the full collapse have the same value to leading order. They only differ in higher order. Hence, one cannot expect a priori that the linear stability analysis provides a good grip on the non-linear stability and thus the numerically observed behaviour cannot be too surprising.

From this all we come to the following conjecture

**Conjecture/Observation 3.4.3** (Regular Patterns II). *When vegetation  $V$ -pulses form a regular pattern and  $m$  is sufficiently large, destabilisation happens either via a period doubling Hopf bifurcation or a full collapse Hopf bifurcation. In these cases the critical eigenvalue has a non-zero imaginary part.*

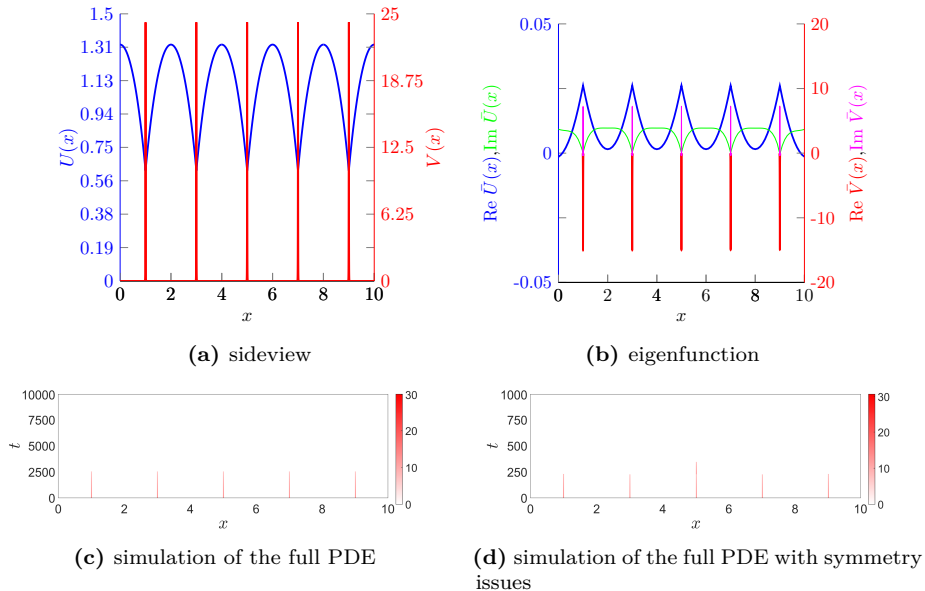


**Figure 3.16** – Sideview (a) of a 5-pulse configuration near a full collapse (Hopf) bifurcation and the destabilising eigenfunction (b) for parameter values  $m = 10$ ,  $h(x) \equiv 0$ ,  $L = 10$ ,  $D = 0.01$  and  $a_{bif} = 2.622$ . The eigenvalue here is  $\hat{\lambda} \approx \pm 0.48i$  indicating a Hopf bifurcation. The PDE simulations ran with  $a$  decreasing from  $a = 3$  to  $a = 0$ . The PDE simulation in (d) does not follow the destabilising eigenfunction from (b), possibly because the decrease in the bifurcation parameter was too fast, or because the eigenvalues are close together in this situation (see main text).

### 3.4.2 The effect of sloped terrains

When the terrain is no longer flat, new phenomena occur. To illustrate this, we first consider a constantly sloped terrain, i.e.  $h(x) = Hx$  on a domain with periodic boundary conditions (section 3.4.2) and on a bounded domain with Neumann boundary conditions (section 3.4.2). Subsequently, we present preliminary results on a terrain that has a slope that varies in  $x$  in section 3.4.2.

#### Periodic domains

Our study of  $N$ -pulse solutions on domains with periodic boundary conditions, indicates that these solutions always converge to a configuration in which all pulses are equidistant; i.e. to a regular pattern. This is in agreement with our proofs for the situation  $\frac{m\sqrt{mD}}{a^2} \ll 1$  in section 3.2.3 and forms a natural extension of our findings in the flat terrain setting of section 3.4.1. Moreover, the story about eigenfunctions and eigenvalues is also similar to the flat terrain setting: bifurcations of irregular configurations favour single-pulse extinction, whereas regular configurations bifurcate with either a period doubling or a full desertification (depending on the magnitude of  $m$  – see section 3.4.1). These regular patterns are again the most stable configuration possible for a  $N$ -pulse solution.

Not everything is the same though: pulses tend to move uphill and therefore solutions are never stationary. Since pulses also try to repel each other this not necessarily

means that all pulses always migrate uphill – this depends on the precise location of all pulses and the size of the slope  $H$ . However, for regular patterns – the attracting configuration of the pulse location ODE (3.2.17) – all pulses move uphill. Moreover, we can explicitly determine their migration speed.

### Uphill migration speed of regular patterns

We consider a regular pattern with  $N$  pulses on a domain with size  $L$ . For these regular patterns, all pulses are equally far apart from each other. We define this separation distance – i.e. the wavelength of the pattern – as  $d := \Delta P_j = L/N$ . Substitution of this separation distance in equation (3.2.22) – that is derived under assumption (A3) – gives the speed  $\hat{c}_0$  of these regularly spaced pulse configurations as

$$\hat{c}_0(d) = \frac{Da^2}{m\sqrt{m}} \frac{\sqrt{H^2 + 4}}{6} \frac{\cosh(Hd/2) - \cosh(\sqrt{H^2 + 4} d/2)}{\sinh(\sqrt{H^2 + 4} d/2)} \times \left( -H + \sqrt{H^2 + 4} \frac{\sinh(Hd/2)}{\sinh(\sqrt{H^2 + 4} d/2)} \right). \quad (3.4.1)$$

Under the weaker assumption (A3'), the value  $\bar{U}(P_j) = \frac{m\sqrt{m}D}{a^2}u_{0j}$  is not necessarily approximately 0, though the value is the same for all pulses. So we define this value as  $u_0 := u_{0j}$ . Therefore we may use equation (3.2.26) to find the speed  $\hat{c}$  in this situation as

$$\hat{c}(d) = \left( 1 - \frac{m\sqrt{m}D}{a^2}u_0(d) \right)^2 \hat{c}_0(d). \quad (3.4.2)$$

with  $\hat{c}_0(d)$  as in (3.4.1). Note that  $u_0$  is not determined in this form and that its value depends on  $d$  and  $H$ . To find this value we need to solve  $\vec{F}(\vec{u}_0) = 0$ , as explained in section 3.2.4. Although the algebraic equation that needs to be solved is only quadratic in this case, we use a numerical approximation to find the value of  $u_0$ . In general one sees that the larger the value of  $\frac{m\sqrt{m}D}{a^2}u_0$ , the slower a (regular) pattern moves – though it will always move uphill.

In Figure 3.17 we have plotted the movement speed  $\hat{c}_0(d)$  and  $\hat{c}(d)$  for several values of  $H$ . From this it is clear that the farther the pulses are apart, the faster they move. In the limit  $d \rightarrow \infty$  we expect them to move at the speed at which a (solitary) homoclinic pulse would move. It follows from equation (3.2.29) that these homoclinic pulses move at the speed  $\hat{c}_h$  given by

$$\hat{c}_h = \left( 1 - \frac{m\sqrt{m}D}{a^2}u_0 \right)^2 \frac{Da^2}{m\sqrt{m}} \frac{H\sqrt{H^2 + 4}}{6}, \quad (3.4.3)$$

which indeed is also the limit of equation (3.4.2) when we take  $d \rightarrow \infty$ . Note that  $u_0$  is known in this case, see equation (3.2.28). To find the homoclinic speed under assumption (A3) we can simply set  $\frac{m\sqrt{m}D}{a^2}u_0 = 0$ .

Note that for  $d \downarrow 0$  the pulses get closer together. When these pulses get too close together, the linear stability theory of section 3.3 indicates that the configuration is unstable under the PDE flow. Therefore there is a minimum wavelength  $d_{min}$  corresponding to a pattern that is marginally stable. Only if  $d \geq d_{min}$  we expect to see (stable) periodic patterns. Because the speed of a pattern is a monotonic function of its wavelength – as directly follows from equation (3.4.1), see also Appendix 3.B – we also know that stable periodic configurations can only have speed that is between  $\hat{c}(d_{min})$  and  $\hat{c}_h$ . This agrees with previous theoretical results on the speed of homoclinic pulse solutions [148, Equation (5.3)].

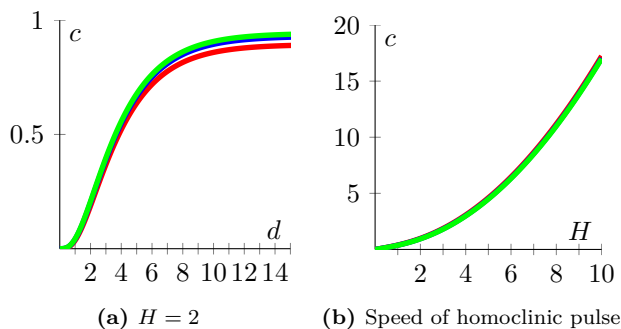


**Figure 3.17** – Rescaled speed  $c$  as a function of  $d$  in (a), where  $\hat{c}(d) = \frac{Da^2}{m\sqrt{m}}c(d)$ . In (b) we show the (rescaled) speed of a homoclinic pulse as a function of the slope  $H$ . In these plots the green line is a plot of the corresponding parameter-independent equation that are valid under assumption (A3) (i.e. equation (3.4.1) for a and equation (3.4.3) for b). The red and blue lines show the evaluations under assumption (A3), when the equations become parameter-dependent (via  $u_{0j}$ ), for  $D = 0.01$ ,  $m = 0.45$ ,  $a = 0.5$  (red line) and for  $D = 0.01$ ,  $m = 10$ ,  $a = 10$  (blue line).

### Bounded domains

Next, we consider  $N$ -pulse solutions with a constantly sloped terrain on a bounded domain with Neumann boundary conditions. Once again, the fixed point analysis of section 3.2.3 – that was valid under assumption (A3) – is verified by PDE simulations. Moreover, the results again carry over to the situation in which (A3') holds (i.e.  $U(P_j) \approx 0$  does not hold); both simulations of the pulse-location ODE (3.2.26) as direct PDE simulations always show that all  $N$ -pulse configurations that start on manifold  $\mathcal{M}_N$  evolve to a specific configuration that depends on the parameters of the model (but not on the initial conditions). This specific configuration is the (stable) fixed point of the pulse-location ODE (3.2.26). In Figure 3.18 we have plotted these fixed points as function of the slope  $H$  and different number of pulses. These fixed points are obtained as the outcome of simulations of the pulse-interaction ODE (3.2.26), with the method as explained in section 3.2.4. From these plots we see an increase in the terrain's slope leads to fixed points that get closer to the boundary of the domain. Moreover, it shows that a simplification of assumption (A3') to (A3) generally leads to the same fixed points, unless the system is close to a saddle-node bifurcation.

It should be noted that these (stable) fixed points of the ODE do not need to be stable fixed points of the full PDE. In fact, it can happen that an  $N$ -pulse configuration evolves under the ODE-flow to another  $N$ -pulse configuration that is unstable under the flow of the complete PDE – even in the case of fixed parameter values. That is, a  $N$ -pulse configuration crosses the boundary of manifold  $\mathcal{M}_N$ . In Figure 3.19 we show a simulation in which this happens. Here we see that the pulses move uphill – as indicated by the ODE flow – and then annihilate – by the PDE flow. This could also be predicted from Figure 3.18, since the ODE does not have a fixed point for these parameters. These simulations also back our generalised-Ni conjecture 1: once again the pulse with the lowest  $V$ -peak disappears at the bifurcation.

Moreover, we also see that the decoupled stability check (DSP) also captures the PDE behaviour very well. This is remarkable here, since the corresponding asymptotic analysis in section 3.3.2 is only valid for  $m \gg 1 + H^2/4$ , whereas here  $m = 0.45 < 1$ . At

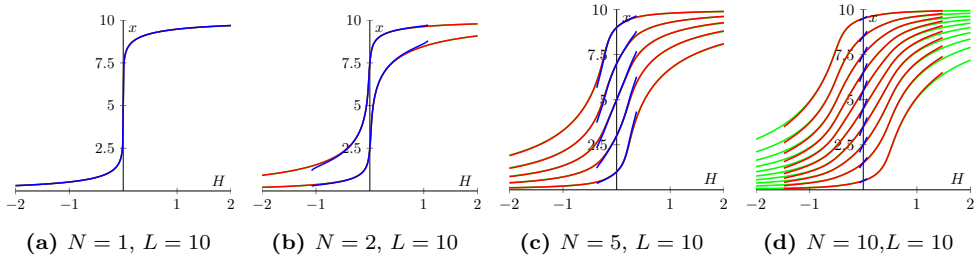


**Figure 3.18** – Stable fixed points of the pulse position ODE on a bounded domain of length  $L = 10$  with Neumann boundary conditions for various number of pulses  $N$ . The green lines (generally laying below the other lines) indicate the fixed point of equation (3.2.22), which is valid under assumption (A3). The blue and red lines indicate the fixed points of equation (3.2.26), which is valid under assumption (A3'), for parameters  $D = 0.01$ ,  $m = 0.45$  and  $a = 0.5$  (blue) or  $a = 5$  (red). These lines are only plotted when the numerical solver could solve  $\vec{F}(\vec{u}_0) = 0$ ; when it could not, a stationary pulse solution does not exist and a saddle-node bifurcation has happened, see section 3.2.4.

first glance the two simulations seem identical. However a better look reveals that the (DSP) ODE simulation gets rid of pulse slightly too early – though it does give a good prediction on the pulse that is going to disappear. This effect gets exaggerated when more pulses are added to the simulation. In Figure 3.20 we have done a simulation with  $N = 10$  pulses. Here the mismatch between ODE and PDE simulation can be seen more easily.

### Varying Terrain

In the previous sections we have studied the extended Klausmeier model on terrains with a constant slope, i.e.  $h(x) = Hx$ . In these situations it was possible to find an exact form of the solution in the outer regions. When we inspect a terrain with non-constant slope, it is in general not possible to find an exact solution in the outer region because these terms make the outer problem a non-autonomous problem, see (3.2.18). It is therefore more complicated to study a varying terrain problem. In this section we briefly consider some cases, in which we use assumption (A3), i.e.  $\tilde{U}(P_j) = 0$ . We use a numerical boundary value problem solver, to find numerical approximations of the solution  $\tilde{U}$  for the ODE (3.2.18) in the outer regions, between the pulses. In these situations we – again – see that the reduction gives a very good description of the movement of the pulses (see Figure 3.21). In the simulation of Figure 3.21, we have used a Gaussian function for the terrain, i.e.  $h(x) = e^{-0.75(x-\frac{L}{2})^2}$ , which resembles a hill with a top at  $x = L/2$ .

In section 3.4.2 we saw that pulses on a constantly sloped terrain want to move uphill. Therefore one might be inclined to conclude that all pulses want to move uphill. Additional simulations with a single pulse reveal that it is also possible for a pulse to move downhill. In Figure 3.22 we show two simulations of the full PDE on a Gaussian terrain of the form  $h(x) = \exp[-B(x - \frac{L}{2})^2]$ . Here we see that the pulse moves uphill when  $B$  is small and downhill when  $B$  is bigger. This not necessarily contradicts the ecological intuition: we know that the movement of a pulse is determined through the water availability, see equation (3.2.17). When the curvature of the terrain gets too

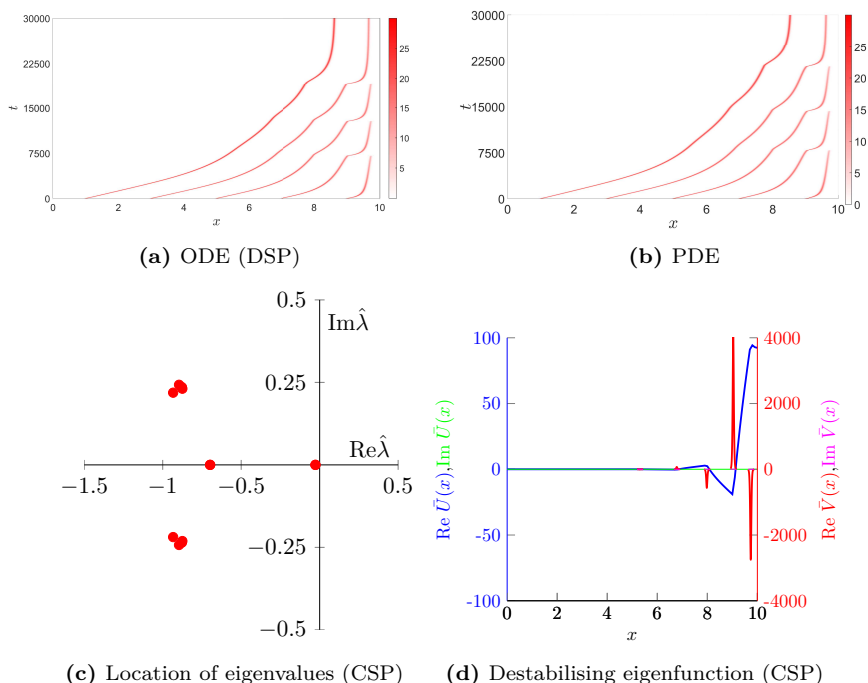


**Figure 3.19** – Simulations of the extended Klausmeier model in which the fixed point of the ODE is unstable under the PDE flow, leading to annihilation of the most uphill pulse. The ODE simulation in (a) uses the decoupled stability approximation (DSP). In these simulations, the pulses start as a regular pattern and we have used the parameters  $a = 0.5$ ,  $H = 1$ ,  $D = 0.01$ ,  $m = 0.45$ ,  $L = 10$ . Moreover we show the location of the eigenvalues close to the moment the first pulse dies out in (c) and the destabilising eigenfunction (corresponding to  $\hat{\lambda} \approx 0$ ) at the same moment is given in (d) – both are determined using the coupled stability approach (CSP). The first destabilization in these simulations occurs at  $t \approx 7.1 \cdot 10^3$  (a,ODE) and  $t \approx 7.9 \cdot 10^3$  (b,PDE). Note that (a) and (b) are also shown in Figure 3.3.

big, it might happen that water streams downhill so fast that water builds up at the base of the hill. This would make this point, at the basis of the hill, the preferred spot for a pulse, because of the abundance of water and therefore the pulse moves downhill towards this point. The extended Klausmeier model with a more general varying terrain term is studied more in-depth in [7].

### Infiltration of vegetation in bare soil

Finally, as an illustration of the applicability of our pulse-location ODE, we turn our attention to the phenomenon of colonisation. Observations of vegetation in semi-arid regions in the Sahel showed an inverse relation between the wavelength of vegetation patterns and the slope of the terrain [58]: when the slope increased, the wavelength decreased. Recently, using numerical methods, it was shown that colonization of bare ground leads to the same inverse relationship, suggesting that those regions in the Sahel may once have been deserts [153]. With our ODE description (3.2.22) it is possible to derive an analytic (approximate) expression for this inverse wavelength-slope relation.



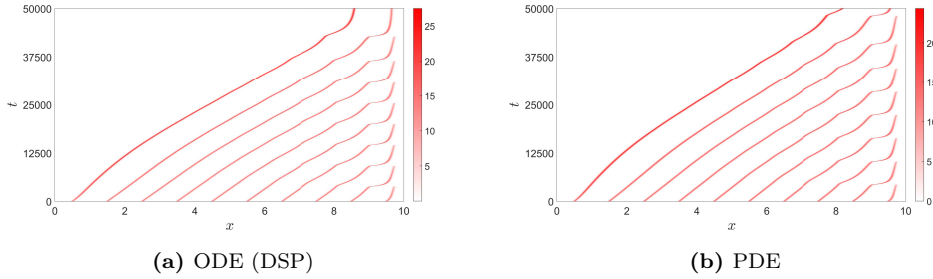


**Figure 3.20** – Simulations of the extended Klausmeier model with 10 pulses in which the fixed point of the pulse-location ODE is unstable under the PDE flow. The ODE simulation in (a) uses the decoupled stability approximation (DSP). In these simulations pulses start as a regular patterns. The mismatch between the ODE simulation in (a) and the direct PDE simulation in (b) can be seen from comparing these plots. Specifically, the first destabilization occurs at  $t \approx 3.9 \cdot 10^3$  (a, ODE) and  $t \approx 4.3 \cdot 10^3$  (b, PDE). The parameters used are  $a = 0.5$ ,  $H = 1$ ,  $D = 0.01$ ,  $m = 0.45$ ,  $L = 10$ .

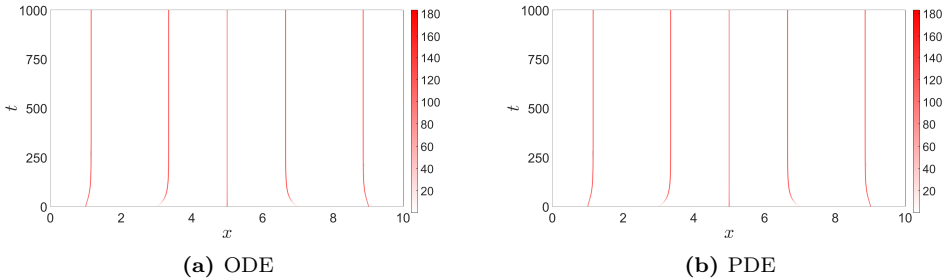


**Figure 3.21** – The evolution of 5 pulses in simulations of the extended Klausmeier model with non-constantly sloped terrain  $h(x) = \exp\left[-0.75\left(x - \frac{L}{2}\right)^2\right]$ , for the reduced pulse-location ODE (a) and the full PDE (b). In both simulations we have taken  $a = 20$ ,  $m = 20$ ,  $D = 0.01$  and  $L = 10$  and the starting configurations are the same, i.e. 5 pulses distributed equally over the domain. From these plots we again see that the ODE reduction agrees with the full PDE dynamics to a great extend.

The critical wavelength  $d_c$  (i.e. the distance between the pulses), for a given terrain with constant slope  $H$ , is the wavelength for which the uphill moving effect due to the slope of the terrain is negated by the repulsive behaviour of the pulses uphill. If  $d > d_c$  the lowest pulse moves uphill and colonization is argued to be unfeasible; if  $d < d_c$  the lowest pulse moves downhill and colonization is possible. In our analysis we use assumption (A3), i.e.  $\tilde{U}(P_j) = 0$ . Therefore we can find the speed of the lowest pulse by only considering the distance to its neighbour pulse. Because the whole problem is symmetric in  $H = 0$ , we can assume for simplicity that  $H \geq 0$ . We let the lowest pulse be located at position  $P_1$  and we let the distance to the neighbouring pulse uphill be denoted by  $d$ . We assume that there are no pulses further downhill (i.e. we put

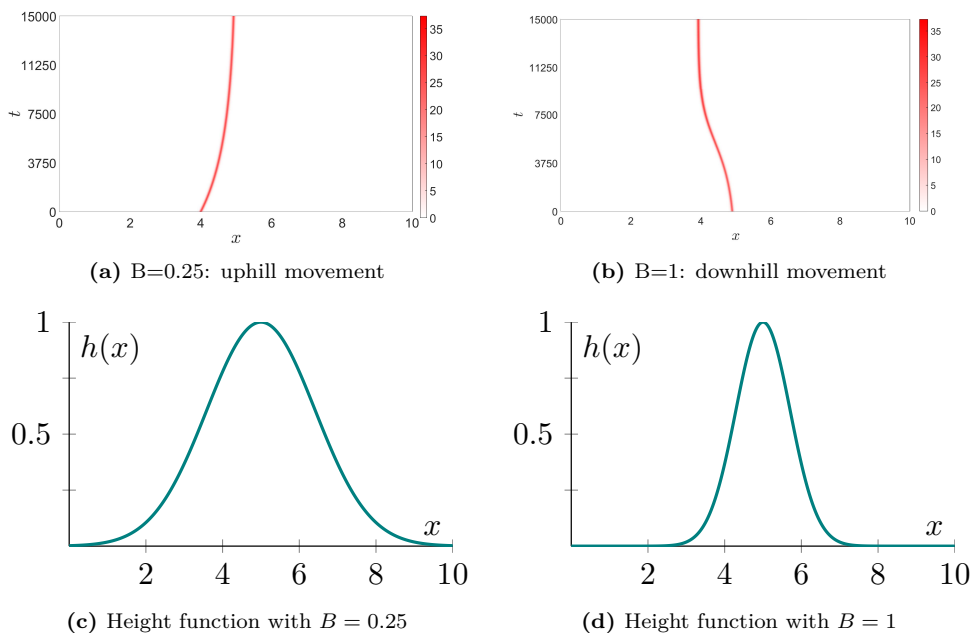


**Figure 3.22** – PDE Simulations of the full extended Klausmeier PDE model with a terrain with non-constants slope,  $h(x) = \exp[-B(x - \frac{L}{2})^2]$  for  $B = 0.25$  (a) and  $B = 1$  (b). Here we see that pulses can move downhill when the width of the hill becomes small. In both simulations we have taken  $a = 0.5$ ,  $m = 0.45$ ,  $D = 0.01$ ,  $L = 10$  and used Neumann boundary conditions. The form of the terrains  $h(x)$  is plotted in Figures (c) and (d). The pulse-location ODE simulations show similar results (not shown).

$P_0 = -\infty$ ). From equation (3.2.22) we then derive the speed of the first pulse as

$$\frac{dP_1}{dt} = \frac{Da^2}{m\sqrt{m}} \frac{1}{6} \left[ \left( \frac{H}{2} - \frac{\sqrt{H^2 + 4}}{2} \frac{e^{Hd/2} - \cosh(\sqrt{H^2 + 4} d/2)}{\sinh(\sqrt{H^2 + 4} d/2)} \right)^2 - \left( \frac{H}{2} - \frac{\sqrt{H^2 + 4}}{2} \right)^2 \right]. \quad (3.4.4)$$

To find the critical values for the wavelength  $d_c$ , we need to find the value  $d$  for which  $\frac{dP_1}{dt} = 0$ . That is, we need to find the roots of the terms between the brackets in equation (3.4.4). In Figure 3.23 the resulting plot is shown. This indeed gives the inverse relationship between the slope  $H$  and  $d_c$  as reported in [153]. It should be noted that these results match up very good when the slope  $H$  is large, but start to differ when the slope  $H$  is small<sup>9</sup>; Unsurprisingly, precisely for these small slopes assumption (A3) is no longer valid.

<sup>9</sup>According to [153, Figure 5.c] the critical rainfall value  $a_c$  increases when the slope  $H$  increases. Therefore small slopes lead to small critical rainfall parameters, which in turn lead to a violation of assumption (A3).

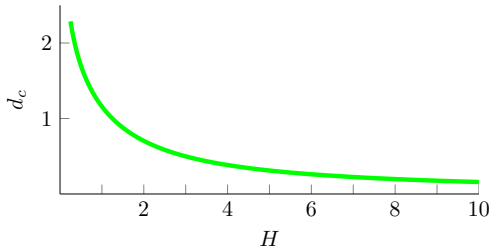


**Figure 3.23** – Inverse relationship between the slope  $H$  and the critical wavelength  $d_c$  for which colonization of bare ground becomes possible. This plot consists of the roots of equation (3.4.4). This graphic agrees with plot 5D in [153]. Because we use a different scaling both the wavelength and the slope should be divided by  $\sqrt{D}$  in [153] to obtain the same qualitative plot. One can see that the plots indeed are in good agreement for steeper slopes, i.e. for higher  $H$ . For less steep slopes, the plots differ. Here the system is closer to the saddle-node bifurcation, which means that assumption (A3) is no longer valid.

### 3.5 Discussion and Outlook

In this paper, we extended existing approaches and developed novel methods to study the dynamics of interacting pulse solutions in singularly perturbed 2-component reaction-diffusion systems with parameters that may vary in time and/or space, focusing on the extended Klausmeier – or generalized Klausmeier-Gray-Scott – model (3.1.1) as prototypical subject of study. We have (formally) shown that the PDE evolution of  $N$ -pulse patterns can be described by an  $N$ -dimensional dynamical system and that the solutions of this system live on an (approximate)  $N$ -dimensional invariant manifold  $\mathcal{M}_N$ . The stability – and thus attractivity – of this manifold is determined by the quasi-steady spectrum that we have determined by Evans function techniques. This analysis also provides insight in the location and nature of the (various components of the) boundary  $\partial\mathcal{M}_N$  of  $\mathcal{M}_N$ , and in the nature of the (linear) destabilization mechanisms associated to  $N$ -pulse configurations crossing through  $\partial\mathcal{M}_N$ . Thus, we have found that the dynamics of  $N$ -pulse patterns can be split in two. Firstly, there is the (slow) dynamics *on* the manifold  $\mathcal{M}_N$  – we captured this behaviour in an ODE (3.2.17) that describes the evolution of the pulse locations. Secondly, there is (fast) dynamics *off* of  $\mathcal{M}_N$ , towards a lower-dimensional (approximate, attracting invariant) manifold  $\mathcal{M}_M$  (with  $M < N$ ). We have determined the linearized nature of this fall; the hybrid numerical-asymptotic method developed in this paper predicts the value of  $M$ , describes the evolution of the resulting  $M$  pulses on  $\mathcal{M}_M$ , and the cascade of jumps towards subsequent manifolds  $\mathcal{M}_{\tilde{M}}$ .

Our formal approach triggers various themes of further research. The validity of the very first step – the reduction of the PDE dynamics to  $\mathcal{M}_N$  – is so far only established rigorously for a restricted region in parameter space – see [12]. Moreover, the analysis of [12] is in the classical setting of non-varying parameters. Some of the numerical experiments presented in this article were conducted under similar conditions for which the results of [12] can be expected to hold; others, however, used parameters way beyond the regions considered in [12]. Nevertheless even in those cases the (formally) reduced system usually captures the dynamical movement of the pulses remarkably well. More surprisingly, the ODE reduction even is correct when the prime small

parameter of our asymptotic analysis, i.e.  $\frac{a}{m}$ , is in fact not small, but order  $\mathcal{O}(1)$ . All in all, the reduction method seems to be valid for settings way beyond the reaches of current validity proofs. It would be extremely valuable to further develop the rigorous theory to understand why the reduction method is so successful.

The behaviour of  $N$ -pulse patterns on manifold  $\mathcal{M}_N$  was studied using the reduced pulse-location ODE (3.2.17). Under the assumption that the coefficients related to  $h(x)$  in (3.1.1) do not explicitly vary in  $x - h'(x) \equiv H$ , a constantly sloped terrain – we found on bounded domains with Neumann boundary conditions that  $N$ -pulse configurations always evolve towards a specific stable fixed point of the ODE; on domains with periodic boundary conditions, the configurations always evolve towards a uniformly traveling solution in which all pulses are equally far apart. Some of these results were proven *for the derived ODE approximation* under assumption (A3) in Appendix 3.B and numerics indicate that these still hold under the less restrictive assumption (A3'). Moreover, when  $h'(x)$  is allowed to vary – i.e. for more realistic topographies – simulations indicate that the pulse-location ODE still has stable fixed points (though there can be multiple fixed points, including unstable ones). A better understanding of the dynamics generated by reduced systems (3.2.17) is necessary, especially from the ecological point of view. For instance, intuitively, pulses are expected to always move uphill (towards the downhill flowing water). However this mechanism only seems to be valid for terrains with constant slope ( $h'(x) \equiv H$ ); on more realistic terrains pulses can move both uphill and downhill – depending on the terrain's curvature. This may explain observations of vegetation patterns, that indeed sometimes evolve counter-intuitively (i.e. not uphill) [41, 57]. As a first step towards these goals – rigorous validation of  $\mathcal{M}_N$  and understanding the dynamics on  $\mathcal{M}_N$  – one first needs to rigorously establish existence and stability of stationary pulse solutions of (3.1.1) with non-trivial  $h(x)$  – this is the subject of [7].

The biggest ‘leap of faith’ our method takes is the assumption that insights obtained from the asymptotic analysis of the quasi-steady spectrum can be extrapolated to capture the nonlinear, fast, PDE dynamics of an  $N$ -pulse configuration crossing through  $\partial\mathcal{M}_N$  and jumping from  $\mathcal{M}_N$  to  $\mathcal{M}_M$  (with  $M < N$ ). Our analysis showed that  $\partial\mathcal{M}_N$  corresponds to ‘quasi-steady bifurcations’ – i.e. bifurcations induced by the intrinsic dynamics of the evolving multi-pulse pattern – of several types: saddle node bifurcations for small values of  $m$  (in (3.1.1)) and Hopf bifurcations and decoupled eigenfunctions for large values of  $m$ . In fact, our linear analysis only yielded information on the appearance of quasi-steady Hopf destabilisations; since all observations of Hopf bifurcations in singularly perturbed reaction-diffusion systems of slowly linear type are subcritical – see [174] and the references therein – we have assumed that all quasi-steady Hopf bifurcations are subcritical. Numerical simulations indicated the correctness of these assumptions in a wide variety of situations; the linear destabilisation arguments predict the fast nonlinear jump mechanisms surprisingly well. Moreover, we found that approximating the stability problem as a decoupled stability problem works convincingly well, even when the leading order asymptotic analysis implied that eigenfunctions are coupled: this a priori oversimplified approximation typically correctly predicts which pulses disappear – i.e. towards which manifold  $\mathcal{M}_M$  an  $N$ -pulse configuration jumps as it crosses through  $\partial\mathcal{M}_N$ ; it does underestimate the stability slightly, leading to pulses that disappear/jump too early. To obtain a fundamental understanding of the ‘desertification dynamics’ of  $N$ -pulse patterns in singularly perturbed reaction-diffusion systems – i.e. the dynamics of pulse patterns jumping from manifolds  $\mathcal{M}_k$  to  $\mathcal{M}_\ell$  (with  $0 \leq \ell < k \leq N$ ) – it is crucial to develop an-

alytical insights in the relative locations of the invariant manifolds  $\mathcal{M}_n$ ,  $n = 1, 2, \dots, N$  within function space, and the nature of the PDE flow between these manifolds. In general, this is a formidable challenge, but such a multi-scale analysis is expected to be possible in specially constructed settings.

Finally, we found that there is a striking difference between the dynamics of regular and irregular patterns. We found that irregular configurations always destabilise gradually – with pulses disappearing one by one – whereas for regular configuration either half or all pulses disappear ‘catastrophically’ when  $\partial\mathcal{M}_N$  is crossed<sup>10</sup>. On the other hand, we also deduced that regularly spaced  $N$ -pulse configurations are more stable than any other  $N$ -pulse configuration – in fact, irregular patterns typically evolve toward regularity on domains with periodic boundary (under specified conditions on  $h(x)$  and the nature of the domain and associated boundary conditions). Thus, in situations in which parameters change (slowly) in time – as  $a(t)$  in (3.1.1) – there is a competition between two ‘desertification scenarios’: the gradual one for ‘sufficiently irregular’ patterns in which the pattern step by step jumps down from  $\mathcal{M}_k$  to  $\mathcal{M}_{k-1}$ , and the catastrophic one in which a ‘sufficiently regular’  $N$ -pulse pattern loses half or all pulses. The relative time scales of the variation of  $a(t)$  versus the intrinsic rate of change of the  $N$ -pulse pattern as it evolves over  $\mathcal{M}_N$  is a decisive ingredient that shapes this competition. A more subtle, but at least as important, ingredient is the – at present not understood – (slow) dynamics of the quasi-steady eigenfunctions as they evolve from the irregular setting of being localized around one pulse location to the global Floquet-type eigenfunctions – see [39] and the references therein – associated with regular spatially periodic patterns.

## Acknowledgments

We thank Tom Bellsky for inspiring discussions. This study was supported by a grant within the Mathematics of Planet Earth program of the Netherlands Organization of Scientific Research (NWO).

---

<sup>10</sup>for small  $m$  there always is a period doubling; for large  $m$  both a period doubling and a full collapse can happen.

## Appendices

### 3.A The movement of water on a varying terrain

Previous versions of the extended Klausmeier model only considered terrains with a constant slope. The model studied in this article, however, is suitable for more generic terrains by the addition of the term  $h_{xx}u$ . In this appendix, we explain how this new term originates from a shallow water approximation. Here, we denote the concentration/height of water by  $U(t, x, y)$ , the height of the terrain by  $H(x, y)$  and the speed of water by  $\vec{v}(t, x, y, z)$ . By the principles of mass conservation, a physical model should obey the continuity equation,

$$\frac{dU}{dt}(t, \vec{x}) = -\vec{\nabla} \cdot \vec{j}(t, \vec{x}) + q(t, \vec{x}), \quad (3.A.1)$$

where  $\vec{j}(t, \vec{x})$  denotes the flux (of water) and  $q$  includes all the sources and sinks of the model. In this situation, the flux constitutes of diffusion  $\vec{j}_{\text{diff}} = -D\vec{\nabla}U$  and advection  $\vec{j}_{\text{adv}} = \vec{v}U$ . Since we want to understand the effect of a terrain, we focus only on the effect of advection. To describe the flow due to advection, we need to determine the velocity  $\vec{v}$  of the water. The starting point for this are the momentum equations,

$$\rho \frac{D\vec{v}}{Dt} = -\vec{\nabla}p + \vec{f}_{\text{gravity}} + \vec{f}_{\text{friction}}. \quad (3.A.2)$$

Here,  $\rho$  is the density of water,  $p$  is the pressure,  $\vec{f}$  denotes the forces that act on the water and  $\frac{D}{Dt}$  is the material derivative. In this formulation friction is included as a force. Because the height of water (i.e.  $U$ ) is small in semi-arid climates, a shallow water approximation can be made. Thus we assume that there is no movement in the  $z$ -direction, and that  $\vec{v}$  and  $\rho$  are constant as function of  $z$ . In addition, we assume that the pressure  $p$  only depends on the  $z$ -coordinate, and that  $\rho$  does not depend on  $x$  or  $y$ . Therefore the  $x$ - and  $y$ -momentum equations simplify to

$$\rho \frac{D\vec{v}}{Dt} = \vec{f}_{\text{gravity}} + \vec{f}_{\text{friction}}. \quad (3.A.3)$$

For the force due to friction we assume Rayleigh friction, i.e.  $\vec{f}_{\text{friction}} = -K\vec{v}$ , where  $K$  is a (Rayleigh) constant. The force due to gravity comes into play because of the sloped terrain. Ultimately, the computation of the contribution of  $\vec{f}_{\text{gravity}}$  boils down to the ‘mass on incline’ problem (see Figure 3.24). In the continuum limit, this leads to  $\vec{f}_{\text{gravity}} = -\rho g \tan(\theta) = -\rho g \vec{\nabla}Z$ , where  $Z$  is the relevant height. There are several choices possible for this height. In this article we have chosen  $Z = H$ , the height of the terrain. Another often used choice is  $Z = H + U$ , the height of the terrain plus the height of the water; see [67].

As a final step, we neglect fluid accelerations as a further approximation (i.e.  $\frac{D\vec{v}}{Dt} = 0$ ). Combining everything yields the velocity

$$\vec{v} = -\frac{\rho g}{K} \vec{\nabla}Z = -C\vec{\nabla}Z, \quad (3.A.4)$$

where  $C = \frac{\rho g}{K}$  is a constant. Therefore the advective flux is  $\vec{j}_{\text{adv}} = -CU\vec{\nabla}Z$ . Substitution in the continuity equation gives

$$\frac{dU}{dt} = C\vec{\nabla} \cdot (U\vec{\nabla}Z) \quad (3.A.5)$$

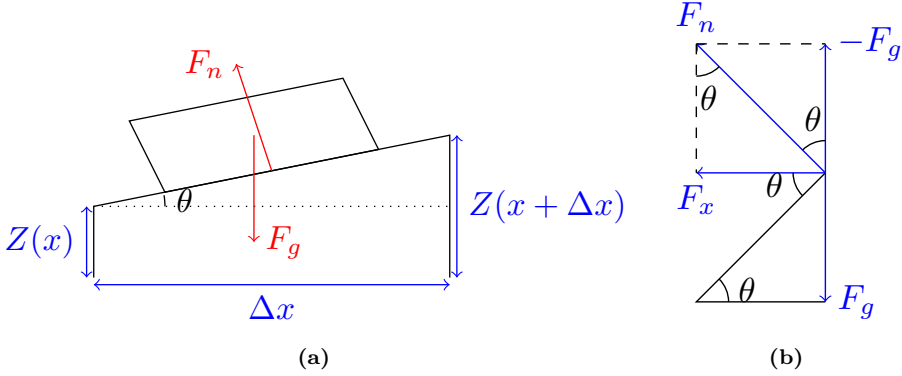


**Figure 3.24** – Sketch of the classic ‘mass on incline’ problem (a). A mass  $M$  is positioned on a slope. Gravity has its effect on this mass and – due to the normal force – the box starts to move downwards. For water, the mass  $M$  can be replaced by the density  $\rho$ . A sketch of the relevant forces and angles of the problem are given in (b).

where we have suppressed the diffusive and reaction terms for clarity of presentation. The choice,  $Z = H$ , which we have made throughout this article, leads to

$$\frac{dU}{dt} = C\vec{\nabla} \cdot (U\vec{\nabla}H) = C\vec{\nabla}U \cdot \vec{\nabla}H + CU\Delta H. \quad (3.A.6)$$

The alternative choice,  $Z = H + U$ , leads to the expression that is used in e.g. [67],

$$\frac{dU}{dt} = C\vec{\nabla} \cdot (U\vec{\nabla}(H + U)) = \frac{C}{2}\Delta U^2 + CU\Delta H + C\vec{\nabla}U \cdot \vec{\nabla}Z \quad (3.A.7)$$

### 3.B Fixed Points of the pulse-location ODE - Proofs

In this appendix we give proofs of the claims in section 3.2.3 about the fixed points of the pulse-location ODE (3.2.22). Crucial in all these proofs is the fact that  $\tilde{U}_x(P_k^\pm)$  is strictly increasing/decreasing as function of the distance to the neighbouring pulse. For notational simplicity we define the functions  $R_\pm$  as

$$R_+(k) := \left( \frac{H}{2} - \frac{\sqrt{H^2 + 4} e^{Hk/2} - \cosh(\sqrt{H^2 + 4}k/2)}{2 \sinh(\sqrt{H^2 + 4}k/2)} \right),$$

$$R_-(k) := \left( \frac{H}{2} + \frac{\sqrt{H^2 + 4} e^{-Hk/2} - \cosh(\sqrt{H^2 + 4}k/2)}{2 \sinh(\sqrt{H^2 + 4}k/2)} \right).$$

The pulse-location ODE (3.2.22) can then be written as

$$\frac{dP_j}{dt} = \frac{Da^2}{m\sqrt{m}} \frac{1}{6} [R_+(\Delta P_j)^2 - R_-(\Delta P_{j-1})^2]$$

### 3.B.1 Properties of $R_{\pm}$

Before we give the proofs for the existence of fixed points, we first need to study the functions  $R_{\pm}$ . First of all, straightforward limit computations reveal that

$$\lim_{k \downarrow 0} R_{\pm}(k) = 0, \quad \lim_{k \rightarrow \infty} R_{\pm}(k) = \frac{H \pm \sqrt{H^2 + 4}}{2}.$$

The derivative of  $R_{\pm}$  is given by

$$R'_{\pm}(k) = \mp \frac{\sqrt{H^2 + 4}}{2} \frac{S_{\pm}(k)}{\sinh(\sqrt{H^2 + 4}k/2)^2},$$

where

$$\begin{aligned} S_{\pm}(k) &= \left[ \pm \frac{H}{2} e^{\pm Hk/2} - \frac{\sqrt{H^2 + 4}}{2} \sinh(\sqrt{H^2 + 4}) \right] \sinh(\sqrt{H^2 + 4}k/2) \\ &\quad - \frac{\sqrt{H^2 + 4}}{2} \cosh(\sqrt{H^2 + 4}k/2) \left[ e^{\pm Hk/2} - \cosh(\sqrt{H^2 + 4}k/2) \right] \\ &= \frac{\sqrt{H^2 + 4}}{2} + e^{\pm Hk/2} \left[ \pm \frac{H}{2} \sinh(\sqrt{H^2 + 4}k/2) - \frac{\sqrt{H^2 + 4}}{2} \cosh(\sqrt{H^2 + 4}k/2) \right] \\ &= \frac{\sqrt{H^2 + 4}}{2} + \frac{\pm H - \sqrt{H^2 + 4}}{4} e^{(\pm H + \sqrt{H^2 + 4})k/2} + \frac{\mp H - \sqrt{H^2 + 4}}{4} e^{(\pm H - \sqrt{H^2 + 4})k/2}. \end{aligned}$$

That means that  $R'_{\pm}(k)$  has a zero at  $k$  only when  $S_{\pm}(k) = 0$ . With straightforward limit computations we can check that  $S_{\pm}(0) = 0$  and that  $\lim_{k \rightarrow \infty} |S_{\pm}(k)| = \infty$ . Now, the derivative of  $S_{\pm}$  is easy to compute:

$$\begin{aligned} S'_{\pm}(k) &= \frac{(\pm H - \sqrt{H^2 + 4})(\pm H + \sqrt{H^2 + 4})}{8} e^{(\pm H + \sqrt{H^2 + 4})k/2} \\ &\quad + \frac{(\mp H - \sqrt{H^2 + 4})(\pm H - \sqrt{H^2 + 4})}{8} e^{(\pm H - \sqrt{H^2 + 4})k/2} \\ &= -\frac{1}{2} e^{(\pm H + \sqrt{H^2 + 4})k/2} + \frac{1}{2} e^{(\pm H - \sqrt{H^2 + 4})k/2} \\ &= -e^{\pm Hk/2} \sinh(\sqrt{H^2 + 4}k/2). \end{aligned}$$

Hence  $S'_{\pm}(k) = 0$  if and only if  $k = 0$ . Thus  $S_+$  and  $S_-$  are strictly decreasing in  $k$ . Since  $S_{\pm}(0) = 0$  this means that  $S_{\pm}$  has the same sign for all  $k > 0$ . Therefore  $R'_+(k) > 0$  and  $R'_-(k) < 0$  for all  $k > 0$ .

Finally we also need to know which function increases faster in absolute value. For that we can suffice to determine the sign of  $R'_+ + R'_-$ , since  $R_+$  is increasing from 0 and  $R_-$  is decreasing from 0. That means we need to look at the sign of  $-(S_+ - S_-)$ . A direct computation reveals

$$\begin{aligned} -[S_+(k) - S_-(k)] &= -H \cosh\left(\frac{Hk}{2}\right) \sinh\left(\frac{\sqrt{H^2 + 4}k}{2}\right) \\ &\quad + \sqrt{H^2 + 4} \sinh\left(\frac{Hk}{2}\right) \cosh\left(\frac{\sqrt{H^2 + 4}k}{2}\right). \end{aligned} \quad (3.B.1)$$

Taking the derivative of this expression gives

$$S'_-(k) - S'_+(k) = 2 \sinh(Hk/2) \sinh(\sqrt{H^2 + 4}k/2)$$



Unless  $H = 0$  this expression is never zero for any  $k > 0$ . Combined with the fact that  $R'_+(0) + R'_-(0) = 0$  this reveals that  $R'_+ + R'_-$  does not change sign. We might now compute the limit for  $k \rightarrow \infty$  to determine which grows faster. Taking the limit of (3.B.1) as  $k \rightarrow \infty$  indicates  $\text{sgn}(R'_+ + R'_-) = \text{sgn}(H)$ . Thus if  $H > 0$  we see that  $R_+$  increases faster and if  $H < 0$   $R_-$  increases faster in size; when  $H = 0$  both increase at the same rate.

Summarizing everything from this section, we do know the following:

- $R_+(k)$  is strictly increasing from 0 to  $\frac{H+\sqrt{H^2+4}}{2}$  and  $R_-(k)$  is strictly decreasing from 0 to  $\frac{H-\sqrt{H^2+4}}{2}$ .
- If  $H > 0$   $|R_+(k)|$  increases faster than  $|R_-(k)|$ ; if  $H < 0$  it is  $|R_-(k)|$  that increases faster; if  $H = 0$  they increase at the same rate.

### 3.B.2 Unbounded domains

**Theorem 3.B.1.** *On unbounded domains the pulse-location ODE (3.2.22) does not have any fixed points, unless  $N = 1$  and  $H = 0$ .*

*Proof.* Without loss of generality we assume  $H \geq 0$ .

To have a fixed point, we need to have  $\frac{dP_j}{dt} = 0$  for all  $j \in \{1, \dots, N\}$ . In particular we need  $\frac{dP_N}{dt} = 0$ . That is,  $R_+(\Delta P_N)^2 = R_-(\Delta P_{N-1})^2$ . Since  $\Delta P_N \rightarrow \infty$  on unbounded domains we know that  $R_+(\Delta P_N)^2 = \left(\frac{H+\sqrt{H^2+4}}{2}\right)^2$ . However, we know that  $R_-(k)^2 \in \left[0, \left(\frac{H-\sqrt{H^2+4}}{2}\right)^2\right]$  and that this function is strictly increasing. To have equality we therefore need  $H = 0$  and  $\Delta P_{N-1} \rightarrow \infty$ . That is only possible if we only have one pulse, i.e.  $N = 1$ .  $\square$

**Theorem 3.B.2.** *On unbounded domains the pulse-location ODE (3.2.22) does not have a uniformly traveling solution in which all pulses move with the same speed, unless  $N = 1$ . The distance between the first and last pulse is always increasing.*

*Proof.* The situation in which  $N = 1$  is trivially true. So we restrict ourselves to the cases  $N > 1$ .

Now, if a solution with all pulses moving with the same speed would exist, then the distance between the first and last pulse needs to be constant, i.e. the following expression needs to hold true

$$0 = \frac{d}{dt}(P_N - P_1) = R_+(\Delta P_N)^2 + R_-(\Delta P_0)^2 - R_+(\Delta P_1)^2 - R_-(\Delta P_{N-1})^2$$

On unbounded domains we have  $\Delta P_N \rightarrow \infty$  and  $\Delta P_0 \rightarrow \infty$ . Thus both  $R_+(\Delta P_N)^2$  and  $R_-(\Delta P_0)^2$  take on their maximum values. Since  $R_\pm(k)^2$  are strictly increasing, the equality above can only hold true if  $\Delta P_1 \rightarrow \infty$  and  $\Delta P_{N-1} \rightarrow \infty$ . That is not possible when  $N > 1$ . In particular we see that  $\frac{d}{dt}(P_N - P_1) > 0$ .  $\square$

### 3.B.3 Bounded domains with periodic boundaries

**Theorem 3.B.3.** *On bounded domains with periodic boundaries, the pulse-location ODE (3.2.22) does not have any fixed points, unless  $H = 0$ .*

*Proof.* In the situation where  $H = 0$  one can easily verify that a continuous family of pulse solutions exist by setting  $\Delta P_j = L/N$  for all  $j$ .

For all  $H \neq 0$  we see that if such a fixed point exists, then the sum of the movement of all pulses needs to be zero, i.e. it is required that the following equality holds true

$$0 = \sum_{j=1}^N \frac{dP_j}{dt} = \sum_{j=1}^N [R_+(\Delta P_j)^2 - R_-(\Delta P_j)^2].$$

However, because the terms  $R_+(k)^2$  and  $R_-(k)^2$  increase with a different rate, the terms  $R_+(\Delta P_j)^2 - R_-(\Delta P_j)^2$  are non-zero and carry the same sign for all  $j$ . Hence the equality does not hold and therefore the ODE does not have a fixed point.  $\square$

**Theorem 3.B.4.** *On bounded domains with periodic boundaries the pulse-location ODE (3.2.22) has a continuous family of uniformly traveling solutions in which all pulses move with the same speed. The distance between pulses for those solutions is always given by  $\Delta P_j = L/N$  for all  $j$ .*

*Proof.* In the situation where  $H = 0$ , we know that  $\sum_{j=1}^N \frac{dP_j}{dt} = 0$ . Therefore each pulse needs to be stationary. That is,  $R_+(\Delta P_j)^2 = R_-(\Delta P_{j-1})^2$ . Because  $R_+(k)^2$  and  $R_-(k)^2$  increase at the same rate (when  $H = 0$ ) this means that  $\Delta P_j = \Delta P_{j-1}$  for all  $j$ . As we need that  $\sum_{j=1}^N \Delta P_j = N$  this indicates that  $\Delta P_j = L/N$ .

Without loss of generality we now assume  $H > 0$ . To find a solution that has the desired property we need  $\frac{dP_j}{dt} = \frac{dP_k}{dt}$  for all  $j, k$ . In particular we thus need to have

$$R_+(\Delta P_j)^2 - R_-(\Delta P_{j-1})^2 = R_+(\Delta P_{j+1})^2 - R_-(\Delta P_j)^2 \text{ for all } j.$$

Since  $R_+(k)^2$  and  $R_-(k)^2$  are strictly increasing, we can deduce the following: if  $\Delta P_j > \Delta P_{j-1}$  then we also need  $\Delta P_{j+1} > \Delta P_j$ . Repeating this argument reveals  $\Delta P_1 > \Delta P_N > \dots > \Delta P_1$ . This obviously cannot hold true and therefore a solution cannot have  $\Delta P_j > \Delta P_{j-1}$  for any pulse  $j$ . Similarly we can exclude the possibility that  $\Delta P_j < \Delta P_{j-1}$  for any  $j$ .

Therefore the only possibility left indicates that  $\Delta P_j = \Delta P_k$  for all  $j, k$ . Since  $\sum_{j=1}^N \Delta P_j = N$  that means that  $\Delta P_j = L/N$ . It is straightforward to check that this indeed gives a solution with the desired property.  $\square$

**Theorem 3.B.5.** *On bounded domains with periodic boundary conditions, the continuous family of regularly spaced solutions, with  $\Delta P_j = L/N$ , is stable under the flow of the ODE.*

*Proof.* By Theorem 3.B.4 the regularly spaced solutions are fixed points of the related ODE

$$\frac{d}{dt} \Delta P_j = \frac{dP_{j+1}}{dt} - \frac{dP_j}{dt}. \quad (3.B.2)$$

We denote the fixed points of this equation by  $\Delta P_j^*$  and we linearise around them by setting  $\Delta P_j = \Delta P_j^* + r_j$ , where  $\sum_{j=1}^N r_j = 0$  because of the bounded domain. We then obtain

$$\begin{aligned} \frac{dr_j}{dt} = \frac{Da^2}{m\sqrt{m}} \frac{1}{3} & \left[ R_+(\Delta P_{j+1}^*) R'_+(\Delta P_{j+1}^*) r_{j+1} + R_-(\Delta P_{j-1}^*) R'_-(\Delta P_{j-1}^*) r_{j-1} \right. \\ & \left. - \left( R_+(\Delta P_j^*) R'_+(\Delta P_j^*) + R_-(\Delta P_j^*) R'_-(\Delta P_j^*) \right) r_j \right]. \end{aligned}$$

Because  $\Delta P_j^* = L/N$  for all  $j \in \{1, \dots, N\}$ , we may define

$$\alpha := R_+(\Delta P_j^*)R'_+(\Delta P_j^*) \quad \beta := R_-(\Delta P_j^*)R'_-(\Delta P_j^*) \quad C := \frac{Da^2}{m\sqrt{m}} \frac{1}{3}.$$

Because  $R_+$  is positive and increasing, and  $R_-$  is negative and decreasing, we know that  $\alpha > 0$  and  $\beta > 0$ .

We then define  $\vec{r} := (r_1, \dots, r_N)^T$  and rewrite the linearised equation as

$$\frac{d}{dt}\vec{r} = CM\vec{r},$$

where

$$M := \begin{pmatrix} -(\alpha + \beta) & \alpha & 0 & \cdots & 0 & \beta \\ \beta & -(\alpha + \beta) & \alpha & 0 & \cdots & 0 \\ 0 & \ddots & \ddots & \ddots & \ddots & \vdots \\ \vdots & \ddots & \ddots & \ddots & \ddots & 0 \\ 0 & & \ddots & \ddots & \ddots & \alpha \\ \alpha & 0 & \cdots & 0 & \beta & -(\alpha + \beta) \end{pmatrix}$$

The matrix  $M$ , with the additional constraint  $\sum_{j=1}^N r_j = 0$  is negative definite, as a straight-forward computation yields (here  $r_0 = r_N$  and  $r_{N+1} = r_1$ )

$$\begin{aligned} f(\vec{r}) &:= \vec{r}^T M \vec{r} = -(\alpha + \beta) \sum_{j=1}^N r_j^2 + \alpha \sum_{j=1}^N r_j r_{j+1} + \beta \sum_{j=1}^N r_j r_{j-1} \\ &= -\frac{\alpha + \beta}{2} \sum_{j=1}^N (r_j - r_{j+1})^2 \end{aligned}$$

Thus  $f(\vec{r}) < 0$  unless  $r_j = r_{j+1}$  for all  $j$  – which is excluded by the condition  $\sum_{j=1}^N r_j = 0$ . Thus the matrix associated with the linearisation is negative definite and therefore possesses only negative eigenvalues, proving that the regularly spaced configuration are stable under the flow of the ODE.  $\square$

**Theorem 3.B.6.** *On bounded domains with periodic boundary conditions, the continuous family of regularly spaced solutions, with  $\Delta P_j = L/N$ , is globally exponentially stable under the flow of the ODE.*

*Proof.* Inspired by [132, Corollary 6] we show that the pulse-distance ODE (3.B.2) has a Lyapunov function given by  $L(\Delta P_1, \dots, \Delta P_N) = \max_{j \in \{1, \dots, N\}} \Delta P_j$ . To that end, we prove that  $\frac{dL}{dt} \leq 0$ . For that, let  $k \in \{1, \dots, N\}$  be such that  $L(\Delta P_1, \dots, \Delta P_N) = \Delta P_k$ . Now,

$$\frac{d\Delta P_k}{dt} = \frac{Da^2}{m\sqrt{m}} \frac{1}{6} \left\{ [R_+(\Delta P_{k+1})^2 + R_-(\Delta P_{k-1})^2] - [R_+(\Delta P_k)^2 + R_-(\Delta P_k)^2] \right\}.$$

Since, per definition,  $\Delta P_k = \max_{j \in \{1, \dots, N\}} \Delta P_j \geq \Delta P_{k-1}, \Delta P_{k+1}$ , by monotonicity of  $R_{\pm}$  it follows that  $R_+(\Delta P_{k+1})^2 + R_-(\Delta P_{k-1})^2 \leq R_+(\Delta P_k)^2 + R_-(\Delta P_k)^2$ . Hence  $\frac{d\Delta P_k}{dt} \leq 0$ , thus proving  $\frac{dL}{dt} \leq 0$ . So  $L$  is a (weak) Lyapunov function. By LaSalle's invariance principle and theorem 3.B.5 this shows that regularly spaced configurations are globally exponentially stable.  $\square$

### 3.B.4 Bounded domains with Neumann boundary conditions

**Theorem 3.B.7.** *On bounded domains with Neumann boundary conditions the pulse-location ODE (3.2.22) does always have precisely one fixed point.*

*Proof.* Without loss of generality we assume  $H \geq 0$ . For all  $H \geq 0$  we have  $R_+(k)^2 \geq R_-(k)^2$  for all  $k > 0$ . Thus for all  $x \geq 0$  there is a  $y = y(x) \geq 0$  such that  $R_+(y(x))^2 = R_-(x)^2$ . Since  $R_{\pm}(k)^2$  is strictly increasing, we know that  $y$  is strictly increasing in  $x$  as well.

Now, to have a fixed point  $P_1^*, \dots, P_N^*$  we need

$$R_-(\Delta P_{j-1})^2 = R_+(\Delta P_j)^2 \text{ for all } j. \quad (3.B.3)$$

Because of our reasoning above there are strictly increasing functions  $y_j$  such that

$$R_-(\Delta P_{j-1})^2 = R_+(y_j(\Delta P_{j-1}))^2 \text{ for all } j. \quad (3.B.4)$$

So we should choose  $P_1, \dots, P_N$  such that  $\Delta P_j = y_j(\Delta P_{j-1})$ . That is,

$$\Delta P_j = (y_j \circ \dots \circ y_1)(\Delta P_0). \quad (3.B.5)$$

In particular we have  $\Delta P_N = (y_N \circ \dots \circ y_1)(\Delta P_0)$ . Because  $\Delta P_0$  is strictly increasing in  $P_1$ , we know that this expression for  $\Delta P_N$  is strictly increasing in  $P_1$ .

At the same time our solution should fit in the domain and therefore we know that  $\Delta P_N$  is strictly decreasing in

$$P_N = P_1 + y_1(\Delta P_0) + \dots + (y_N \circ \dots \circ y_1)(\Delta P_0).$$

Therefore this expression for  $\Delta P_N$  is also strictly decreasing in  $P_1$ .

So we now have two descriptions of  $\Delta P_N$  which should be equal. One of these is strictly increasing in  $P_1$  starting from 0 and the other is strictly decreasing in  $P_1$  starting from  $L$ . Therefore there is precisely one location  $P_1 = P_1^*$  that leads to equality of these descriptions. The other locations follow from equation (3.B.5). This leads to a unique fixed point of (3.2.22).  $\square$

**Theorem 3.B.8.** *On bounded domains with Neumann boundary conditions, the unique fixed point solution of (3.2.22) is stable under the flow of the ODE.*

*Proof.* We denote the fixed point as  $P_1^*, \dots, P_N^*$ . Then we linearise by setting  $P_j = P_j^* + r_j$ , which results in

$$\begin{aligned} \frac{d}{dt} r_1 &= \frac{Da^2}{m\sqrt{m}} \frac{1}{3} [\alpha_1 r_2 - (\alpha_j + \beta_j) r_1 - \beta_j \gamma_1 r_1]; \\ \frac{d}{dt} r_j &= \frac{Da^2}{m\sqrt{m}} \frac{1}{3} [\alpha_j r_{j+1} - (\alpha_j + \beta_j) r_j + \beta_j r_{j-1}]; \quad (j = 2, \dots, N_1) \\ \frac{d}{dt} r_N &= \frac{Da^2}{m\sqrt{m}} \frac{1}{3} [-\alpha_N \gamma_N r_N - (\alpha_N + \beta_N) r_N + \beta_N r_{N-1}], \end{aligned}$$

where

$$\begin{aligned}\alpha_j &:= R_+(P_{j+1}^* - P_j^*)R'_+(P_{j+1}^* - P_j^*) \\ \beta_j &:= R_-(P_j^* - P_{j-1}^*)R'_-(P_j^* - P_{j-1}^*) \\ C &:= \frac{Da^2}{m\sqrt{m}} \frac{1}{3} \\ \gamma_1 &:= -\frac{d}{dP_1}P_0(P_1^*) \\ \gamma_N &:= -\frac{d}{dP_N}P_{N+1}(P_N^*)\end{aligned}$$

Note that the function  $R_+$  is positive and increasing,  $R_-$  is negative and decreasing,  $P_0$  is decreasing and  $P_{N+1}$  is decreasing. Therefore  $\alpha_j > 0$ ,  $\beta_j > 0$ ,  $\gamma_1 > 0$  and  $\gamma_N > 0$ . We then define  $\vec{r} := (r_1, \dots, r_N)^T$  and rewrite the linearised equation as

$$\frac{d}{dt}\vec{r} = CM\vec{r},$$

where

$$M = \begin{pmatrix} -(\alpha_1 + \beta_1) - \gamma_1\beta_1 & \alpha_1 & \cdots & \cdots & \cdots & 0 \\ \beta_2 & -(\alpha_2 + \beta_2) & \ddots & & & \vdots \\ 0 & \ddots & \ddots & & & \vdots \\ \vdots & \ddots & \ddots & & & \vdots \\ \vdots & \cdots & \beta_{N-1} & -(\alpha_{N-1} + \beta_{N-1}) & \cdots & 0 \\ 0 & \cdots & \cdots & \beta_N & -(\alpha_N + \beta_N) - \gamma_N\alpha_N & \alpha_{N-1} \end{pmatrix}$$

Because of the structure of  $M$ , the Gerschgorin circle theorem [66] immediately indicates that all eigenvalues lie in a Gerschgorin disc. Because  $M$  is weak diagonal dominant, the only non-negative eigenvalue that is not yet excluded is  $\lambda = 0$ . The rest of this proof consists of proving that  $\lambda = 0$  cannot be an eigenvalue.

If  $\lambda = 0$  would be an eigenvalue, there is an eigenvector  $\vec{x} = (x_1, \dots, x_N)^T \neq 0$  such that  $M\vec{x} = 0$ . This vector needs to satisfy

$$-(\alpha_1 + \beta_1 + \gamma_1\beta_1)x_1 + \alpha_1x_2 = 0 \quad (3.B.6)$$

$$\beta_jx_{j-1} - (\alpha_j + \beta_j)x_j + \alpha_jx_{j+1} = 0 \quad (j = 2, \dots, N_1) \quad (3.B.7)$$

$$\beta_Nx_{N-1} - (\alpha_N + \beta_N + \gamma_N\alpha_N)x_N = 0 \quad (3.B.8)$$

From the first  $N - 1$  of these expressions one can formulate each  $x_j$  in terms of  $x_1$ . We find  $x_j = \delta_jx_1$ , with

$$\delta_{j+1} = \delta_j + \frac{\beta_j}{\alpha_j}(\delta_j - \delta_{j-1}), \quad \delta_1 = 1, \quad \delta_2 = 1 + \frac{\beta_1}{\alpha_1}(1 + \gamma_1) > \delta_1.$$

One might easily verify that  $\delta_j > \delta_{j-1}$  for all  $j$ .

Finally, if  $\vec{x}$  is an eigenvector it should also satisfy the  $N$ -th expression (3.B.8). Substitution of the found expressions results in the condition

$$[\beta_N(\delta_{N-1} - \delta_N) - (1 + \gamma_N)\alpha_N\delta_N] = 0.$$

Because  $\delta_N > \delta_{N-1}$  the left-hand side of this equation is always negative. Therefore this condition can never be fulfilled and hence  $\lambda = 0$  cannot be an eigenvalue of  $M$ . Thus all eigenvalues of  $M$  need to be negative and the fixed point is thus stable under the flow of the ODE.  $\square$

# 4

## Pulse solutions for an extended Klausmeier model with spatially varying coefficients

Motivated by its application in ecology, we consider an extended Klausmeier model, a singularly perturbed reaction-advection-diffusion equation with spatially varying coefficients. We rigorously establish existence of stationary pulse solutions by blending techniques from geometric singular perturbation theory with bounds derived from the theory of exponential dichotomies. Moreover, the spectral stability of these solutions is determined, using similar methods. It is found that, due to the break-down of translation invariance, the presence of spatially varying terms can stabilize or destabilize a pulse solution. In particular, this leads to the discovery of a pitchfork bifurcation and existence of stationary multi-pulse solutions.

### 4.1 Introduction

Since Alan Turing's revolutionary insight that patterns can emerge spontaneously in systems with multiple species if these diffuse at different rates [165], systems of reaction-diffusion equations have served as prototypical pattern forming models. Scientists have been using these reaction-diffusion models successfully to describe for instance animal markings [98], embryo development [115] and the faceted eye of *Drosophila* [113]. Special interest has been given to localized solutions (e.g. pulses, fronts), that arise when the diffusivity of species involved is very different. The prototypical (two-component) model (in one spatial dimension) is a singularly perturbed equation of the (scaled) form

$$\begin{cases} \partial_t U &= \partial_x^2 U + \mathcal{H}_1(x, u, u_x, v, v_x; \tilde{\varepsilon}), \\ \partial_t V &= \tilde{\varepsilon}^2 \partial_x^2 V + \mathcal{H}_2(x, u, u_x, v, v_x; \tilde{\varepsilon}), \end{cases} \quad (4.1.1)$$

where  $0 < \tilde{\varepsilon} \ll 1$  is a measure for the ratio of diffusion constants, and  $\mathcal{H}_1, \mathcal{H}_2$  are sufficiently smooth functions. Because of the singular perturbed nature of (4.1.1), it is possible to establish existence and determine (linear) stability of localized patterns in these models. In the past, this has been done successfully for the Gray-Scott model [28, 46, 47, 49, 99, 160], the Gierer-Meinhardt model [48, 49, 160, 175], and in several other settings [39, 56, 120, 141, 178]. However, these studies are usually limited to models with constant coefficients. Some research has focused on the introduction of localized spatial inhomogeneities [55, 122, 123, 171, 183, 184]; also (often formal) research has been done on reaction-diffusion equations with (less restricted) spatially varying coefficients [3, 13, 15, 16, 179, 180]. In this article, we aim to expand

the knowledge of such systems, by studying a reaction-diffusion system with fairly generic spatially varying coefficients rigorously; motivated by its use in ecology (see Remark 4.1.2), we consider the following extended Klausmeier model with spatially varying coefficients [8, 95]:

$$\begin{cases} \partial_t U &= \partial_x^2 U + f(x)\partial_x U + g(x)U + a - U - UV^2, \\ \partial_t V &= D^2\partial_x^2 V - mV + UV^2, \end{cases} \quad (4.1.2)$$

with  $x \in \mathbb{R}, t \geq 0, U = U(x, t), V = V(x, t) \in \mathbb{R}$ , parameters  $D, a, m > 0$  and functions  $f, g \in C_b^1(\mathbb{R})$ . Certain conditions are imposed on the parameters and functions  $f$  and  $g$  – these will be explained in section 4.1.1.

**Remark 4.1.1.** *The model (4.1.2) can be brought into the form of (4.1.1) by a series of scalings – see section 4.2 and [49].*

**Remark 4.1.2** (Application of the extended Klausmeier model). *This system of equations is used as a model in ecology to describe the dynamics of vegetation ( $U$ ) and water ( $V$ ). The extended Klausmeier model (4.1.2) takes into account the amount of rainfall ( $a > 0$ ) and mortality rate of the vegetation ( $m > 0$ ) and goes beyond its classical version by modeling a smooth, spatially varying terrain  $h = h(x)$  which then enters (4.1.2) as  $f(x) = h'(x), g(x) = h''(x)$  (see [8]). Variants of the Klausmeier model have been studied in various articles ranging from ecological studies [9, 95] to mathematical analysis [8, 151, 153, 158]. The focus of all these studies are vegetation patterns, which have been found to play a crucial role in the process of desertification. A starting point for the analysis of more complicated patterns is a thorough understanding of their building blocks, namely, localized solutions. The present paper is motivated by observations – both in numerical simulations and in real ecosystems [8, 9] – of the impact of nontrivial topographies on the dynamics of localized vegetation patterns.*

The focus of this article is to analyze existence, stability and (some) bifurcations of stationary pulse solutions to (4.1.2). The presence of spatially varying coefficients, however, alters the approach that usually is taken in the case of constant coefficients models. For one, with spatially constant coefficients, (4.1.2) possesses a uniform stationary state, with  $V \equiv 0$ , to which pulse solutions converge for  $x \rightarrow \pm\infty$ . In the case of spatially varying coefficients, however, typically such uniform stationary state does not exist; instead, a bounded solution  $(u, v) = (u_b, 0)$  exists and pulse solutions converge to this bounded solution for  $x \rightarrow \pm\infty$  – see Figure 4.1. Moreover, standard proofs using geometric singular perturbation theory typically rely on the availability of closed form expressions for orbits of subsystems of (4.1.2) – see below. These are no longer available in case of generic spatially varying coefficients, and only bounds can be found. Indeed, the core contribution of the present work is to overcome these difficulties, which we do by blending geometric singular perturbation theory [62] with the theory of exponential dichotomies [31] in a new way.

In this article, we initially follow the ‘standard’ approach of geometric singular perturbation theory. That is, we introduce a small parameter  $\varepsilon := \frac{a}{m}$  – see assumption (A1) in section 4.1.1– and construct a stationary pulse solution to (4.1.2) in the limit  $\varepsilon = 0$ , which present itself as a homoclinic orbit in the related stationary fast-slow ODE system – in case of spatially varying coefficients it is homoclinic to the bounded solution. For this construction, the full system is split into a fast subsystem, and a (super)slow subsystem on a so-called slow manifold  $\mathcal{M}$  that consists of fixed points of the fast subsystem. We establish fast connections to and from  $\mathcal{M}$  that take off from

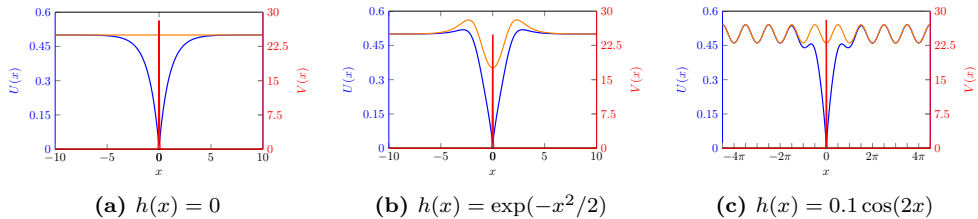


**Figure 4.1** – Numerical simulation resulting in a stationary pulse solution for (4.1.2) with  $f(x) = h'(x)$ ,  $g(x) = h''(x)$ , where  $h(x) = 0$  (a),  $h(x) = \exp(-x^2/2)$  (b) and  $h(x) = 0.1 \cos(2x)$  (c).  $U, V$  components are blue and red respectively, while the orange curve depicts the bounded solution  $u_b$  to which the  $U$ -component converges for  $|x| \rightarrow \infty$ . Parameters used are  $a = 0.5$ ,  $m = 0.45$  and  $D = 0.01$ .

submanifold  $T_o \subset \mathcal{M}$  and touch down on submanifold  $T_d \subset \mathcal{M}$ . On  $\mathcal{M}$ , we construct stable and unstable submanifolds  $W^{s/u}(u_b) \subset \mathcal{M}$  that consists of points on  $\mathcal{M}$  that converge to the bounded solution for  $x \rightarrow \infty$  respectively  $x \rightarrow -\infty$ . Intersections between these unstable/stable manifolds and take-off/touch-down submanifolds (and a symmetry assumption) then establish the existence of pulse solutions to (4.1.2). Finally, persistence of these pulse solutions for  $\varepsilon > 0$  is guaranteed by geometric singular perturbation theory [62].

Specifically, stationary solutions  $(U(x, t), V(x, t)) = (\tilde{u}(x), \tilde{v}(x))$  of (4.1.2) fulfill the system of ODEs

$$\begin{cases} 0 &= \tilde{u}_{xx} + f(x)\tilde{u}_x + g(x)\tilde{u} + a - \tilde{u} - \tilde{u}\tilde{v}^2, \\ 0 &= \frac{D^2}{m}\tilde{v}_{xx} - \tilde{v} + \frac{1}{m}\tilde{u}\tilde{v}^2. \end{cases} \quad (4.1.3)$$

After a sequence of (re)scalings, it can be seen that the associated fast subsystem is not affected by the spatially varying terms and can be studied using standard methods. However, the slow subsystem, on the slow manifold  $\mathcal{M}$ , is affected by the spatially varying terms. This subsystem is given (when rescaling  $\hat{u} = a\tilde{u}$ ) by

$$\begin{cases} \partial_x \hat{u} &= \hat{p}, \\ \partial_x \hat{p} &= -f(x)\hat{p} - g(x)\hat{u} - 1 + \hat{u}. \end{cases} \quad (4.1.4)$$

For  $f$  and  $g$  constant, (4.1.4) can be solved explicitly and the stable and unstable manifolds  $W^{s,u}(u_b)$  are known explicitly. In case of (spatially) varying  $f$  and  $g$ , typically no closed form solutions are available; however, when these varying coefficients are sufficiently small – specifically, when  $\delta := \sup_{x \in \mathbb{R}} \sqrt{f(x)^2 + g(x)^2} < \frac{1}{4}$  (so  $\delta$  can be  $\mathcal{O}(1)$  with respect to  $\varepsilon$ ); see section 4.2.3 – the dynamics of (4.1.4) can be related to the constant coefficient case  $f, g \equiv 0$  using the theory of exponential dichotomies.

In particular, the saddle structure – present for  $f, g \equiv 0$  – persists as exponential dichotomy. Therefore, (4.1.4) possesses a  $1D$  family of solutions that converge to the (unique) bounded solution to (4.1.4) for  $x \rightarrow \infty$  and a  $1D$  family of solutions that converge to the bounded solution for  $x \rightarrow -\infty$ . These families of solutions essentially form the stable and unstable manifolds  $W^{s,u}(u_b)$ . Due to the linear nature of (4.1.4), these (un)stable manifolds are made up of straight lines, i.e.  $W^{s,u}(u_b) = \cup_{x \in \mathbb{R}} (x, l^{s,u}(x))$  where  $l^{s,u}(x)$  describes a straight line in  $\mathbb{R}^2$ . An important difference now arises between the cases of constant and varying coefficients: when  $f, g \equiv 0$ , the lines  $l^{s,u}(x)$  do not depend on  $x$ ; when  $f$  and  $g$  are spatially varying, they do. Hence,



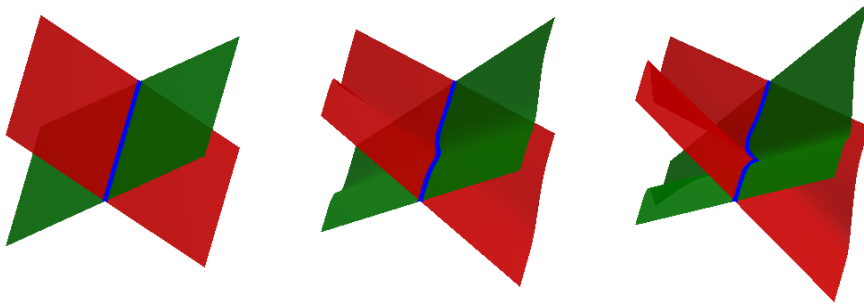


**Figure 4.2** – Sketches of the bounded solution (blue) and its stable (green) respectively unstable (red) manifolds in case of constant coefficients (left) and varying coefficients (center and right).

$W^{s,u}(u_b)$  appears wiggly in case of varying coefficients – see Figure 4.2. The theory of exponential dichotomies enables us to bound the variation of the lines  $l^{s,u}(x)$ ; if  $\delta$  is small enough (i.e.  $\delta < \delta_c(a, m, D)$ , where  $\delta_c \leq 1/4$  is  $\mathcal{O}(1)$  with respect to  $\varepsilon$ ), these bounds are strict enough that a non-empty intersection  $(0, l^u(0)) \cap T_o$  is guaranteed – thus establishing existence of a (symmetric) pulse solution to (4.1.2). See Figure 4.3 for a sketch.

Next, the spectral stability of the thus created pulse solutions is studied. Using similar bounds as in the existence problem, it is shown that eigenvalues are  $\delta$ -close to their counterparts in case of constant coefficients – see Figure 4.4. That is, under several conditions, typical for these systems, the ‘large’ eigenvalues can be bounded to the stable half-plane  $\{\lambda \in \mathbb{C} : \text{Re}\lambda < 0\}$ . For the ‘small’ eigenvalue – located close to the origin – it is more subtle. In case of  $f, g \equiv 0$  this small eigenvalue is located precisely at the origin due to the translation invariance of (4.1.2). The introduction of spatially varying coefficients to the system breaks this invariance and as a result the small eigenvalue moves to the stable or the unstable half-plane.

Tracking of this eigenvalue indicates that it can, indeed, move to either half-plane, depending on the form of the functions  $f$  and  $g$ . In particular, when taking  $f = h'$ ,  $g = h''$ , the location of the small eigenvalue is related to the curvature  $g = h''$  of  $h$ : when the curvature is weak, the pulse solution is stable if  $g(0) = h''(0) < 0$  and unstable if  $g(0) = h''(0) > 0$ ; for strong curvature, this is flipped, due to a pitchfork bifurcation.

Finally, the break-down of the translation invariance in (4.1.2) has another novel effect. In case of constant coefficients, stationary multi-pulse solutions – solutions with multiple fast excursions – do not exist, due to the presence of the translation invariance. If this invariance is broken, they can exist; the introduction of functions  $f$  and  $g$  now allows for these stationary multi-pulse solutions (under some conditions on  $f$  and  $g$ ) and their existence can be established (although we refrain from going in the details).

The set-up for the rest of this paper is as follows. In section 4.2, we establish existence of stationary pulse solutions to (4.1.2); here we first consider the classical case  $f, g \equiv 0$  to illustrate the typical arguments used. Subsequently, we consider the

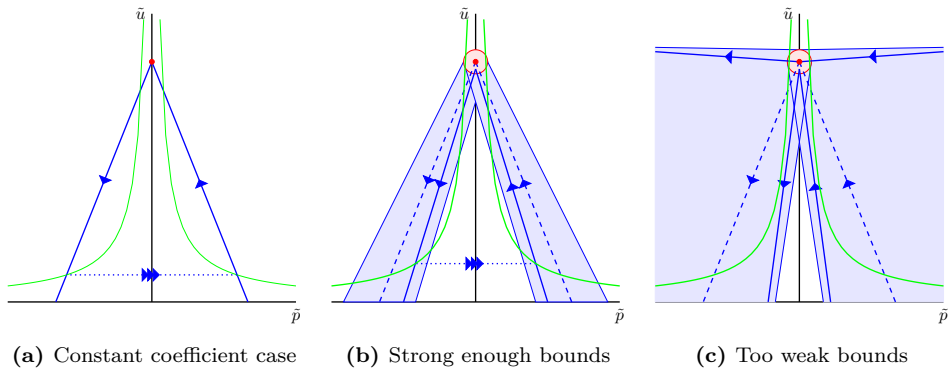


**Figure 4.3** – Sketches of a cross section of  $\mathcal{M}$  that illustrate the heart of the existence proof. In green the takeoff and touchdown curves are shown, the solid blue lines indicate (possible)  $l^{s/u}(0)$ , the dashed blue lines  $l^{s/u}(0)$  for the constant coefficient case  $f = 0, g = 0$ . The shaded blue area indicates all possible locations of  $l^{s/u}(0)$ ; the shaded red region the possible locations of the bounded solution. The existence proof works when bounds on  $u_b$  and  $l^{s/u}(0)$  are strong enough such that  $l^u(0)$  necessarily intersects with  $T_o(0)$  – this happens when all straight lines that start from the red region and stay within the blue region intersect the green curves. If bounds are strong enough this is the case – as illustrated in (b) – but when bounds are too weak this is not the case and existence is not guaranteed by this method – as illustrated in (c). In (a) the situation for the constant coefficient case is shown.

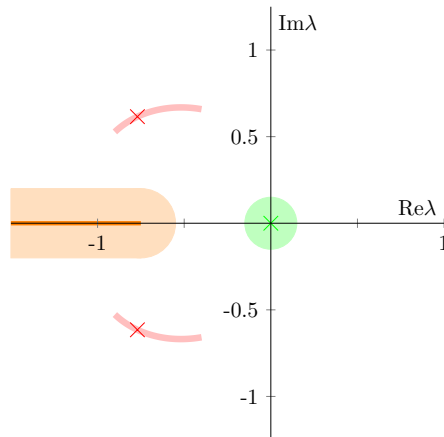


**Figure 4.4** – Sketch of the spectral bounds obtained in this paper. The shaded areas indicate the possible locations of spectra in the case of varying coefficients. The solid lines and crosses indicate the location of the essential and point spectra in the case of constant coefficients: the essential spectrum (orange), the ‘large’ eigenvalues (red) and the ‘small’ eigenvalue (green).

case of generic (bounded)  $f$  and  $g$ . Then, using the theory of exponential dichotomies, both cases are related to each other, resulting in bounds for the generic case that allow us to prove existence. In section 4.3 we study the spectral stability of found pulse solutions, again by relating the generic case to the constant coefficient case of  $f, g \equiv 0$ . Then, in section 4.4 we consider the small eigenvalues more in-depth using formal and numerical techniques, focusing on the possible occurrence of bifurcations; we also present stationary multi-pulse solutions. We conclude with a discussion of the results in section 4.5.

### 4.1.1 Assumptions

The analysis presented in this paper does not hold for all (magnitudes of) parameter values, and all functions  $f$  and  $g$ . Hence, we will make several assumptions throughout the manuscript on the relative sizes of the model parameters. Some of these are essential, while some serve to simplify exposition; here and throughout the text remarks are made about violations of these.

Since this work builds upon decades of studies on Klausmeier/Gray-Scott type models, i.e. (4.1.2), we first list the typical assumptions on the relative sizes of the parameters  $D$ ,  $a$  and  $m$  [8, 28, 46, 47, 148]; we also denote in brackets the type of bifurcation that occurs when these assumptions are violated with references for more information about these bifurcations.

$$(A1) : \quad \varepsilon := \frac{a}{m} \ll 1 \quad [\text{Pulse splitting bifurcation, [46, 51, 101]}] \quad (4.1.5)$$

$$(A2) : \quad \mu := \frac{Dm\sqrt{m}}{a^2} \leq \mathcal{O}(1) \quad [\text{Saddle-node bifurcation, [8, 46, 51, 100]}] \quad (4.1.6)$$

$$(A3) : \quad \tau := \frac{Da^2}{m\sqrt{m}} \leq \mathcal{O}(1) \quad [\text{Traveling wave bifurcation, [46]}] \quad (4.1.7)$$

$$(A4) : \quad \nu := \frac{m^2D}{a^2} \leq \mathcal{O}(1) \quad [\text{Hopf bifurcation, [8, 28, 47, 148]}] \quad (4.1.8)$$

where  $\mathcal{O}(1)$  is to be interpreted with respect to  $\varepsilon = \frac{a}{m}$ . We thus explicitly assume  $\mu$ ,  $\tau$  and  $\nu$  are no larger than  $\mathcal{O}(1)$ . Throughout the manuscript we will find  $\mathcal{O}(1)$  critical values  $\mu^*$ ,  $\tau^*$  and  $\nu^*$  ( $\mu^*$  in Theorem 4.2.19,  $\tau^*$  in Theorem 4.3.5, and  $\nu^*$  in Theorem 4.3.2). In the classical studies of similar systems  $\varepsilon := \frac{a}{m}$  is used as the primary singular perturbation parameters – as will be done in this paper. Then, assumptions (A1)-(A3) can be used to show existence of stationary pulse solutions if  $\mu < \mu^*$  and  $\tau < \tau^*$ , and together with assumption (A4) it can be established that these solutions are spectrally stable if additionally  $\nu < \nu^*$  [8, 28, 148]. See also [148] for a more extended introduction to the above scalings, and a discussion of the relation between the present scaling and (equivalent) alternative scalings in the literature.

The novelty of current work is the inclusion of non-trivial heterogeneities to this already existing framework. To facilitate that, in addition to the classical assumptions

(A1)-(A4), we also need the following assumptions on functions  $f$  and  $g$ .

$$\text{(A5)} : \quad f(-x) = -f(x), \quad g(-x) = g(x), \quad \text{for all } x \in \mathbb{R}; \quad (4.1.9)$$

$$\text{(A6)} : \quad \sup_{x \in \mathbb{R}} \sqrt{f(x)^2 + g(x)^2} < \frac{1}{4}; \quad (4.1.10)$$

$$\text{(A7)} : \quad \lim_{x \rightarrow \pm\infty} f(x), g(x) = 0; \quad (4.1.11)$$

$$\text{(A8)} : \quad \|f\|_{C_b} = \mathcal{O}(1), \quad \|g\|_{C_b} = \mathcal{O}(1) \quad \left( \text{w.r.t. } \frac{a}{m} \right) \quad (4.1.12)$$

(A5) is a symmetry assumption, that ensures (4.1.2) possesses a (point) symmetry in  $x = 0$ ; this technicality significantly simplifies our rigorous proof; pulse solutions can also be found formally and/or numerically when (A5) does not hold (and we expect that their existence can be established rigorously by extending our methods). Then, assumption (A6) stems from the theory of exponential dichotomies: when this holds, solutions to (4.1.4) for generic  $f$  and  $g$  can be linked to solutions of (4.1.4) with  $f, g \equiv 0$ ; when (A6) does not hold, this link is not provided by the theory of exponential dichotomies. Assumption (A7) is a technicality that is only needed in the stability section (specifically for the elephant-trunk method to work); for the existence theorems it is not necessary; in fact, it is suspected that even stability results continue to hold when (A7) is violated – see also Remarks 4.3.18 and 4.3.19. Finally, assumption (A8) is needed to pass limits in the treatment of the fast-slow system.

**Remark 4.1.3.** *In this article we use geometric singular perturbation theory to establish existence of stationary pulse solutions to (4.1.2) for  $\varepsilon$  ‘sufficiently small’; hence assumption (A1) stipulates  $\varepsilon \ll 1$  for clarity. However, typical results of this kind seem to hold, at least numerically, for relatively large values of the singular perturbation parameter, i.e.  $\varepsilon [8]$ . This is illustrated by our numerical results which are made for not-so-small values of  $\varepsilon$ , following previous studies [8, 9, 47, 51, 148, 158].*

## 4.2 Analysis of stationary pulse solutions

A crucial step for making the stationary ODE (4.1.3) amenable to analytic considerations is to find a parameter regime convenient for rigorous perturbation techniques. While there are various choices, we pick a specific one for clarity, since our focus is on novel phenomena due to the non-autonomous character of the system and not to classify all possible dynamics across parameter regimes.

Following [8, 28, 46], we rescale the spatial coordinate (motivated by the diffusivity of the  $v$ -component) and the amplitudes of the unknowns by

$$\xi := \frac{\sqrt{m}}{D}x, \quad \tilde{u} = \frac{m\sqrt{m}D}{a}u, \quad \tilde{v} = \frac{a}{\sqrt{m}D}v, \quad (4.2.1)$$

to get

$$\begin{cases} u_{\xi\xi} &= \frac{a^2}{m^2} \left[ \frac{D^2m}{a^2}u - \frac{Dm\sqrt{m}}{a^2}f\left(\frac{D}{\sqrt{m}}\xi\right)u_{\xi} - \frac{D^2m}{a^2}g\left(\frac{D}{\sqrt{m}}\xi\right)u - \frac{D}{\sqrt{m}} + uv^2 \right], \\ v_{\xi\xi} &= v - uv^2. \end{cases} \quad (4.2.2)$$

It is now convenient to introduce

$$0 < \varepsilon := \frac{a}{m}, \quad 0 < \mu := \frac{m\sqrt{m}D}{a^2}, \quad (4.2.3)$$

and write the above ODEs as the first order system of ODEs

$$\begin{cases} \dot{u} &= \varepsilon p, \\ \dot{p} &= \varepsilon [\varepsilon^2 \mu^2 u - \varepsilon \mu f(\varepsilon^2 \mu \xi) p - \varepsilon^2 \mu^2 g(\varepsilon^2 \mu \xi) u - \varepsilon^2 \mu + uv^2], \\ \dot{v} &= q, \\ \dot{q} &= v - uv^2. \end{cases} \quad (4.2.4)$$

In order to use geometric singular perturbation theory, we make the customary assumption (A1), that is,

$$0 < \varepsilon \ll 1, \quad (4.2.5)$$

and stipulate assumption (A2) and (A8) so we can pass to limits.

In the autonomous case  $f \equiv 0$  and  $g \equiv 0$ , system (4.2.4) has a fixed point  $(1/\mu, 0, 0, 0)$  and stationary pulse solutions of (4.1.2) correspond to orbits that are homoclinic to  $(1/\mu, 0, 0, 0)$ ; see Figure 4.1a for an example. In the non-autonomous case  $f \neq 0, g \neq 0$  there is no fixed point, but instead a unique bounded solution  $(u_b, p_b, 0, 0)$ . In this case, stationary pulse solutions of (4.1.2) correspond to orbits that are homoclinic to this bounded solution; see Figures 4.1b and 4.1c for examples. The existence of said unique bounded solution  $(u_b, p_b, 0, 0)$  is established in the following proposition proven later in section 4.2.3 (in the proof of Proposition 4.2.14).

**Proposition 4.2.1** (Existence of a bounded solution for (4.2.4)). *Let assumptions (A6) and (A8) be fulfilled. Then (4.2.4) has a unique bounded solution  $(u_b, p_b, 0, 0)$  that satisfies*

$$\lim_{\xi \rightarrow \pm\infty} (u_b, p_b, 0, 0) = (1/\mu, 0, 0, 0). \quad (4.2.6)$$

**Remark 4.2.2** (Orbits homoclinic to bounded solutions). *Note that the asymptotic assumption  $\lim_{x \rightarrow \pm\infty} f(x), g(x) = 0$  in (A7) is not necessary for the existence proof, but will be used in the stability analysis. In case  $f, g$  are only bounded without approaching a constant state when  $|x| \rightarrow \infty$ , the corresponding constructed pulse solution is also a homoclinic to the respective bounded solution. An illustration of such a case is given in Figure 4.1c, where, due to the periodicity of the coefficients  $f, g$ , the bounded background solution is periodic and so is the pulse solution in its tails.*

To highlight the novelty of the presented approach, we first briefly explain how the construction is carried out in the constant coefficient case  $f = g = 0$ , to then proceed to the non-autonomous case.

#### 4.2.1 Stationary pulse solutions for $f = 0$ and $g = 0$

The fast system reads

$$\begin{cases} \dot{u} &= \varepsilon p, \\ \dot{p} &= \varepsilon [\varepsilon^2 \mu^2 u - \varepsilon^2 \mu + uv^2], \\ \dot{v} &= q, \\ \dot{q} &= v - uv^2. \end{cases} \quad (4.2.7)$$

Note that this system possesses the symmetry  $(\xi, u, p, v, q) \rightarrow (-\xi, u, -p, v, -q)$ . The corresponding slow system in the slow scaling  $\eta = \varepsilon\xi$  is given by

$$\begin{cases} u' &= p, \\ p' &= \varepsilon^2 \mu^2 u - \varepsilon^2 \mu + uv^2, \\ \varepsilon v' &= q, \\ \varepsilon q' &= v - uv^2. \end{cases} \quad (4.2.8)$$

Restricted to the invariant manifold

$$\widetilde{\mathcal{M}} := \{(u, p, 0, 0) \mid u, p \in \mathbb{R}\} \quad (4.2.9)$$

it reads

$$\begin{cases} u' &= p, \\ p' &= \varepsilon^2 \mu^2 u - \varepsilon^2 \mu, \end{cases} \quad (4.2.10)$$

which has a saddle structure around the fixed point  $(\frac{1}{\mu}, 0)$  with stable and unstable manifolds given by

$$\tilde{u}^{u/s} := \left\{ (u, p) \mid p = \pm \varepsilon \mu \left(u - \frac{1}{\mu}\right) \right\}. \quad (4.2.11)$$

**Remark 4.2.3.** *Note that this step is much more intricate in the case of varying coefficients  $f, g$  where explicit solutions are possible only for very specific choices of coefficients. Therefore, one must resort to estimation techniques for the general case. Overcoming this difficulty using exponential dichotomies is the core contribution of the present work.*

The reduced fast system has the form

$$\begin{cases} \dot{u} &= 0, \quad \dot{p} = 0, \\ \dot{v} &= q, \\ \dot{q} &= v - uv^2. \end{cases} \quad (4.2.12)$$

A sketch of its planar subsystem  $\dot{v} = q, \dot{q} = v - uv^2$  can be found in Figures 4.5a; this planar subsystem is a Hamiltonian system with Hamiltonian

$$H(v, q; u) = \frac{1}{2}q^2 - \frac{1}{2}v^2 + \frac{1}{3}uv^3. \quad (4.2.13)$$

Its fixed point  $(v, q) = (0, 0)$  features a saddle structure and a family of homoclinic orbits

$$\begin{cases} v_{hom}^{(0)}(\xi; u_0) &= \frac{1}{u_0} \omega(\xi) & \omega(\xi) &:= \frac{3}{2} \operatorname{sech}^2(\xi/2), \\ q_{hom}^{(0)}(\xi; u_0) &= \dot{v}_{hom}(\xi; u_0) & &= -\frac{1}{u_0} \frac{3}{2} \operatorname{sech}^2(\xi/2) \tanh(\xi/2), \quad u_0 \in \mathbb{R} \setminus \{0\}, \end{cases} \quad (4.2.14)$$

connecting its stable and unstable manifolds. Hence, (4.2.12) is a Hamiltonian system with Hamiltonian

$$\widetilde{K}(u, p, v, q) = H(v, q; u). \quad (4.2.15)$$

The invariant manifold  $\widetilde{\mathcal{M}}$  from (4.2.9) is the collection of saddle points  $(u, p, 0, 0)$ ,  $u, p \in \mathbb{R}$ , for (4.2.12) and is, hence, normally hyperbolic. For its stable and unstable manifolds  $W_0^{s/u}(\widetilde{\mathcal{M}})$  it holds true that  $\dim[W_0^{s/u}(\widetilde{\mathcal{M}})] = 3$  and, in fact,  $W_0^s(\widetilde{\mathcal{M}})$  and  $W_0^u(\widetilde{\mathcal{M}})$  (partly) coincide, where the intersection is simply given by the family of homoclinic orbits. Moreover, we have that  $\widetilde{K}(u, p, v, q)|_{(u,p,v,q) \in \widetilde{\mathcal{M}}} = 0$ .

For  $\varepsilon > 0$ , we note that  $\widetilde{\mathcal{M}}$  is still an invariant manifold of the full system (4.2.7). It is a standard result in geometric singular perturbation theory (see, e.g. the classic articles [62, 86, 164] or, more recent, [105]) that, for  $\varepsilon$  sufficiently small, its stable and unstable manifolds persist as  $W_\varepsilon^{s/u}(\widetilde{\mathcal{M}})$  with  $\dim[W_\varepsilon^{s/u}(\widetilde{\mathcal{M}})] = 3$ , but do not necessarily coincide anymore. In fact, they generically meet in a 2D intersection in  $\mathbb{R}^4$ .

In order to analyze the persistence of homoclinic orbits we measure the distance of  $W_\varepsilon^s(\widetilde{\mathcal{M}})$  and  $W_\varepsilon^u(\widetilde{\mathcal{M}})$  in the hyperplane  $\widetilde{R} = \{(u, p, v, q) \mid q = 0\}$ , that is, we fix an even homoclinic orbit  $(u_{hom}, p_{hom}, v_{hom}, q_{hom})$  with  $(u_{hom}(0), p_{hom}(0), v_{hom}(0), q_{hom}(0)) = (u_0, p_0, v_{max}, 0)$ . To this end we use the Hamiltonian  $\widetilde{K}$  and analyze its difference during the jump of the orbit through the fast field, which is defined – following e.g. [48, 148] – as

$$I_f := \left( -\frac{1}{\sqrt{\varepsilon}}, \frac{1}{\sqrt{\varepsilon}} \right), \quad (4.2.16)$$

by setting up

$$\Delta_{I_f} \widetilde{K} = \widetilde{K}(1/\sqrt{\varepsilon}) - \widetilde{K}(-1/\sqrt{\varepsilon}) = \int_{I_f} \frac{d}{d\xi} \widetilde{K}(\xi) d\xi = \frac{1}{3} \varepsilon \int_{I_f} p(\xi) v_{hom}(\xi)^3 d\xi + h.o.t. \quad (4.2.17)$$

where we used that  $\frac{d}{d\xi} \widetilde{K} = \frac{\partial}{\partial u} H(v, q; u) \left( \frac{du}{d\xi} \right) + \frac{d}{d\xi} H(v, q; u) = \frac{1}{3} v^3 \left( \frac{du}{d\xi} \right) + 0 = \frac{1}{3} \varepsilon v^3 p$ . We may set (using the fact that  $p$  is constant to leading order)  $p(\xi) = p^{(0)} + \varepsilon p^{(1)}(\xi) + h.o.t.$  Therefore, in order to make this difference vanish to leading order, we evidently need that  $p^{(0)} = 0$  and  $p^{(1)}(0) = 0$ .

Now that a departure and return mechanism from and back to  $\widetilde{\mathcal{M}}$  is established through the intersection  $W_\varepsilon^s(\widetilde{\mathcal{M}}) \cap W_\varepsilon^u(\widetilde{\mathcal{M}}) \cap R$ , the remaining task is to determine possible take-off and touch-down points on  $\widetilde{\mathcal{M}}$  and investigate if these intersect the stable and unstable eigenspaces  $l^{s/u}$  appropriately to form a homoclinic. To this end we observe that

$$\Delta_{I_f} u = u(1/\sqrt{\varepsilon}) - u(-1/\sqrt{\varepsilon}) = \int_{I_f} \frac{d}{d\xi} u(\xi) d\xi = \varepsilon^2 \int_{I_f} p^{(1)}(\xi) d\xi = \mathcal{O}(\varepsilon^{3/2}), \quad (4.2.18)$$

$$\Delta_{I_f} p = p(1/\sqrt{\varepsilon}) - p(-1/\sqrt{\varepsilon}) = \int_{I_f} \frac{d}{d\xi} p(\xi) d\xi = \varepsilon u_0 \int_{I_f} v_{hom}^{(0)}(\xi)^2 d\xi = \frac{6}{u_0} \varepsilon + h.o.t., \quad (4.2.19)$$

so, to leading order, only the  $p$ -variable changes during the fast jump, and therefore, the take-off and touch-down curves on  $\widetilde{\mathcal{M}}$  are to leading order given by

$$\widetilde{T}_{o/d} := \left\{ (u, p, 0, 0) \mid p = \mp \frac{3\varepsilon}{u}, u \neq 0 \right\}, \quad (4.2.20)$$

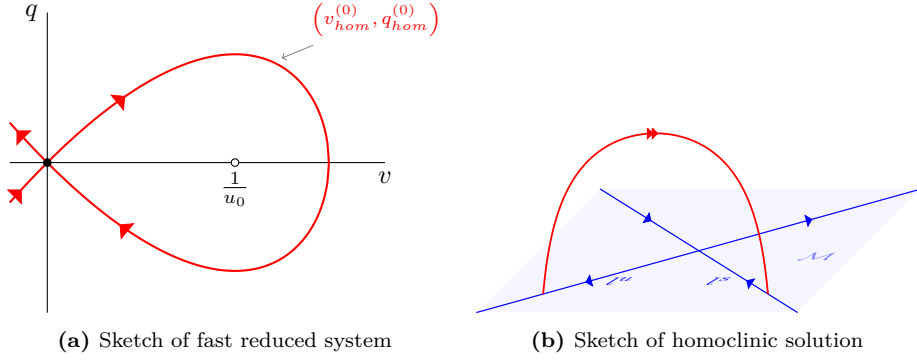


**Figure 4.5** – Sketches of the fast reduced system (4.2.12) (a) and the dynamics on the slow manifold  $\mathcal{M}$  along with, in red, the excursion through the fast field (b).

where we used that, by symmetry, to leading order

$$p(\pm 1/\sqrt{\varepsilon}) = p(0) \pm \frac{1}{2} \Delta_{I_f} p = \varepsilon \left( p^{(1)}(0) \pm \frac{3}{u_0} \right). \quad (4.2.21)$$

Finally, a straightforward computation of the intersection points of these with the stable and unstable eigenspaces  $l^{s/u}$  gives two possible homoclinics when  $\mu \leq \frac{1}{12}$ , with

$$u_0^\pm = \frac{1 \pm \sqrt{1 - 12\mu}}{2\mu} \quad \left( \text{for } \mu \leq \frac{1}{12} \right). \quad (4.2.22)$$

**Remark 4.2.4.** When  $\mu \ll 1$ , the expression for  $u_0^\pm$ , (4.2.22), can be expanded in terms of  $\mu$ ; this yields for  $u_0^\pm$  the following expansions

$$\begin{aligned} u_0^- &= 3 + 9\mu + \mathcal{O}(\mu^2) \\ u_0^+ &= \frac{1}{\mu} - 3 - 9\mu + \mathcal{O}(\mu^2) \end{aligned} \quad (4.2.23)$$

A conceptual sketch of the dynamics on  $\widetilde{\mathcal{M}}$ , along with an excursion through the fast field, is given in Figure 4.5b. Moreover, in Figures 4.6a and 4.6b, the evolution of a homoclinic solution is projected onto manifold  $\mathcal{M}$ .

## 4.2.2 Stationary pulse solutions for varying $f$ and $g$

First, we convert the non-autonomous system into an autonomous one by setting

$$s(\xi) := \frac{D}{\sqrt{m}} \xi = \varepsilon^2 \mu \xi, \quad (4.2.24)$$

which gives the extended (autonomous) fast system

$$\begin{cases} \dot{s} = \varepsilon^2 \mu, \\ \dot{u} = \varepsilon p, \\ \dot{p} = \varepsilon [\varepsilon^2 \mu^2 u - \varepsilon \mu f(s) p - \varepsilon^2 \mu^2 g(s) u - \varepsilon^2 \mu + uv^2], \\ \dot{v} = q, \\ \dot{q} = v - uv^2. \end{cases} \quad (4.2.25)$$



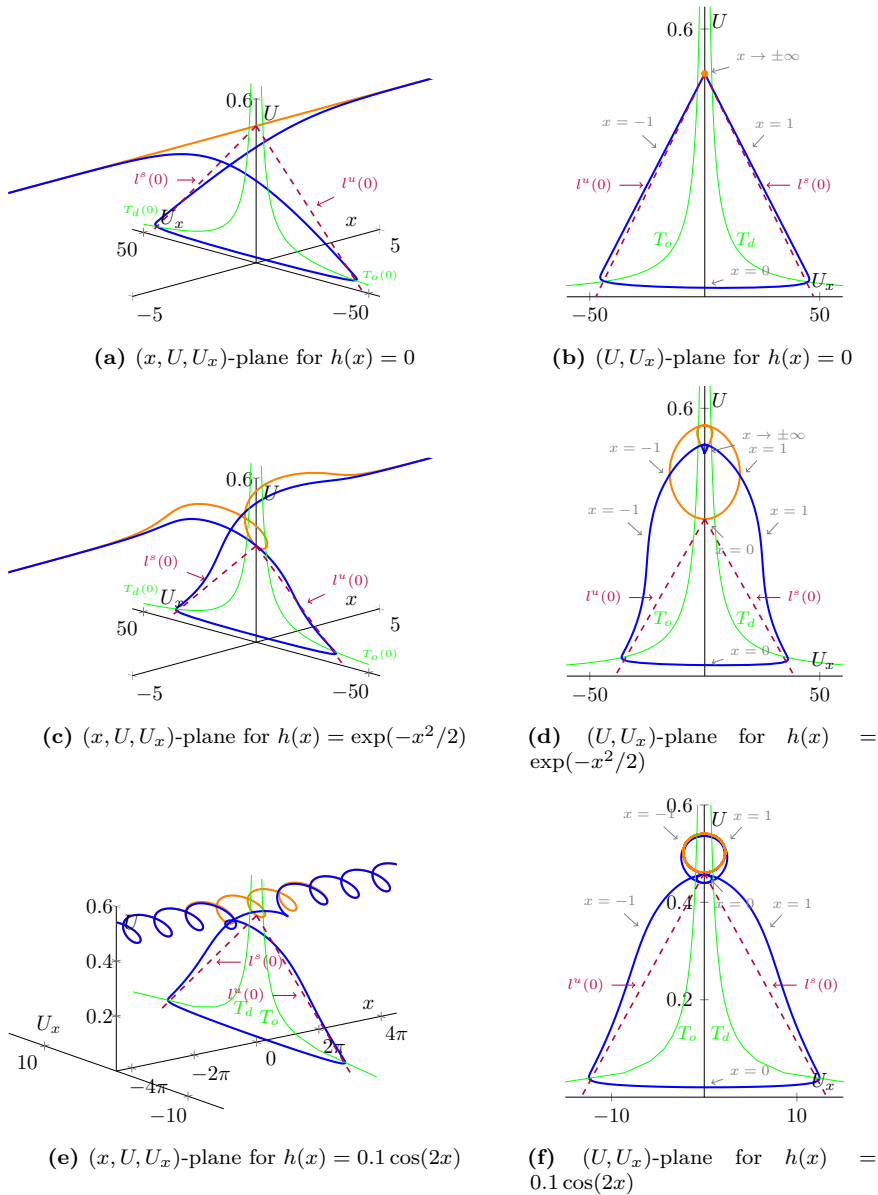


**Figure 4.6** – Numerical simulations resulting in a stationary pulse solution for (4.1.2) with  $f(x) = h'(x)$ ,  $g(x) = h''(x)$ , where  $h(x) = 0$  (a,b),  $h(x) = \exp(-x^2/2)$  (c,d) and  $h(x) = 0.1 \cos(2x)$  (e,f). Shown are projections to the  $(x, U, U_x)$ -plane (a,c,e) and the  $(U, U_x)$ -plane (b,d,f) of a stationary pulse solution (blue) and the bounded solution  $u_b$  (orange) to which the  $U$ -component converges for  $|x| \rightarrow \infty$ . Parts of the take-off and touch-down curves ( $T_o/d$ ) along with stable and unstable manifolds at  $x = 0$  are also sketched in green respectively red. Parameters used are  $a = 0.5$ ,  $m = 0.45$  and  $D = 0.01$ . Note that the plots in this figure correspond to the plots in Figure 4.1.

It is important to note that the symmetry assumptions (A5) on  $f$  and  $g$  translate directly into a symmetry for (4.2.25) which is crucial for the construction of a homoclinic.

**Lemma 4.2.5** (Symmetry of (4.2.25)). *Let the symmetry assumptions (A5) be fulfilled, that is, let  $f$  be an odd function and  $g$  be an even function. Then we have for (4.2.25) the symmetry  $(s, u, p, v, q) \rightarrow (-s, u, -p, v, -q)$ ,  $\xi \rightarrow -\xi$ .*

The slow system corresponding to (4.2.25) in the slow variable  $\eta = \varepsilon\xi$  is given by

$$\begin{cases} s' &= \varepsilon\mu, \\ u' &= p, \\ p' &= \varepsilon^2\mu^2u - \varepsilon\mu f(s)p - \varepsilon^2\mu^2g(s)u - \varepsilon^2\mu + uv^2, \\ \varepsilon v' &= q, \\ \varepsilon q' &= v - uv^2. \end{cases} \quad (4.2.26)$$

It possesses a three-dimensional invariant manifold

$$\mathcal{M} := \{(s, u, p, 0, 0) \mid u, s, p \in \mathbb{R}\} \subset \mathbb{R}^5, \quad (4.2.27)$$

on which it takes the form

$$\begin{cases} s' &= \varepsilon\mu, \\ u' &= p, \\ p' &= \varepsilon^2\mu^2u - \varepsilon\mu f(s)p - \varepsilon^2\mu^2g(s)u - \varepsilon^2\mu. \end{cases} \quad (4.2.28)$$

which is an extension of the non-autonomous system

$$\begin{cases} u' &= p, \\ p' &= \varepsilon^2\mu^2u - \varepsilon\mu f(\varepsilon\mu\eta)p - \varepsilon^2\mu^2g(\varepsilon\mu\eta)u - \varepsilon^2\mu. \end{cases} \quad (4.2.29)$$

It is now convenient to introduce (or, actually, return to) the super-slow variable  $x = \varepsilon\mu\eta$ . We set  $u(\eta) = \frac{1}{\mu}\hat{u}(\varepsilon\mu\eta) = \frac{1}{\mu}\hat{u}(x)$  and return to the second order non-autonomous setting

$$\begin{cases} \frac{d}{dx}\hat{u} &= \hat{p}, \\ \frac{d}{dx}\hat{p} &= \hat{u} - f(x)\hat{p} - g(x)\hat{u} - 1. \end{cases} \quad (4.2.30)$$

**Lemma 4.2.6** (Symmetry of (4.2.30)). *Let the symmetry assumptions (A5) be fulfilled, that is, let  $f$  be an odd function and  $g$  be an even function. Then we have for (4.2.30) the symmetry  $(x, \hat{u}, \hat{p}) \rightarrow (-x, \hat{u}, -\hat{p})$ ,  $\xi \rightarrow -\xi$ .*

**Remark 4.2.7.** *For conciseness, we note that we have three different scales:*

**fast scale**  $\xi$ ,    **slow scale**  $\eta = \varepsilon\xi$ ,    **super-slow scale**  $x = \varepsilon\mu\eta = \varepsilon^2\mu\xi$

*The construction that we illustrate in this article therefore relies heavily on assumption (A1). The specific definition of the small parameter is convenient since the fast reduced system is an ODE which is known to have homoclinic solutions and the slow system on the critical manifold  $\mathcal{M}$  is a linear planar system.*

**Remark 4.2.8.** Note the difference between  $p = \frac{du}{d\eta}$  and  $\hat{p} = \frac{d\hat{u}}{dx}$ . Hence,  $p = \varepsilon\hat{p}$ .

**Proposition 4.2.9** (Dynamics on  $\mathcal{M}$ ). Consider the slow system on  $\mathcal{M}$  (4.2.28) with  $f, g$  fulfilling (A6). Then there exists a unique bounded solution  $(\hat{u}_b, \hat{p}_b)$  of (4.2.30) and corresponding connected set  $\Gamma \subset \mathbb{R} \cup \{\infty\}$  such that the following holds true: For each fixed  $x \in \mathbb{R}$  there exists  $C^{s/u}(x) \in \Gamma$  and lines

$$l^{s/u}(x) := \{(\hat{u}, \hat{p}) \mid \hat{p} - \hat{u}'_b(x) = C^{s/u}(x)(\hat{u} - \hat{u}_b(x))\}, \quad (4.2.31)$$

such that the solution to the initial value problem (4.2.30) with  $(\hat{u}(x), \hat{p}(x)) = (\hat{u}_0, \hat{p}_0) \in l^s(x)$  converges to  $(\hat{u}_b, \hat{p}_b)$  for  $x \rightarrow \infty$ , while with  $(\hat{u}(x), \hat{p}(x)) = (\hat{u}_0, \hat{p}_0) \in l^u(x)$  it converges to  $(\hat{u}_b, \hat{p}_b)$  for  $x \rightarrow -\infty$ . Moreover, if  $f$  and  $g$  fulfill the symmetry assumption (A5),  $C^{s/u}$  possess the symmetry  $C^s(x) = -C^u(-x)$  for all  $x \in \mathbb{R}$ . In particular,  $C^s(0) = -C^u(0)$ .

The proof of Proposition 4.2.9 constitutes the contents of section 4.2.4. Also note the similarities with Proposition 4.2.1, since the bounded solutions mentioned in both Propositions are identical up to the scaling  $\hat{u}_b(x) = \mu u_b(\xi)$ .

**Remark 4.2.10.** When  $\lim_{x \rightarrow \pm\infty} f(x), g(x) = 0$  (i.e. assumption (A7)), the unique bounded solution  $(\hat{u}_b, \hat{p}_b)$  limits to the fixed point of the autonomous equation (4.1.4). That is,

$$\lim_{x \rightarrow \pm\infty} (\hat{u}_b(x), \hat{p}_b(x)) = (1, 0). \quad (4.2.32)$$

This result implies that there are trajectories on  $\mathcal{M}$  that lead to and away from the bounded solution  $(\hat{u}_b, \hat{p}_b)$ . Hence, the only remaining construction steps are the analysis of persistence of orbits biasymptotic to  $\mathcal{M}$  and their touch-down/take-off locations. We therefore switch back to the fast system and examine the dynamics during the jump of an orbit through the fast field. In order to pass to the reduced fast system, we use the assumption (A8) so, in the limit  $\varepsilon \rightarrow 0$ , we get the reduced fast system

$$\begin{cases} \dot{s} = 0, & \dot{u} = 0, & \dot{p} = 0, \\ \dot{v} = q, \\ \dot{q} = v - uv^2. \end{cases} \quad (4.2.33)$$

Note that in the reduced fast system the non-autonomous character of our problem is not visible. The only difference is the added trivial equation  $\dot{s} = 0$ . As alluded to in the constant coefficient case in section 4.2.1, the planar subsystem  $\dot{v} = q, \dot{q} = v - uv^2$  is known to be Hamiltonian and features a homoclinic to the saddle point  $(v, q) = (0, 0)$  which can be specified explicitly (see (4.2.14)). As a result, also (4.2.33) is Hamiltonian with

$$K(s, u, p, v, q) = H(v, q; u). \quad (4.2.34)$$

The invariant manifold  $\mathcal{M}$  from (4.2.27) is the collection of saddle points  $(s, u, p, 0, 0)$ ,  $u, s, p \in \mathbb{R}$ , for (4.2.33) and is, hence, normally hyperbolic. For its stable and unstable manifolds  $W_0^{s/u}(\mathcal{M})$  it holds true that  $\dim[W_0^{s/u}(\mathcal{M})] = 4$  and, in fact,  $W_0^s(\mathcal{M})$  and  $W_0^u(\mathcal{M})$  (partly) coincide, where the intersection is simply given by the family of homoclinic orbits. Moreover, we have that  $K(s, u, p, v, q)|_{(s,u,p,v,q) \in \mathcal{M}} = 0$ .

The analogy with the constant coefficient case continues for  $\varepsilon > 0$  sufficiently small; we still have that  $\mathcal{M}$  is an invariant manifold of the full system (4.2.25) and that its stable and unstable manifolds persist as  $W_\varepsilon^{s/u}(\mathcal{M})$  with  $\dim[W_\varepsilon^{s/u}(\mathcal{M})] = 4$ , but do not necessarily coincide anymore. In fact, they generically meet in a 3-D intersection in  $\mathbb{R}^5$ .

**Proposition 4.2.11** (Persistence of a homoclinic connection). *Let  $\varepsilon$  be sufficiently small, and let assumptions (A2), (A3), (A5) and (A8) be satisfied.*

1. Define the hyperplane  $R = \{(s, u, p, v, q) \mid q = 0\}$ . Then  $\dim[W_\varepsilon^s(\mathcal{M}) \cap W_\varepsilon^u(\mathcal{M}) \cap R] = 2$  and orbits in this intersection fulfill  $p(\xi) = \varepsilon p^{(1)}(\xi) + h.o.t.$ , that is, the leading order constant term  $p^{(0)}$  vanishes.
2. The take-off and touch-down surfaces on  $\mathcal{M}$  of orbits in the intersection  $W_\varepsilon^s(\mathcal{M}) \cap W_\varepsilon^u(\mathcal{M}) \cap R$  are to leading order given by

$$T_{o/d}(s) := \left\{ (s, u, p, 0, 0) \mid p = \mp \frac{3\varepsilon}{u}, u \neq 0 \right\}. \quad (4.2.35)$$

3. For orbits in the intersection  $W_\varepsilon^s(\mathcal{M}) \cap W_\varepsilon^u(\mathcal{M}) \cap R$  the touch-down curve  $T_d(0)$  and stable line  $l^s(0)$  from (4.2.31) intersect in at most two points

$$u_0^\pm = \frac{u_b(0) \pm \sqrt{u_b(0)^2 + 12/(\mu C^s(0))}}{2}, \quad (4.2.36)$$

where  $C^s(0)$  is the slope of the stable line  $l^s(0)$  from (4.2.31) and  $\hat{u}_b = \mu u_b$  is the (rescaled) bounded background solution from Proposition 4.2.9. By symmetry, the analogous is true for the take-off curve  $T_o(0)$  and unstable line  $l^u(0)$  from (4.2.31). In particular, the thus computed  $u_0^\pm$ -values coincide by the aforementioned symmetry  $C^u(0) = -C^s(0)$  – see Proposition 4.2.9.

4. There are two even homoclinic orbits for (4.1.3) with  $u_0^\pm > 0$  in case  $u_b(0)^2 + 12/(\mu C^s(0)) > 0$  and  $u_b(0) - \sqrt{u_b(0)^2 + 12/(\mu C^s(0))} > 0$ .

**Remark 4.2.12.** *If we set  $u_b(0) = \frac{1}{\mu}$  and  $C^s(0) = -1$  in (4.2.36), we recover (4.2.22).*

*Proof.* Measuring the distance of  $W_\varepsilon^s(\mathcal{M})$  and  $W_\varepsilon^u(\mathcal{M})$  in the hyperplane  $R$  can again be accomplished using the difference of the Hamiltonian  $K$  during the fast the jump of the orbit through the fast field (4.2.16). Exactly as in the constant coefficient case, we obtain (4.2.17) where (using that  $p$  is constant to leading order) we have set  $p(\xi) = p^{(0)} + \varepsilon p^{(1)}(\xi) + h.o.t.$ , and used that  $\frac{d}{d\xi}K = \frac{\partial}{\partial s}K(s, u, p, v, q)\left(\frac{ds}{d\xi}\right) + \frac{\partial}{\partial u}H(v, q; u)\left(\frac{du}{d\xi}\right) + \frac{d}{d\xi}H(v, q; u) = 0 + \frac{1}{3}v^3\left(\frac{du}{d\xi}\right) + 0 = \frac{1}{3}\varepsilon v^3 p$ . In order to make this difference vanish to leading order, we evidently need that  $p^{(0)} = 0$  and  $p^{(1)}(0) = 0$ . This proves the first statement.

In order to construct the take-off and touch-down curves, we again investigate the

change of the fast variables during the jump through the fast field:

$$\Delta_{I_f} s = s(1/\sqrt{\varepsilon}) - s(-1/\sqrt{\varepsilon}) = \int_{I_f} \frac{d}{d\xi} s(\xi) d\xi = \frac{2}{\sqrt{\varepsilon}} \varepsilon^2 \mu = \mathcal{O}(\varepsilon^{3/2}), \quad (4.2.37)$$

$$\Delta_{I_f} u = u(1/\sqrt{\varepsilon}) - u(-1/\sqrt{\varepsilon}) = \int_{I_f} \frac{d}{d\xi} u(\xi) d\xi = \varepsilon^2 \int_{I_f} p^{(1)}(\xi) d\xi = \mathcal{O}(\varepsilon^{3/2}), \quad (4.2.38)$$

$$\Delta_{I_f} p = p(1/\sqrt{\varepsilon}) - p(-1/\sqrt{\varepsilon}) = \int_{I_f} \frac{d}{d\xi} p(\xi) d\xi = \varepsilon u_0 \int_{I_f} v_{hom}^{(0)}(\xi)^2 d\xi = \frac{6}{u_0} \varepsilon + h.o.t., \quad (4.2.39)$$

Hence, to leading order, only the  $p$ -variable changes during the fast jump, and therefore, the take-off and touch-down curves on  $\mathcal{M}$  are to leading order given by (4.2.35) where we used that, by symmetry,  $p(\pm 1/\sqrt{\varepsilon}) = p(0) \pm \frac{1}{2} \Delta_{I_f} p$ . This proves the second statement.

Equating (4.2.35) and (4.2.31) (where we used that  $p = \varepsilon \hat{p}$  – see Remark 4.2.8) gives the equality

$$\varepsilon \mu C^s(0) (u_0 - u_b(0)) = \frac{3\varepsilon}{u_0}; \quad (4.2.40)$$

the solutions of which give the claimed expression (4.2.36) in the third statement. Finally, the fourth statement follows from inspecting (4.2.36).  $\square$

Two examples of homoclinic solutions for varying  $f$  and  $g$  can be found in Figures 4.6c–4.6f. In these figures the evolution of a homoclinic solution is projected onto the manifold  $\mathcal{M}$ , which shows the essence of Proposition 4.2.11.

Proposition 4.2.11 thus establishes existence of homoclinic solutions for (4.1.3) under the conditions stated in Proposition 4.2.11(4). However, in the case of varying coefficients, there typically are no explicit expressions available for the bounded solution  $u_b(0)$  and the constant  $C^s(0)$ . To circumvent this, in the next section we derive bounds on these using the theory of exponential dichotomy, which simultaneously forms the proof of Proposition 4.2.9.

### 4.2.3 Some basic results from the theory of exponential dichotomies

When  $f$  and/or  $g$  are non-constant, generically it is not possible to capture the dynamics on manifold  $\mathcal{M}$  in explicit expressions. Instead, our main tools for constructing a saddle-like structure on  $\mathcal{M}$  are from the theory of exponential dichotomies. To fix notation and keep the exposition self-contained, we state (following [31]) the definition of exponential dichotomies along with a selection of results that we use here.

**Definition 4.2.13** (Exponential Dichotomy). *Consider the planar differential equation  $\frac{d}{dx} Y = B(x)Y$  for the unknown  $Y : \mathbb{R} \rightarrow \mathbb{R}^2$  and with  $B : \mathbb{R} \rightarrow \mathbb{R}^{2 \times 2}$  a matrix-valued function which is continuous on  $\mathbb{R}$ . Let  $\Phi = \Phi(x)$  be the associated canonical solution operator. This ODE is said to have an exponential dichotomy if there is a projection matrix  $P$  and positive constants  $K$  and  $\rho$  such that*

$$\begin{aligned} \|\Phi(x) P \Phi^{-1}(\tilde{x})\| &\leq K e^{-\rho(x-\tilde{x})}, & x \geq \tilde{x}, \\ \|\Phi(x) (I - P) \Phi^{-1}(\tilde{x})\| &\leq K e^{+\rho(x-\tilde{x})}, & x \leq \tilde{x}. \end{aligned}$$

In the next section we will be interested in first order ODEs of the form

$$\frac{d}{dx}Y = [A_0 + A(x)]Y + F, \quad (4.2.41)$$

with  $x \in \mathbb{R}$ ,  $Y : \mathbb{R} \rightarrow \mathbb{R}^2$ ,  $A_0 \in \mathbb{R}^{2 \times 2}$ ,  $A : \mathbb{R} \rightarrow \mathbb{R}^{2 \times 2}$ ,  $F \in \mathbb{R}^2$ . In particular, we would like to corroborate knowledge of the autonomous version (which is often available in terms of explicit solutions) to deduce qualitative results for the full non-autonomous one. For the sake of clarity, we assemble first all auxiliary systems in one place:

First, we have the homogeneous, autonomous system

$$\frac{d}{dx}Z_h = A_0 Z_h. \quad (4.2.42)$$

Then, there is the homogeneous, non-autonomous system

$$\frac{d}{dx}Y_h = [A_0 + A(x)]Y_h. \quad (4.2.43)$$

Finally, we have the inhomogeneous, autonomous system

$$\frac{d}{dx}Z = A_0 Z + F. \quad (4.2.44)$$

**Proposition 4.2.14** (Roughness and closeness of bounded solutions). *Let  $K_{aut} > 0$  and  $\rho_{aut} > 0$  be the exponential dichotomy constants of the homogeneous, autonomous ODE (4.2.42) and  $\Phi_{aut}, P_{aut}$  the corresponding solution and projection operators. If*

$$\delta := \sup_{x \in \mathbb{R}} \| |A(x)| \| < \frac{\rho_{aut}}{4K_{aut}^2}, \quad (4.2.45)$$

*the non-autonomous ODE (4.2.43) has an exponential dichotomy for which the following holds true.*

1. (*Roughness*) *The exponential dichotomy constants of the homogeneous, non-autonomous ODE (4.2.43) are  $K = \frac{5}{2}K_{aut}^2$  and  $\rho = \rho_{aut} - 2K_{aut}\delta$ , and concerning the solution and projection operators  $\Phi, P$  of (4.2.43) we have upon defining*

$$Q(x) := \Phi(x)P\Phi^{-1}(x), \quad Q_{aut}(x) := \Phi_{aut}(x)P_{aut}\Phi_{aut}^{-1}(x) \quad (4.2.46)$$

*the estimate*

$$\| |Q(x) - Q_{aut}(x)| \| \leq \frac{4K_{aut}^3\delta}{\rho_{aut}}, \quad x \in \mathbb{R}. \quad (4.2.47)$$

2. (*Closeness of bounded solutions*) *There exist unique bounded solutions  $Z_{b,aut}, Y_b$  of the inhomogeneous, autonomous and non-autonomous ODEs (4.2.44) and (4.2.41). In particular, they satisfy*

$$\sup_{x \in \mathbb{R}} \| |Y_b(x) - Z_{b,aut}(x)| \| \leq \frac{4\delta K_{aut}K}{\rho_{aut}\rho} \|F\|. \quad (4.2.48)$$

*Proof.* The first statement is the persistence of exponential dichotomies, known as “roughness”, and is a standard result (see [31, Ch.4, Prop.1]). Moreover, another standard result from the theory of exponential dichotomies stipulates that inhomogeneous equations have unique bounded solutions, when the homogeneous equations have an exponential dichotomy and the inhomogeneous terms are bounded (see [31, Ch.8, Prop.2]). Then, to demonstrate the rest of the second statement, we define  $W(x) = Y_b(x) - Z_{b,aut}(x)$  which gives  $W'(x) = A_0W(x) + G(x)$  with  $G(x) = A(x)Y_b(x)$ . The unique bounded solution  $W_b$  of this ODE satisfies the estimate  $\sup_{x \in \mathbb{R}} \|W_b(x)\| \leq \frac{2K_{aut}}{\rho_{aut}} \sup_{x \in \mathbb{R}} \|G(x)\| \leq \frac{4\delta K_{aut}K}{\rho_{aut}\rho} \|F\|$ , where we used that  $\sup_{x \in \mathbb{R}} \|Y_b(x)\| \leq \frac{2K}{\rho} \|F\|$ .  $\square$

#### 4.2.4 Dynamics on $\mathcal{M}$ (Proof of Proposition 4.2.9)

Let us introduce the more concise notation  $Y = (\hat{u}, \frac{d}{dx}\hat{u})^T$  such that (4.2.30) has the form of (4.2.41) from the previous section; that is,

$$\frac{d}{dx}Y = [A_0 + A(x)]Y + F, \quad (4.2.49)$$

with

$$A_0 = \begin{pmatrix} 0 & 1 \\ 1 & 0 \end{pmatrix}, \quad A(x) = \begin{pmatrix} 0 & 0 \\ -g(x) & -f(x) \end{pmatrix}, \quad F = \begin{pmatrix} 0 \\ -1 \end{pmatrix}. \quad (4.2.50)$$

**Lemma 4.2.15** (Exponential Dichotomy Constants and Roughness). *With the notation of Proposition 4.2.14, let*

$$\delta = \sup_{x \in \mathbb{R}} \sqrt{f(x)^2 + g(x)^2} < \frac{1}{4}. \quad (4.2.51)$$

Then we have  $\rho_{aut} = K_{aut} = 1$ ,  $\rho = 1 - 2\delta$ ,  $K = 5/2$  and

$$\|Q(x) - Q_{aut}(x)\| \leq 4\delta, \quad x \in \mathbb{R}. \quad (4.2.52)$$

*Proof.* We have the canonical solution operator  $\Phi(x) = e^{A_0x}$ . The eigenvalues of the matrix  $A_0$  are  $\pm 1$  and the corresponding normed eigenvectors are  $v = \frac{1}{\sqrt{2}}(1, 1)^T$ ,  $w = \frac{1}{\sqrt{2}}(1, -1)^T$ . Thus the fixed point  $Y = (0, 0)^T$  is a saddle. From this it is clear that we can choose

$$P = ww^T = \frac{1}{2} \begin{pmatrix} 1 & -1 \\ -1 & 1 \end{pmatrix}.$$

With the basis transformation matrix  $B = (v \mid w)$  and the diagonal matrix  $D = \text{diag}(1, -1)$  we then get

$$\|\Phi(x)P\Phi^{-1}(s)\| = \|Be^{Dx}B^{-1}PBe^{-Ds}B^{-1}\| = \left\| \begin{pmatrix} 1 & -1 \\ -1 & 1 \end{pmatrix} \right\| \frac{e^{-(x-s)}}{2} = e^{-(x-s)}.$$

A similar reasoning – where one can use that  $I - P = vv^T$  – gives

$$\|\Phi(x)(I - P)\Phi^{-1}(s)\| = e^{(x-s)}.$$

Thus we have the estimate for exponential dichotomies from Definition 4.2.13 with  $\rho_{aut} = 1$  and  $K_{aut} = 1$ . The remaining statements can now be read off Proposition 4.2.14.  $\square$

The roughness of exponential dichotomies established in Lemma 4.2.15 provides a bound on the projection operator  $Q(x)$  of the non-autonomous system. However, this bound cannot be used directly to prove existence of homoclinic solutions using geometric singular perturbation theory, as geometric properties need to be derived. In particular, we need to find the stable and unstable manifolds for the unique bounded solution  $Y_b = (\hat{u}_b, \hat{u}_b)^T$  of (4.2.49). These can be defined as

$$W^s(Y_b) := \{(x, Y^s(x)) \mid Y^s(x) = Y_b(x) + \Phi(x)P\Phi^{-1}(x)r, r \in \mathbb{R}^2\}, \quad (4.2.53)$$

$$W^u(Y_b) := \{(x, Y^u(x)) \mid Y^u(x) = Y_b(x) + \Phi(x)(Id - P)\Phi^{-1}(x)r, r \in \mathbb{R}^2\}, \quad (4.2.54)$$

where  $\Phi, P$  are the solution and projection operator for (4.2.49). For the construction that we have in mind, it is convenient to notice that

$$W^{s/u}(Y_b) = \bigcup_{x \in \mathbb{R}} (x, l^{s/u}(x)), \quad (4.2.55)$$

with lines

$$l^s(x) = \{Y^s(x) \mid Y^s(x) = Y_b(x) + \Phi(x)P\Phi^{-1}(x)r, r \in \mathbb{R}^2\}, \quad (4.2.56)$$

$$l^u(x) = \{Y^u(x) \mid Y^u(x) = Y_b(x) + \Phi(x)(I - P)\Phi^{-1}(x)r, r \in \mathbb{R}^2\}. \quad (4.2.57)$$

**Remark 4.2.16.** *If (4.2.49) possesses the symmetry  $(x, u, p) \rightarrow (-x, u, -p)$  this symmetry carries over to the lines  $l^{s,u}(x)$ . That is, for given  $x \in \mathbb{R}$ , a point  $(u_\circ, p_\circ) \in l^s(x)$  if and only if  $(u_\circ, -p_\circ) \in l^u(-x)$ . The symmetry statement in Proposition 4.2.9 is a direct consequence of this.*

While, in general, it is not possible to find explicit expressions for these objects, we can derive estimates for their locations. For this we first observe that the line  $l^s$  can be written equivalently as

$$l^s(x) = \{(\hat{u}, \hat{p}) \mid \hat{p} - \hat{u}'_b(x) = C(x)(\hat{u} - \hat{u}_b(x))\}, \quad (4.2.58)$$

where  $C(x)$  is the slope of the line. Starting from the bound on the projection operator  $Q(x) = \Phi(x)P\Phi^{-1}(x)$  derived in Lemma 4.2.15, a bound on the projection lines will be established in Lemma 4.2.17, which is then subsequently used to find a bound on the slope  $C(x)$  via the angle  $\theta(x)$  of the line in Lemma 4.2.18.

In particular, for the case of (4.2.30), we thus obtain

$$l^s(x) = \{(\hat{u}, \hat{p}) \mid \hat{p} - \hat{u}'_b(x) = (-1 + \tilde{C}(x))(\hat{u} - \hat{u}_b(x))\}, \quad (4.2.59)$$

with  $\tilde{C}(x)$  as in Lemma (4.2.18) taking into account that the projection operator depends on  $x$ , that is,  $Q = Q(x)$  and so does the angle  $\theta = \theta(x)$ , which defines  $C = C(x)$  and, hence, also  $\tilde{C} = \tilde{C}(x)$ .

The rest of this section consists of the two technical lemmas that ultimately derive a bound for  $\tilde{C}$ .

**Lemma 4.2.17** (Closeness of projection lines). *Let  $Q$  and  $Q_{aut}$  be the projection matrices with rank 1 as defined in Proposition 4.2.14(i), i.e. there are unit vectors  $q$  and  $q_{aut}$  such that  $Q = qq^T$  and  $Q_{aut} = q_{aut}q_{aut}^T$ , and  $\|Q - Q_{aut}\| < 4\delta$  holds true. Then either  $\|q - q_{aut}\| < \sqrt{8\delta}$  or  $\|q + q_{aut}\| < \sqrt{8\delta}$ .*



*Proof.* We prove the equivalent statement that from  $\|q - q_{aut}\| \geq \sqrt{8\delta}$  and  $\|q + q_{aut}\| \geq \sqrt{8\delta}$  it follows that  $\|Q - Q_{aut}\| \geq 4\delta$ . First we observe that

$$\begin{aligned} & (q - q_{aut})(q^T + q_{aut}^T)(q + q_{aut}) \\ &= (qq^T - q_{aut}q_{aut}^T)(q + q_{aut}) + (qq_{aut}^T - q_{aut}q^T)(q + q_{aut}) \\ &= 2(qq^T - q_{aut}q_{aut}^T)(q + q_{aut}) = 2(Q - Q_{aut})(q + q_{aut}). \end{aligned} \quad (4.2.60)$$

Therefore, by assumption

$$\begin{aligned} & \|Q - Q_{aut}\| \|q + q_{aut}\| \geq \|(Q - Q_{aut})(q + q_{aut})\| \\ &= \frac{1}{2} \|(q - q_{aut})(q^T + q_{aut}^T)(q + q_{aut})\| \\ &= \frac{1}{2} \|q + q_{aut}\|^2 \|q - q_{aut}\| \\ &\geq 4\delta \|q + q_{aut}\|, \end{aligned}$$

from which it follows that  $\|Q - Q_{aut}\| \geq 4\delta$ .  $\square$

The previous lemma establishes closeness of projection lines of the autonomous and the non-autonomous case. The thus obtained bounds on norms can be transferred to bounds on the slope  $C$  by use of elementary geometry. Note that transforming the norm bounds in this way leads to singularities when a projection line passes the vertical axis (which also leads to a seemingly disjoint set of admissible slopes). A visualisation of the results of Lemma 4.2.18 are given in Figure 4.7. In particular, the resulting bounds for the slope are shown.

**Lemma 4.2.18** (Closeness of slopes). *Let  $Q$  and  $Q_{aut}$  be projection matrices with rank 1, i.e. there are unit vectors  $q$  and  $q_{aut}$  such that  $Q = qq^T$  and  $Q_{aut} = q_{aut}q_{aut}^T$ , and  $\|Q - Q_{aut}\| < 4\delta$  holds true. Furthermore, let  $\theta, \theta_{aut} \in [-\pi, \pi)$  be defined by  $q = (\cos(\theta), \sin(\theta))$ ,  $q_{aut} = (\cos(\theta_{aut}), \sin(\theta_{aut}))$  such that the slopes of the lines spanned by  $q$  and  $q_{aut}$  are given by*

$$C := \tan(\theta), \quad C_{aut} := \tan(\theta_{aut}). \quad (4.2.61)$$

Then there exist constants  $C_{min/max}(\delta, C_{aut})$  defined by

$$C_{\min}(\delta, C_{aut}) := \begin{cases} -(1 + C_{aut}^2) \frac{2\sqrt{2}\sqrt{\delta}\sqrt{1-2\delta}}{(1-4\delta)+2C_{aut}\sqrt{2}\sqrt{\delta}\sqrt{1-2\delta}}, & \text{if } \delta \neq \frac{1}{4} \left(1 + \frac{C_{aut}}{\sqrt{1+C_{aut}^2}}\right) \\ -\infty, & \text{if } \delta = \frac{1}{4} \left(1 + \frac{C_{aut}}{\sqrt{1+C_{aut}^2}}\right) \end{cases} \quad (4.2.62)$$

$$C_{\max}(\delta, C_{aut}) := \begin{cases} +(1 + C_{aut}^2) \frac{2\sqrt{2}\sqrt{\delta}\sqrt{1-2\delta}}{(1-4\delta)-2C_{aut}\sqrt{2}\sqrt{\delta}\sqrt{1-2\delta}}, & \text{if } \delta \neq \frac{1}{4} \left(1 - \frac{C_{aut}}{\sqrt{1+C_{aut}^2}}\right); \\ +\infty, & \text{if } \delta = \frac{1}{4} \left(1 - \frac{C_{aut}}{\sqrt{1+C_{aut}^2}}\right), \end{cases} \quad (4.2.63)$$

such that  $C - C_{aut} \in \Gamma(\delta, C_{aut})$ , where

$$\Gamma(\delta, C_{aut}) := \begin{cases} (C_{\min}(\delta, C_{aut}), C_{\max}(\delta, C_{aut})), & \text{if } C_{\min}(\delta, C_{aut}) < C_{\max}(\delta, C_{aut}); \\ (-\infty, C_{\max}(\delta, C_{aut})) \cup (C_{\min}(\delta, C_{aut}), +\infty), & \text{if } C_{\max}(\delta, C_{aut}) < C_{\min}(\delta, C_{aut}). \end{cases} \quad (4.2.64)$$

In particular, for  $q_{aut} = \frac{1}{\sqrt{2}}(1, -1)^T$  we have  $C_{aut} = -1$  and, hence,

$$C = -1 + \tilde{C}, \quad \tilde{C} \in \Gamma(\delta, -1). \quad (4.2.65)$$

*Proof.* For technical reasons we assume that  $\|q - q_{aut}\| \leq \|q + q_{aut}\|$ ; if this inequality does not hold, we can scale  $q \rightarrow -q$  without changing the projection matrix  $Q$ . Then, with

$$\Delta\theta := \theta - \theta_{aut}, \quad (4.2.66)$$

we have

$$\begin{aligned} C - C_{aut} &= \tan(\theta) - \tan(\theta_{aut}) \\ &= \tan(\Delta\theta + \theta_{aut}) - \tan(\theta_{aut}) = (1 + C_{aut}^2) \left( \frac{\tan(\Delta\theta)}{1 - C_{aut} \tan(\Delta\theta)} \right). \end{aligned} \quad (4.2.67)$$

From  $\|Q - Q_{aut}\| < 4\delta$  we know by the previous lemma that  $\|q - q_{aut}\| < \sqrt{8\delta}$  and, hence, since  $q$  and  $q_{aut}$  are unit vectors, we have

$$0 \leq 2(1 - q^T q_{aut}) = \|q - q_{aut}\|^2 < 8\delta \quad \implies \quad 1 - 4\delta < q^T q_{aut}. \quad (4.2.68)$$

Since  $\arccos(z)$  is monotonically decreasing, we hence get from  $|\Delta\theta| = \arccos(q^T q_{aut})$  that

$$-\arccos(1 - 4\delta) < \Delta\theta < \arccos(1 - 4\delta). \quad (4.2.69)$$

Furthermore, since  $\frac{\tan(z)}{1 - C_{aut} \tan(z)}$  is monotonically increasing in  $z$ , we have the claimed result by using

$$\tan(\pm \arccos(z)) = \pm \frac{\sqrt{1 - z^2}}{z}$$

and some simplifications in (4.2.67).  $\square$

## 4.2.5 Existence results

Here, we first state our main existence results in detail. Their proofs are given in section 4.2.6.

**Theorem 4.2.19** (Existence for general  $f, g$ ). *Let assumptions (A1)-(A3), (A5), (A6) and (A8) be satisfied. Then there is a  $\mu^*$  with  $0 < \mu^* < \frac{1}{12}$  and corresponding  $\varepsilon^* = \varepsilon^*(\mu) > 0, 0 < \delta^* = \delta^*(\mu) < \frac{2-\sqrt{2}}{8}$  such that the following holds true: For any  $\varepsilon, \mu, \delta$  with*

$$0 < \mu < \mu^*, \quad 0 < \varepsilon < \varepsilon^* = \varepsilon^*(\mu), \quad \delta = \sup_{x \in \mathbb{R}} \sqrt{f(x)^2 + g(x)^2} < \delta^* = \delta^*(\mu), \quad (4.2.70)$$

the stationary wave ODE (4.2.25) has (two) orbits  $(s_p(\xi), u_p(\xi), p_p(\xi), v_p(\xi), q_p(\xi))$ , that are homoclinic to the bounded solution  $\left( \xi, \frac{\hat{u}_b(\varepsilon^2 \mu \xi)}{\mu}, \varepsilon \hat{u}'_b(\varepsilon^2 \mu \xi), 0, 0 \right)$ , with  $(u_p(\xi), v_p(\xi))$  to leading order given by

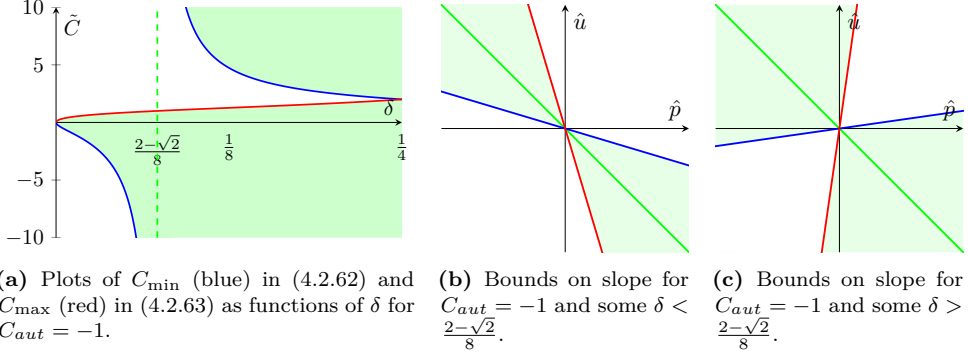


**Figure 4.7** – Visualisation of the results of Lemma 4.2.18. In (a) plots of  $C_{\min}$  (blue) and  $C_{\max}$  (red) are shown as function of  $\delta$  for  $C_{aut} = -1$ , i.e. the set  $\Gamma(\delta, -1)$ . The green region indicates all possible values for the difference between slopes,  $C - C_{aut}$ . In (b) and (c) plots of the possible slopes  $C$  are shown for some  $\delta < \frac{2-\sqrt{2}}{8}$  (b) and  $\delta > \frac{2-\sqrt{2}}{8}$  (c). The green line indicates the slope value  $C_{aut} = -1$ .

$$\begin{aligned} & \left[ \begin{array}{c} \frac{(\hat{u}_b(\varepsilon^2 \mu \xi) - (\hat{u}_b(0) - \mu u_0) \hat{u}_-(\varepsilon^2 \mu \xi))}{\mu} \\ 0 \end{array} \right] \chi_s^-(\xi) + \left[ \begin{array}{c} u_0 \\ \frac{3}{2u_0} \operatorname{sech}\left(\frac{\xi}{2}\right)^2 \end{array} \right] \chi_f(\xi) \\ & + \left[ \begin{array}{c} \frac{(\hat{u}_b(\varepsilon^2 \mu \xi) - (\hat{u}_b(0) - \mu u_0) \hat{u}_+(\varepsilon^2 \mu \xi))}{\mu} \\ 0 \end{array} \right] \chi_s^+(\xi) \end{aligned} \quad (4.2.71)$$

with  $u_0 = u_0^-$  or  $u_0 = u_0^+$  from (4.2.36), i.e.

$$u_0 = \frac{\hat{u}_b(0) - \sqrt{\hat{u}_b(0)^2 + 12\mu/C^s(0)}}{2\mu}; \quad (4.2.72)$$

$\hat{u}_b$  the bounded solution from Proposition 4.2.9 and where the indicator functions

$$\chi_s^-(\xi) = \chi_{(-\infty, -1/\sqrt{\varepsilon})}, \quad \chi_f(\xi) = \chi_{(-1/\sqrt{\varepsilon}, 1/\sqrt{\varepsilon})}, \quad \chi_s^+(\xi) = \chi_{(1/\sqrt{\varepsilon}, \infty)} \quad (4.2.73)$$

distinguishes the behavior of the solution in the fast and super-slow fields. Furthermore, for  $\hat{u}_\pm$  we have the estimates

$$|\hat{u}_\pm(x)| \leq C e^{-(1-2\delta)|x|}, \quad x \geq 0,$$

for some  $C > 0$ , the bounded solution  $u_b$  obeys

$$\sup_{x \in \mathbb{R}} \sqrt{(\hat{u}_b(x) - 1)^2 + \hat{u}_b'(x)^2} \leq \frac{10\delta}{1-2\delta}.$$

Finally, this homoclinic orbit gives rise to a stationary pulse solution

$$\begin{bmatrix} U_p(x, t) \\ V_p(x, t) \end{bmatrix} = \begin{bmatrix} \frac{m\sqrt{m}D}{a} u\left(\frac{\sqrt{m}}{D}x\right) \\ \frac{a}{D\sqrt{m}} v\left(\frac{\sqrt{m}}{D}x\right) \end{bmatrix} \quad (4.2.74)$$

for the Klausmeier model (4.1.2); this pulse solution is biasymptotic to the bounded state  $(a\hat{u}_b(\frac{\sqrt{m}}{D}x), 0)$ .

**Corollary 4.2.20** (Existence for  $f, g = 0$ ). *Let  $f, g = 0$ , and the conditions from Theorem 4.2.19 be fulfilled. Then*

$$\hat{u}_{\pm}(x) = e^{\mp x}, \quad \hat{u}_b \equiv 1.$$

**Corollary 4.2.21** (Existence for small  $f, g$ ). *Let the conditions from Theorem 4.2.19 be fulfilled and assume  $f = \delta \tilde{f}$ ,  $g = \delta \tilde{g}$  where  $\tilde{f}, \tilde{g} = \mathcal{O}(1)$ ,  $0 < \delta \ll 1$  (that is,  $\sup_{x \in \mathbb{R}} \sqrt{\tilde{f}(x)^2 + \tilde{g}(x)^2} = 1$ ). Then*

$$\begin{aligned} \hat{u}_+(x) &= e^{-x} + \frac{\delta}{2} \left[ -e^x \int_x^{\infty} (\tilde{f}(z) - \tilde{g}(z)) e^{-2z} dz \right. \\ &\quad \left. + e^{-x} \left( \int_0^{\infty} (\tilde{f}(z) - \tilde{g}(z)) e^{-2z} dz + \int_0^x (\tilde{f}(z) - \tilde{g}(z)) dz \right) \right] + h.o.t. \\ \hat{u}_-(x) &= e^x + \frac{\delta}{2} \left[ e^{-x} \int_{-\infty}^x (\tilde{f}(z) + \tilde{g}(z)) e^{-2z} dz \right. \\ &\quad \left. - e^{-x} \left( \int_{-\infty}^0 (\tilde{f}(z) + \tilde{g}(z)) e^{-2z} dz + \int_0^x (\tilde{f}(z) + \tilde{g}(z)) dz \right) \right] + h.o.t., \\ \hat{u}_b(x) &= 1 + \frac{\delta}{2} \left[ e^x \int_x^{\infty} \tilde{g}(z) e^{-z} dz + e^{-x} \int_{-\infty}^x \tilde{g}(z) e^z dz \right] + h.o.t.. \end{aligned}$$

Moreover,  $u_0$  as in (4.2.72) can be expressed in terms of  $\delta$  as

$$u_0 = u_{00} + \delta u_{01} + h.o.t., \quad (4.2.75)$$

where  $u_{00}$  corresponds to the  $u_0$ -value for the autonomous case, i.e.  $u_{00}$  is given by (4.2.22).

**Corollary 4.2.22** (Existence for  $h(x) = -2 \ln \cosh(\beta x)$ ). *Let the conditions from Theorem 4.2.19 be fulfilled and let  $h(x) = -2 \ln \cosh(\beta x)$ ,  $\beta > 0$ ,  $f = h'$ ,  $g = h''$ . Then*

$$\begin{aligned} \hat{u}_{\pm}(x) &= e^{\mp \sqrt{1+\beta^2} x} \cosh(\beta x), \\ \hat{u}_b(x) &= \frac{u_-(x)}{2\sqrt{1+\beta^2}} \int_x^{\infty} e^{-\sqrt{1+\beta^2} z} \operatorname{sech}(\beta z) dz \\ &\quad + \frac{u_+(x)}{2\sqrt{1+\beta^2}} \int_{-\infty}^x e^{\sqrt{1+\beta^2} z} \operatorname{sech}(\beta z) dz. \end{aligned}$$

**Remark 4.2.23.** *Pulses solutions as in Corollary 4.2.22 exist for any  $\beta > 0$  without the need of the general assumption on  $\delta$  as in Theorem 4.2.19; since the flow on  $\mathcal{M}$  can be solved explicitly for these functions  $f$  and  $g$ , no condition on  $\delta$  is needed.*

**Remark 4.2.24.** *Since the flow on  $\mathcal{M}$  can be solved explicitly for the functions  $f$  and  $g$  as in Corollary 4.2.22, it is also possible to prove existence of symmetric, stationary 2-pulse solutions (and, in fact, any symmetric, stationary  $N$ -pulse solution). Note that normally, for  $f, g \equiv 0$ , these do not exist, since pulses in (4.1.2) repel each other [8, 45]; this repulsive force can only be overcome by driving forces due to the spatially varying functions  $f$  and  $g$ . We come back to these multi-pulse solutions in section 4.4.5.*

## 4.2.6 Proof of existence results

The proofs of the existence results in section 4.2.5 follow from the theory developed in the preceding sections. The heart of these proofs is formed by Proposition 4.2.11 and the bounds on the bounded solution  $u_b$  and the slopes  $C^{s/u}$  as found in Proposition 4.2.9. Ultimately, it boils down to taking  $\delta$  small enough such that an intersection between  $l^s(0)$  and  $T_o(0)$  is guaranteed. A sketch of this idea is given in Figure 4.3; the rest of this section is devoted to the rigorous proof of the existence theorem and the corollaries in section 4.2.5.

*Proof of Theorem 4.2.19.* Existence of the homoclinic orbits is established by Proposition 4.2.11 if the conditions in Proposition 4.2.11(4) are satisfied. Since  $u_b(0) = \hat{u}_b(0)/\mu$ , these hold if and only if the following three bounds hold true:

- (i)  $\hat{u}_b(0) > 0$ ;
- (ii)  $C^s(0) < 0$ ;
- (iii)  $\hat{u}_b(0)^2 + 12\mu/C^s(0) > 0$ .

By Proposition 4.2.14 and Lemma 4.2.15, we have

$$\hat{u}_b(0) > \frac{1 - 12\delta}{1 - 2\delta}, \quad (4.2.76)$$

and by Lemma 4.2.18 we have

$$C^s(0) = -1 + \tilde{C}, \quad \tilde{C} \in \Gamma(\delta, -1), \quad (4.2.77)$$

where  $\Gamma$  is as in (4.2.64). Using these, bound (i) is satisfied when  $\delta < \frac{1}{12}$  and bound (ii) when  $\delta < \frac{2-\sqrt{2}}{8}$ . Since the bound (iii) holds true when  $\delta = 0$  and  $\mu < \frac{1}{12}$ , continuity of mentioned bounds on  $\hat{u}_b(0)$  and  $C^s(0)$  guarantees the existence of the critical value  $0 < \delta^*(\mu) < \frac{2-\sqrt{2}}{8}$ .  $\square$

*Proof of Corollary 4.2.20.* This follows immediately from solving (4.2.30) with  $f, g \equiv 0$ , and is also carried out in more detail in section 4.2.1.  $\square$

*Proof of Corollary 4.2.21.* The super-slow system on  $\mathcal{M}$  in (4.2.30) can be solved using a regular expansion in  $0 < \delta \ll 1$ . By requiring that  $\lim_{x \rightarrow \infty} \hat{u}_+(x)$  and  $\lim_{x \rightarrow -\infty} \hat{u}_-(x)$  exist, the results follow by a straightforward calculation.  $\square$

*Proof of Corollary 4.2.22.* One can easily verify that  $\hat{u}_\pm$  solve (4.2.30), and that we have  $\lim_{x \rightarrow \pm\infty} \hat{u}_\pm(x) = 0$ . The bounded solution  $\hat{u}_b$  follows from a standard variation of constants method.  $\square$

## 4.3 Linear stability analysis

In the previous section, we proved the existence of stationary 1-pulse solutions to (4.1.2). In this section we study the linear stability of these solutions. For  $(U_p, V_p)$  a pulse solution from Theorem 4.2.19 we define the linear operator

$$\mathcal{L} \begin{pmatrix} \bar{U} \\ \bar{V} \end{pmatrix} = \begin{pmatrix} \partial_x^2 \bar{U} + f(x) \partial_x \bar{U} + g(x) \bar{U} - \bar{U} - V_p^2 \bar{U} - 2U_p V_p \bar{V} \\ D^2 \partial_x^2 \bar{V} - m \bar{V} + V_p^2 \bar{U} + 2U_p V_p \bar{V} \end{pmatrix}, \quad (4.3.1)$$

with  $\mathcal{L} : H^2(\mathbb{R}) \times H^2(\mathbb{R}) \subset L^2(\mathbb{R}) \times L^2(\mathbb{R}) \rightarrow L^2(\mathbb{R}) \times L^2(\mathbb{R})$  and its spectrum by  $\Sigma(\mathcal{L})$ , where we distinguish between the point spectrum  $\Sigma_{\text{pt}}(\mathcal{L})$  and the essential spectrum  $\Sigma_{\text{ess}}(\mathcal{L}) = \Sigma(\mathcal{L}) \setminus \Sigma_{\text{pt}}(\mathcal{L})$  – we denote the elements of  $\Sigma_{\text{ess}}(\mathcal{L})$  by  $\underline{\lambda}$ . As customary, we say that  $(U_p, V_p)$  is linearly stable if there is no spectrum in the right half plane. In order to keep the exposition at reasonable length, we will concentrate here on characterizing parameter regimes where the only instability that can occur is through the (translational) zero eigenvalue which starts moving due to the introduction of spatially varying  $f$  and/or  $g$ . In particular, there are no essential instabilities:

**Lemma 4.3.1** (Essential spectrum). *Let the conditions of Theorem 4.2.19 and assumption (A7) be fulfilled, and let  $(U_p, V_p)$  be a pulse solution to (4.1.2) as in Theorem 4.2.19. Then the essential spectrum of  $\mathcal{L}$  from (4.3.1) is*

$$\Sigma_{\text{ess}}(\mathcal{L}) = (-\infty, \max\{-m, -1\}], \quad (4.3.2)$$

and, hence, lies in the left half-plane.

*Proof.* The limiting operator of  $\mathcal{L}$  at  $x \rightarrow \pm\infty$  is  $\mathcal{L}_\infty := \text{diag}[\partial_x^2 - 1, D^2\partial_x^2 - m]$  (note that we thus explicitly use assumption (A7)). Therefore, we have that the boundaries of the essential spectrum are  $\underline{\lambda}_1(k) = -(k^2 + 1)$ ,  $\underline{\lambda}_2(k) = -(D^2k^2 + m)$ ,  $k \in \mathbb{R}$ , which immediately gives the claimed result.  $\square$

The assumptions on  $f, g$  allow (again through the use of exponential dichotomies) the derivation of bounds on the location of the point spectrum, which, under the assumption that  $f, g$  are chosen ‘small’, can be further refined to track the one small eigenvalue that can possibly lead to bifurcations. The proof of the following statements will be the subject of the next sections.

**Theorem 4.3.2** (Point spectrum). *Let the conditions of Theorem 4.2.19 and assumptions (A4) and (A7) be fulfilled, and let  $(U_p, V_p)$  be a pulse solution to (4.1.2) with  $u_0 = u_0^-$  as in (4.2.72). Then there exist constants  $m_c, \mu^*, \nu^* > 0$  such that if either (i)  $m < m_c$  and  $\mu < \mu^*$  or (ii)  $m > m_c$  and  $\mu\sqrt{m} < \nu^*$ , then there exists a  $\delta_c > 0$  such that if  $0 \leq \delta < \delta_c$  precisely one eigenvalue  $\underline{\lambda}_0$  is  $\mathcal{O}(\varepsilon)$ -close to 0 and all other eigenvalues of  $\mathcal{L}$  lie in the left-half plane.*

*Proof.* The statement is demonstrated in section 4.3.1 by combining the setup of an Evans function and the theory of exponential dichotomies.  $\square$

**Remark 4.3.3.** *Note that Theorem 4.3.2 only holds for pulse solutions with  $u_0 = u_0^-$ ; pulse solutions with  $u_0 = u_0^+$  are always unstable. See also Remark 4.3.16.*

**Remark 4.3.4.** *The constants  $m_c, \mu^*$  and  $\nu^*$  in Theorem 4.3.2 can be computed explicitly (see Lemma 4.3.14).*

**Theorem 4.3.5** (Small eigenvalue close to  $\underline{\lambda} = 0$  for small  $f, g$ ). *Assuming that  $f = \delta\tilde{f}$ ,  $g = \delta\tilde{g}$  with  $0 < \delta \ll 1$ ,  $\tilde{f}, \tilde{g} = \mathcal{O}(1)$  (i.e.  $\sup_{x \in \mathbb{R}} \sqrt{\tilde{f}(x)^2 + \tilde{g}(x)^2} = 1$ ), there exists a constant  $\tau^* > 0$  such that if  $\tau := \varepsilon^4 \mu m < \tau^*$  the small eigenvalue  $\underline{\lambda}_0$  close to  $\underline{\lambda} = 0$  is located, to leading order, at*

$$\underline{\lambda}_0 = \frac{2\tau\delta}{u_0 - \tau(1 - \mu u_0)} \int_0^{+\infty} e^{-2x} \left( \tilde{f}'(x)(1 - \mu u_0) + \tilde{g}'(x)[e^x + \mu u_0 - 1] \right) dx, \quad (4.3.3)$$

where  $u_0$  is as in (4.2.72) and Corollary 4.2.21.

*Proof.* This statement is derived in section 4.3.2 by employing a regular expansion in  $\delta$ .  $\square$

**Corollary 4.3.6.** *Let the conditions of Theorem 4.3.5 be fulfilled. Then, in the double asymptotic limit  $\mu \ll 1$  and  $\tau := \varepsilon^4 \mu m \ll 1$  the leading order expression for  $\lambda_0$  becomes*

$$\lambda_0 = \frac{2}{3} \tau \delta \int_0^\infty e^{-2x} \left( \tilde{f}'(x) + \tilde{g}'(x)[e^x - 1] \right) dx. \quad (4.3.4)$$

**Remark 4.3.7.** *When the term  $\tau = \varepsilon^4 \mu m = \frac{a^2 D}{m \sqrt{m}}$  in (4.3.3) becomes too large (larger than  $\tau^*$ ), the pulse becomes unstable due to a traveling wave bifurcation/drift instability [28, 46].*

### 4.3.1 Qualitative description of the point spectrum location (Proof of Theorem 4.3.2)

This section is devoted to finding the point spectrum of the operator  $\mathcal{L}$ . For that, we use a decomposition method for the Evans function, first developed in [1, 48], which is supplemented by the theory of exponential dichotomies to treat the varying coefficients in (4.1.2). As before, the following computations will again heavily rely on the singularly perturbed structure. Therefore, we introduce for the eigenvalue problem  $(\mathcal{L} - \lambda I)(\bar{U}, \bar{V})^T = 0$ , that is,

$$\begin{cases} \lambda \bar{U} &= \frac{d^2}{dx^2} \bar{U} + f(x) \frac{d}{dx} \bar{U} + g(x) \bar{U} - \bar{U} - V_p^2 \bar{U} - 2U_p V_p \bar{V}, \\ \frac{1}{m} \lambda \bar{V} &= \frac{D^2}{m} \frac{d^2}{dx^2} \bar{V} - \bar{V} + \frac{1}{m} V_p^2 \bar{U} + \frac{2}{m} U_p V_p \bar{V}, \end{cases} \quad (4.3.5)$$

and the scalings (analogous to (4.2.1) and (4.2.3))

$$\xi = \frac{D}{\sqrt{m}} = \varepsilon^2 \mu x, \quad \bar{U} = m \varepsilon \mu \bar{u}, \quad U_p = m \varepsilon \mu u_p, \quad \bar{V} = \frac{1}{\varepsilon \mu} \bar{v}, \quad V_p = \frac{1}{\varepsilon \mu} v_p, \quad (4.3.6)$$

to get the fast eigenvalue problem

$$\begin{cases} \varepsilon^4 \mu^2 \lambda \bar{u} &= \ddot{u} - \varepsilon^2 [2u_p v_p \bar{v} + v_p^2 \bar{u}] - \varepsilon^4 \mu^2 \bar{u} + \varepsilon^2 \mu f(\varepsilon^2 \mu \xi) \dot{u} + \varepsilon^4 \mu^2 g(\varepsilon^2 \mu \xi) \bar{u}, \\ \frac{1}{m} \lambda \bar{v} &= \ddot{v} - \bar{v} + [2u_p v_p \bar{v} + v_p^2 \bar{u}], \end{cases} \quad (4.3.7)$$

which suggests (just as in [8, 28, 46]) the introduction of the scaled eigenvalue parameter

$$\underline{\lambda} = m \lambda, \quad (4.3.8)$$

so, finally,

$$\begin{cases} \varepsilon^4 \mu^2 m \lambda \bar{u} &= \ddot{u} - \varepsilon^2 [2u_p v_p \bar{v} + v_p^2 \bar{u}] - \varepsilon^4 \mu^2 \bar{u} + \varepsilon^2 \mu f(\varepsilon^2 \mu \xi) \dot{u} + \varepsilon^4 \mu^2 g(\varepsilon^2 \mu \xi) \bar{u}, \\ \lambda \bar{v} &= \ddot{v} - \bar{v} + [2u_p v_p \bar{v} + v_p^2 \bar{u}]. \end{cases} \quad (4.3.9)$$

It is convenient to introduce  $\phi := (\bar{u}, \dot{\bar{u}}/(\varepsilon^2 \mu), \bar{v}, \dot{\bar{v}})$  and to write the above ODEs as the system of first order ODEs

$$\dot{\phi} = A(\xi; \lambda, \varepsilon, \mu, m) \phi, \quad (4.3.10)$$

where

$$A(\xi; \lambda, \varepsilon, \mu, m) = \begin{pmatrix} 0 & \varepsilon^2 \mu & 0 & 0 \\ v_p^2/\mu + \varepsilon^2 \mu [1 + m\lambda - g(\varepsilon^2 \mu \xi)] & -\varepsilon^2 \mu f(\varepsilon^2 \mu \xi) & 2u_p v_p/\mu & 0 \\ 0 & 0 & 0 & 1 \\ -v_p^2 & 0 & 1 + \lambda - 2u_p v_p & 0 \end{pmatrix}. \quad (4.3.11)$$

From the existence analysis in section 4.2, we have seen that the real line  $\mathbb{R}$  can be split in one fast region,  $I_f$ , near the pulse location and two super slow fields  $I_s^\pm$  to both sides of the fast field:

$$I_s^- := \left(-\infty, -\frac{1}{\sqrt{\varepsilon}}\right), \quad I_f := \left[-\frac{1}{\sqrt{\varepsilon}}, \frac{1}{\sqrt{\varepsilon}}\right], \quad I_s^+ := \left(\frac{1}{\sqrt{\varepsilon}}, \infty\right).$$

Since we know that  $v_p$  vanished to leading order in the slow fields, we have in those regions the system matrix

$$A_s(\xi; \lambda, \varepsilon, \mu, m) := \begin{pmatrix} 0 & \varepsilon^2 \mu & 0 & 0 \\ \varepsilon^2 \mu [1 + m\lambda - g(\varepsilon^2 \mu \xi)] & -\varepsilon^2 \mu f(\varepsilon^2 \mu \xi) & 0 & 0 \\ 0 & 0 & 0 & 1 \\ 0 & 0 & 1 + \lambda & 0 \end{pmatrix}, \quad (4.3.12)$$

that is, the dynamics for slow and fast variables are decoupled. Any value  $\lambda \in \mathbb{C}$  for which this system of ODEs has a non-trivial solution in  $L^2(\mathbb{R}) \times L^2(\mathbb{R})$  corresponds to an eigenvalue  $\underline{\lambda} = m\lambda$  of  $\mathcal{L}$ . A mechanism (that is by now standard) for detecting eigenvalues is the construction of an Evans function, whose roots coincide with the eigenvalues of  $\mathcal{L}$ . Although the Evans function can also be extended into the essential spectrum, we do not need this in the present work and rather restrict  $\lambda$  to

$$\mathcal{C}_e := \mathbb{C} \setminus \{\lambda \in \mathbb{R} : \lambda \leq \max\{-1, -1/m\}\} = \left\{ \lambda = \frac{\underline{\lambda}}{m} : \underline{\lambda} \notin \Sigma_{\text{ess}}(\mathcal{L}) \right\}, \quad (4.3.13)$$

on which the Evans function is analytic.

### Evans function construction

By (conditions and results of) Theorem 4.2.19 and assumption (A7), we know that the limiting matrix for  $|\xi| \rightarrow \infty$  is given by

$$A_\infty(\lambda, \varepsilon, \mu, m) := \begin{pmatrix} 0 & \varepsilon^2 \mu & 0 & 0 \\ \varepsilon^2 \mu [1 + m\lambda] & 0 & 0 & 0 \\ 0 & 0 & 0 & 1 \\ 0 & 0 & 1 + \lambda & 0 \end{pmatrix}. \quad (4.3.14)$$

Its eigenvalues  $\Lambda_{1,2,3,4}$  and eigenvectors  $E_{1,2,3,4}$  are

$$\begin{aligned} \Lambda_{1,4}(\lambda) &= \pm\sqrt{1 + \lambda}, & \Lambda_{2,3}(\lambda) &= \pm\varepsilon^2 \mu \sqrt{1 + m\lambda} \\ E_{1,4}(\lambda) &= (0, 0, 1, \Lambda_{1,4})^T, & E_{2,3}(\lambda) &= (1, \pm\sqrt{1 + m\lambda}, 0, 0)^T. \end{aligned} \quad (4.3.15)$$

where  $\text{Re}(\Lambda_1(\lambda)) < \text{Re}(\Lambda_2(\lambda)) < 0 < \text{Re}(\Lambda_3(\lambda)) < \text{Re}(\Lambda_4(\lambda))$  for  $\lambda \in \mathcal{C}_e$ .

The system  $\dot{\phi}_\infty = A_\infty(\lambda, \varepsilon, \mu, m)\phi_\infty$  admits exponential dichotomies on  $\mathcal{C}_e$ . Since  $A_\infty$  is exponentially close to  $A$  for large  $|\xi|$ , the stable and unstable subspaces of  $\dot{\phi} = A(\xi; \lambda, \varepsilon, \mu, m)\phi$  and  $\dot{\phi}_\infty = A_\infty(\lambda, \varepsilon, \mu, m)\phi_\infty$  are similar when  $|\xi| \rightarrow \infty$ . In



particular, for all  $\lambda \in \mathcal{C}_e$  there is a two-dimensional family of solutions,  $\Phi_{\infty}^{-}(\lambda)$ , to  $\dot{\phi}_{\infty} = A_{\infty}(\lambda, \varepsilon, \mu, m)\phi_{\infty}$  such that  $\lim_{\xi \rightarrow -\infty} \phi_{\infty}^{-}(\xi) = 0$  for all  $\phi_{\infty}^{-} \in \Phi_{\infty}^{-}(\lambda)$ , and a two-dimensional family of solutions,  $\Phi_{\infty}^{+}(\lambda)$ , to  $\dot{\phi}_{\infty} = A_{\infty}(\lambda, \varepsilon, \mu, m)\phi_{\infty}$  such that  $\lim_{\xi \rightarrow \infty} \phi_{\infty}^{+}(\xi) = 0$  for all  $\phi_{\infty}^{+} \in \Phi_{\infty}^{+}(\lambda)$ , which implies that the system  $\dot{\phi} = A(\xi; \lambda, \varepsilon, \mu, m)\phi$  also possesses two two-dimensional families of solutions,  $\Phi^{-}(\lambda)$  and  $\Phi^{+}(\lambda)$  with the same properties.

For the system  $\dot{\phi} = A(\xi; \lambda, \varepsilon, \mu, m)\phi$ , however, it is possible that the intersection  $\Phi^{+}(\lambda) \cap \Phi^{-}(\lambda)$  is nonempty. The values  $\lambda \in \mathcal{C}_e$  for which this happens correspond to  $\underline{\lambda} = m\lambda$  in the point spectrum  $\Sigma_{\text{pt}}$ . To find these, we use a Evans function [1, 48], which is defined as

$$\mathcal{D}(\lambda) = \det [\phi_1(0; \lambda), \phi_2(0; \lambda), \phi_3(0; \lambda), \phi_4(0; \lambda)] , \quad (4.3.16)$$

where  $\{\phi_1(\cdot; \lambda), \phi_2(\cdot; \lambda)\}$  spans the space  $\Phi^{-}(\lambda)$  and  $\{\phi_3(\cdot; \lambda), \phi_4(\cdot; \lambda)\}$  spans the space  $\Phi^{+}(\lambda)$ . For notational clarity we have suppressed the dependence on the other parameters. Essentially, the Evans function  $\mathcal{D}(\lambda)$  measures the linear independence of the solution functions  $\phi_{1,\dots,4}$ . Therefore, zeros of  $\mathcal{D}(\lambda)$  correspond to values of  $\lambda$  for which  $\Phi^{+}(\lambda) \cap \Phi^{-}(\lambda) \neq \emptyset$ , and thus to eigenvalues in the point spectrum [1].

In (4.3.16) the solutions  $\phi_{1,\dots,4}$  are not uniquely defined, and any choice leads to the same eigenvalues. However, for singularly perturbed partial differential equations a specific choice enables the use of the scale separation in these equations, which in turn makes it possible to determine the eigenvalues.

**Lemma 4.3.8.** *Let the conditions of Theorem 4.2.19 be fulfilled and let  $(U_p, V_p)$  be a pulse solution to (4.1.2) as in Theorem 4.2.19. Then all eigenvalues  $\lambda \in \Sigma_{\text{pt}}$  associated to (4.3.9) are roots of the Evans function*

$$\mathcal{D}(\lambda) = t_{11}(\lambda)t_{22}(\lambda)(1 + m\lambda)(1 + \lambda) \exp \left( \int_0^{\infty} f(x) dx \right) , \quad (4.3.17)$$

where  $t_{11}$  and  $t_{22}$  are analytic (transmission) functions of  $\lambda$ , defined by

$$\lim_{\xi \rightarrow \infty} \phi_1(\xi; \lambda)e^{-\Lambda_1(\lambda)\xi} = t_{11}E_1; \quad (4.3.18)$$

$$\lim_{\xi \rightarrow \infty} \phi_2(\xi; \lambda)e^{-\Lambda_2(\lambda)\xi} = t_{22}E_2, \quad (4.3.19)$$

where  $\phi_1$  is the (unique) solution to (4.3.10) for which

$$\lim_{t \rightarrow -\infty} \phi_1(\xi; \lambda)e^{-\Lambda_1(\lambda)\xi} = E_1; \quad (4.3.20)$$

and  $\phi_2$  is the (unique) solution to (4.3.10) (if  $t_{11}(\lambda) \neq 0$ ) for which

$$\lim_{t \rightarrow -\infty} \phi_2(\xi; \lambda)e^{-\Lambda_2(\lambda)\xi} = E_2; \quad (4.3.21)$$

$$\lim_{t \rightarrow \infty} \phi_2(\xi; \lambda)e^{\Lambda_1(\lambda)\xi} = 0 \quad (4.3.22)$$

*Proof.* The proof is heavily based on [48, section 3.2]. Therefore, we present here only an outline of the proof and refer the interested reader to [48] for more details.

The heart of the proof is based on choosing  $\phi_{1,\dots,4}$  in such way that the scale separation of (4.1.2) can be exploited. Because  $A$  and  $A_{\infty}$  are exponentially close when  $\xi \rightarrow -\infty$ , there is a unique solution  $\phi_1$  such that  $\phi_1$  closely follows  $E_1(\lambda)e^{\Lambda_1(\lambda)\xi}$  as

$\xi \rightarrow -\infty$ . More precisely, we define  $\phi_1$  uniquely such that  $\lim_{\xi \rightarrow -\infty} \phi_1(\xi; \lambda) e^{-\Lambda_1(\lambda)\xi} = E_1(\lambda)$ . For  $\xi \rightarrow \infty$ , we do not know the precise form of  $\phi_1$ , but we do know that, asymptotically, it is a combination of the eigenfunctions of the system  $\dot{\phi}_\infty = A_\infty \phi_\infty$ . That is,  $\phi_1(\xi; \lambda) \rightarrow t_{11}(\lambda)E_1 e^{\Lambda_1(\lambda)\xi} + t_{12}(\lambda)E_2 e^{\Lambda_2(\lambda)\xi} + t_{13}(\lambda)E_3 e^{\Lambda_3(\lambda)\xi} + t_{14}(\lambda)E_4 e^{\Lambda_4(\lambda)\xi}$  as  $\xi \rightarrow \infty$ , where  $t_{11}, \dots, t_{14}$  are analytic transmission functions.

Next,  $\phi_2$  must be chosen such that  $\{\phi_1(\cdot, \lambda), \phi_2(\cdot, \lambda)\}$  spans  $\Phi^-(\lambda)$ . As this does not determine  $\phi_2$  uniquely, we may, additionally, require that  $\phi_2$  grows, at most, as  $E_2(\lambda)e^{\Lambda_2(\lambda)\xi}$  for  $\xi \rightarrow \infty$ . More precisely, we define  $\phi_2$  uniquely such that we have  $\lim_{\xi \rightarrow -\infty} \phi_2(\xi; \lambda) e^{-\Lambda_2(\lambda)\xi} = E_2$  and  $\lim_{\xi \rightarrow +\infty} \phi_2(\xi; \lambda) e^{-\Lambda_1(\lambda)\xi} = 0$  (note that this construction is based on insight in  $t_{11}$  – that may not be 0 – that is obtained by the ‘elephant trunk procedure’, see [48, 65] and Remark 4.3.18). For  $\xi \rightarrow \infty$ ,  $\phi_2$  is then asymptotically given by  $\phi_2(\xi; \lambda) \rightarrow t_{22}(\lambda)E_2(\lambda)e^{\Lambda_2(\lambda)\xi} + t_{23}(\lambda)E_3(\lambda)e^{\Lambda_3(\lambda)\xi} + t_{24}(\lambda)E_4(\lambda)e^{\Lambda_4(\lambda)\xi}$  as  $\xi \rightarrow \infty$ , where  $t_{21}, t_{23}, t_{24}$  are analytical transmission functions.

In a similar vein the solutions  $\phi_3$  and  $\phi_4$  can be defined in such a way that  $\lim_{\xi \rightarrow \infty} \phi_4(\xi; \lambda) e^{-\Lambda_4(\lambda)\xi} = E_4(\lambda)$  and  $\lim_{\xi \rightarrow \infty} \phi_3(\xi; \lambda) e^{-\Lambda_3(\lambda)\xi} = E_3(\lambda)$ .

Then, using that  $\sum_{j=1}^4 \Lambda_j(\lambda) = 0$  and by Liouville’s formula, the Evans function (4.3.16) can be rewritten:

$$\begin{aligned} \mathcal{D}(\lambda) &= \lim_{\xi \rightarrow \infty} \det [\phi_1(\xi; \lambda), \phi_2(\xi; \lambda), \phi_3(\xi; \lambda), \phi_4(\xi; \lambda)] \exp \left( - \int_0^\xi \text{Tr} A(z) dz \right) \\ &= \lim_{\xi \rightarrow \infty} \det \left[ \phi_1(\xi; \lambda) e^{-\Lambda_1(\lambda)\xi}, \phi_2(\xi; \lambda) e^{-\Lambda_2(\lambda)\xi}, \phi_3(\xi; \lambda) e^{-\Lambda_3(\lambda)\xi}, \phi_4(\xi; \lambda) e^{-\Lambda_4(\lambda)\xi} \right] \\ &\quad \times \exp \left( - \int_0^\xi \text{Tr} A(z) dz \right) \\ &= \det [t_{11}(\lambda)E_1(\lambda), t_{22}(\lambda)E_2(\lambda), E_3(\lambda), E_4(\lambda)] \exp \left( \int_0^\infty f(x) dx \right) \\ &= t_{11}(\lambda)t_{22}(\lambda)(1+m\lambda)(1+\lambda) \exp \left( \int_0^\infty f(x) dx \right). \end{aligned}$$

□

The roots  $\lambda \in \mathcal{C}_e$  of  $\mathcal{D}(\lambda)$  thus correspond to the roots of  $t_{11}(\lambda)t_{22}(\lambda)$ . The next goal, therefore, is to determine the roots of these transmission functions.

### Fast transmission function $t_{11}$

The transmission function  $t_{11}$  is closely related to the linearization around the pulse in the fast field,

$$(\mathcal{L}^r - \lambda)v = 0, \quad \mathcal{L}^r v := \partial_\xi^2 v - [1 - 3 \text{sech}(\xi/2)^2]v. \quad (4.3.23)$$

The eigenvalues of  $\mathcal{L}^r$  are well-known to be  $\lambda_0^r = 5/4$ ,  $\lambda_1^r = 0$  and  $\lambda_2^r = -3/4$ . By a standard winding number argument, it follows that roots of  $t_{11}$  lie  $\mathcal{O}(\varepsilon)$ -close to these eigenvalues  $\lambda_0^r$ ,  $\lambda_1^r$  and  $\lambda_2^r$ .

**Lemma 4.3.9** (Properties of  $t_{11}$ ). *Let the conditions of Proposition 4.3.8 be fulfilled. The roots of  $t_{11}$  lie  $\mathcal{O}(\varepsilon)$  close to the eigenvalues (counting multiplicity) of  $\mathcal{L}^r$ , i.e. close to  $\lambda_0^r = 5/4$ ,  $\lambda_1^r = 0$  and  $\lambda_2^r = -3/4$ .*

*Proof.* See [48, Lemma 4.1].  $\square$

Although  $t_{11}$  has a root (with multiplicity 1) close to  $\lambda_0^r = 5/4$ , this does not mean that  $\mathcal{D}(\lambda)$  has a root for the same value of  $\lambda$ , since – as will be discussed in the next section – the transmission function  $t_{22}$  has a pole of order 1 for the same  $\lambda$ , thus preventing it from being an eigenvalue of  $\mathcal{L}$  – in the literature, this is known as the ‘NLEP paradox’.

In studies of autonomous systems, the root of  $t_{11}$  close to  $\lambda = 0$  is actually located precisely at  $\lambda = 0$  because of the translation invariance of those autonomous systems. However, (4.1.2) is non-autonomous and therefore this reasoning no longer holds and the eigenvalue close to  $\lambda_1^r = 0$  can have negative or positive real part. As  $t_{22}$  does *not* have a pole for this  $\lambda$  – as will be discussed in the next section – the Evans function  $\mathcal{D}(\lambda)$  has a root for this value; it thus corresponds to an eigenvalue of  $\mathcal{L}$ . To our best knowledge, it is, in general, not possible to determine the precise location of this eigenvalue; in section 4.3.2 we compute its location using standard regular perturbation techniques when the non-autonomous terms are small.

### Slow transmission function $t_{22}$

To determine the transmission function  $t_{22}$ , we focus on the function  $\phi_2$ , as defined in Proposition 4.3.8. Per construction, we know that  $\phi_2(\xi; \lambda) \rightarrow t_{22}(\lambda)E_2(\lambda)e^{\Lambda_2(\lambda)\xi} + t_{23}(\lambda)E_3(\lambda)e^{\Lambda_3(\lambda)\xi} + t_{24}(\lambda)e^{\Lambda_4(\lambda)\xi}$  as  $\xi \rightarrow \infty$ . As  $|\Lambda_4(\lambda)| \gg |\Lambda_{2,3}(\lambda)|$  for  $\lambda \in \mathcal{C}_e$ , the term  $e^{\Lambda_4(\lambda)\xi}$  is exponentially small in the slow fields  $I_s^\pm$ . Therefore, we have that  $\phi_2(\xi; \lambda) \approx t_{22}(\lambda)E_2(\lambda)e^{\Lambda_2(\lambda)\xi} + t_{23}(\lambda)E_3(\lambda)e^{\Lambda_3(\lambda)\xi}$  for  $\xi \in I_s^+$  sufficiently large. In this way,  $\phi_2$  in the slow fields is related to the properties of the exponentially asymptotic constant-coefficient system  $\dot{\phi}_\infty = A_\infty(\lambda, \varepsilon, \mu, m)\phi_\infty$ . However, we need to relate  $\phi_2$  in the slow fields to the exponentially asymptotic non-autonomous system  $\dot{\phi}_s = A_s(\xi; \lambda, \varepsilon, \mu, m)\phi_s$  to determine  $t_{22}$ .

In the slow fields the system  $\dot{\phi}_s = A_s(\xi; \lambda, \varepsilon, \mu, m)\phi_s$  has the dynamics for the  $(\bar{u}, \bar{p})$  part completely separated from the dynamics of the  $(\bar{v}, \bar{q})$  part. The  $(\bar{u}, \bar{p})$  part is governed by the non-autonomous ODE

$$\begin{pmatrix} \dot{\bar{u}} \\ \dot{\bar{p}} \end{pmatrix} = \varepsilon^2 \mu [B_0(\lambda) + B_1(\xi)] \begin{pmatrix} \bar{u} \\ \bar{p} \end{pmatrix}, \quad (4.3.24)$$

where

$$B_0(\lambda) = \begin{pmatrix} 0 & 1 \\ 1 + m\lambda & 0 \end{pmatrix}; \quad B_1(\xi) = \begin{pmatrix} 0 & 0 \\ -g(\varepsilon^2 \mu \xi) & -f(\varepsilon^2 \mu \xi) \end{pmatrix}.$$

Here, only the matrix  $B_1$  carries the non-autonomous part of the differential equation and the system without  $B_1$  corresponds to the  $(\bar{u}, \bar{p})$  part of the system  $\dot{\phi}_\infty = A_\infty(\lambda, \varepsilon, \mu, m)\phi_\infty$ , which has spatial eigenvalues  $\Lambda_{2,3} = \pm \varepsilon^2 \mu \sqrt{1 + m\lambda}$ . When  $\lambda \in \mathcal{C}_e$  this autonomous system admits an exponential dichotomy on  $\mathbb{R}$  and, therefore, by roughness the non-autonomous system (4.3.24) does so as well, provided that  $\delta = \sup_{x \in \mathbb{R}} \sqrt{f(x)^2 + g(x)^2} = \sup_{x \in \mathbb{R}} \|B_1(x)\|$  is sufficiently small. Under these conditions, there exist  $\tilde{\psi}_2(\xi; \lambda) = (u_2(\xi; \lambda), p_2(\xi; \lambda), 0, 0)^T$  and  $\tilde{\psi}_3(\xi; \lambda) = (u_3(\xi; \lambda), p_3(\xi; \lambda), 0, 0)^T$  such that  $\tilde{\psi}_2(\xi; \lambda) \rightarrow E_2(\lambda)e^{\Lambda_2(\lambda)\xi}$  and  $\tilde{\psi}_3(\xi; \lambda) \rightarrow E_3(\lambda)e^{\Lambda_3(\lambda)\xi}$  as  $|\xi| \rightarrow \infty$ . The same reasoning as before can now be used to deduce that  $\phi_2(\xi; \lambda) \approx \tilde{\psi}_2(\xi; \lambda)$  for  $\xi \in I_s^-$  and  $\phi_2(\xi; \lambda) \approx t_{22}(\lambda)\tilde{\psi}_2(\xi; \lambda) + t_{23}(\lambda)\tilde{\psi}_3(\xi; \lambda)$  for  $\xi \in I_s^+$ .

To compute  $t_{22}$  we need to track the changes of  $\bar{u}$  and  $\bar{p}$  during the fast transition when  $\xi \in I_f$ . From (4.3.9), it follows that  $\bar{u}$  stays constant to leading order. Hence, matching  $\phi_2$  at the ends of both super-slow fields  $I_s^\pm$  gives the leading order matching condition

$$u_2(0; \lambda) = t_{22}(\lambda)u_2(0; \lambda) + t_{23}(\lambda)u_3(0; \lambda). \quad (4.3.25)$$

The  $\bar{p}$  component changes in the fast field. On the one hand, this change is given by the difference of  $\bar{p}$  values at both ends of the slow fields  $I_s^\pm$ , i.e.

$$\Delta_s \bar{p} = t_{22}(\lambda)p_2(0; \lambda) + t_{23}(\lambda)p_3(0; \lambda) - p_2(0; \lambda). \quad (4.3.26)$$

On the other hand, the accumulated jump over the fast field is

$$\Delta_f \bar{p} = \frac{1}{\mu} \int_{I_f} (v_p(\xi)^2 u_2(0; \lambda) + 2u_p(\xi)v_p(\xi)\bar{v}(\xi; \lambda)) d\xi, \quad (4.3.27)$$

where  $\bar{v}$  satisfies  $(\mathcal{L}^r - \lambda)\bar{v} = -u_2(0; \lambda)v_p(\xi)^2$ . We recall that, in the fast field, to leading order,  $u_p = u_0$  and  $v_p = \frac{\omega}{u_0}$ , where  $\omega(\xi) = \frac{3}{2} \operatorname{sech}(\xi/2)^2$ . We rescale  $\bar{v}(\xi; \lambda) = -\frac{u_2(0; \lambda)}{u_0^2} V_{\text{in}}(\xi; \lambda)$ . Then (4.3.27) becomes

$$\Delta_f \bar{p} = \frac{1}{\mu} \frac{u_2(0; \lambda)}{u_0^2} \int_{I_f} (\omega(\xi)^2 - 2\omega(\xi)V_{\text{in}}(\xi; \lambda)) d\xi = \frac{1}{\mu} \frac{u_2(0; \lambda)}{u_0^2} (6 - 2\mathcal{R}(\lambda)) + h.o.t. \quad (4.3.28)$$

where

$$\mathcal{R}(\lambda) := \int_{-\infty}^{\infty} \omega(\xi)V_{\text{in}}(\xi; \lambda) d\xi \quad (4.3.29)$$

and  $V_{\text{in}}$  satisfies

$$(\mathcal{L}^r - \lambda)V_{\text{in}}(\xi; \lambda) = \omega(\xi)^2. \quad (4.3.30)$$

Equating  $\Delta_s \bar{p} = \Delta_f \bar{p}$  and by (4.3.25) one readily derives (at leading order in  $\varepsilon$ )

$$t_{22}(\lambda) = 1 + \frac{1}{\mu} \frac{1}{u_0^2} \frac{6 - 2\mathcal{R}(\lambda)}{\frac{p_2(0; \lambda)}{u_2(0; \lambda)} - \frac{p_3(0; \lambda)}{u_3(0; \lambda)}}. \quad (4.3.31)$$

Because of the symmetry  $f(x) = f(-x)$ ,  $g(x) = -g(-x)$ , it follows that  $u_2(0; \lambda) = u_3(0; \lambda)$  and  $p_2(0; \lambda) = -p_3(0; \lambda)$ . Hence

$$t_{22}(\lambda) = 1 + \frac{1}{\mu} \frac{1}{u_0^2} \frac{3 - \mathcal{R}(\lambda)}{\frac{p_2(0; \lambda)}{u_2(0; \lambda)}}. \quad (4.3.32)$$

The inhomogeneous ODE  $(\mathcal{L}^r - \lambda)V_{\text{in}} = \omega^2$  admits bounded solutions for all  $\lambda$  that are not eigenvalues of  $\mathcal{L}^r$ . When  $\lambda$  is an eigenvalue, though, a bounded solution only exists if the following Fredholm condition is satisfied:

$$\int_{-\infty}^{\infty} \omega^2 v^* d\xi = 0, \quad (4.3.33)$$

where  $v^*$  is the corresponding eigenfunction. Therefore, by Sturm-Liouville theory, it is clear that there is a bounded solution for  $\lambda_1^r = 0$ , but not for  $\lambda_0^r = 5/4$  or  $\lambda_2^r = -3/4$ . That is,  $\mathcal{R}(\lambda)$ , and therefore  $t_{22}$ , has poles of order 1 at  $\lambda_0^r$  and  $\lambda_2^r$ .

We have, hence, demonstrated the following:

**Lemma 4.3.10 (Evans function).** *Let the conditions of Theorem 4.2.19 and assumption (A7) be fulfilled, and let  $(U_p, V_p)$  be a pulse solution to (4.1.2) as described in Theorem 4.2.19. It then holds true that the eigenvalues of the operator  $\mathcal{L}$  in (4.3.1) arising from linearization around the pulse solution  $(U_p, V_p)$  coincide on  $\mathcal{C}_e$  with the roots of the Evans function*

$$\mathcal{D}(\lambda) = t_{11}(\lambda)t_{22}(\lambda)\tilde{\mathcal{D}}(\lambda), \quad (4.3.34)$$

with  $\tilde{\mathcal{D}}(\lambda) \neq 0, \lambda \in \mathcal{C}_e$  and where the so-called fast transmission function is given by

$$t_{11}(\lambda) = C_1 \left( \lambda - \lambda_0^f \right) \left( \lambda - \lambda_1^f \right) \left( \lambda - \lambda_2^f \right), \quad (4.3.35)$$

with  $\lambda_1^f = \mathcal{O}(\varepsilon)$ , while the so-called slow transmission function is given by

$$t_{22}(\lambda) = C_2 \frac{\tilde{t}_{22}(\lambda)}{\left( \lambda - \lambda_0^f \right) \left( \lambda - \lambda_2^f \right)}, \quad (4.3.36)$$

with some  $C_1, C_2, \lambda_0^f, \lambda_2^f \in \mathbb{R} \setminus \{0\}$  and  $\tilde{t}_{22}$  an analytic function on  $\mathcal{C}_e$ . In particular,

$$t_{22}(\lambda) = 1 + \frac{1}{u_0^2 \mu} \left( \frac{3 - \mathcal{R}(\lambda)}{p_2(0; \lambda)/u_2(0; \lambda)} \right), \quad (4.3.37)$$

where  $p_2(0; \lambda)/u_2(0; \lambda)$  is the slope of the unstable manifold of the trivial solution to (4.3.24) at  $x = 0$ , and  $\mathcal{R}$  is given (at leading order in  $\varepsilon$ ) by

$$\mathcal{R}(\lambda) = \int_{-\infty}^{\infty} \frac{3}{2} \operatorname{sech}(\xi/2)^2 V_{\text{in}}(\xi; \lambda) d\xi, \quad (4.3.38)$$

where  $V_{\text{in}}$  satisfies  $(\mathcal{L}^r - \lambda) V_{\text{in}} = \frac{9}{4} \operatorname{sech}(\xi/2)^4$ .

**Remark 4.3.11.** *The function  $\mathcal{R}$  has been extensively studied in [8, section 3.1.1], [54, section 4.1] and [53, section 5]. We would like to stress, however, that  $\mathcal{R}$  in this article has a different factor in front of it and is defined in terms of  $\lambda$ , whereas in [53, 54] it is defined as function of  $P := 2\sqrt{1 + \lambda}$ . A plot of  $\mathcal{R}$  has been included in Figure 4.8.*

**Remark 4.3.12.** *The eigenvalue problem is often written as a nonlocal eigenvalue problem (NLEP). This can be achieved via the transformation*

$$V_{\text{in}}(\xi; \lambda) = \frac{3 - \mu u_0^2 \frac{p_2(0; \lambda)}{u_2(0; \lambda)}}{\int_{-\infty}^{\infty} \omega(\xi) f(\xi; \lambda) d\xi} z(\xi; \lambda),$$

which results in the NLEP

$$(\mathcal{L}^r - \lambda) z = \frac{\omega^2 \int_{-\infty}^{\infty} \omega z d\xi}{3 - \mu u_0^2 \frac{p_2(0; \lambda)}{u_2(0; \lambda)}}.$$

#### Roots of transmission function $t_{22}$

In the constant coefficient case  $f, g \equiv 0$ , we have that  $p_2(0; \lambda)/u_2(0; \lambda) = \sqrt{1 + m\lambda}$  and so  $t_{22}(\lambda) = 0$  reduces to

$$\mu u_0^2 = \frac{\mathcal{R}(\lambda) - 3}{\sqrt{1 + m\lambda}}, \quad (4.3.39)$$

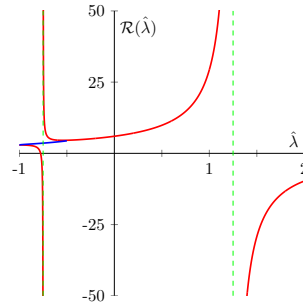


**Figure 4.8** – A plot of the function  $\mathcal{R}(\lambda)$ . The red lines show the form of  $\mathcal{R}(\lambda)$  for real-valued  $\lambda$ , whereas the blue lines also show the complex  $\lambda$  for which  $\mathcal{R}(\lambda)$  is real-valued; the green, dashed lines indicate the poles of the  $\mathcal{R}(\lambda)$ .

with  $u_0$  as in (4.2.72), and eigenvalues can be readily extracted from this condition – see [8]; in Figure 4.9, we show plots of the right-hand side for various  $m$ . With additional asymptotic approximations,  $m \ll 1$  and  $m \gg 1$ , this can be reduced even further, to leading order to,

$$\begin{aligned} \mu u_0^2 &= \mathcal{R}(\lambda) - 3, & \text{when } m \ll 1; \\ \nu u_0^2 &= \frac{\mathcal{R}(\lambda) - 3}{\sqrt{\lambda}}, & \text{when } m \gg 1; \end{aligned} \quad (4.3.40)$$

where

$$\nu = \frac{m^2 D}{a^2} = \mu \sqrt{m}. \quad (4.3.41)$$

Now, when  $\mu \ll 1$ , respectively  $\nu \ll 1$ , the left-hand side of these expressions becomes asymptotically small (since  $u_0 = u_0^- = \mathcal{O}(1)$ , see (4.2.72) and Remark 4.2.4), but stays positive. Hence solutions  $\lambda$  accumulate at points for which  $\mathcal{R}(\lambda) - 3 \approx 0$ , which happens to be at the tip of the essential spectrum, i.e.  $\lambda = \underline{\lambda}/m \approx -1$ , see Figure 4.9 and [8]. Certainly, no eigenvalues with positive real parts are found.

This idea can be expanded to include the non-autonomous cases. For this, as in the existence problem, we relate the non-autonomous equation to the autonomous equation. Here, it is useful to rescale (4.3.24) such that it has the form of (4.2.49). Specifically, we set  $\tilde{x} = \varepsilon^2 \mu |\sqrt{1+m\lambda}| \xi$  and  $\tilde{p} = |\sqrt{1+m\lambda}| \tilde{p}$ , under which (4.3.24) turns into the system

$$\begin{pmatrix} \tilde{u}' \\ \tilde{p}' \end{pmatrix} = \left[ \begin{pmatrix} 0 & 1 \\ 1 & 0 \end{pmatrix} + \begin{pmatrix} 0 & 0 \\ -\frac{g(\tilde{x}/|\sqrt{1+m\lambda}|)}{|1+m\lambda|} & -\frac{f(\tilde{x}/|\sqrt{1+m\lambda}|)}{|\sqrt{1+m\lambda}|} \end{pmatrix} \right] \begin{pmatrix} \tilde{u} \\ \tilde{p} \end{pmatrix}. \quad (4.3.42)$$

The autonomous part of this equation corresponds to the autonomous part for the existence problem – see section 4.2.4 – and thus possesses an exponential dichotomy with constants  $K = 1$  and  $\rho = 1$ . Therefore, for a given  $\lambda \in \mathcal{C}_e$ , by roughness (Proposition 4.2.14) it follows that the full non-autonomous equation has an exponential dichotomy as well when

$$\sup_{x \in \mathbb{R}} \frac{1}{|\sqrt{1+m\lambda}|} \sqrt{\frac{g(x)^2}{|1+m\lambda|} + f(x)^2} < \frac{1}{4}. \quad (4.3.43)$$

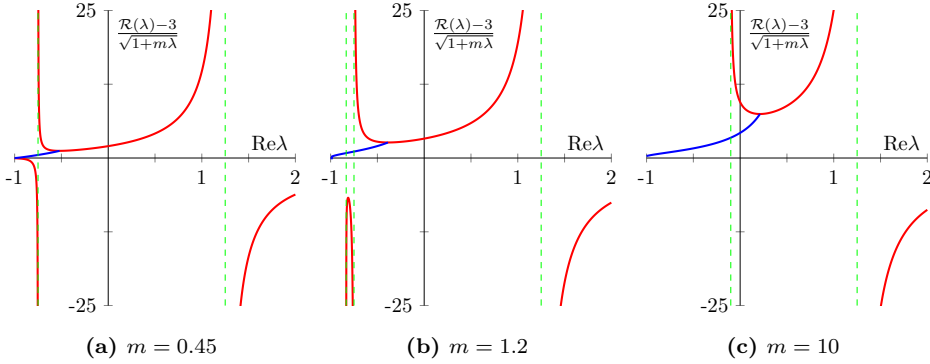


**Figure 4.9** – Plots of the right-hand side of (4.3.39) for various  $m$ . The red lines indicate the values for real-valued  $\lambda$ , whereas the blue lines indicate complex  $\lambda$  for which the right-hand side of (4.3.39) is real-valued; in green the poles are shown; see [8] for more details.

It is easily verified that this condition is satisfied when

$$\delta = \sup_{x \in \mathbb{R}} \sqrt{f(x)^2 + g(x)^2} < \delta_c(\lambda) := \frac{1}{4} |\sqrt{1+m\lambda}| \left| \sqrt{\frac{1+m\lambda}{2+m\lambda}} \right|. \quad (4.3.44)$$

Thus, for all  $\lambda \in \mathcal{C}_e$ , we obtain a (different) bound  $\delta_c(\lambda)$ . Since  $\delta_c(\lambda) \downarrow 0$  as  $|\sqrt{1+m\lambda}| \downarrow 0$  – i.e. when  $\lambda$  approaches  $-1/m$  – we cannot take the infimum over the region  $\mathcal{C}_e$ . Instead, we further restrict  $\lambda$  to  $\lambda \in \tilde{\mathcal{C}}_e := \mathcal{C}_e \cap \{\lambda \in \mathbb{C} : |\lambda + \frac{1}{m}| > \frac{1}{2m}\}$ . Note that  $\mathbb{C}^+ \subset \tilde{\mathcal{C}}_e$ . Then the infimum of  $\delta_c(\lambda)$  over this region exists, and we define it as  $\delta_c := \inf_{\lambda \in \tilde{\mathcal{C}}_e} \delta_c(\lambda) = \frac{\sqrt{6}}{24} \approx 0.102$ . Thus, if  $\delta < \delta_c$ , (4.3.42) possesses an exponential dichotomy for all  $\lambda \in \tilde{\mathcal{C}}_e$ .

Moreover, for all  $\lambda \in \tilde{\mathcal{C}}_e$  and  $\delta < \delta_c$ , the slope  $p_2(0; \lambda)/u_2(0; \lambda)$  of the non-autonomous case can be related to that of the autonomous case, along the same lines as in the existence proof in section 4.2.4 (specifically, as in Lemma 4.2.18). That is, there are  $\mathcal{O}(1)$  constants  $0 < C_-(\delta) \leq 1 \leq C_+(\delta)$  such that  $\tilde{p}(0; \lambda) = C\bar{u}(0; \lambda)$  for some  $C \in (C_-(\delta), C_+(\delta))$ . Rescaling back to the original variables then yields  $p_2(0; \lambda)/u_2(0; \lambda) = C\sqrt{1+m\lambda}$ . Therefore  $t_{22}(\lambda) = 0$  reduces to

$$C\mu u_0^2 = \frac{\mathcal{R}(\lambda) - 3}{\sqrt{1+m\lambda}}. \quad (4.3.45)$$

The asymptotic arguments for the autonomous case can now be repeated and it readily follows that no solutions are found with  $\lambda \in \tilde{\mathcal{C}}_e$ . In particular  $t_{22}(\lambda) = 0$  does not have solutions with  $\text{Re}\lambda > 0$ . We, hence, have the following result.

**Proposition 4.3.13** (Roots of the slow transmission function). *Let  $t_{22}$  be the slow transmission function from Lemma 4.3.10. Then, for  $\lambda \in \{\lambda \in \mathcal{C}_e : \|\lambda + \frac{1}{m}\| > \frac{1}{2m}\}$ ,*

$$t_{22}(\lambda) = 1 + \frac{1}{u_0^2 \mu} \left( \frac{3 - \mathcal{R}(\lambda)}{C\sqrt{1+m\lambda}} \right), \quad (4.3.46)$$

with  $u_0 = u_0^-$  as in (4.2.72) and for some  $C \in \mathbb{R}$  with

$$0 < C_{\min}(\delta) < C < C_{\max}(\delta) < \infty \quad (4.3.47)$$

and  $C_{\min/\max}(\delta)$  defined as in Lemma 4.2.18.

Moreover, if either of the following two asymptotic approximations hold true,

(i)  $m \ll 1$  and  $\mu \ll 1$ ;

(ii)  $m \gg 1$  and  $\nu \ll 1$ ,

then  $t_{22}(\lambda) = 0$  does not have any solution  $\lambda \in C_e$  with  $\text{Re}\lambda > 0$ .

Combining Lemma 4.3.10 with Proposition 4.3.13 readily demonstrates Theorem 4.3.2.

### Further remarks

If the asymptotic conditions on  $m$ ,  $\mu$  and  $\nu$  from Proposition 4.3.13 do not hold, equation (4.3.45) still holds. By restricting  $\delta$  further (i.e. taking a lower bound  $\delta_c$ ) stronger bounds on the constant  $C_+$  can be enforced that guarantee all roots of  $t_{22}$  lie to the left of the imaginary axis. The proof of this heavily relies on the proof for the autonomous case (see e.g. [8]) and a careful estimation of the constant  $C_+$ . Specifically, the following lemma can be established:

**Lemma 4.3.14.** *Let the conditions of Proposition 4.3.8 be fulfilled. Then there exists critical values  $m_c = 3$ ,  $0 < \mu^*(m) < \frac{1}{12}$  (see Theorem 4.2.19) and  $\nu^*(m) > 0$  such that if either of the following holds*

(i)  $m < m_c$  and  $\mu < \mu^*(m)$ ;

(ii)  $m > m_c$  and  $\nu < \nu^*(m)$ ;

(iii)  $m = m_c$  and  $\mu < \mu^*(m)$  and  $\nu < \nu^*(m)$ ,

then there exists a  $\delta_c > 0$  such that if  $\delta < \delta_c$  the condition (4.3.45) has no solutions with  $\text{Re}\lambda > 0$ ; that is,  $t_{22}$  has no roots with positive real part.

**Remark 4.3.15.** *In (4.3.45), the left-hand side is always real-valued. Hence, only  $\lambda \in \mathbb{C}$  for which the right-hand side is real-valued can satisfy (4.3.45). Due to this, eigenvalues can only appear on a skeleton in  $\mathbb{C}$ , of which the form only depends on  $m$ . In Figure 4.10 we show several skeletons for different  $m$ . Note that this is the reason for (the shape of) the bounds on the ‘large’ eigenvalues shown in Figure 4.4 (in red).*

**Remark 4.3.16.** *The arguments in this section have been applied to pulse solutions with  $u_0 = u_0^-$  (see (4.2.72);  $u_0^-$  as in (4.2.36) and (4.2.22)). There also exist pulse solutions with  $u_0 = u_0^+$  (with  $u_0^+$  as in (4.2.36) and (4.2.22)) and the reasoning also holds for these, up to equation (4.3.45). However,  $u_0^+ = \mathcal{O}\left(\frac{1}{\mu}\right)$  for these solutions (see Remark 4.2.4) and as an effect the left-hand side of (4.3.45) thus is asymptotically large (for  $\mu \ll 1$ ). As result, eigenvalues accumulate around the poles of the right-hand side. In particular, because of this, these alternative pulse solution necessarily have an eigenvalue close to  $\lambda = 5/4 > 0$ , making these pulse solutions unstable.*

**Remark 4.3.17.** *If  $\delta \ll 1$ , a direct application of roughness of exponential dichotomies can be used to directly prove that eigenvalues of (4.3.10) necessarily lie  $\mathcal{O}(\delta)$  close to eigenvalues of the problem with  $f \equiv 0$ ,  $g \equiv 0$ .*

**Remark 4.3.18.** *If  $\lim_{x \rightarrow \pm\infty} f(x), g(x)$  exist but are not (all) equal to zero, a similar result can be found with minor changes to the proof – provided that the essential spectrum lies to the left of the imaginary axis.*



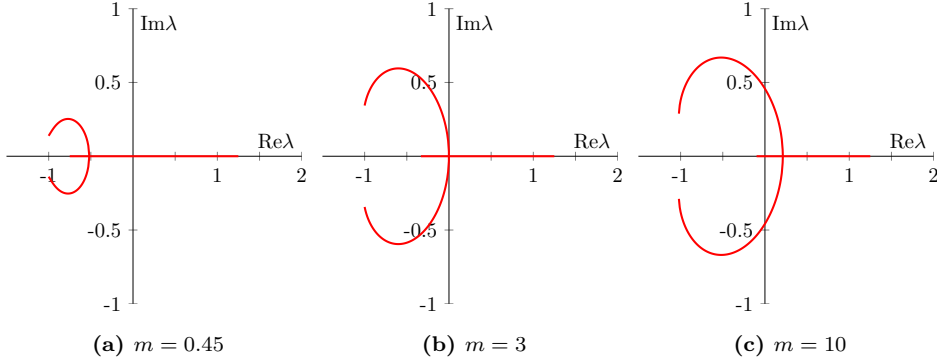


**Figure 4.10** – Plots of skeletons on which  $\lambda$  that satisfy (4.3.45) necessarily need to lie.

**Remark 4.3.19.** *If  $\lim_{x \rightarrow \pm\infty} f(x), g(x)$  do not exist, the outlined proof fails because the ‘elephant trunk’ procedure used in the proof of Lemma 4.3.8 does no longer work. If  $f$  and  $g$  approach (possibly different) period functions for  $x \rightarrow \infty$  a variant of this proof using a Ricatti transformation such as in [39] seems possible.*

### 4.3.2 Small eigenvalue close to $\lambda = 0$ (Proof of Theorem 4.3.5)

In this section we assume that

$$f(x) = \delta \tilde{f}(x), \quad g(x) = \delta \tilde{g}(x), \quad 0 < \delta \ll 1, \quad \tilde{f}, \tilde{g} = \mathcal{O}(1), \quad \sup_{x \in \mathbb{R}} \sqrt{\tilde{f}(x)^2 + \tilde{g}(x)^2} = 1, \quad (4.3.48)$$

which will ease the derivation of a more detailed estimate (as given in Theorem 4.3.5) of the location of the small eigenvalue around  $\lambda = 0$  (in terms of  $\delta$ ), so we set

$$\lambda = \delta \tilde{\lambda}. \quad (4.3.49)$$

The strategy to derive such an estimate is to relate the eigenvalue and existence problems in an appropriate way and then use the Fredholm alternative. To this end, let us write the eigenvalue problem in the fast field (4.3.9) in the more concise form

$$\delta \tilde{\lambda} \begin{pmatrix} \varepsilon^4 \mu^2 m & 0 \\ 0 & 1 \end{pmatrix} \begin{pmatrix} \bar{u} \\ \bar{v} \end{pmatrix} = \mathbb{L}_{u_p, v_p} \begin{pmatrix} \bar{u} \\ \bar{v} \end{pmatrix}, \quad (4.3.50)$$

and the existence problem in the fast field (4.2.2) as

$$0 = L_h \begin{pmatrix} u_p \\ v_p \end{pmatrix} + \delta L_{in}(\xi) \begin{pmatrix} u_p \\ v_p \end{pmatrix} + N \begin{pmatrix} u_p \\ v_p \end{pmatrix} + \begin{pmatrix} a \\ 0 \end{pmatrix}, \quad (4.3.51)$$

with (the linear part with constant coefficients)

$$L_h = \begin{pmatrix} \partial_\xi^2 - \varepsilon^4 \mu^2 & 0 \\ 0 & \partial_\xi^2 - 1 \end{pmatrix}, \quad (4.3.52)$$

and

$$L_{in}(\xi) = \begin{pmatrix} \varepsilon^2 \mu \tilde{f}(\varepsilon^2 \mu \xi) \partial_\xi + \varepsilon^4 \mu^2 \tilde{g}(\varepsilon^2 \mu \xi) & 0 \\ 0 & 0 \end{pmatrix}, \quad (4.3.53)$$

and  $N$  the nonlinear terms. Recall that in the autonomous case the derivative of the pulse solution is an eigenfunction for the zero eigenvalue. Motivated by this, we take a derivative w.r.t.  $\xi$  of the non-autonomous existence problem which gives

$$0 = \underbrace{[L_h + \delta L_{in}(\xi) + DN(u_p, v_p)]}_{=\mathbb{L}_{u_p, v_p}} \begin{pmatrix} \dot{u}_p \\ \dot{v}_p \end{pmatrix} + \delta \left( \frac{d}{d\xi} L_{in}(\xi) \right) \begin{pmatrix} u_p \\ v_p \end{pmatrix}, \quad (4.3.54)$$

and plug into the above eigenvalue problem (4.3.50) the ansatz

$$\begin{pmatrix} \bar{u} \\ \bar{v} \end{pmatrix} = \begin{pmatrix} \dot{u}_p \\ \dot{v}_p \end{pmatrix} + \delta \begin{pmatrix} \tilde{u} \\ \tilde{v} \end{pmatrix}, \quad (4.3.55)$$

which results in

$$\begin{aligned} \delta \tilde{\lambda} \begin{pmatrix} \varepsilon^4 \mu^2 m & 0 \\ 0 & 1 \end{pmatrix} \begin{pmatrix} \dot{u}_p \\ \dot{v}_p \end{pmatrix} + \delta^2 \tilde{\lambda} \begin{pmatrix} \varepsilon^4 \mu^2 m & 0 \\ 0 & 1 \end{pmatrix} \begin{pmatrix} \tilde{u} \\ \tilde{v} \end{pmatrix} \\ = \mathbb{L}_{u_p, v_p} \begin{pmatrix} \dot{u}_p \\ \dot{v}_p \end{pmatrix} + \delta \mathbb{L}_{u_p, v_p} \begin{pmatrix} \tilde{u} \\ \tilde{v} \end{pmatrix}. \end{aligned} \quad (4.3.56)$$

Upon using (4.3.54) to replace the term featuring  $\mathbb{L}_{u_p, v_p}(\dot{u}_p, \dot{v}_p)^T$ , we get

$$\delta \tilde{\lambda} \begin{pmatrix} \varepsilon^4 \mu^2 m & 0 \\ 0 & 1 \end{pmatrix} \begin{pmatrix} \dot{u}_p \\ \dot{v}_p \end{pmatrix} + \delta^2 \tilde{\lambda} \begin{pmatrix} \varepsilon^4 \mu^2 m & 0 \\ 0 & 1 \end{pmatrix} \begin{pmatrix} \tilde{u} \\ \tilde{v} \end{pmatrix} \quad (4.3.57)$$

$$= -\delta \left( \frac{d}{d\xi} L_{in}(\xi) \right) \begin{pmatrix} u_p \\ v_p \end{pmatrix} + \delta \mathbb{L}_{u_p, v_p} \begin{pmatrix} \tilde{u} \\ \tilde{v} \end{pmatrix} \quad (4.3.58)$$

For the perturbation analysis to follow we will use the notation  $u_{p,0}, v_{p,0}, \bar{u}_0, \bar{v}_0$  to indicate the leading order in  $\delta$  of the corresponding terms. In particular,  $u_{p,0}, v_{p,0}$  are the pulse solutions for the homogeneous case  $f = g = 0$  as described in Corollary 4.2.20. We, hence, arrive at the leading order in  $\delta$  of the previous equation

$$\mathbb{L} \begin{pmatrix} \tilde{u}_0 \\ \tilde{v}_0 \end{pmatrix} = \begin{pmatrix} \alpha \\ \beta \end{pmatrix} \quad (4.3.59)$$

with

$$\mathbb{L} := \mathbb{L}_{u_{p,0}, v_{p,0}} = \begin{pmatrix} \partial_\xi^2 - \varepsilon^4 \mu^2 - \varepsilon^2 v_{p,0}^2 & -2\varepsilon^2 u_{p,0} v_{p,0} \\ v_{p,0}^2 & \partial_\xi^2 - 1 + 2u_{p,0} v_{p,0} \end{pmatrix}, \quad (4.3.60)$$

and

$$\begin{pmatrix} \alpha \\ \beta \end{pmatrix} := \tilde{\lambda} \begin{pmatrix} \varepsilon^4 \mu^2 m & 0 \\ 0 & 1 \end{pmatrix} \begin{pmatrix} \dot{u}_{p,0} \\ \dot{v}_{p,0} \end{pmatrix} + \left( \frac{d}{d\xi} L_{in}(\xi) \right) \begin{pmatrix} u_{p,0} \\ v_{p,0} \end{pmatrix} \quad (4.3.61)$$

$$= \begin{pmatrix} \varepsilon^4 \mu^2 m \tilde{\lambda} \dot{u}_{p,0} + \varepsilon^4 \mu^2 \tilde{f}'(\varepsilon^2 \mu \xi) \dot{u}_{p,0} + \varepsilon^6 \mu^3 \tilde{g}'(\varepsilon^2 \mu \xi) u_{p,0} \\ \tilde{\lambda} \dot{v}_{p,0} \end{pmatrix}. \quad (4.3.62)$$

In order to find an expression for the eigenvalue correction  $\tilde{\lambda}$ , we will make use of the Fredholm alternative for (4.3.59). Hence, we first need to study the kernel of the adjoint operator

$$\mathbb{L}^* = \begin{pmatrix} \partial_\xi^2 - \varepsilon^4 \mu^2 - \varepsilon^2 v_{p,0}^2 & v_{p,0}^2 \\ -2\varepsilon^2 u_{p,0} v_{p,0} & \partial_\xi^2 - 1 + 2u_{p,0} v_{p,0} \end{pmatrix},$$

that is, to find  $(u^*, v^*)^T$  with

$$\mathbb{L}^* \begin{pmatrix} u^* \\ v^* \end{pmatrix} = 0, \quad (4.3.63)$$

and rearrange the solvability condition

$$\left\langle \begin{pmatrix} u^* \\ v^* \end{pmatrix}, \begin{pmatrix} \alpha \\ \beta \end{pmatrix} \right\rangle_{L^2 \times L^2} = 0, \quad (4.3.64)$$

to get an expression for  $\tilde{\lambda}$ . Since (4.3.63) is again a singularly perturbed problem (in  $\varepsilon$ ), we split this problem into three regions: two slow regions,  $I_s^\pm$ , and one fast region,  $I_f$ . As described in Theorem 4.2.19 and Corollary 4.2.20, we have

$$u_{p,0,0}(\xi) = \begin{cases} \frac{1}{\mu} [1 - (1 - \mu u_0) e^{+\varepsilon^2 \mu \xi}] & , \quad \xi \in I_s^-; \\ u_0, & \xi \in I_f; \\ \frac{1}{\mu} [1 - (1 - \mu u_0) e^{-\varepsilon^2 \mu \xi}] & , \quad \xi \in I_s^+, \end{cases} \quad v_{p,0,0}(\xi) = \begin{cases} 0, & \xi \in I_s^-; \\ \frac{1}{u_0} \omega(\xi), & \xi \in I_f; \\ 0, & \xi \in I_s^+, \end{cases} \quad (4.3.65)$$

where  $\omega(\xi) = \frac{3}{2} \operatorname{sech}(\xi/2)^2$  and the notation “ $p, 0, 0$ ” indicates that this the leading order in both,  $\delta$  and  $\varepsilon$ . In the slow regions we have  $v_{p,0,0} = 0$  to leading order and therefore (again to leading order)

$$u^*(\xi) = \begin{cases} C^- e^{-\varepsilon^2 \mu \xi}, & \xi \in I_s^-; \\ C^+ e^{-\varepsilon^2 \mu \xi}, & \xi \in I_s^+; \end{cases} \quad v^*(\xi) = \begin{cases} D^- e^\xi, & \xi \in I_s^-; \\ D^+ e^{-\xi}, & \xi \in I_s^+, \end{cases} \quad (4.3.66)$$

where  $C^\pm$  and  $D^\pm$  are constants that need to be found via matching with the fast field at  $\xi = \pm 1/\sqrt{\varepsilon}$ . In the fast region, the adjoint problem is to leading order given by

$$\begin{cases} 0 & = \ddot{u}^* + \frac{1}{u_0^2} \omega^2 v^*, \\ 0 & = \ddot{v}^* - v^* + 2\omega v^*. \end{cases}$$

Up to a multiplicative constant, the only bounded solution to the  $v^*$ -equation is  $v^* = \frac{1}{u_0} \omega'$ . Matching with the slow fields indicates  $D^\pm = 0$ . The expression for  $u^*$  in  $I^f$  can be found by integrating twice, which reveals

$$\begin{aligned} \sigma(\xi) := u^*(\xi) &= -\frac{1}{3u_0^3} \int_0^\xi \omega^3(z) dz + C_2 \\ &= -\frac{1}{3u_0^3} \frac{9}{20} [6 \cosh(\xi) + \cosh(2\xi) + 8] \tanh(\xi/2) \operatorname{sech}(\xi/2)^4 + C_2. \end{aligned}$$

The value of  $C_2$  turns out to be irrelevant and therefore we choose  $C_2 = 0$  for simplicity of presentation. Matching with the slow fields then gives  $C^- = \frac{6}{5u_0^3}$  and  $C^+ = -\frac{6}{5u_0^3}$ . In summary, we have to leading order in  $\varepsilon$

$$u^*(\xi) = \begin{cases} +\frac{6}{5u_0^3} e^{+\varepsilon^2 \mu \xi}, & \xi \in I_s^-; \\ \sigma(\xi), & \xi \in I_f; \\ -\frac{6}{5u_0^3} e^{-\varepsilon^2 \mu \xi}, & \xi \in I_s^+, \end{cases} \quad v^*(\xi) = \begin{cases} 0, & \xi \in I_s^-; \\ \frac{1}{u_0} \omega'(\xi), & \xi \in I_f; \\ 0, & \xi \in I_s^+, \end{cases} \quad (4.3.67)$$

and

$$\alpha(\xi) = \begin{cases} \varepsilon^6 \mu^2 e^{+\varepsilon^2 \mu \xi} [-m\tilde{\lambda}(1 - \mu u_0) - \tilde{f}'(\varepsilon^2 \mu \xi)(1 - \mu u_0) + \tilde{g}'(\varepsilon^2 \mu \xi) (e^{-\varepsilon^2 \mu \xi} + \mu u_0 - 1)], & \xi \in I_s^-; \\ \varepsilon^6 \mu^3 \tilde{g}'(\varepsilon^2 \mu \xi) u_0, & \xi \in I_f; \\ \varepsilon^6 \mu^2 e^{-\varepsilon^2 \mu \xi} [m\tilde{\lambda}(1 - \mu u_0) + \tilde{f}'(\varepsilon^2 \mu \xi)(1 - \mu u_0) + \tilde{g}'(\varepsilon^2 \mu \xi) (e^{+\varepsilon^2 \mu \xi} + \mu u_0 - 1)], & \xi \in I_s^+, \end{cases} \quad (4.3.68)$$

$$\beta(\xi) = \begin{cases} 0, & \xi \in I_s^-; \\ \frac{\tilde{\lambda}}{u_0} \omega'(\xi), & \xi \in I_f; \\ 0, & \xi \in I_s^+; \end{cases} \quad (4.3.69)$$

We can now assemble the different terms for the solvability condition

$$\left\langle \begin{pmatrix} u^* \\ v^* \end{pmatrix}, \begin{pmatrix} \alpha \\ \beta \end{pmatrix} \right\rangle_{L^2 \times L^2} = \int_{I_s^- \cup I_f \cup I_s^+} u^*(\xi) \alpha(\xi) d\xi + \int_{I_s^- \cup I_f \cup I_s^+} v^*(\xi) \beta(\xi) d\xi \quad (4.3.70)$$

Using that  $f$  is odd and  $g$  is even, which makes  $f'$  even and  $g'$  odd, we get to leading order

$$\begin{aligned} \int_{I_s^-} u^*(\xi) \alpha(\xi) d\xi &= +\varepsilon^6 \mu^2 \left( \frac{6}{5u_0^3} \right) \int_{I_s^-} e^{+2\varepsilon^2 \mu \xi} \left( -m\tilde{\lambda}(1 - \mu u_0) - \tilde{f}'(\varepsilon^2 \mu \xi)(1 - \mu u_0) \right. \\ &\quad \left. - \tilde{g}'(\varepsilon^2 \mu \xi)[e^{-\varepsilon^2 \mu \xi} + \mu u_0 - 1] \right) d\xi \\ &= +\varepsilon^4 \mu \left( \frac{6}{5u_0^3} \right) \int_0^{+\infty} e^{-2x} \left( -m\tilde{\lambda}(1 - \mu u_0) - \tilde{f}'(x)(1 - \mu u_0) \right. \\ &\quad \left. - \tilde{g}'(x)[e^x + \mu u_0 - 1] \right) dx + h.o.t. \\ &= -\varepsilon^4 \mu \left( \frac{6}{5u_0^3} \right) \int_0^{+\infty} e^{-2x} \left( m\tilde{\lambda}(1 - \mu u_0) + \tilde{f}'(x)(1 - \mu u_0) \right. \\ &\quad \left. + \tilde{g}'(x)[e^x + \mu u_0 - 1] \right) dx + h.o.t. \\ &= -\varepsilon^4 \mu \left( \frac{6}{5u_0^3} \right) \left( \frac{1}{2} m(1 - \mu u_0) \tilde{\lambda} + \int_0^{+\infty} e^{-2x} \left( \tilde{f}'(x)(1 - \mu u_0) \right. \right. \\ &\quad \left. \left. + \tilde{g}'(x)[e^x + \mu u_0 - 1] \right) dx \right) + h.o.t. \\ \int_{I_s^+} u^*(\xi) \alpha(\xi) d\xi &= -\varepsilon^6 \mu^2 \left( \frac{6}{5u_0^3} \right) \int_{I_s^+} e^{-2\varepsilon^2 \mu \xi} \left( m\tilde{\lambda}(1 - \mu u_0) + \tilde{f}'(\varepsilon^2 \mu \xi)(1 - \mu u_0) \right. \\ &\quad \left. + \tilde{g}'(\varepsilon^2 \mu \xi)[e^{+\varepsilon^2 \mu \xi} + \mu u_0 - 1] \right) d\xi \\ &= -\varepsilon^4 \mu \left( \frac{6}{5u_0^3} \right) \left( \frac{1}{2} m(1 - \mu u_0) \tilde{\lambda} + \int_0^{+\infty} e^{-2x} \left( \tilde{f}'(x)(1 - \mu u_0) \right. \right. \\ &\quad \left. \left. + \tilde{g}'(x)[e^x + \mu u_0 - 1] \right) dx \right) + h.o.t. \\ \int_{I_f} u^*(\xi) \alpha(\xi) d\xi &= \int_{I_f} \varepsilon^6 \mu^2 \tilde{g}'(\varepsilon^2 \mu \xi) u_0 d\xi = \mathcal{O}(\varepsilon^{6-1/2} \mu^2) \\ \int_{I_s^\pm} v^*(\xi) \beta(\xi) d\xi &= h.o.t. \\ \int_{I_f} v^*(\xi) \beta(\xi) d\xi &= \int_{I_f} \tilde{\lambda} \frac{1}{u_0^2} \omega'(\xi)^2 d\xi = \tilde{\lambda} u_0 \left( \frac{6}{5u_0^3} \right) + h.o.t.. \end{aligned}$$

Putting all pieces together, the solvability condition reads

$$\left\langle \left( \begin{array}{c} u^* \\ v^* \end{array} \right), \left( \begin{array}{c} \alpha \\ \beta \end{array} \right) \right\rangle_{L^2 \times L^2} = \left( \frac{6}{5u_0^3} \right) \left[ \tilde{\lambda}u_0 - \varepsilon^4 \mu \left( m\tilde{\lambda}(1 - \mu u_0) \right. \right. \\ \left. \left. + 2 \int_0^{+\infty} e^{-2x} \left( \tilde{f}'(x)(1 - \mu u_0) + \tilde{g}'(x)[e^x + \mu u_0 - 1] \right) dx \right) \right] + h.o.t. = 0,$$

which can be rearranged to

$$\tilde{\lambda} = \frac{2\varepsilon^4 \mu}{u_0 - \varepsilon^4 \mu m(1 - \mu u_0)} \int_0^{+\infty} e^{-2x} \left( \tilde{f}'(x)(1 - \mu u_0) + \tilde{g}'(x)[e^x + \mu u_0 - 1] \right) dx + h.o.t. \quad (4.3.71)$$

Since the problem is solved by a regular perturbation approach, the asymptotic analysis may be validated rigorously by classical methods (i.e. by rigorously controlling the higher order terms); alternatively a geometrical approach based on Lin's method may be employed (see e.g. [6]).

To show Corollary 4.3.6, we observe that in the double asymptotic limit  $\tau := \varepsilon^4 \mu m \ll 1$  and  $\mu \ll 1$ , the leading order expression for  $\tilde{\lambda}$  becomes

$$\tilde{\lambda} = \frac{2\varepsilon^4 \mu}{3} \int_0^{\infty} e^{-2x} \left( \tilde{f}'(x) + \tilde{g}'(x)[e^x - 1] \right) dx + h.o.t. \quad (4.3.72)$$

where we used that  $u_0 = u_0^-(\mu) \rightarrow 3$  for  $\mu \rightarrow 0$  (see Corollary 4.2.21 and (4.2.23)).

### Interpretation of results for ecological applications

Going back to the ecological application, we set  $f(x) = h'(x)$  and  $g(x) = h''(x)$ . Depending on the rate of topographical variation, several different simplifications can be made to Theorem 4.3.5, that allow us to make generic statements about stability of pulse solutions on these terrains.

First, if the topographical changes are small, i.e. when  $h = \mathcal{O}(\delta)$ , we can write  $h(x) = \delta \tilde{h}(x)$  and then (4.3.3) can be simplified (via integration by parts):

**Corollary 4.3.20** (small eigenvalue for height function  $h$ ). *Let the conditions of Theorem 4.3.5 be fulfilled. If  $\tilde{f}(x) = \tilde{h}'(x)$  and  $\tilde{g}(x) = \tilde{h}''(x)$ , then (4.3.3) becomes*

$$\underline{\lambda}_0 = \frac{2\delta\tau}{u_0 - \tau(1 - \mu u_0)} \left[ -\mu u_0 \tilde{h}''(0) + \tilde{h}(0)(1 - 2\mu u_0) + \int_0^{\infty} \tilde{h}(x) (e^{-x} - 4(1 - \mu u_0)e^{-2x}) dx \right]; \quad (4.3.73)$$

additionally, in the double asymptotic limit  $\tau := \varepsilon^4 \mu m \ll 1$ ,  $\mu \ll 1$  this further reduces to

$$\underline{\lambda}_0 = \frac{2}{3} \delta \tau \left[ \tilde{h}(0) + \int_0^{\infty} \tilde{h}(x) (e^{-x} - 4e^{-2x}) dx \right] + h.o.t. \quad (4.3.74)$$

**Remark 4.3.21.** *Note that  $\tilde{h}$  appears in (4.3.73), while it does not appear in the original PDE (4.1.2), where only its derivatives appear. Thus, increasing  $\tilde{h}$  by an additive constant does not affect the system, and in particular should not affect (4.3.73). Since  $\int_0^{\infty} (e^{-x} - 4(1 - \mu u_0)e^{-2x}) dx = -(1 - 2\mu u_0)$  the result in (4.3.73) is indeed not changed when adding a constant to the height function  $\tilde{h}$ .*

Second, if topographical variation happens only over long spatial scales (i.e. for terrains with weak curvature), we can write  $\tilde{h}(x) = \hat{h}(\sigma x)$ , where  $0 < \sigma \ll 1$  to indicate the large-scale spatial variability. Hence,  $\tilde{f}(x) = \sigma \hat{h}'(\sigma x) = \mathcal{O}(\sigma)$  and  $\tilde{g}(x) = \sigma^2 \hat{h}''(\sigma x) = \mathcal{O}(\sigma^2)$ . Because of the difference in size of  $\tilde{f}$  and  $\tilde{g}$ , the sign of  $\underline{\lambda}_0$  can be related to the sign of  $\hat{h}''(0)$ , i.e. to the local curvature at the location of the pulse.

**Corollary 4.3.22** (small eigenvalue for terrains with weak curvature). *Let the conditions of Theorem 4.3.5 be fulfilled. If  $\tilde{f}(x) = \sigma \hat{h}'(\sigma x)$  and  $\tilde{g}(x) = \sigma^2 \hat{h}''(\sigma x)$  with  $0 < \sigma \ll 1$ , the leading order expansion of (4.3.3) becomes*

$$\lambda_0 = \frac{\tau \delta \sigma^2 (1 - \mu u_0)}{u_0 - \tau(1 - \mu u_0)} \hat{h}''(0); \quad (4.3.75)$$

additionally, in the double asymptotic limit  $\tau := \varepsilon^4 \mu m \ll 1$ ,  $\mu \ll 1$ , this further reduces to

$$\lambda_0 = \frac{1}{3} \tau \delta \sigma^2 \hat{h}''(0) + h.o.t. \quad (4.3.76)$$

Furthermore, it follows that  $\text{sgn } \lambda_0 = \text{sgn } \hat{h}''(0)$ , i.e. (vegetation) pulses on hilltops are stable and in valleys are unstable.

*Proof.* Since  $|\tilde{f}'(x)| \gg |\tilde{g}'(x)|$  we can neglect the terms with  $\tilde{g}'(x)$  in (4.3.3), thus obtaining

$$\lambda_0 = \frac{2\tau\delta(1 - \mu u_0)}{u_0 - \tau(1 - \mu u_0)} \int_0^\infty \tilde{f}'(x) e^{-2x} dx. \quad (4.3.77)$$

Substitution of  $\tilde{f}'(x) = \sigma^2 \hat{h}''(\sigma x)$  and Taylor expanding  $\hat{h}''$  as  $\hat{h}''(x) = \hat{h}''(0) + \mathcal{O}(\sigma^3)$  immediately yields (4.3.75); the rest of the statement follows straightforwardly.  $\square$

Third, if topographical variation happens over short spatial scales (i.e. for terrains with strong curvature), we can write  $\tilde{h}(x) = \check{h}(x/\sigma)$ , where  $0 < \sigma \ll 1$  to indicate the short spatial scales. Hence,  $\tilde{f}(x) = \check{h}'(x/\sigma)/\sigma = \mathcal{O}(1/\sigma)$  and  $\tilde{g}(x) = \check{h}''(x/\sigma)/\sigma^2 = \mathcal{O}(1/\sigma^2)$ . Again, the sign of  $\lambda_0$  can be related to the sign of  $\check{h}''(0)$ , though the results are now flipped:

**Corollary 4.3.23** (small eigenvalue for terrains with strong curvature). *Let the conditions of Theorem 4.3.5 be fulfilled. If  $\tilde{f}(x) = \check{h}'(x/\sigma)/\sigma$  and  $\tilde{g}(x) = \check{h}''(x/\sigma)/\sigma^2$  with  $0 < \sigma \ll 1$  and  $\check{h}(y), \check{h}'(y), \check{h}''(y) \rightarrow 0$  exponentially fast for  $|y| \rightarrow \infty$ , the leading (and next-leading) order expansion of (4.3.3) becomes*

$$\lambda_0 = \frac{2\tau\delta}{u_0 - \tau(1 - \mu u_0)} \left[ \frac{-\mu u_0}{\sigma^2} \check{h}''(0) + (1 - 2\mu u_0) \check{h}(0) \right]; \quad (4.3.78)$$

additionally, in the double asymptotic limit  $\tau := \varepsilon^4 \mu m \ll 1$ ,  $\mu \ll 1$ , this further reduces to

$$\lambda_0 = \frac{2}{3} \tau \delta \check{h}(0). \quad (4.3.79)$$

Furthermore, it follows that  $\text{sgn } \lambda_0 = -\text{sgn } \check{h}''(0)$  when  $\mu \neq 0$ , i.e. (vegetation) pulses on hilltops are unstable and in valleys are stable; and  $\text{sgn } \lambda_0 = \text{sgn } \check{h}(0)$  when  $\mu = 0$ .

*Proof.* Substitution of  $\tilde{h}(x) = \check{h}(x/\sigma)$  and the use of the transformation  $y = x/\sigma$  in (4.3.73) yields

$$\lambda_0 = \frac{2\delta\tau}{u_0 - \tau(1 - \mu u_0)} \left[ -\frac{\mu u_0}{\sigma^2} \check{h}''(0) + (1 - 2\mu u_0) \check{h}(0) + \sigma \int_0^\infty \check{h}(y) (e^{-\sigma y} - 4(1 - \mu u_0) e^{-2\sigma y}) dy \right]. \quad (4.3.80)$$

Taylor expanding the exponential functions then indicates the integral contributes only at order  $\mathcal{O}(\delta\tau\sigma)$ . Hence the claimed results follow.  $\square$

Thus, the corollaries in this section indicate that – under certain assumptions on the limiting behavior of the topography function  $h$  – vegetation patterns concentrated on hilltops are stable if the terrain has weak curvature and unstable if the terrain has strong curvature; similarly, patterns concentrated in valleys are unstable for terrains with weak curvature, but they become stable if the terrain has strong curvature. A more in-depth inspection of this phenomena can be found in section 4.4.4, where a few explicit terrain functions  $h$  are studied numerically.

## 4.4 The effect of the small eigenvalue: movement of pulse

In the previous section we found that, under certain ‘standard’ assumptions on the system’s parameters, all large eigenvalues of a homoclinic pulse solution reside to the left of the imaginary axis. Only one small eigenvalue can lead to destabilization of the pulse solution. Since this small eigenvalue is closely related to the translation invariance of the system without spatially varying coefficients, it is possible to study its effects by projecting the whole system unto the corresponding eigenspace.

This derivation enables us to reduce the full PDE dynamics of (4.1.2) to a simpler ODE that describes the movement of the pulse’s location. Concretely, let  $P$  denote the location of the center of the pulse. Then the time-evolution of  $P$  is given by

$$\frac{dP}{dt} = \tau \frac{1}{6} [\tilde{u}_x(P^+)^2 - \tilde{u}_x(P^-)^2], \quad (4.4.1)$$

where the superscripts  $\pm$  denote taking the upper respectively lower limit,  $\tau := \varepsilon^4 \mu m = \frac{Da^2}{m\sqrt{m}}$  and  $\tilde{u}$  solves the differential-algebraic equation

$$\begin{cases} \tilde{u}_{xx} + f(x)\tilde{u}_x + g(x)\tilde{u} + 1 - \tilde{u} &= 0 \\ \tilde{u}(P) &= \mu u_0 \\ \tilde{u}_x(P^+) - \tilde{u}_x(P^-) &= \frac{6}{u_0} \end{cases} \quad (4.4.2)$$

We follow [8] and only give a short formal derivation of this PDE-to-ODE reduction, in section 4.4.1. We refrain from going into the details of (proving) the validity of this reduction. Although the renormalization group approach of [12, 50] for semi-strong pulse interactions has not yet been applied to systems with inhomogeneous terms, it can naturally be extended to include these effects. However, it should be noted that, so far, the results and techniques of [12, 50] only cover a strongly restricted region in parameter space: the general issue of validity of the reduction of semi-strong pulse interactions to finite dimensional settings still largely remains an open question in the field – see also [8]. As a consequence, we formulate the main results of this section as Propositions and only provide their formal derivations.

Using the pulse location ODE (4.4.1) we use formal analysis in section 4.4.2 to present a scheme by which we can determine the stability of the homoclinic pulse patterns of Theorem 4.2.5 for any functions  $f$  and  $g$ , i.e. without the restriction on their size by which we obtained Theorem 4.3.5; in section 4.4.3 we (formally) validate this scheme by reducing it to the setting of Theorem 4.3.5, i.e. by assuming that  $f, g = \mathcal{O}(\delta)$  (with  $\delta \ll 1$ ), and showing that this indeed confirms the results of Theorem 4.3.5. Next, we study a few explicit functions in section 4.4.4 – focusing on what happens when the pulse solution changes stability type. Finally, we briefly consider multi-pulse dynamics in section 4.4.5.

### 4.4.1 Formal derivation of pulse location ODE

In this section we formally derive the pulse location ODE (4.4.1). Mathematically, this amounts to tracking perturbations along translational eigenvalues; this approach is sometimes called the ‘collective coordinate method’. Specifically, in this section, we show

**Proposition 4.4.1.** *Let  $\varepsilon = \frac{a}{m} \ll 1$ ,  $\tau = \frac{Da^2}{m\sqrt{m}} \ll 1$  and  $\mu = \frac{Dm\sqrt{m}}{a^2} \leq \mathcal{O}(1)$  (w.r.t.  $\varepsilon$ ). Let  $P$  denote the location of the homoclinic pulse’s center. Then the evolution of  $P$  is described by the pulse location ODE (4.4.1).*

*Formal derivation, cf. [8].* We introduce the stretched travelling-wave coordinate

$$\xi = \frac{\sqrt{m}}{D} (x - P(t)) = \frac{\sqrt{m}}{D} \left( x - P(0) - \int_0^t \frac{dP}{dt}(s) ds \right),$$

scale  $\frac{dP}{dt} = \frac{Da^2}{m\sqrt{m}} c(t)$  and use scalings (4.2.1) to transform (4.1.2) to get

$$\begin{cases} -\frac{a^2}{m^2} \frac{Dm\sqrt{m}}{a^2} \frac{Da^2}{m\sqrt{m}} c(t) u_\xi &= u_{\xi\xi} - \frac{a^2}{m^2} \left[ \frac{D^2 m}{a^2} u - \frac{D}{\sqrt{m}} + uv^2 \right. \\ &\quad \left. - \frac{Dm\sqrt{m}}{a^2} f\left(\frac{D}{\sqrt{m}}\xi\right) u_\xi - \frac{D^2 m}{a^2} g\left(\frac{D}{\sqrt{m}}\xi\right) u \right] \\ -\frac{a^2}{m^2} c(t) v_\xi &= v_{\xi\xi} - v + uv^2 \end{cases} \quad (4.4.3)$$

To find the solution in the fast region  $I_f = [-1/\sqrt{\varepsilon}, 1/\sqrt{\varepsilon}]$ , close to the pulse location, we expand  $u$  and  $v$  in terms of  $\varepsilon$  and look for solution of the form

$$\begin{cases} u &= u_0 + \varepsilon^2 u_1 + \dots \\ v &= v_0 + \varepsilon^2 v_1 + \dots \end{cases} \quad (4.4.4)$$

To leading order (4.4.3) is given by

$$\begin{cases} 0 &= u_0'', \\ 0 &= v_0'' - v_0 + u_0 v_0^2. \end{cases} \quad (4.4.5)$$

Hence we find  $u_0$  to be constant and

$$v_0(\xi) = \frac{3}{2} \frac{1}{u_0} \operatorname{sech}(\xi/2)^2. \quad (4.4.6)$$

The next order of (4.4.3) is

$$\begin{cases} u_1'' &= u_0 v_0^2, \\ v_1'' - v_1 + 2u_0 v_0 v_1 &= -c(t) v_0' - v_0^2 u_1. \end{cases} \quad (4.4.7)$$

It is not a priori clear whether the  $v$ -equation is solvable; the self-adjoint operator  $\mathcal{L} := \partial_\xi^2 - 1 + 2u_0 v_0$  has a non-empty kernel, since  $\mathcal{L}v_0' = 0$ , and therefore the inhomogeneous  $v$ -equation is only solvable when the following Fredholm condition holds

$$\int_{I_f} c(t) v_0'(\eta)^2 d\eta = - \int_{I_f} v_0(\eta)^2 u_1(\eta) v_0'(\eta) d\eta. \quad (4.4.8)$$

Upon integrating by parts twice on the right-hand side we obtain

$$\int_{I_f} c(t) v_0'(\eta)^2 d\eta = -\frac{1}{3} \left[ u_1'(\eta) \int_0^\eta v_0(y)^3 dy \right]_{\eta=-1/\sqrt{\varepsilon}}^{\eta=+1/\sqrt{\varepsilon}} + \frac{1}{3} \int_{I_f} u_1''(\eta) \int_0^\eta v_0(y)^3 dy d\eta + h.o.t. \quad (4.4.9)$$



Since  $v_0$  is an even function,  $u_1''$  is an even function and  $\eta \mapsto \int_0^\eta v_0(y)^3 dy$  is an odd function. Therefore the last integral vanishes and we obtain

$$c(t) \int_{I_f} v_0'(\eta)^2 d\eta = \frac{1}{6} \left[ u_1' \left( \frac{1}{\sqrt{\varepsilon}} \right) + u_1' \left( -\frac{1}{\sqrt{\varepsilon}} \right) \right] \int_{I_f} v_0(\eta)^3 d\eta. \quad (4.4.10)$$

The integrals over the fast field  $I_f$  can be approximated by integrals over  $\mathbb{R}$ , since  $v_0$  decays exponentially within fast field. Hence we find

$$c(t) = \frac{1}{u_0} \left[ u_1' \left( \frac{1}{\sqrt{\varepsilon}} \right) + u_1' \left( -\frac{1}{\sqrt{\varepsilon}} \right) \right]. \quad (4.4.11)$$

Finally, it follows from the  $u$ -equation in (4.4.7) that

$$u_1' \left( \frac{1}{\sqrt{\varepsilon}} \right) - u_1' \left( -\frac{1}{\sqrt{\varepsilon}} \right) = \int_{I_f} u_1''(\eta) d\eta = \int_{I_f} u_0 v_0(\eta)^2 d\eta = \frac{6}{u_0} + h.o.t. \quad (4.4.12)$$

Combining this with (4.4.11) we obtain

$$c(t) = \frac{1}{6} \left[ u_1' \left( \frac{1}{\sqrt{\varepsilon}} \right)^2 - u_1' \left( -\frac{1}{\sqrt{\varepsilon}} \right)^2 \right] \quad (4.4.13)$$

The values of  $u_1'(\pm 1/\sqrt{\varepsilon})$  can be matched to the solutions  $\hat{u}$  in the slow fields. Careful inspection of the scalings involved reveals  $u_1'(\pm 1/\sqrt{\varepsilon}) = \hat{u}_x(P^\pm)$ , where  $\hat{u}$  satisfies the differential-algebraic equation (4.4.2). Since  $\frac{dP}{dt} = \tau c(t)$  this concludes the proof.

**Remark 4.4.2.** Note the link with the notation in section 4.2:  $u_1' = \hat{p}$ . See also Remark 4.2.8.

## 4.4.2 Stability of fixed points of pulse location ODE (4.4.1)

The pulse location ODE (4.4.1) describes the movement of a pulse over time. In general, for generic functions  $f$  and  $g$ , it is not possible to solve (4.4.2) in closed form, and therefore the pulse location ODE (4.4.1) cannot be expressed more explicitly for generic functions  $f$  and  $g$ . Thus, in general, (4.4.1) can only be solved numerically – for instance using the numerical scheme developed in [8]. Moreover, for generic  $f$  and  $g$  fixed points of (4.4.1) can only be obtained numerically. However, when  $f$  and  $g$  obey the symmetry assumptions (A5), one can readily obtain that  $P_* = 0$  is a fixed point. It is possible to determine the stability of fixed points using (4.4.1) via direct numerics, but this can be rather time-intensive and is prone to errors close to bifurcation points. Instead, it is better to first use asymptotic expansions to derive a stability condition that can be checked (numerically) more easily.

**Proposition 4.4.3.** Let the conditions of Proposition 4.4.1 be satisfied, let  $\mu \ll 1$  and let  $P_*$  be a fixed point of (4.4.1). Then, the eigenvalue  $\lambda$  – where  $\lambda = m\lambda$ , see (4.3.8) – corresponding to the pulse solution with a pulse located at the fixed point  $P_*$  is given by

$$\lambda = \frac{\tau}{6} \left\{ 2\tilde{u}'(P_*^+) [\tilde{u}''(P_*^+) + \tilde{w}'(P_*^+)] - 2\tilde{u}'(P_*^-) [\tilde{u}''(P_*^-) + \tilde{w}'(P_*^-)] \right\}. \quad (4.4.14)$$

Here  $\tilde{u}$  and  $\tilde{w}$  solve the coupled ODE system

$$\begin{cases} 0 &= \tilde{u}'' + f\tilde{u}' + g\tilde{u} - \tilde{u} + 1, \\ 0 &= \tilde{w}'' + f\tilde{w}' + g\tilde{w} - \tilde{w}, \\ \tilde{u}(P_*) &= 0, \\ \tilde{w}(P_*^\pm) &= -\tilde{u}'(P_*^\pm). \end{cases} \quad (4.4.15)$$

**Remark 4.4.4.** If  $f$  and  $g$  satisfy the symmetry assumption (A5) and  $P_*$  is located at the point of symmetry, i.e.  $P_* = 0$ , then symmetry forces  $\tilde{u}'(P_*^+) = -\tilde{u}'(P_*^-)$ ,  $\tilde{u}''(P_*^+) = \tilde{u}''(P_*^-)$  and  $\tilde{w}'(P_*^+) = \tilde{w}'(P_*^-)$ . Therefore, (4.4.14) reduces to

$$\underline{\lambda} = \frac{2\tau}{3} \tilde{u}'(P_*^+) [\tilde{u}''(P_*^+) + \tilde{w}'(P_*^+)]. \quad (4.4.16)$$

**Remark 4.4.5.** The condition  $\mu \ll 1$  in Theorem (4.4.3) is not strictly necessary. When this condition holds, the differential-algebraic system (4.4.2) simplifies to a normal boundary value problem, since  $\tilde{u}(P) = 0$  to leading order. However, when  $\mu = \mathcal{O}(1)$  (w.r.t.  $\varepsilon$ ) the procedure explained below is still applicable and one can derive a similar result; only this time,  $u_0$  in (4.4.2) needs to be expanded as well and  $\tilde{u}$  and  $\tilde{w}$  satisfy the coupled differential-algebraic system

$$\left\{ \begin{array}{l} 0 = \tilde{u}'' + f\tilde{u}' + g\tilde{u} - \tilde{u} + 1, \\ 0 = \tilde{w}'' + f\tilde{w}' + g\tilde{w} - \tilde{w}, \\ \tilde{u}(P_*) = \mu u_0, \\ \tilde{w}(P_*^\pm) = -\tilde{u}'(P_*^\pm) + \mu w_0, \\ \tilde{u}'(P_*^+) - \tilde{u}'(P_*^-) = \frac{6}{u_0}, \\ \tilde{w}'(P_*^+) - \tilde{w}'(P_*^-) = \frac{6w_0}{u_0^2} + \tilde{u}''(P_*^-) - \tilde{u}''(P_*^+). \end{array} \right. \quad (4.4.17)$$

*Formal derivation.* To find the eigenvalue  $\underline{\lambda}$  we need to evaluate the derivative of the right-hand side of (4.4.1) at the fixed point  $P_*$ . That is,

$$\begin{aligned} \underline{\lambda} &= \frac{d}{dP} \left[ \frac{\tau}{6} (\tilde{u}'(P^+)^2 - \tilde{u}'(P^-)^2) \right]_{P=P_*} \\ &= \frac{\tau}{6} \left[ 2\tilde{u}'(P_*^+) \left( \frac{d}{dP} \tilde{u}'(P^+) \right)_{P=P_*} - 2\tilde{u}'(P_*^-) \left( \frac{d}{dP} \tilde{u}'(P^-) \right)_{P=P_*} \right]. \end{aligned} \quad (4.4.18)$$

By definition of the derivative

$$\frac{d}{dP} [\tilde{u}'(P^\pm)] = \lim_{\phi \rightarrow 0} \frac{\tilde{u}'_\phi((P + \phi)^\pm) - \tilde{u}'(P^\pm)}{\phi}, \quad (4.4.19)$$

where  $\tilde{u}_\phi$  solves (4.4.2) with every  $P$  replaced by  $P + \phi$ . For small  $\phi$ ,  $\tilde{u}_\phi$  can be related to  $\tilde{u}$  via a regular expansion. Specifically, let  $|\phi| \ll 1$ , and expand  $\tilde{u}_\phi = \tilde{u} + \phi\tilde{w}$ . Substitution in (4.4.2) and careful bookkeeping readily shows that  $\tilde{u}$  and  $\tilde{w}$  satisfy (4.4.15). Finally, upon substituting the expansion for  $\tilde{u}_\phi$  into (4.4.19) and the use of a Taylor expansion we obtain

$$\begin{aligned} \frac{d}{dP} [\tilde{u}'(P^\pm)] &= \lim_{\phi \rightarrow 0} \frac{\tilde{u}'((P + \phi)^\pm) + \phi\tilde{w}'((P + \phi)^\pm) - \tilde{u}'(P^\pm)}{\phi} \\ &= \lim_{\phi \rightarrow 0} \frac{\tilde{u}'(P^\pm) + \phi\tilde{u}''(P^\pm) + \phi\tilde{w}'(P^\pm) - \tilde{u}'(P^\pm)}{\phi} \\ &= \tilde{u}''(P^\pm) + \tilde{w}'(P^\pm). \end{aligned}$$

Finally, substitution into (4.4.18) gives (4.4.14).

### 4.4.3 Small eigenvalue in case of small spatially varying coefficients

As an example of the use of Proposition 4.4.3, in this section we use Proposition 4.4.3 to give another proof for Theorem 4.3.5 in the limit  $\mu \ll 1$ . This not only shows

the applicability of Proposition 4.4.3 but especially the relevance of the pulse location ODE (4.4.1). Moreover, it also provides a confirmation of the validity of the formal results in this section.

*Alternative formal derivation of Theorem 4.3.5 for  $\mu \ll 1$ .* Since  $f$  and  $g$  satisfy the symmetry assumption (A5), the eigenvalue  $\underline{\lambda}$  is given by (4.4.16). Therefore, it suffices to only look at the solutions  $\tilde{u}$  and  $\tilde{w}$  to (4.4.15) for  $x > 0$ . Since  $f, g = \mathcal{O}(\delta)$  with  $\delta \ll 1$ , we use regular expansions for  $\tilde{u}$  and  $\tilde{w}$ ; that is, we set

$$\begin{aligned}\tilde{u} &= \tilde{u}_0 + \delta \tilde{u}_1 + \dots, \\ \tilde{w} &= \tilde{w}_0 + \delta \tilde{w}_1 + \dots\end{aligned}$$

Substitution in (4.4.15) gives at leading order

$$\begin{cases} 0 &= \tilde{u}_0'' - \tilde{u}_0 + 1, \\ 0 &= \tilde{w}_0'' - \tilde{w}_0, \\ \tilde{u}_0(0) &= 0, \\ \tilde{w}_0(0^+) &= -\tilde{w}_0'(0^+); \end{cases} \quad (4.4.20)$$

and at the next order,  $\mathcal{O}(\delta)$ , we find

$$\begin{cases} \tilde{u}_1'' - \tilde{u}_1 &= -\tilde{f}\tilde{u}_0' - \tilde{g}\tilde{u}_0, \\ \tilde{w}_1'' - \tilde{w}_1 &= -\tilde{f}\tilde{w}_0' - \tilde{g}\tilde{w}_0, \\ \tilde{u}_1(0) &= 0, \\ \tilde{w}_1(0^+) &= -\tilde{u}_1'(0^+). \end{cases} \quad (4.4.21)$$

Using the usual techniques to solve these ODEs, one can verify that

$$\tilde{u}_0(x) = 1 - e^{-x} \quad (4.4.22)$$

$$\tilde{u}_1(x) = \frac{1}{2}e^x \int_x^\infty F(z)e^{-z} dz - \frac{1}{2} \int_0^\infty F(z)e^{-z} dz + \frac{1}{2}e^{-x} \int_0^x F(z)e^z dz \quad (4.4.23)$$

$$\tilde{w}_0(x) = -e^{-x} \quad (4.4.24)$$

$$\begin{aligned}\tilde{w}_1(x) &= \frac{1}{2}e^x \int_x^\infty G(z)e^{-z} dz - \frac{1}{2}e^{-x} \int_0^\infty G(z)e^{-z} dz + \frac{1}{2}e^{-x} \int_0^x G(z)e^z dz \\ &\quad - e^{-x} \int_0^\infty F(z)e^{-z} dz\end{aligned} \quad (4.4.25)$$

where

$$F(z) := \tilde{f}(z)e^{-z} + \tilde{g}(z)(1 - e^{-z}), \quad (4.4.26)$$

$$G(z) := \tilde{f}'(z)e^{-z} - \tilde{g}'(z)e^{-z}. \quad (4.4.27)$$

Substitution of these expansions in (4.4.16) then yields

$$\begin{aligned}\underline{\lambda} &= \frac{2}{3}\tau [\tilde{u}_0'(0) + \delta \tilde{u}_1'(0)] [\tilde{u}_0''(0) + \delta \tilde{u}_1''(0) + \tilde{w}_0'(0) + \delta \tilde{w}_1'(0)] + \mathcal{O}(\delta^2) \\ &= \frac{2}{3}\tau \left[ 1 + \delta \int_0^\infty F(z)e^{-z} e^{-z} \right] \left[ -1 + 1 + \delta \int_0^\infty (F(z) + G(z)) e^{-z} dz \right] + \mathcal{O}(\delta^2) \\ &= \frac{2}{3}\delta\tau \int_0^\infty (F(z) + G(z)) e^{-z} dz + \mathcal{O}(\delta^2) \\ &= \frac{2}{3}\delta\tau \int_0^\infty \left( 2\tilde{f}(z)e^{-2z} + \tilde{g}(z)[1 - 2e^{-z}]e^{-z} \right) dz + \mathcal{O}(\delta^2) \\ &= \frac{2}{3}\delta\tau \int_0^\infty \left( \tilde{f}'(z)e^{-2z} + \tilde{g}'(z)(1 - e^{-z})e^{-z} \right) dz + \mathcal{O}(\delta^2).\end{aligned}$$

Finally, we note that the eigenvalue has been rescaled as  $\underline{\lambda} = m\lambda$  in Theorem 4.3.2. Since  $\tau/m = \varepsilon^4\mu$  and  $u_0 = 3$  in the limit  $\mu \ll 1$ , we have indeed recovered (4.3.72), i.e. Theorem 4.3.5, in the case  $\mu \ll 1$ .

#### 4.4.4 Examples of stationary single-pulse solutions

In this section, we study a few explicit functions  $f$  and  $g$ ; in all examples we specify a function  $h$  and take  $f = h'$ ,  $g = h''$ . Not all functions we consider here limit to 0 as  $|x| \rightarrow \infty$ ; that is, some violate assumption (A5). Therefore, these examples also form an outlook, illustrating how the results in this paper are expected to extend beyond the imposed assumptions on functions  $f$  and  $g$ . Specifically, we consider the following four examples:

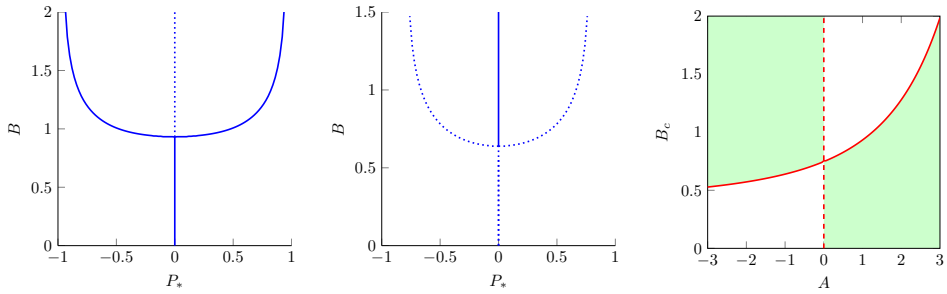
- (i)  $h(x) = Ae^{-Bx^2}$ , ( $A \in \mathbb{R}$ ,  $B > 0$ );
- (ii)  $h(x) = A \operatorname{sech}(Bx)$ , ( $A \in \mathbb{R}$ ,  $B > 0$ );
- (iii)  $h(x) = A \cos(Bx)$ , ( $A \in \mathbb{R}$ ,  $B > 0$ );
- (iv)  $h(x) = -2 \ln(\cosh(\beta x))$ , ( $\beta > 0$ ).

Note that  $\lim_{|x| \rightarrow \infty} f(x), g(x) = 0$  in cases (i)–(ii), which therefore satisfy assumption (A5). In case (iii)  $f$  and  $g$  are periodic when  $|x| \gg 1$ ; in case (iv)  $f$  and  $g$  do have well-defined (though non-zero) limits for  $|x| \rightarrow \infty$ .

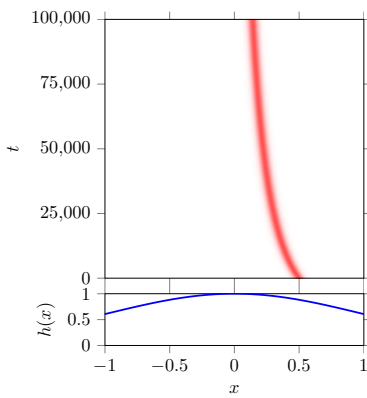
**Remark 4.4.6.** *Note that  $A > 0$  in (i)–(ii) corresponds to ‘hill-like’ topographies and  $A < 0$  to ‘valley-like’ topographies. The value of  $B$  in (i)–(iii) is a measure of the curvature of the terrain; the higher the value of  $B$ , the stronger the curvature of the terrain modeled by the function  $h$ .*

Using the pulse location ODE (4.4.1) and Proposition 4.4.3, we have tracked the fixed points and their stability for these examples in the limit  $\mu \ll 1$ , using numerical continuation methods. The resulting bifurcation diagrams for (i) are shown in Figure 4.11(a-b), for (ii) in Figure 4.12(a-b) and for (iii) in Figure 4.13(a). In all of these cases, we find fixed points at the point of symmetry, corroborating the results in section 4.2. For small  $B$  values – i.e. for weak curvature topographies – the stability of these fixed points is determined by the sign of  $A$ :  $A > 0$  leads to stable and  $A < 0$  to unstable fixed points – corroborating previous intuition indicating that pulses migrate in uphill direction [8, 148, 158]. However, for sufficiently large values of  $B$  – i.e. topographies with strong curvature – the stability of those fixed points changes through a pitchfork bifurcation and new behavior is observed. In case (iii) this even leads to the possibility that both the tops ( $BP = 0$ ) as well as the valleys ( $BP = \pm\pi$ ) form stable fixed points of (4.4.1). The bifurcation value of the pitchfork bifurcation,  $B_c(A)$ , depends on the value of  $A$ . Using numerical continuation methods we also tracked this value; the results are in Figures 4.11(c), 4.12(c) and 4.13(b) (for topographies (i), (ii) and (iii)).

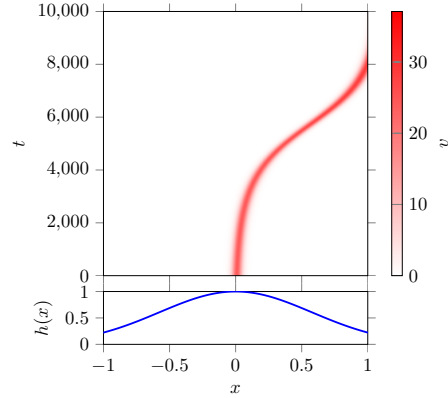
**Remark 4.4.7.** *Theorem 4.3.5, and in particular (4.3.72) and (4.3.74), provide a leading order analytic expression for  $B_c(0)$ . Evaluating these yields  $B_c(0) \approx 0.75$  (i),  $B_c(0) \approx 1.23$  (ii) and  $B_c(0) = \sqrt{2}$  (iii), which is confirmed by the numerical continuation that indicate  $B_c(0) \approx 0.75$  (i),  $B_c(0) \approx 1.24$  (ii) and  $B_c(0) = 1.43$  (iii). Note that  $A = 0$  is, indeed, just the flat terrain  $h(x) \equiv 0$ ; however, these results for  $A = 0$  should be interpreted to apply to ‘small’ topographical functions only, where  $A$  is asymptotically small.*



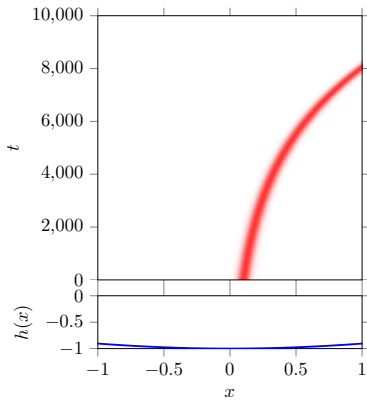
(a) Bifurcation diagram for  $A = 1$  (b) Bifurcation diagram for  $A = -1$  (c) Bifurcation value  $B_c(A)$



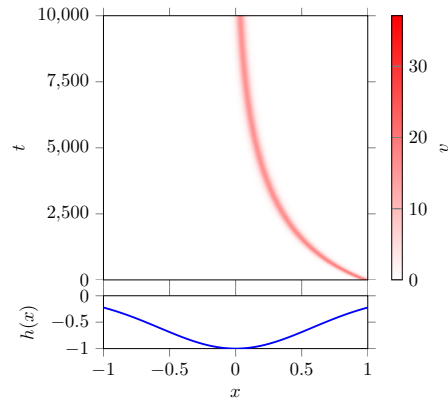
(d)  $A = 1, B = 0.5$



(e)  $A = 1, B = 1.5$



(f)  $A = -1, B = 0.1$



(g)  $A = -1, B = 1.5$

**Figure 4.11** – Numerical results for  $h(x) = Ae^{-Bx^2}$ . Shown are bifurcation diagrams for  $A = 1$  (a) and  $A = -1$  (b), the bifurcation value  $B_c(A)$  of the pitchfork bifurcation (c), and (parts of) various simulations of the full PDE illustrating the change of stability along with a plot of the function  $h(x)$  (d-g). The green areas in (c) indicate the parameter region in which the fixed point  $P_* = 0$  is stable. In the PDE simulations we have used parameters  $a = 0.5$ ,  $m = 0.45$ ,  $D = 0.01$  and taken  $x \in [-30, 30]$ .

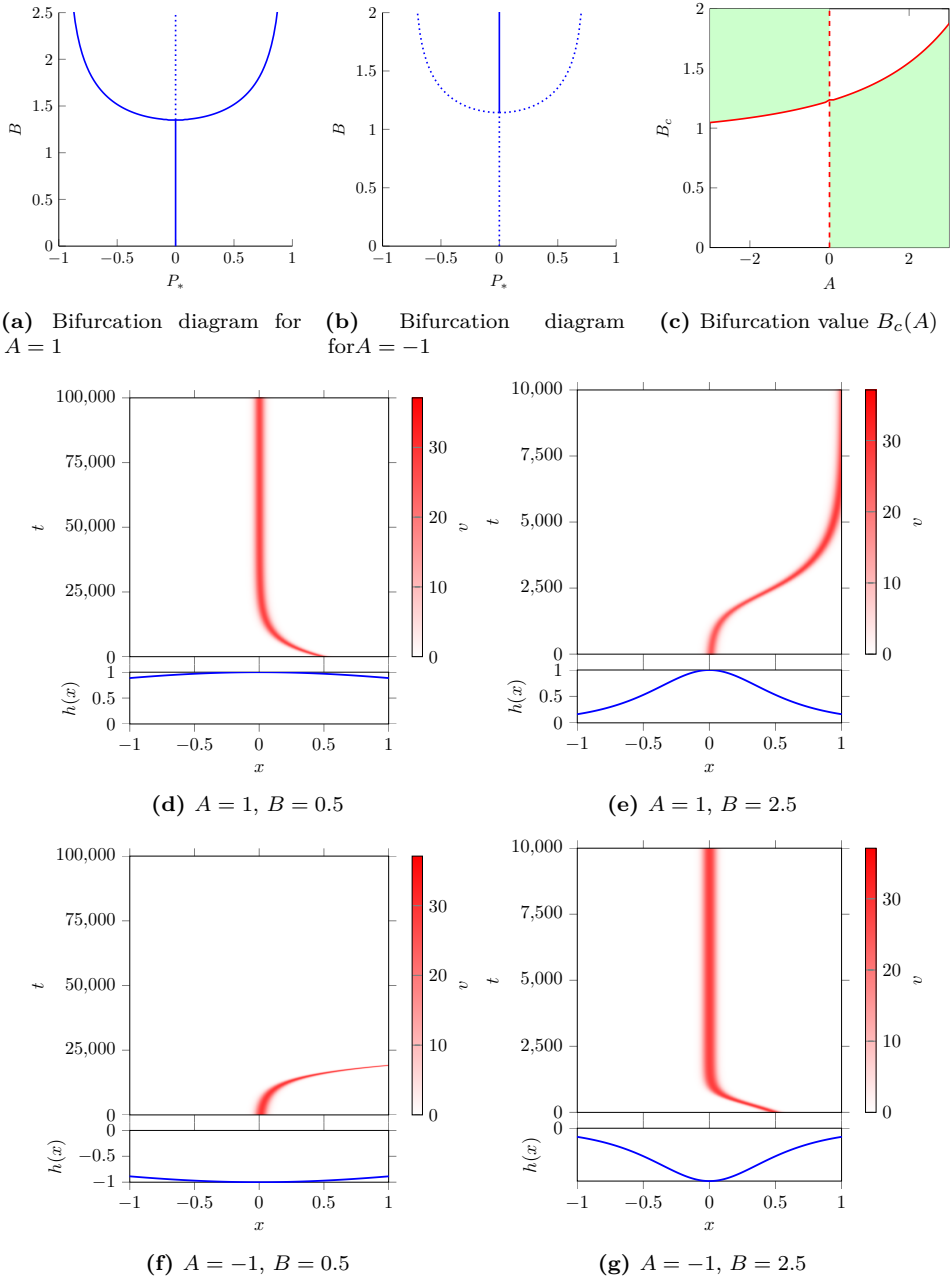


**Figure 4.12** – Numerical results for  $h(x) = A \operatorname{sech}(Bx)$ . Shown are bifurcation diagrams (solid for stable; dashed for unstable fixed points) for  $A = 1$  (a) and  $A = -1$  (b), the bifurcation value  $B_c(A)$  of the pitchfork bifurcation (c), and (parts of) various simulations of the full PDE illustrating the change of stability along with a plot of the function  $h(x)$  (d-g). The green areas in (c) indicate the parameter region in which the fixed point  $P_* = 0$  is stable. In the PDE simulations we have used parameters  $a = 0.5$ ,  $m = 0.45$ ,  $D = 0.01$  and taken  $x \in [-30, 30]$ .

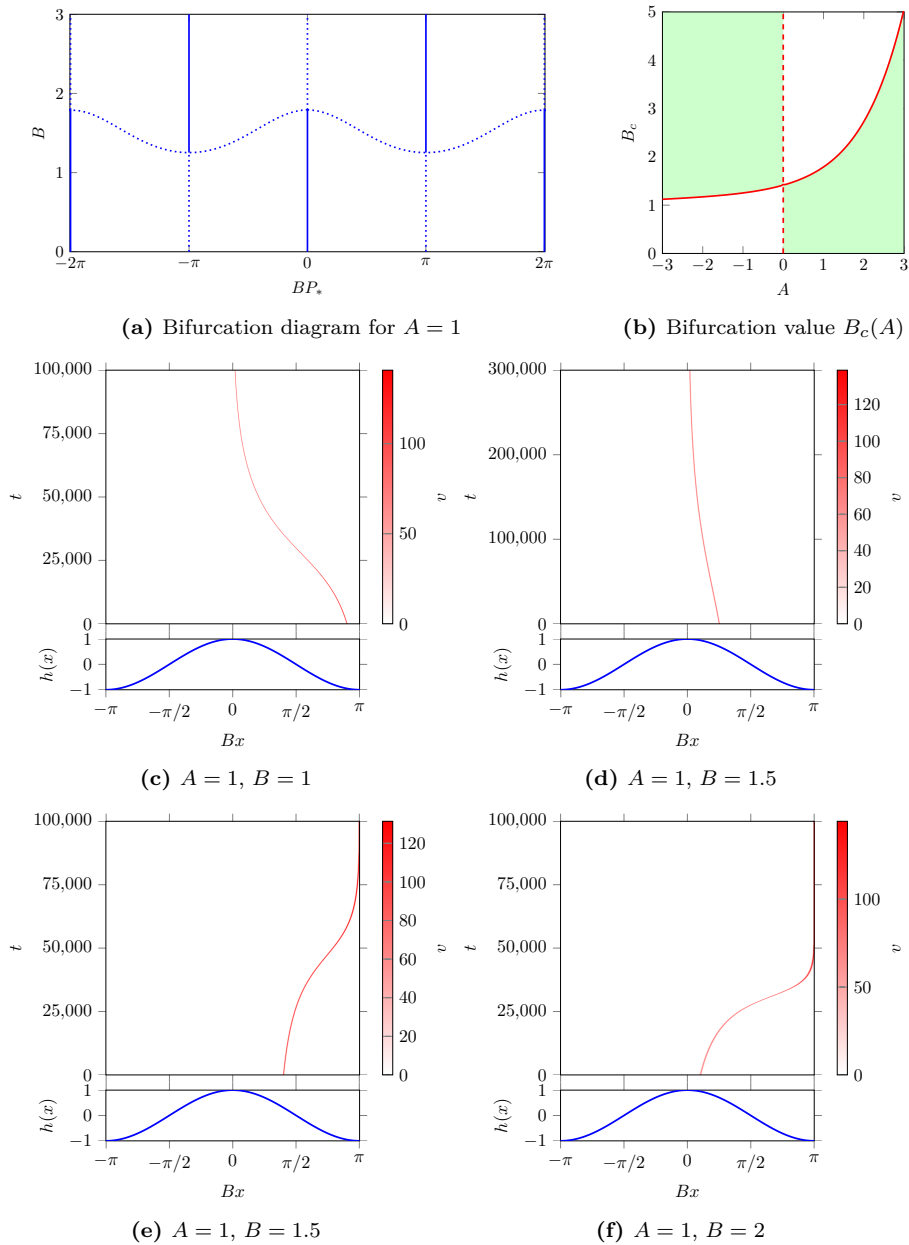


**Figure 4.13** – Numerical results for  $h(x) = A \cos(Bx)$ . Shown are the bifurcation diagram (solid for stable; dashed for unstable fixed points) for  $A = 1$  (a), the bifurcation value  $B_c(A)$  of the pitchfork bifurcation at  $x = 0$  (b), and (parts of) various simulations of the full PDE illustrating the change of stability along with a plot of the function  $h(x)$  (c-f). The green areas in (b) indicate the parameter region in which the fixed point  $P_* = 0$  is stable. In the PDE simulations we have used parameters  $a = 0.4$ ,  $m = 0.45$ ,  $D = 0.002$  and taken  $x \in [-30, 30]$ .

Moreover, these observations are validated by numerical simulation of the full PDE – see Figure 4.11(d-g) for (i), Figure 4.12(d-g) for (ii) and Figure 4.13(c-f) for (iii). Here, we observe the change in stability of the fixed points and, for well-chosen parameter values, these simulations show convergence to fixed points not located at the point of symmetry. Note also that in the case of periodic topography (i.e. case (iii)), there indeed is a region of  $B$ -values for which both a pulse at the top of a hill and one at the bottom of a valley can be stable (for the same  $B$  value). Thus, we are led to conclude that a pitchfork bifurcation occurs at the critical values  $B_c(0)$ . Simulations indicate that these exist also when the asymptotic limit  $\mu \ll 1$  does not hold.

For the last function, (iv), it is possible to derive the pulse location ODE (4.4.1) explicitly, since (4.4.2) can be solved explicitly – see Corollary 4.2.22. Using the expressions given in Corollary 4.2.22, a straightforward computation reduces (4.4.1) to

$$\frac{dP}{dt} = \frac{\tau}{6} \left[ (\cosh(\beta P) \mathcal{I}_1(P))^2 - (\cosh(\beta P) \mathcal{I}_2(P))^2 \right], \quad (4.4.28)$$

where

$$\mathcal{I}_1(P) := \int_P^\infty e^{r(P-z)} \operatorname{sech}(\beta z) dz; \quad \mathcal{I}_2(P) := \int_{-\infty}^P e^{-r(P-z)} \operatorname{sech}(\beta z) dz. \quad (4.4.29)$$

Thus, a point  $P_*$  is a fixed point if and only if  $\mathcal{I}_1(P_*) = \mathcal{I}_2(P_*)$ . Straightforward inspection reveals that  $P_* = 0$  therefore is the unique fixed point in case (iv) for all values of  $\beta > 0$ . By Proposition 4.4.3 and equation (4.4.16) the corresponding (small) eigenvalue  $\underline{\lambda}$  can be approximated by

$$\underline{\lambda} = \frac{2\tau}{3} \mathcal{I}_1(0) (r\mathcal{I}_1(0) - 1). \quad (4.4.30)$$

Upon noting that

$$r\mathcal{I}_1(0) - 1 = -\beta \int_0^\infty \operatorname{sech}(\beta z) \tanh(\beta z) e^{-rz} dz < 0, \quad (4.4.31)$$

it is clear that  $\underline{\lambda} < 0$ . Hence,  $P_* = 0$  is the only fixed point of (4.4.28) in case (iv), which is (globally) stable – for all  $\beta > 0$ . Direct PDE simulations verify this – even when the asymptotic limit  $\mu \ll 1$  does not hold – see Figure 4.14.

**Remark 4.4.8** (Interpretation of downhill movement). *Previous studies have shown that (homoclinic) pulses move uphill [8, 148, 158]. However, this intuition is primarily based on model studies with infinitely large domains. In this setting, for a pulse, the uphill direction is infinitely large, which – in combination with downhill flow of water – guarantees a pulse can always find more water on its uphill side compared to its downhill side. Hence, this causes pulses to move in the uphill direction indefinitely. However, when the uphill direction is only finitely large – such as in this article – this intuition is flawed; that is, in this setting, it can happen that the downhill side of a pulse provides more water, causing the pulse to move downhill instead. Moreover, a pulse located at a top is only stable if it has access to enough water; as more water flows downhill, away from it – as caused by increasing  $B$  in our examples – at some point the pulse at the top loses stability.*

### 4.4.5 Stationary multi-pulse solutions

The focus in this article has been on single pulse solutions to (4.1.2). As a short encore we briefly discuss the possibility of stationary multi-pulse solutions – i.e. solutions with



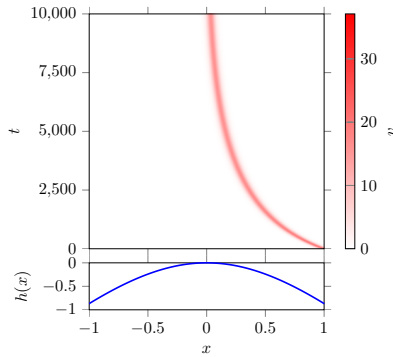


**Figure 4.14** – Direct numerical PDE simulation for  $h(x) = -2 \ln(\cosh(\beta x))$  for  $\beta = 1$  along with a plot of the function  $h(x)$ . In the PDE simulation we have used the parameters  $a = 0.5, m = 0.45, D = 0.01$  and taken  $x \in [-30, 30]$ .

multiple fast excursions. The movement of these solutions can be captured in an ODE much akin to 4.4.1. Specifically, let  $P_1, \dots, P_N$  denote the location of  $N$  pulses. Then their movement is described by the ODE

$$\frac{dP_j}{dt} = \frac{\tau}{6} [\tilde{u}_x(P_j^+)^2 - \tilde{u}_x(P_j^-)^2], \quad (j = 1, \dots, N) \quad (4.4.32)$$

where  $\tilde{u}$  satisfies the differential-algebraic system

$$\begin{cases} \tilde{u}_{xx} + f(x)\tilde{u}_x + g(x)\tilde{u} + 1 - \tilde{u} = 0 \\ \tilde{u}(P_j) = \mu u_{0j} & (j = 1, \dots, N) \\ \tilde{u}_x(P_j^+) - \tilde{u}_x(P_j^-) = \frac{6}{u_{0j}} & (j = 1, \dots, N) \end{cases} \quad (4.4.33)$$

The derivation is similar to that of Proposition 4.4.3; we omit the details here and refer the interested reader to [8] for a full coverage.

In case of constant coefficients  $f, g \equiv 0$ , it is well-known that stationary multi-pulse solutions do not exist [8, 45]. In fact, from (4.4.32) one can verify that in 2-pulse solutions the pulses typically move away from each other with a speed proportional to  $e^{-\Delta P}$ , where  $\Delta P := P_2 - P_1$  is the distance between the pulses – see [8, 45].

However, the non-autonomous terms  $f$  and  $g$  affect the movement speed and can cancel this repulsive movement. Therefore stationary pulse solutions do exist in (4.1.2) for well-chosen  $f$  and  $g$ . In Figure 4.15 we show several numerical examples of (stable) stationary multi-pulse solutions for various choices of  $f$  and  $g$ .

**Remark 4.4.9.** *The spatially varying  $f$  and  $g$  have a order  $\mathcal{O}(f, g)$  effect on the movement speed of the pulses. Finding fixed points of (4.4.32) – i.e. finding stationary multi-pulse solutions to (4.1.2) – thus boils down to balancing two effects of different size. In particular, if  $f, g = \mathcal{O}(\delta)$ , only multi-pulse solutions exist with  $\Delta P = \mathcal{O}(-\ln(\delta)) \gg 1$ . In this case, existence of stationary multi-pulse solutions can be established rigorously by asymptotic analysis and the methods of geometric singular perturbation theory.*

**Remark 4.4.10.** *We do not present a full analysis of the spectrum of (evolving) multi-pulse solutions here; they can be stable and unstable depending on the parameter values – similar to the one-pulse variants. A description of how to find the spectrum of multi-pulse solutions can be found in [8].*

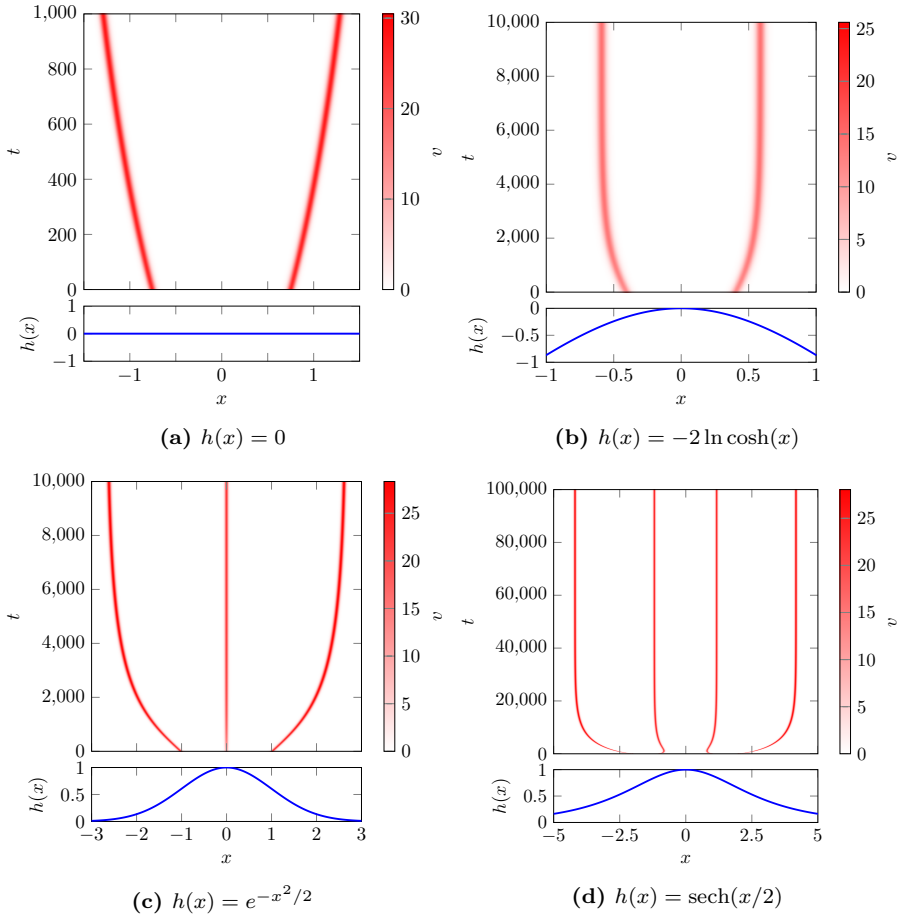


**Figure 4.15** – Numerical simulation of several multi-pulse solutions to (4.1.2) for various  $h$ , with  $f = h'$  and  $g = h''$ . (a)  $h(x) = 0$ : no stable stationary multi-pulse solution is found; (b)  $h(x) = -2 \ln \cosh(x)$ : the existence of a stable two-pulse solution; (c)  $h(x) = e^{-x^2/2}$ : a stable three-pulse solution; (d)  $h(x) = \operatorname{sech}(x/2)$ : a stable four-pulse solution. In blue the form of the terrain is plotted. Note that only part of  $x$ -domain is shown for clarity. Also note that, using (4.4.35), it is found that  $P_* \approx 0.51$  in (b). In the PDE simulations we have used parameters  $a = 0.5$ ,  $m = 0.45$ ,  $D = 0.01$ .

For generic functions  $f$  and  $g$  it is, at the moment, not possible to prove existence of stationary multi-pulse solutions (however, see Remark 4.4.9 for the case of small  $f$ ,  $g$ ). We do remark however that stationary multi-pulse solutions can be constructed for  $f$  and  $g$  such that (4.4.33) can be solved explicitly, as illustrated by the following proposition.

**Proposition 4.4.11.** *Let  $h(x) = -2 \ln \cosh(\beta x)$ ,  $\beta > 0$ ,  $f = h'$ ,  $g = h''$  and let  $\mu \ll 1$ . Then there exists a  $P_* > 0$  such that (4.1.2) admits a stationary symmetric two-pulse solution with pulses at  $P_1 = -P_*$  and  $P_2 = P_*$ .*

*Formal derivation.* By symmetry of the desired two-pulse solution, we may set  $P_2 = P$ ,  $P_1 = -P$ . Moreover, necessarily  $\tilde{u}'(0) = 0$ . Since  $\mu \ll 1$ , to leading order we have  $\tilde{u}(P) = \tilde{u}(-P) = 0$ . Therefore  $\tilde{u}$  is given to leading order by

$$\tilde{u}(x) = \begin{cases} \hat{u}_b(x) - \frac{\hat{u}_b(-P)}{\hat{u}_-(-P)} \hat{u}_-(x), & x < -P, \\ \hat{u}_b(x) - \frac{\hat{u}_b(P)}{\hat{u}_+(P) + \hat{u}_-(P)} (\hat{u}_+(x) + \hat{u}_-(x)), & -P < x < P; \\ \hat{u}_b(x) - \frac{\hat{u}_b(P)}{\hat{u}_+(P)} \hat{u}_+(x), & x > P; \end{cases} \quad (4.4.34)$$

where  $\tilde{u}_\pm$  and  $\tilde{u}_b$  are as in Corollary 4.2.22. To have stationary pulse solutions, by (4.4.32) we need to have

$$\mathcal{T}(P) := \hat{u}'_b(P) - \hat{u}_b(P) \left[ \frac{\sqrt{1 + \beta^2}}{2} \left( \tanh(\sqrt{1 + \beta^2}P) - 1 \right) + \beta \tanh(\beta P) \right] = 0, \quad (4.4.35)$$

Upon noting that

$$\mathcal{T}(0) = \frac{1}{2} \int_0^\infty e^{-\sqrt{1 + \beta^2}z} \operatorname{sech}(\beta z) dz > 0, \quad (4.4.36)$$

and, since  $\lim_{P \rightarrow \infty} \hat{u}_b(P) = 1$  and  $\lim_{P \rightarrow \infty} \hat{u}'_b(P) = 0$ ,

$$\lim_{P \rightarrow \infty} \mathcal{T}(P) = -\beta < 0, \quad (4.4.37)$$

continuity of  $\mathcal{T}$  guarantees the existence of  $P_* > 0$  as claimed.

**Remark 4.4.12.** *This result can be established rigorously by geometric singular perturbation theory, using the methods detailed in section 4.2. We refrain from giving the details of this procedure.*

## 4.5 Discussion

In this paper, we studied pulse solutions in a reaction-advection-diffusion system with spatially varying coefficients. The existence of stationary (one) pulse solutions at a point of symmetry was established by combining the usual techniques from geometric singular perturbation theory with the tools from the theory of exponential dichotomies. The latter has been used to generate a saddle-like structure in the slow subsystem, and to obtain bounds on the stable/unstable manifolds of this subsystem. These techniques have also been used to determine the spectral stability of these pulse solutions. None of these concepts or ideas are model-dependent and therefore could be used in a wider variety of models, including Gierer-Meinhardt type models.

Analysis of the spectrum associated to these pulse solutions showed that ‘large’ eigenvalues can be bounded to the stable half-plane  $\{\lambda \in \mathbb{C} : \text{Re}\lambda < 0\}$ , under conditions similar to the usual, constant coefficient case. Although we did not focus on the dynamics of solutions when a large eigenvalue crosses the imaginary axis, simulations show the usual pulse annihilation and pulse splitting phenomena. However, the introduction of spatially varying coefficients does have a significant effect on the so-called ‘small’ eigenvalues (close to  $\lambda = 0$ ) because of the break-down of the translation invariance in the system. Therefore, well-chosen  $f$  and  $g$  can either stabilize or destabilize solutions. When the small eigenvalue is in the unstable half-plane  $\{\lambda \in \mathbb{C} : \text{Re}\lambda > 0\}$ , the pulse solution is unstable and as an effect its *position* changes. In some cases, this in turn can subsequently lead to a pulse annihilation or a pulse splitting [8]. We expect that a careful tuning of  $f$  and  $g$  can either prevent or force these subsequent bifurcations, which may have a relevance in the maintenance of vegetation patterns in semi-arid climates.

The small eigenvalues were studied more in-depth in the case of  $f = h'$ ,  $g = h''$  (where  $h$  is used to model the topography of a dryland ecosystem). Here, we were able to link the stability of (stationary) pulse solution to the curvature of  $h$ . If the curvature is weak, the pulse is stable if  $h''(0) < 0$  and unstable if  $h''(0) > 0$ ; for strong curvature the opposite is true: the pulse is stable if  $h''(0) > 0$  and unstable if  $h''(0) < 0$ . We found that this change in stability typically happens via a pitchfork bifurcation, and showed that the associated parameter combinations can be obtained numerically. However, we did not consider a fully general class of functions  $f$  and  $g$ , and we do not know in which way these results generalize to other functions  $f$  and  $g$  – although for choices  $f$  and  $g$  for which (4.1.2) does not possess the symmetry  $(x, u) \rightarrow (-x, u)$  (i.e. when assumption (A5) does not hold), the pitchfork bifurcation will break down. A precise treatment of such generic functions could be the topic of subsequent work.

Moreover, in case of spatially varying coefficients, the system (4.1.2) can also possess stationary multi-pulse solutions – i.e. solutions that have multiple fast excursions. When  $f, g \equiv 0$ , these solutions do not exist. Because the spatially varying coefficients break the translation invariance of the system, these multi-pulse solutions can exist – for well-chosen functions  $f$  and  $g$ . In this article we gave numerical evidence for this and showed their existence for a specific choice of functions. We do not think their existence can be proven in as much generality as the existence of stationary one pulse solutions – certainly, the bounds used in this paper, provided by the theory of exponential dichotomies, are not sufficient in the regions between pulses. For sufficiently small  $f$  and  $g$ , an asymptotic analysis can be developed to overcome this issue, although the distance between subsequent pulses then becomes asymptotically large and asymptotic analysis needs to be done with great care to keep track of the right scalings; this is topic of ongoing research.

Finally, the extended Klausmeier model studied in this paper has its application in ecology, where it is used to model dryland ecosystems. The studied pulse solutions in this model correspond to vegetation ‘patches’ that are typically found in those ecosystems. Naturally, the results in this paper can therefore be used for this application. Specifically, the treatment of a spatially varying height function  $h$  is new and is inherently more realistic than taking a constant topography (or a constantly sloped topography) as has been done in the past (see e.g. [6, 9, 95, 158]). Typically, the constant coefficient models exhibit pulses that only move uphill. However, as illustrated with numerics, we have shown that a varying topography can lead to both uphill *and* downhill movement of pulses. This aligns better with measurements, where

also both uphill and downhill movement can be observed – even within the same general region [9, 57] – and also refutes claims, based on these measurements, stating the invalidity of ecosystem models of reaction-diffusion type based on the vegetation-water feedback [57]. In this regard, the study in this paper can be seen as a first step to better understand the role of topographic variability in pattern formation.

## **Acknowledgments**

We like to thank Marco Wolters for his exploratory (bachelor) research on the migration of vegetation pulses on periodic topographies.

# 5

## Stable planar vegetation stripe patterns on sloped terrain in dryland ecosystems

In water-limited regions, competition for water resources results in the formation of vegetation patterns; on sloped terrain, one finds that the vegetation typically aligns in stripes or arcs. We consider a two-component reaction-diffusion-advection model of Klausmeier type describing the interplay of vegetation and water resources and the resulting dynamics of these patterns. We focus on the large advection limit on constantly sloped terrain, in which the diffusion of water is neglected in favor of advection of water downslope. Planar vegetation pattern solutions are shown to satisfy an associated singularly perturbed traveling wave equation, and we construct a variety of traveling stripe and front solutions using methods of geometric singular perturbation theory. In contrast to prior studies of similar models, we show that the resulting patterns are spectrally stable to perturbations in two spatial dimensions using exponential dichotomies and Lin's method. We also discuss implications for the appearance of curved stripe patterns on slopes in the absence of terrain curvature.

### 5.1 Introduction

Large parts of earth have an arid climate (deserts) with low mean annual precipitation and little to no vegetation; even larger parts of earth have a semi-arid climate with somewhat more precipitation, which allows (some) vegetation to grow. However, human pressure and global climate change have been turning semi-arid climates into arid climates, with severe consequences for life in these areas [68, 167]. This so-called desertification process has been studied extensively over the years, from both ecological and mathematical perspectives. These studies have shown the importance and omnipresence of spatial patterning of vegetation, which is widely recognized as the first step in the desertification process [9, 68, 69, 114, 124, 137, 138, 139]. On flat ground, the reported patterns are gaps, labyrinths and spots, while on sloped terrain, (curved) banded or striped patterns can form [42, 64, 136, 176]; this article is focused on the latter, and in particular the stabilizing effect of terrain slope on striped vegetation patterns.

To understand the formation and dynamics of vegetation patterns in semi-arid climates, many conceptual models have been formulated [67, 95, 136, 176]. All of these dryland models describe the interplay between the available water and the density of vegetation, in different levels of detail. The simplest models only have two components:  $U$ , the water in the system and  $V$ , the vegetation. These two-component models

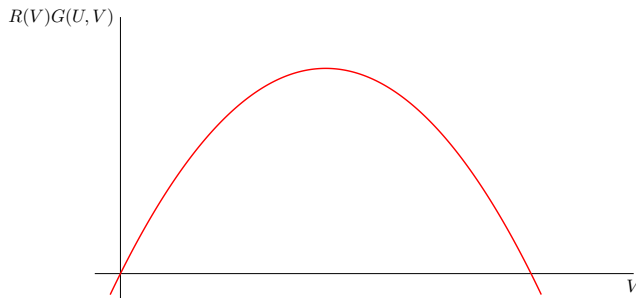


**Figure 5.1** – The qualitative form of  $R(V)G(U, V)$  for fixed  $U$  based on ecological intuition of dryland ecosystems.

generally have the following (rescaled) form:

$$\begin{cases} U_t &= D\Delta U + SU_x + a - U - G(U, V)V, \\ V_t &= \Delta V - mV + R(V)G(U, V)V. \end{cases} \quad (5.1.1)$$

In (5.1.1), the movement of water is modeled as a combined effect of diffusion ( $D\Delta U$ ) and advection ( $SU_x$ ), where  $D$  is the diffusion constant and  $S$  is a measure for the slope of the terrain. We assume the terrain is constantly sloped, so that uphill corresponds to the positive  $x$  direction. The dispersal of plants is described by diffusion ( $\Delta V$ ). The reaction terms describe the change in water due to rainfall ( $+a$ ), evaporation of water ( $-U$ ) and uptake by plants ( $-G(U, V)V$ ). Simultaneously, the change of plant biomass is due to mortality ( $-mV$ ) and plant growth ( $R(V)G(U, V)V$ ).

In this formulation,  $G$  and  $R$  are functions that describe, respectively, the amount of water that is taken up by the plant's roots and the density-dependent growth rate of the vegetation. Because the presence of vegetation increases the soil's permeability,  $G$  is typically assumed to increase with both  $U$  and  $V$ . The conversion rate  $R$  is decreasing with  $V$  and for a specific  $V^* > 0$  we have  $R(V^*) = 0$ . This value,  $V^*$ , is called the carrying capacity of the system and describes the total concentration of vegetation that can be supported at a certain location. In light of these ecological intuitions, one expects that the function  $R(V)G(U, V)$  should take the form as depicted in Figure 5.1 (for fixed  $U$ ). A simple choice which satisfies these constraints is given by  $R(V) = 1 - bV$  and  $G(U, V) = UV$ , where  $1/b$  is the carrying capacity. For clarity of presentation, we fix this choice for the remainder of this paper; however, we emphasize that, with minor modifications, the following analysis can be shown to hold for a different choice of the functions  $R$  and/or  $G$  which take the same qualitative form.

Finally, in (5.1.1), the displacement of water is modeled as a combined effect of diffusion and advection. However, in reality banded patterns are mainly observed on sloping grounds, where movement of water is dominated by the downhill flow and diffusive motion is of lesser importance [42, 64, 136, 176]. Note that this agrees with recent studies on ecosystem models that show banded vegetation is unstable against lateral perturbations of sufficiently small wavenumber when diffusion is large enough (i.e.  $D$  large enough compared to  $S$ ) [148, 155]. Therefore, as a first step, we ignore the diffusion of water completely (as in [95]) and set  $D = 0$ . Moreover, due to the separation of scales between movement of water and dispersion of vegetation, we take  $S = \frac{1}{\varepsilon}$ , where  $0 < \varepsilon \ll 1$  is a small parameter.

To summarize, the dryland model we consider in this article is given by

$$\begin{cases} U_t &= \frac{1}{\varepsilon}U_x + a - U - G(U, V)V, \\ V_t &= \Delta V - mV + R(V)G(U, V)V, \end{cases} \quad (5.1.2)$$

where  $a, m, b > 0$ ,  $0 < \varepsilon \ll 1$  and the functions  $R$  and  $G$  are given by

$$G(U, V) = UV, \quad R(V) = 1 - bV \quad (5.1.3)$$

**Remark 5.1.1.** *Notably, one of the first dryland ecosystem models, by Klausmeier [95], takes  $G(U, V) = UV$  and  $R(V) = 1$ . This corresponds to the assumption that vegetation growth in drylands is always water-limited, and hence to the assumption of infinite carrying capacity, i.e. taking  $b = 0$ , in our formulation. Therefore in the limit  $b \downarrow 0$  our model is the original Klausmeier model, and our model can thus be seen as a modified Klausmeier model. We emphasize, however, that the results in this article hold only for  $b > 0$ . The limiting case  $b = 0$  turns out to be highly degenerate (see Remark 5.2.12) and requires additional technical considerations; this is analyzed in detail in [23].*

The model (5.1.2) admits a spatially homogeneous steady state

$$(U, V) = (U_0, V_0) = (a, 0), \quad (5.1.4)$$

corresponding to the desert-state of the system. When  $\frac{a}{m} > 2(b + \sqrt{1 + b^2})$  there are also two additional vegetated steady state solutions,  $(U_1, V_1)$  and  $(U_2, V_2)$ , where

$$\begin{aligned} U_{1,2} &= m \left( \frac{a}{m} - \frac{V_{1,2}}{1 - bV_{1,2}} \right) = m \frac{\frac{a}{m} + 2\frac{a}{m}b^2 + 2b \pm \sqrt{\left(\frac{a}{m}\right)^2 - 4\left(1 + \frac{a}{m}b\right)}}{2(1 + b^2)}; \\ V_{1,2} &= \frac{\frac{a}{m} \mp \sqrt{\left(\frac{a}{m}\right)^2 - 4\left(1 + \frac{a}{m}b\right)}}{2\left(1 + \frac{a}{m}b\right)}. \end{aligned} \quad (5.1.5)$$

For  $\frac{a}{m} = 2(b + \sqrt{1 + b^2})$  these two steady states coincide. The desert state,  $(U_0, V_0)$ , is stable against all homogeneous perturbations; the first vegetated state,  $(U_1, V_1)$ , is unstable against these perturbations and the last steady state,  $(U_2, V_2)$ , is stable if  $V_2 > \frac{1}{2b}$  – see Appendix 5.A. The condition  $V_2 > \frac{1}{2b}$ , corresponding to  $\frac{a}{m} > 4b + \frac{1}{b}$ , is not strict; however in the following analysis of banded vegetation patterns we nonetheless restrict our results to this region.

**Remark 5.1.2.** *Ecologically, the parameter  $a$  is a measure for the rainfall and  $m$  for the mortality of plants. Therefore,  $\frac{a}{m}$  is a natural measure for the amount of resources needed for vegetation (patterns) to exist: if  $m$  is large, vegetation dies faster and more water is needed to maintain vegetation; when  $m$  is small, plants die slowly and less water is needed. Hence,  $\frac{a}{m}$  is a natural bifurcation parameter. Also note that  $\frac{a}{m}$  usually is taken as a small bifurcation parameter in studies of the extended-Klausmeier or generalized Klausmeier-Gray-Scott systems [8, 45, 148, 170].*

In this article we aim to study patterned solutions to (5.1.2), which arise as traveling wave solutions to (5.1.2). We define the traveling wave coordinate  $\xi := x - ct$ , where  $c$  is the movement speed. Here,  $c < 0$  corresponds to downhill movement of the traveling



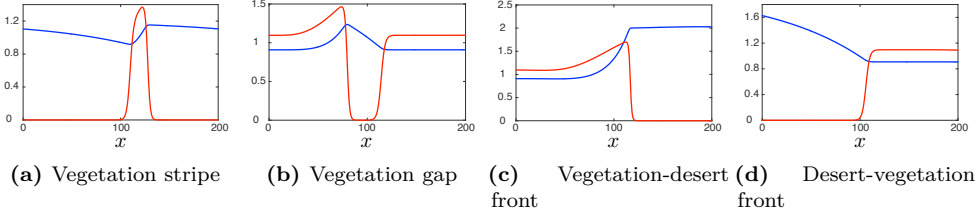


**Figure 5.2** – Shown are the different patterned solutions of (5.1.2) that are studied in this paper. Presented figures show cross-sections of the water,  $u(x)$ , (blue) and the vegetation,  $v(x)$ , (red) of direct numerical simulations with  $\varepsilon = 0.01$ ,  $m = 0.45$ ,  $b = 0.5$  and  $a = 1.2$  (a) or  $a = 2.0$  (b-d). The 2D pattern is a trivial extension of these patterns in the  $y$ -direction, visualization of which is shown in Figure 5.19.

wave and  $c > 0$  to uphill movement. Moreover, we set  $(U, V)(x, y, t) = (u, v)(\xi, y, t)$ , which results in the equation

$$\begin{cases} u_t &= \frac{1}{\varepsilon} u_\xi + cu_\xi + a - u - G(u, v)v, \\ v_t &= (\partial_\xi^2 + \partial_y^2)v + cv_\xi - mv + R(v)G(u, v)v. \end{cases} \quad (5.1.6)$$

Stationary solutions to (5.1.6) which are constant in  $y$  correspond to traveling wave solutions of (5.1.2); these solutions satisfy the first order traveling wave ODE

$$\begin{cases} u_\xi &= \frac{\varepsilon}{1+\varepsilon c} (u - a + G(u, v)v), \\ v_\xi &= q, \\ q_\xi &= mv - R(v)G(u, v)v - cq. \end{cases} \quad (5.1.7)$$

This equation has an equilibrium at  $(u, v, q) = (a, 0, 0)$  which represents the homogeneous desert state  $(U_0, V_0)$  of (5.1.2). There are two additional equilibrium points at  $(u, v, q) = (u_{1,2}, v_{1,2}, 0)$  corresponding to the other homogeneous steady states  $(U_{1,2}, V_{1,2})$  of (5.1.2).

Based on the parameters of the model, several different patterned solutions to (5.1.2) can emerge that correspond to homoclinic or heteroclinic orbits of (5.1.7). Single vegetation stripe patterns occur as orbits that are homoclinic to the desert state. Similarly, vegetation gap patterns occur as orbits that are homoclinic to the vegetated state  $(u_2, v_2, 0)$ . Besides these, there are also heteroclinic connections between the vegetated state and the desert state (and vice-versa) that represent transitions, or infiltration waves, between these uniform stationary states. Plots of these patterned solutions are shown in Figure 5.2.

In this article, we first establish existence of the aforementioned patterns rigorously. To that end, we exploit the scale separation in (5.1.7) using the methods of geometric singular perturbation theory [62]. Using a fast-slow decomposition, these patterns are shown to correspond to the union of trajectories on so-called invariant slow manifolds of (5.1.7) and fast connections between these slow manifolds. Specifically, (5.1.7) has three slow manifolds: one manifold,  $\mathcal{M}^\ell$  ( $\ell$  for left), consists of states without vegetation and the two others,  $\mathcal{M}^m$  (middle) and  $\mathcal{M}^r$  (right), consist of states with vegetation. Fast front-type solutions  $\phi_\dagger$  exist which connect  $\mathcal{M}^\ell$  to  $\mathcal{M}^r$ , and likewise there exist fast front solutions  $\phi_\diamond$  which connect  $\mathcal{M}^r$  to  $\mathcal{M}^\ell$ . Using these, stripes, gaps and fronts can be constructed for various parameter values. Pulse solutions

to (5.1.2) consist of trajectories on  $\mathcal{M}^\ell$  and  $\mathcal{M}^r$  and *two* fast front-type connections; front solutions to (5.1.2) only possess *one* fast front-type connection. In Figure 5.3 these patterns are shown in the  $\varepsilon = 0$  limit, where they are characterized by their speed in a sample bifurcation diagram.

The main theme of this paper is the spectral stability of the patterns. Because the main building blocks of all of the patterns are normally hyperbolic slow manifolds and fast front-type connections between these, we argue that destabilization can, a priori, only be caused by a ‘small’ eigenvalue, one of which is created by every front-type connection. However, using formal asymptotic computations this possibility is excluded: all described patterns to (5.1.2) – stripes, gaps and fronts – are thus (always) stable against two-dimensional perturbations. These formal arguments are also verified rigorously by carefully constructing eigenfunctions using techniques previously employed to prove stability of traveling pulses in the FitzHugh–Nagumo system in [22]; similar arguments were also used in [83, 84]. However, in those previous works, only stability with respect to perturbations in one spatial dimension was considered. By performing a Fourier decomposition in the transverse ( $y$ ) direction, we show that these methods can also be used to obtain 2D spectral stability of the full planar traveling waves.

Furthermore, in this paper we show that the 2D stability of the (straight) planar vegetation patterns implies that slightly curved variants of the same patterns, sometimes called corner defect solutions, are also solutions to (5.1.2) that are – again – 2D stable. An example of one of these solutions is given in Figure 5.4. Existing techniques developed in [76, 77] can be applied to infer that the orientation of these patterns is related to the speed  $c$  of their associated straight patterns; in particular we predict that when  $c > 0$  the corresponding corners are oriented convex upslope, and when  $c < 0$  they are convex downslope.

Besides these mathematical findings, this paper also provides novel insights in the context of ecology – and the study of desertification in particular. In simple dryland ecosystem models, typically vegetation patterns are found where the vegetation stripes (or gaps) have only a (very) small width, which is not very realistic [42, 64, 136, 176]. In this article, however, patterns are found that do have a more sizable width, that can even be expressed in terms of the model parameters. These larger widths are caused by the addition of a carrying capacity in (5.1.2) which limits the amount of vegetation at one place and forces the patterns to become wider instead. Moreover, this study indicates the kind of (striped) patterns that are possible based on the values of the model parameters; see Figure 5.3. Vegetation stripe patterns only exist in relatively dry conditions (i.e. when  $\frac{a}{m}$  is small). For ever so slightly more humid conditions, it is possible to find vegetation gap patterns and invading front patterns (both invading vegetation and invading desert fronts). For even more humid conditions, only invading vegetation fronts can be found. Finally, we also found slightly curved variants of the aforementioned planar vegetation patterns, an example of which is given in Figure 5.4. In this paper, we show that these curved vegetation patterns can be formed through the internal dynamics of (5.1.2), and provide a possible explanation for the observed vegetation arcs – even in the absence of topographic mechanisms [64].

**Remark 5.1.3.** *In an ecological context, traveling (spatially) periodic orbits are perhaps more relevant than the traveling pulse solutions constructed in this paper. However, once these pulse solutions are found, the periodic ones typically follow naturally [148] – as is the case here. Furthermore, properties of these periodic orbits are closely related to those of the pulse solutions. See also section 5.2.4.*

The set-up for the rest of this article is as follows. In section 5.2, we study (5.1.7)

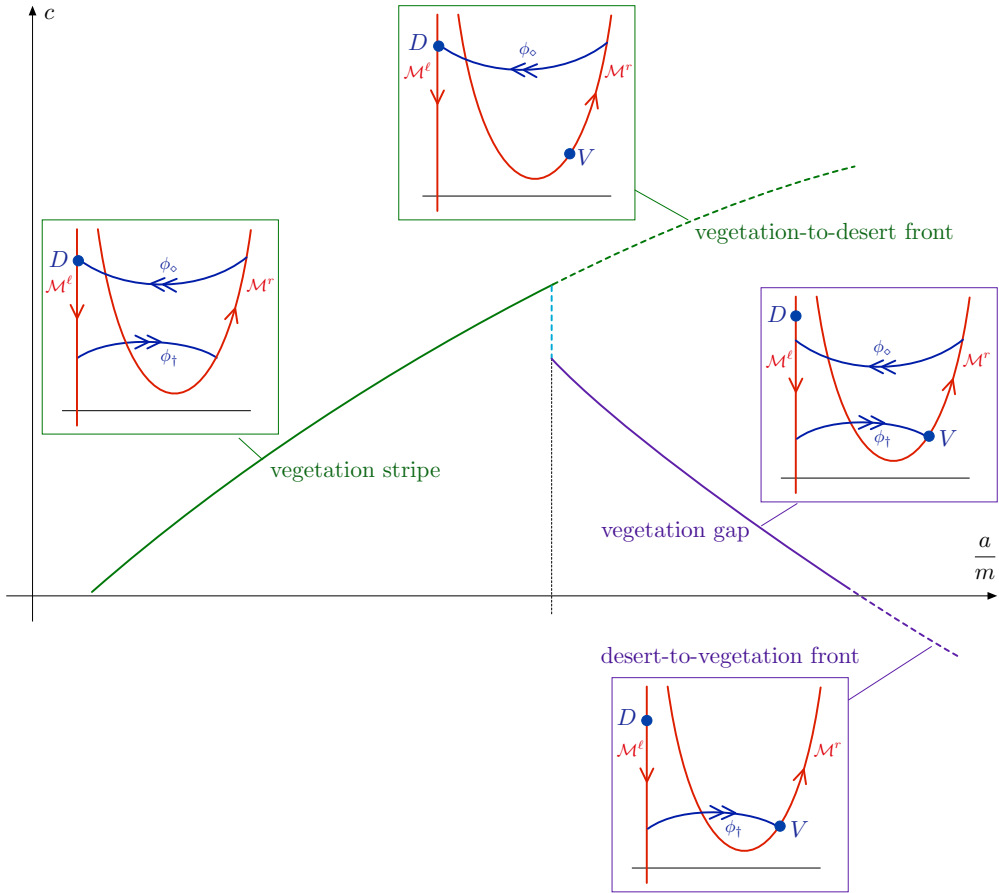


**Figure 5.3** – A sample singular  $\varepsilon = 0$  bifurcation diagram in  $(a/m, c)$  parameter space. The solid green line indicates stripe solutions, while the solid purple line denotes the gap solutions. Vegetation-to-desert fronts are indicated by the dashed green line. Finally, desert-to-vegetation front solutions are given by the dashed and solid purple lines. Schematic depictions of the associated singular limit geometries are depicted in the insets, where the labels  $D$  and  $V$  denote the locations of the desert and vegetated equilibrium states, respectively. The precise bifurcation structure depends on the value of the parameter  $b$ ; see section 5.2.4.

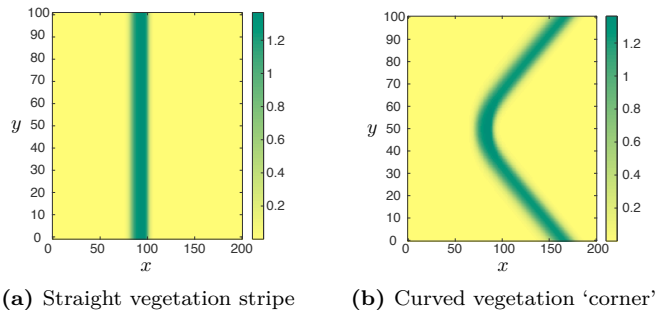


**Figure 5.4** – A snapshot of a straight (a) and slightly bent (b) traveling vegetation stripe solution (with  $c > 0$ ), obtained via direct numerical simulation of (5.1.2) with  $\varepsilon = 0.01$ ,  $m = 0.45$ ,  $b = 0.5$  and  $a = 1.2$ .

as a slow/fast system in the context of geometric singular perturbation theory. We determine the slow manifolds  $\mathcal{M}^\ell$ ,  $\mathcal{M}^m$  and  $\mathcal{M}^r$  and the fast connections  $\phi_\dagger$  and  $\phi_\diamond$  that connect the manifolds  $\mathcal{M}^\ell$  and  $\mathcal{M}^r$ , which are then used to construct singular stripe, gap and front solutions to (5.1.7). In section 5.3, we prove the persistence of these solutions for sufficiently small  $\varepsilon > 0$ . Next, in section 5.4, we compute the essential and point spectra of all these patterns using (formal) asymptotic computations, and show that all patterns are stable against all two dimensional perturbations. Subsequently, in section 5.5 these stability statements are made rigorous by carefully constructing eigenfunctions. In section 5.6 we inspect existence and stability of weakly bent (corner) solutions to (5.1.7). Then, in section 5.7 we present the results of numerical computations on closely related spatially periodic patterns and numerical simulations of both straight and bent patterns. We conclude with a brief discussion of the results in section 5.8.

## 5.2 Slow-fast analysis of traveling wave equation

In this section, we study the traveling wave equation (5.1.7) as a slow-fast system in the singular limit  $\varepsilon = 0$ . A discussion of the critical manifolds is given in section 5.2.1. In section 5.2.2, we describe the singular layer problem, and we construct families of singular front solutions. We describe the reduced flow on the critical manifolds in section 5.2.3, and we construct singular traveling front and stripe solutions in section 5.2.4, which consists of fast segments that are heteroclinic solutions to the singular layer problem and of slow segments that are solutions of the reduced flow on the critical manifolds.. Finally, section 5.2.5 contains statements of our main existence results.

### 5.2.1 Critical manifolds

The traveling wave ODE (5.1.7) is a two-fast-one-slow system. We obtain the fast subsystem or layer problem by setting  $\varepsilon = 0$  in (5.1.7), which results in the system

$$\begin{cases} u' &= 0, \\ v' &= q, \\ q' &= mv - R(v)G(u, v)v - cq, \end{cases} \quad (5.2.1)$$

or, equivalently, the collection of planar ODEs

$$\begin{cases} v' &= q, \\ q' &= mv - R(v)G(u, v)v - cq, \end{cases} \quad (5.2.2)$$

parameterized by  $u$ . We note that  $(v, q) = (0, 0) =: p_0(u)$  is always an equilibrium of (5.2.2); there are additional equilibria  $(v, 0)$  whenever  $v$  satisfies  $R(v)G(u, v) = m$ . Thus we see that there are additional equilibria  $p_{\pm}(u) := (v_{\pm}(u), 0)$ , where

$$v_{\pm}(u) = \frac{1 \pm \sqrt{1 - 4bm/u}}{2b}, \quad (5.2.3)$$

provided  $u \geq 4bm$ . We see that (5.2.2) admits three equilibria for  $u > 4bm$ , two equilibria for  $u = 4bm$ , and a single equilibrium for  $u < 4bm$ .

Denoting the right-hand-side of (5.2.2) by

$$F(v, q; u) := \begin{pmatrix} q \\ mv - R(v)G(u, v)v - cq \end{pmatrix}, \quad (5.2.4)$$

we consider the linearization of (5.2.2) about each of the three equilibria  $p_0, p_{\pm}$  that is given by

$$D_{(v,q)}F(0, 0; u) = \begin{pmatrix} 0 & 1 \\ m & -c \end{pmatrix}, \quad (5.2.5)$$

$$D_{(v,q)}F(v_{\pm}(u), 0; u) = \begin{pmatrix} 0 & 1 \\ \frac{u - 4mb \pm \sqrt{u^2 - 4mbu}}{2b} & -c \end{pmatrix}. \quad (5.2.6)$$

For  $c > 0$ , we deduce that the equilibrium  $p_0(u)$  is always a saddle. When  $u > 4bm$ , the equilibrium  $p_-(u)$  is a stable node or spiral, and the equilibrium  $p_+(u)$  is a saddle. When  $u = 4bm$ , the equilibrium  $p_+(4bm) = p_-(4bm)$  is not hyperbolic.

In the full system, the equilibria of the layer problem (5.2.2) form critical manifolds, given by three normally hyperbolic branches

$$\begin{aligned} \mathcal{M}_0^{\ell} &= \{v = q = 0\}, \\ \mathcal{M}_0^m &= \{p_-(u) : u > 4bm\}, \\ \mathcal{M}_0^r &= \{p_+(u) : u > 4bm\}, \end{aligned} \quad (5.2.7)$$

with the branches  $\mathcal{M}_0^m, \mathcal{M}_0^r$  meeting at a nonhyperbolic fold point  $\mathcal{F} = p_+(4bm) = p_-(4bm)$ ; see Figure 5.5. For  $u_1, u_2 \in \mathbb{R}$ , we will use the notation

$$\mathcal{M}_0^j[u_1, u_2] := \mathcal{M}_0^j \cap \{u_1 \leq u \leq u_2\} \quad (5.2.8)$$

to refer to a compact segment of one of the critical manifolds  $\mathcal{M}_0^j$ ,  $j = \ell, m, r$ .

We recall that there are (up to) three equilibria of the full system, given by  $(u, v, q) = (a, 0, 0)$  and  $(u, v, q) = (u_{1,2}, v_{1,2}, 0)$ ; see Figures 5.5 and 5.6. The equilibrium at  $(u, v, q) = (a, 0, 0)$  lies on the left branch  $\mathcal{M}_0^{\ell}$  and corresponds to  $p_0(a)$ , while that at  $(u, v, q) = (u_1, v_1, 0)$  corresponds to  $p_-(u_1)$  and lies on the middle branch  $\mathcal{M}_0^m$ . The location of the equilibrium  $(u, v, q) = (u_2, v_2, 0)$  depends on the parameter values: if  $a/m < 4b + 1/b$ , then it lies on the middle branch  $\mathcal{M}_0^m$  at  $p_-(u_2)$ , while if  $a/m > 4b + 1/b$ , then it lies on the right branch  $\mathcal{M}_0^r$  at  $p_+(u_2)$ . When  $a/m = 4b + 1/b$ , the equilibrium  $(u, v, q) = (u_2, v_2, 0)$  coincides with the fold  $\mathcal{F}$ .

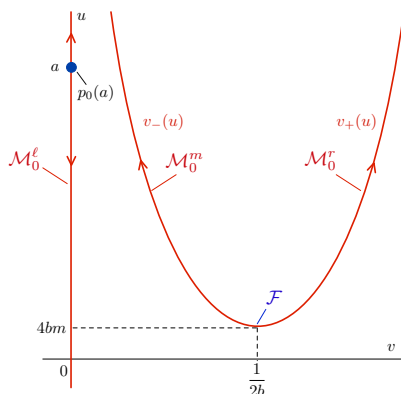


**Figure 5.5** – Shown are the three branches of the critical manifold  $\mathcal{M}_0$  and the associated reduced flow (5.2.20)-(5.2.22) in the case  $\frac{a}{m} < 2(b + \sqrt{1 + b^2})$ . There is a single equilibrium at  $p_0(a)$  on the left branch  $\mathcal{M}_0^\ell$  corresponding to the desert state  $(u, v, q) = (a, 0, 0)$ .

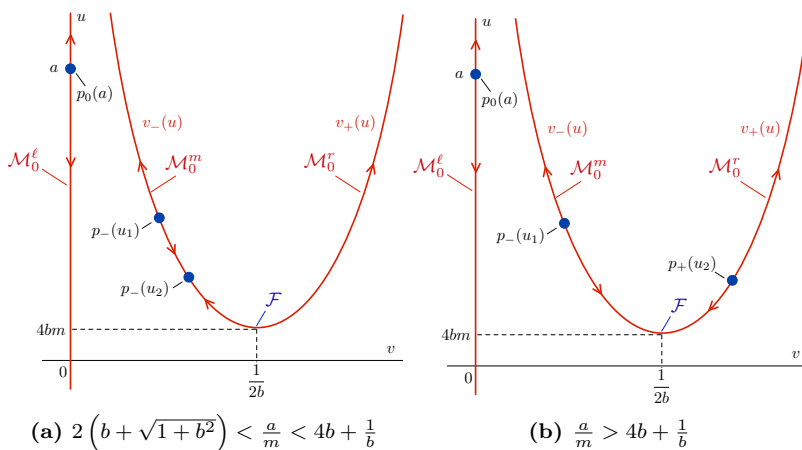


**Figure 5.6** – Shown are the three branches of the critical manifold  $\mathcal{M}_0$  and the associated reduced flow (5.2.20)-(5.2.22) in the case  $\frac{a}{m} > 2(b + \sqrt{1 + b^2})$ . The reduced problem admits two additional equilibria corresponding to the vegetated states  $(u, v, q) = (u_j, v_j, 0)$ ,  $j = 1, 2$ . The equilibrium  $(u, v, q) = (u_1, v_1, 0)$  corresponds to  $p_-(u_1)$  and lies on the middle branch  $\mathcal{M}_0^m$ . If  $\frac{a}{m} < 4b + 1/b$ , the equilibrium  $(u, v, q) = (u_2, v_2, 0)$  lies on the middle branch  $\mathcal{M}_0^m$  and corresponds to  $p_-(u_2)$ , while if  $\frac{a}{m} > 4b + 1/b$ , it lies on the right branch  $\mathcal{M}_0^r$  at  $p_+(u_2)$ .

## 5.2.2 Layer fronts

In the previous section we have constructed the critical manifolds  $\mathcal{M}_0^\ell$ ,  $\mathcal{M}_0^m$  and  $\mathcal{M}_0^r$ , and determined the location of the desert state  $p_0(a)$  on  $\mathcal{M}_0^\ell$  and the vegetation state  $p_+(u_2)$  on  $\mathcal{M}_0^r$  – under certain conditions on the parameters. In this section, we study the connections between the outer manifolds  $\mathcal{M}_0^\ell$  and  $\mathcal{M}_0^r$  – which present themselves as fronts in the fast layer problem (5.2.2) for certain values of  $u$  and  $c$ . Ultimately, the goal is to construct homoclinic and heteroclinic solutions to the equilibrium states  $p_0(a)$  and/or  $p_+(u_2)$ . Therefore, it is necessary to find front solutions that land on these states (because of the instability of these points on their respective critical manifolds). As these fronts are characterized by a specific speed  $c$ , a homoclinic connection can then only be constructed if a front connection going the other way can also be found for the same speed  $c$  (but possibly different value of  $u$ ). In this section, we first catalogue the possible front connections between  $\mathcal{M}_0^\ell$  and  $\mathcal{M}_0^r$ , and give the corresponding speeds. Subsequently, we determine whether we can find a pair of fast front connections – one from  $\mathcal{M}_0^r$  to  $\mathcal{M}_0^\ell$ , and one from  $\mathcal{M}_0^\ell$  to  $\mathcal{M}_0^r$  – that exist for the same speed  $c$ , such that one lands precisely at an equilibrium state and a singular homoclinic connection can be found. We first find those relevant pairs that land on  $p_0(a)$  and then those that land on  $p_+(u_2)$ .

### Front connections between $\mathcal{M}_0^\ell$ and $\mathcal{M}_0^r$

We are interested in fronts between the two saddle equilibria  $p_0(u) = (0, 0)$  and  $p_+(u) = (v_+(u), 0)$ ; equivalently, we search for connections between the outer branches  $\mathcal{M}_0^\ell, \mathcal{M}_0^r$ . For each value of  $u > 4mb$ , there are two such fronts,  $\phi_\diamond(\xi; u) = (v_\diamond(\xi; u), q_\diamond(\xi; u))^T$  and  $\phi_\dagger(\xi; u) = (v_\dagger(\xi; u), q_\dagger(\xi; u))^T$ , with explicit  $v$  profiles given by

$$\begin{aligned} v_\diamond(\xi; u) &= \frac{v_+(u)}{2} \left( 1 - \tanh \left( \frac{v_+ \sqrt{ub}}{2\sqrt{2}} \xi \right) \right), \\ v_\dagger(\xi; u) &= \frac{v_+(u)}{2} \left( 1 + \tanh \left( \frac{v_+ \sqrt{ub}}{2\sqrt{2}} \xi \right) \right), \end{aligned} \quad (5.2.9)$$

and wave speeds

$$\begin{aligned} c_\diamond^*(u) &= \frac{\sqrt{2bu}}{2} (v_+(u) - 2v_-(u)) \\ c_\dagger^*(u) &= -\frac{\sqrt{2bu}}{2} (v_+(u) - 2v_-(u)). \end{aligned} \quad (5.2.10)$$

The  $\diamond$ -fronts connect  $p_+$  to  $p_0$ , while the  $\dagger$ -fronts connect  $p_0$  to  $p_+$ ; see Figure 5.7.

When  $u = 4mb$ , the situation is slightly different as the equilibria  $p_\pm(u)$  collide in a saddle-node bifurcation at the fold point  $\mathcal{F}$ , and the equilibrium  $p_+(u)$  is no longer a saddle. However, it is still possible to find fronts between  $p_0$  and  $p_+(4bm) = p_-(4bm)$ . In particular, there exists a front connecting  $p_+(4bm)$  to  $p_0(4bm)$  for any

$$\begin{aligned} c &\leq c_{\diamond, \text{crit}} = b\sqrt{2m} (v_+(4bm) - 2v_-(4bm)) \\ &= -\sqrt{\frac{m}{2}}. \end{aligned} \quad (5.2.11)$$

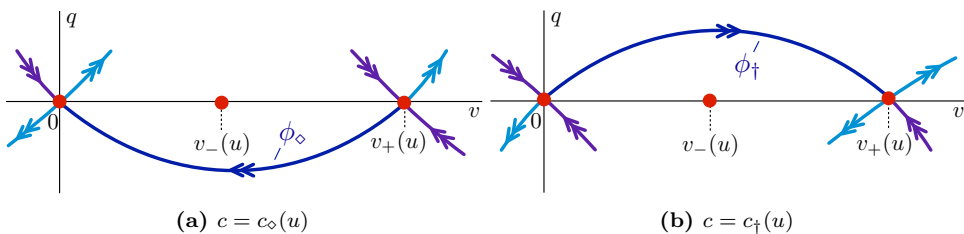


**Figure 5.7** – Shown are the singular fronts  $\phi_\diamond(\xi; u)$ ,  $\phi_\dagger(\xi; u)$  of the layer problem (5.2.2).

When  $c = c_{\diamond, \text{crit}}$  this front decays exponentially in backwards time, while for lesser speeds it decays only algebraically. Similarly, there exists a front connecting  $p_0(4bm)$  to  $p_+(4bm)$  for any

$$\begin{aligned} c &\geq c_{\dagger, \text{crit}} = -b\sqrt{2m}(v_+(4bm) - 2v_-(4bm)) \\ &= \sqrt{\frac{m}{2}}. \end{aligned} \quad (5.2.12)$$

When  $c = c_{\dagger, \text{crit}}$  this front decays exponentially in forwards time, while for greater speeds it decays only algebraically.

### Fronts asymptotic to $p_0(a)$

In particular, provided  $a > 4bm$ , the fronts (5.2.9) exist when  $u = a$ . Therefore we have a front connecting  $p_+(a)$  to  $p_0(a)$  – the equilibrium  $(a, 0, 0)$  of the full system (5.1.7) – when

$$\begin{aligned} c &= c_\diamond^*(a) \\ &= \frac{1}{2\sqrt{2b}} \left( -\sqrt{a} + 3\sqrt{a - 4bm} \right). \end{aligned} \quad (5.2.13)$$

We now search for fronts which exist simultaneously for the same speed but different value of  $u$ , in particular for  $u \leq a$ . We have the following.

**Lemma 5.2.1.** *For each  $\frac{a}{m} \geq \frac{9}{2}b$ , there exists a pair of fronts  $\phi_\diamond(\xi; a)$ ,  $\phi_\dagger(\xi; u^*(a))$  with speed*

$$c = c^*(a) := \frac{1}{2\sqrt{2b}} \left( -\sqrt{a} + 3\sqrt{a - 4bm} \right). \quad (5.2.14)$$

The front  $\phi_\diamond(\xi; a)$  connects  $p_+(a)$  to  $p_0(a)$  in the layer system (5.2.2) for  $u = a$ , while the front  $\phi_\dagger(\xi; u^*(a))$  connects  $p_0(u^*(a))$  to  $p_+(u^*(a))$  in the layer system (5.2.2) for  $u = u^*(a) \leq a$ , where

$$u^*(a) := \begin{cases} \frac{1}{8} (17a - 18bm - 15\sqrt{a^2 - 4abm}), & \frac{9}{2}b \leq \frac{a}{m} < \frac{25}{4}b; \\ 4bm, & \frac{a}{m} \geq \frac{25}{4}b. \end{cases} \quad (5.2.15)$$

*Proof.* When  $\frac{a}{m} = \frac{9}{2}b$ , we have  $c_\diamond^*(a) = 0 = c_\dagger^*(a)$ . Thus, the layer problem is Hamiltonian and therefore both heteroclinic orbits lie simultaneously in the plane  $u = a$ , forming a heteroclinic loop. For values of  $\frac{9}{2}b < \frac{a}{m} < \frac{25}{4}b$ , the second heteroclinic orbit



exists for a value of  $4bm < u^* < a$  given by (5.2.15), which can be obtained by solving the relation  $c_\diamond^*(a) = c_\dagger^*(u)$  for  $u = u^*(a)$ .

For  $a \geq \frac{25bm}{4}$ , the second heteroclinic orbit occurs when  $u = u^*(a) = 4bm$ ; the decay is exponential in forward time when  $a = \frac{25bm}{4}$ , and algebraic for  $a > \frac{25bm}{4}$ .  $\square$

**Remark 5.2.2.** *In the case  $4b \leq \frac{a}{m} \leq \frac{9}{2}b$ , there (also) exists a second front  $\phi_\dagger(\xi; u^*(a))$  with speed  $c = c^*(a)$  that connects  $p_0(u^*(a))$  to  $p_+(u^*(a))$  in the layer system (5.2.2) for  $u = u^*(a)$ , where*

$$u^*(a) = \frac{1}{8} \left( 17a - 18bm - 15\sqrt{a^2 - 4abm} \right).$$

*However, in this case  $u^*(a) > a$ , which – because of the flow on  $\mathcal{M}_0^r$  (see section 5.2.3) – prevents the existence of a homoclinic connection in the full system.*

### Fronts asymptotic to $p_+(u_2)$

We recall that for  $a/m > 4b + 1/b$ , the equilibrium  $p_+(u_2)$  on the right branch  $\mathcal{M}_0^r$  corresponds to the equilibrium  $(u_2, v_2, 0)$  of the full system (5.1.7). For  $a/m = 4b + 1/b$ , this equilibrium lies precisely on the fold  $\mathcal{F}$ . We now search for singular fronts to this equilibrium for values of  $a/m \geq 4b + 1/b$ , and the argument is similar as above. When  $a/m > 4b + 1/b$ , there exists a front connecting  $p_0(u_2)$  to  $p_+(u_2)$  when

$$\begin{aligned} c &= c_\dagger^*(u_2) \\ &= -\frac{1}{2\sqrt{2b}} \left( -\sqrt{u_2} + 3\sqrt{u_2 - 4bm} \right), \end{aligned} \tag{5.2.16}$$

and when  $a/m = 4b + 1/b$  this front exists for each  $c \geq c_{\dagger, \text{crit}}$ , with exponential decay in forward time for  $c = c_{\dagger, \text{crit}}$  and algebraic decay when  $c > c_{\dagger, \text{crit}}$ . We again search for fronts which exist simultaneously for the same speed but different value of  $u$ , and we have the following lemma, analogous to Lemma 5.2.1.

**Lemma 5.2.3.** *Concerning the layer problem (5.2.2), the following hold.*

- (i) *For each  $4b + \frac{1}{b} < \frac{a}{m} \leq \frac{9}{2}b + \frac{2}{b}$ , there exists a pair of fronts  $\phi_\diamond(\xi; \hat{u}_2(a))$ ,  $\phi_\dagger(\xi; u_2)$  with speed  $\hat{c}(a) = c_\dagger^*(u_2)$ . The front  $\phi_\dagger(\xi; u_2)$  connects  $p_0(u_2)$  to  $p_+(u_2)$  in the layer system (5.2.2) for  $u = u_2$ , while the front  $\phi_\diamond(\xi; \hat{u}_2(a))$  connects  $p_+(\hat{u}_2(a))$  to  $p_0(\hat{u}_2(a))$  in the layer system (5.2.2) for  $u = \hat{u}_2(a)$ , where*

$$\hat{u}_2(a) := \frac{1}{8} \left( 17u_2 - 18bm - 15\sqrt{u_2^2 - 4u_2bm} \right). \tag{5.2.17}$$

- (ii) *When  $a/m = 4b + 1/b$ , for each  $c \geq c_{\dagger, \text{crit}}$ , there exists a pair of fronts  $\phi_\dagger(\xi; u_2)$ ,  $\phi_\diamond(\xi; \hat{u}(c))$ , where  $\hat{u}(c)$  is an increasing function of  $c$  which satisfies  $\hat{u}(c_{\dagger, \text{crit}}) = \hat{u}_2(4mb + m/b)$ .*

*Proof.* For (i), when  $\frac{a}{m} = \frac{9}{2}b + \frac{2}{b}$ , we have  $c_\diamond^*(u_2) = 0 = c_\dagger^*(u_2)$ , and therefore both heteroclinic orbits lie simultaneously in the plane  $u = u_2$ , forming a heteroclinic loop. For values of  $4b + \frac{1}{b} < \frac{a}{m} < \frac{9}{2}b + \frac{2}{b}$ , the second heteroclinic orbit exists for a value of  $\hat{u}_2 > u_2$  given by the solution of (5.2.17), which can be obtained by solving the relation  $c_\diamond^*(u) = c_\dagger^*(u_2)$  for  $u = \hat{u}_2$ .

For (ii), when  $a/m = 4b + 1/b$ , the equilibrium  $p_+(u_2)$  lies precisely on the fold  $\mathcal{F}$  and hence we obtain the fronts  $\phi_{\dagger}(\xi; u_2)$  for each  $c \geq c_{\dagger, \text{crit}}$ . The facts regarding  $\hat{u}(c)$  follow by noticing that the relation

$$\begin{aligned} c_{\diamond}^*(u) &= \frac{\sqrt{2bu}}{2} (v_+(u) - 2v_-(u)) \\ &= \frac{1}{2\sqrt{2b}} \left( -\sqrt{u} + 3\sqrt{u - 4bm} \right) \end{aligned} \quad (5.2.18)$$

defines  $c_{\diamond}^*(u)$  as a strictly increasing function of  $u$ , and that  $u_2 = 4bm$  when  $a/m = 4b + 1/b$ , so that  $\hat{u}_2(4mb + m/b) = 25bm/4$ , and  $c_{\diamond}^*(25bm/4) = c_{\dagger, \text{crit}}$ .  $\square$

### 5.2.3 Slow flow

We now examine the slow flow restricted to the critical manifolds  $\mathcal{M}_0^{\ell}$  and  $\mathcal{M}_0^r$ . We rescale  $\tau = \varepsilon\xi$  and obtain the corresponding slow system

$$\begin{cases} u_{\tau} &= \frac{1}{1+\varepsilon c} (u - a + G(u, v)v) \\ \varepsilon v_{\tau} &= q \\ \varepsilon q_{\tau} &= mv - R(v)G(u, v)v - cq. \end{cases} \quad (5.2.19)$$

By setting  $\varepsilon = 0$ , we obtain the reduced flow on  $\mathcal{M}_0^{\ell}$  as

$$u_{\tau} = u - a, \quad (5.2.20)$$

on  $\mathcal{M}_0^m$  as

$$u_{\tau} = u - a + G(u, v_-(u))v_-(u), \quad (5.2.21)$$

and on  $\mathcal{M}_0^r$  as

$$u_{\tau} = u - a + G(u, v_+(u))v_+(u). \quad (5.2.22)$$

See Figures 5.5 and 5.6 for depictions of the reduced flow, depending on the value of  $a/m$ . We see that for  $u < a$ , under the reduced flow on  $\mathcal{M}_0^{\ell}$ ,  $u$  is always decreasing, while on  $\mathcal{M}_0^r$ ,  $u$  is always increasing, provided  $a/m < 4b + 1/b$ . When  $a/m = 4b + 1/b$ , there exists an equilibrium of the full system  $(u_2, v_2, 0)$  which coincides with the fold  $\mathcal{F}$ , which thus takes the form of a canard point [104]. As  $a$  increases through this value, this equilibrium moves up along the right branch  $\mathcal{M}_0^r$ . In that case, the flow is away from this equilibrium point; that is,  $u$  is decreasing when  $u < u_2$  and increasing when  $u > u_2$ .

### 5.2.4 Singular orbits

In the previous sections we have studied the slow flow on the manifolds  $\mathcal{M}_0^{\ell}$  and  $\mathcal{M}_0^r$  and the dynamics of fast transitions between these manifolds. In this section, we use this knowledge to construct families of singular orbits, which will serve as the basis for constructing traveling front and pulse solutions to (5.1.2). These singular orbits are constructed for open regions in  $(a, b, m)$  parameter space, with the wavespeed  $c$  in general determined uniquely by the value of  $(a, b, m)$ . The bifurcation structure, as well as the singular limit geometry of the associated solution orbits, is depicted in the

bifurcation diagrams in Figures 5.8a and 5.8b. These diagrams show the dependence of the wave speed  $c$  on the value of the quantity  $a/m$ , in the regions  $b < 2/3$  and  $b > 2/3$ , as the bifurcation structure changes qualitatively as  $b$  crosses through the critical value  $2/3$ .

We first consider traveling pulse solutions, which can be thought of as two front-type solutions glued together to create a profile which is bi-asymptotic to one of the equilibrium states with a plateau in between. These come in two varieties: vegetation stripe solutions, considered first in this section, which manifest as homoclinic orbits to the desert equilibrium state  $p_0(a)$ , and vegetation gap solutions, considered second in this section, which arise as homoclinic orbits to the equilibrium  $p_+(u_2)$ . In both cases, the corresponding homoclinic orbits are composed of two portions of the slow manifolds  $\mathcal{M}_0^\ell$  and  $\mathcal{M}_0^r$  concatenated with two fast jumps in between, which exist for the same value of  $c$ . The singular limit geometry for these solutions is shown in the bifurcation diagrams Figures 5.8a and 5.8b (see also Figure 5.9 for more details), in which the stripe solutions are defined along the upper solid green, and the gap solutions are defined along the upper solid purple curve. The distinction between the cases  $b < 2/3$  and  $b > 2/3$  is related to the manner in which these two curves interact.

Next, we consider singular front solutions, characterized by a sharp transition from the uniform desert state to the uniformly vegetated state or vice versa. In the slow/fast framework of the traveling wave equation (5.1.7), these solutions manifest as heteroclinic orbits between the equilibria  $p_0(a)$  and  $p_+(u_2)$ , and are composed of a single slow segment along one of the manifolds  $\mathcal{M}_0^\ell$  and  $\mathcal{M}_0^r$  concatenated with a fast jump to the opposite slow manifold. In the diagrams Figures 5.8a and 5.8b, these singular front solutions are defined along the upper solid and dashed green and purple curves in the region  $a/m > 4b + 1/b$ . The green curves correspond to front solutions in which the vegetated state is downslope of the desert state, while the desert state is downslope of the vegetated state along the purple curves.

We briefly discuss periodic orbits at the end of this section, and in the following section, section 5.2.5, we state our main existence results regarding traveling front, stripe, and gap solutions to (5.1.2).

### Homoclinic orbits to the desert state $p_0(a)$

By Lemma 5.2.1, for each  $\frac{a}{m} \geq \frac{9b}{2}$ , there exists a pair of fronts  $\phi_\circ(\xi; a), \phi_\dagger(\xi; u^*(a))$  with the same speed

$$c = c^*(a) := \frac{1}{2\sqrt{2b}} \left( -\sqrt{a} + 3\sqrt{a - 4bm} \right). \quad (5.2.23)$$

We can concatenate these fronts with portions of the critical manifolds  $\mathcal{M}_0^{\ell,r}$  in order to construct singular homoclinic solutions to the equilibrium  $p_0(a)$ . However, when  $a/m > 4b + 1/b$ , the equilibrium  $p_+(u_2)$  lies on  $\mathcal{M}_0^r$  and can block these orbits. For each  $\frac{a}{m} \geq \frac{9b}{2}$ , we have a candidate singular homoclinic orbit to the desert state  $p_0(a)$  given by

$$\mathcal{H}_d(a) := \mathcal{M}_0^\ell[u^*(a), a] \cup \phi_\dagger(u^*(a)) \cup \mathcal{M}_0^r[u^*(a), a] \cup \phi_\circ(a), \quad (5.2.24)$$

corresponding to a vegetation stripe solution (see Figure 5.9), where the notation  $\mathcal{M}_0^\ell[u_1, u_2]$  was defined in (5.2.8). This orbit will be blocked if the equilibrium  $p_+(u_2)$  lies on  $\mathcal{M}_0^r$  with  $u^*(a) \leq u_2$ . There are two cases based on the expression for  $u^*(a)$  in (5.2.15). If  $a/m \geq 25b/4$ , then this orbit is blocked whenever  $p_+(u_2)$  lies on  $\mathcal{M}_0^r$ ,

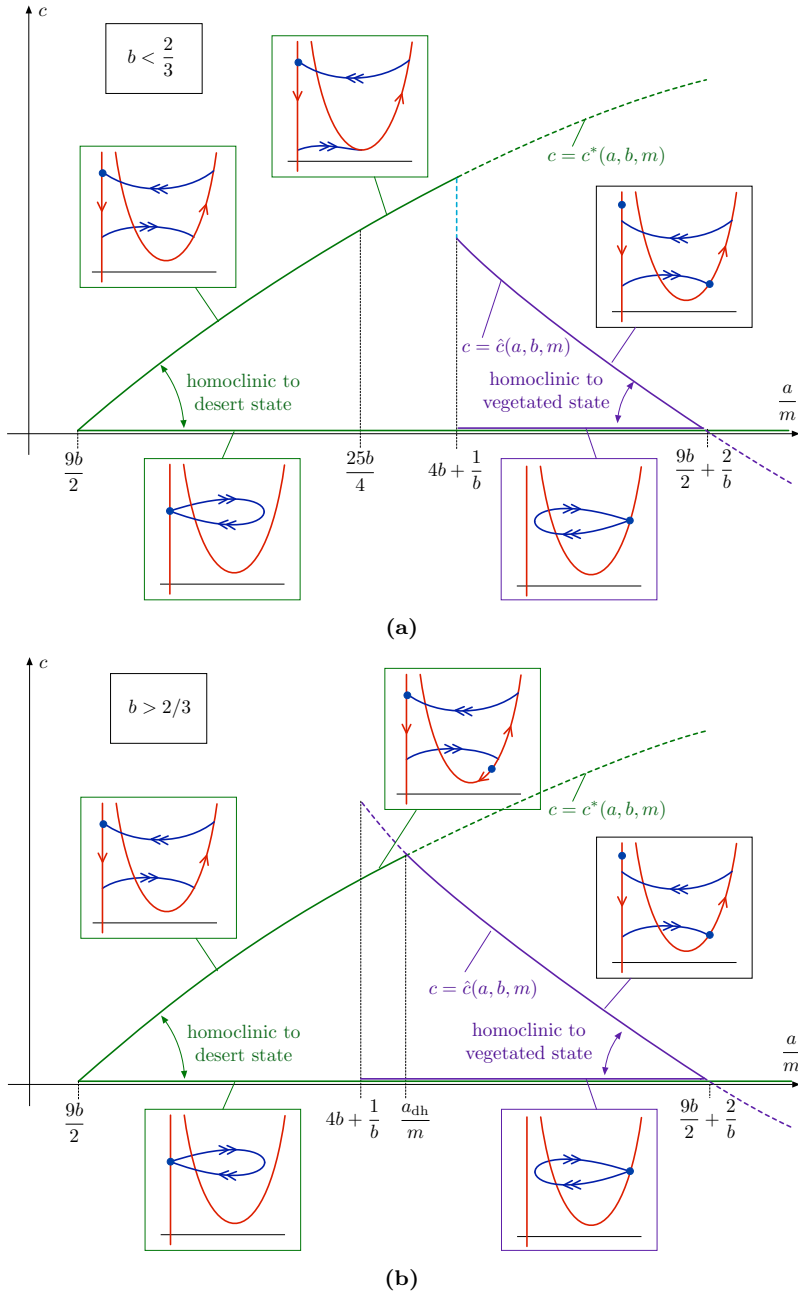


**Figure 5.8** – Shown are the singular  $\varepsilon = 0$  bifurcation diagrams in  $(a, c)$  parameter space in the cases  $b < 2/3$  (a) and  $b > 2/3$  (b).

that is, for any value of  $a/m \geq 4b + 1/b$ . If  $a/m < 25b/4$ , then this orbit is blocked if  $u_2 \geq u^*(a)$ , which occurs when

$$\frac{a}{m} \geq \bar{a}_{\text{dh}} := 2b + \frac{5\sqrt{3}b^2}{2\sqrt{4+3b^2}} + \frac{8}{\sqrt{12+9b^2}}. \quad (5.2.25)$$

We therefore expect a different singular bifurcation diagram for the cases  $4b + 1/b > 25b/4$  or  $4b + 1/b < 25b/4$  (i.e.  $b < 2/3$  respectively  $b > 2/3$ ). In the former case the singular front  $\phi_{\dagger}(\xi; u^*(a))$  can jump precisely onto the fold point  $\mathcal{F}$ ; in the latter case this is not possible. Equivalently, the structure changes depending on whether  $b < 2/3$  or  $b > 2/3$  (see Figures 5.8a and 5.8b). We define the quantity

$$\bar{a}(b) := \begin{cases} 4b + 1/b & b \leq 2/3 \\ \bar{a}_{\text{dh}} & b > 2/3 \end{cases}. \quad (5.2.26)$$

Then for each  $b, m > 0$ , we can construct the singular homoclinic orbits  $\mathcal{H}_d(a)$  for  $\frac{9}{2}b \leq \frac{a}{m} \leq \bar{a}(b)$ . We note that when  $b \leq 2/3$  and  $\frac{a}{m} \in [4b + 1/b, 25b/4]$ , the front  $\phi_{\dagger}(u^*(a))$  jumps precisely onto the nonhyperbolic fold point  $\mathcal{F}$ . While it is possible to construct homoclinic orbits in this regime as well as determine the stability of the underlying traveling wave solution [10, 22, 25] using geometric blow-up methods, we do not consider this case here. Rather we restrict our attention to orbits which jump on/off normally hyperbolic portions of the critical manifold. To that end, we define the quantity

$$\bar{a}_{\text{hyp}}(b) := \begin{cases} 25b/4 & b \leq 2/3 \\ \bar{a}_{\text{dh}} & b > 2/3 \end{cases}, \quad (5.2.27)$$

and consider only the singular homoclinic orbits  $\mathcal{H}_d(a)$  for  $\frac{9}{2}b \leq \frac{a}{m} < \bar{a}_{\text{hyp}}(b)$ .

**Remark 5.2.4.** *In addition to the class of homoclinic orbits described above, there also exist singular homoclinic orbits to the equilibrium  $p_0(a)$  lying entirely in the plane  $u = a$ . These orbits in fact correspond to solutions of the layer problem (5.2.2) for  $u = a$  and  $c = 0$ , and they are depicted along the lower green curves in the bifurcation diagrams in Figures 5.8a and 5.8b. As with the singular homoclinic orbits  $\mathcal{H}_d(a)$  constructed in this section, it is possible to show that these layer homoclinic orbits also persist for sufficiently small  $\varepsilon > 0$  using geometric singular perturbation arguments, and in fact they lie on the same continuation branch; see Figure 5.16. Furthermore, the bifurcation structure near these orbits is surprisingly rich; a detailed analysis is carried out in [24]. However, unlike the orbits  $\mathcal{H}_d(a)$ , the resulting traveling wave solutions are typically unstable as solutions to (5.1.2), and we therefore refrain from analyzing these solutions in this work.*

### Homoclinic orbits to the vegetated state $p_+(u_2)$

Similarly, we can construct singular homoclinic orbits to the vegetated state  $p_+(u_2)$  using the fronts from Lemma (5.2.3). By similar arguments as above, we obtain singular homoclinic orbits

$$\mathcal{H}_v(a) := \mathcal{M}_0^r[u_2, \hat{u}_2(a)] \cup \phi_{\circ}(\hat{u}_2(a)) \cup \mathcal{M}_0^{\ell}[u_2, \hat{u}_2(a)] \cup \phi_{\dagger}(u_2), \quad (5.2.28)$$

corresponding to vegetation gap solutions. For each  $b, m > 0$ , these orbits can be constructed for parameters  $\bar{a}(b) \leq \frac{a}{m} \leq \frac{9}{2}b + 2/b$ .

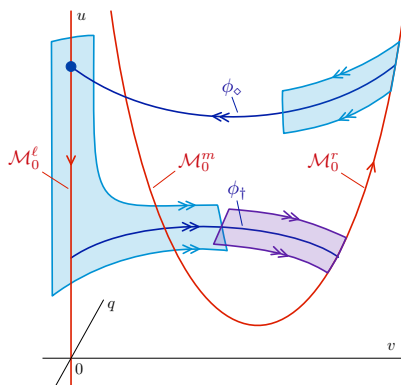


**Figure 5.9** – Shown is the singular orbit  $\mathcal{H}_d(a)$  homoclinic to the desert state  $p_0(a)$ . The orbit first traverses a portion of the manifold  $\mathcal{M}_0^\ell$ , then the front  $\phi_\dagger(u^*(a))$ , followed by a portion of the critical manifold  $\mathcal{M}_0^r$ , and finally the front  $\phi_\circ(a)$ .

**Remark 5.2.5.** *Additionally, in the case  $b < 2/3$ , using Lemma 5.2.3 (ii), when  $a = 4bm + m/b$ , we also obtain homoclinic orbits*

$$\widehat{\mathcal{H}}_v(c) := \mathcal{M}_0^r[u_2, \hat{u}(c)] \cup \phi_\circ(\hat{u}(c)) \cup \mathcal{M}_0^\ell[u_2, \hat{u}(c)] \cup \phi_\dagger(u_2) \quad (5.2.29)$$

for each  $c_{\dagger, \text{crit}} \leq c \leq c^*(4bm + m/b)$ .

**Remark 5.2.6.** *Similarly as in section 5.2.4, there exist singular homoclinic orbits  $p_+(u_2)$  lying entirely in the plane  $u = u_2$  for  $c = 0$ ; see Remark 5.2.4. These orbits are depicted in Figures 5.8a and 5.8b along the lower purple curves. We remark on their presence here, but we refer to [24] for a detailed singular bifurcation analysis.*

### Heteroclinic orbits connecting desert state $p_0(a)$ and vegetated state $p_+(u_2)$

To construct singular heteroclinic solutions that connect the steady state  $p_0(a)$  to the steady state  $p_+(u_2)$ , we can concatenate  $\mathcal{M}_0^\ell$  with a front  $\phi_\dagger$  that limits onto the fixed point  $p_+(u_2)$ . The latter fronts only exist when  $p_+(u_2)$  lies on  $\mathcal{M}_0^r$ , i.e. when  $\frac{a}{m} > 4b + \frac{1}{b}$ . Hence, a singular heteroclinic orbit connecting  $p_0(a)$  to  $p_+(u_2)$  is given by

$$\mathcal{H}_{dv}(a) := \mathcal{M}_0^\ell[u_2, a] \cup \phi_\dagger(u_2), \quad (5.2.30)$$

the speed of which is  $c = \hat{c}(a)$ .

Similarly, a heteroclinic orbit connecting  $p_+(u_2)$  to  $p_0(a)$  can be found by concatenating  $\mathcal{M}_0^r$  with a front  $\phi_\circ$  that limits onto the fixed point  $p_0(a)$ . Again, this can only happen when  $\frac{a}{m} > 4b + \frac{1}{b}$ ; a candidate orbit is given by

$$\mathcal{H}_{vd}(a) := \mathcal{M}_0^r[u_2, a] \cup \phi_\circ(a), \quad (5.2.31)$$

the speed of which is  $c = c^*(a)$ .

**Remark 5.2.7.** *We note that there exist additional heteroclinic orbits for values of  $2(b + \sqrt{1 + b^2}) < \frac{a}{m} < 4b + \frac{1}{b}$ . However, in this parameter regime, the steady state  $(U_2, V_2)$  corresponding to the equilibrium  $p_+(u_2)$  is unstable (against some non-uniform perturbations) in the original PDE (5.1.2). Hence a heteroclinic orbit in this regime corresponds to a front which invades the unstable vegetated state. We do not analyze such invasion fronts in this work; rather, we focus on the bistable regime, corresponding to the singular heteroclinic orbits  $\mathcal{H}_{vd}(a)$  described above.*

## Periodic orbits

In this section, we comment briefly on periodic orbits. Following the construction as for singular homoclinic orbits in section 5.2.4, it is also possible to construct singular periodic orbits by concatenating portions of the critical manifolds  $\mathcal{M}_0^\ell, \mathcal{M}_0^r$  with fast layer transitions in between, provided the relevant segments of  $\mathcal{M}_0^\ell, \mathcal{M}_0^r$  do not contain either of the equilibria  $p_0(a)$  or  $p_+(u_2)$ . Hence, one expects to find singular periodic orbits for any value of  $\frac{9b}{2} < \frac{a}{m} < \frac{9b}{2} + \frac{2}{b}$ , and any value of the wavespeed  $0 < c < \min\{c^*(a, b, m), \hat{c}(a, b, m)\}$ . Further, general theory predicts that such periodic orbits persist for small  $\varepsilon > 0$  [159]; these solutions correspond to wavetrain solutions of (5.1.2), or periodic vegetation stripes. While such solutions are perhaps more ecologically relevant, in the following we focus on traveling pulse solutions as the question of stability, particularly in two spatial dimensions, is more analytically tractable.

We remark that periodic wavetrain solutions have been found in a similar slow-fast context in the FitzHugh–Nagumo equation [21, 79], and furthermore, their spectral stability (in one spatial dimension) has been studied in [60].

### 5.2.5 Main existence results

In this section, we have studied (5.1.2) in the singular limit  $\varepsilon \downarrow 0$ . Here, we have found several singular homoclinic and heteroclinic orbits. These orbits persist for  $\varepsilon > 0$ , as we will prove in section 5.3. To summarize our findings, we end this section with our main existence results.

**Theorem 5.2.8** (Vegetation stripe solution). *Fix  $b, m > 0$  and  $a$  such that  $a/m \in (\frac{9}{2}b, \bar{a}_{\text{hyp}}(b))$ . There exists  $\varepsilon_0 > 0$  such that for  $\varepsilon \in (0, \varepsilon_0)$ , (5.1.2) admits a traveling pulse solution  $\phi_d(\xi; a, \varepsilon) = (u_d, v_d)(\xi; a, \varepsilon)$  with speed*

$$c_d(a, \varepsilon) = c^*(a) + \mathcal{O}(\varepsilon) \quad (5.2.32)$$

and satisfying  $\lim_{|\xi| \rightarrow \infty} (u_d, v_d)(\xi; a, \varepsilon) = (U_0, V_0)$ . The length of the vegetation stripe is given to leading order by

$$\varepsilon L_d := \int_{u^*(a)}^a \frac{du}{u - a + uv_+(u)^2}. \quad (5.2.33)$$

**Theorem 5.2.9** (Vegetation gap solution). *Fix  $b, m > 0$  and  $a$  such that  $a/m \in (\bar{a}(b), \frac{9}{2}b + \frac{2}{b})$ . There exists  $\varepsilon_0 > 0$  such that for  $\varepsilon \in (0, \varepsilon_0)$ , (5.1.2) admits a traveling pulse solution  $\phi_v(\xi; a, \varepsilon) = (u_v, v_v)(\xi; a, \varepsilon)$  with speed*

$$c_v(a, \varepsilon) = \hat{c}(a) + \mathcal{O}(\varepsilon) \quad (5.2.34)$$

and satisfying  $\lim_{|\xi| \rightarrow \infty} (u_v, v_v)(\xi; a, \varepsilon) = (U_2, V_2)$ . The length of the vegetation gap is given to leading order by

$$\varepsilon L_v := \int_{\hat{u}_2}^{u_2} \frac{du}{u - a} = \log \left( \frac{u_2(a) - a}{\hat{u}_2 - a} \right). \quad (5.2.35)$$

**Theorem 5.2.10** (Desert front solution). *Fix  $b, m > 0$  and  $a$  such that  $a/m > 4b + \frac{1}{b}$ . There exists  $\varepsilon_0 > 0$  such that for  $\varepsilon \in (0, \varepsilon_0)$ , (5.1.2) admits a traveling front solution  $\phi_{dv}(\xi; a, \varepsilon) = (u_{dv}, v_{dv})(\xi; a, \varepsilon)$  with speed*

$$c_{dv}(a, \varepsilon) = c^*(a) + \mathcal{O}(\varepsilon) \quad (5.2.36)$$

and satisfying  $\lim_{\xi \rightarrow -\infty} (u_{dv}, v_{dv})(\xi; a, \varepsilon) = (U_0, V_0)$  and  $\lim_{\xi \rightarrow \infty} (u_{dv}, v_{dv})(\xi; a, \varepsilon) = (U_2, V_2)$ .

**Theorem 5.2.11** (Vegetation front solution). *Fix  $b, m > 0$  and  $a$  such that  $a/m > 4b + \frac{1}{6}$ . There exists  $\varepsilon_0 > 0$  such that for  $\varepsilon \in (0, \varepsilon_0)$ , (5.1.2) admits a traveling front solution  $\phi_{vd}(\xi; a, \varepsilon) = (u_{vd}, v_{vd})(\xi; a, \varepsilon)$  with speed*

$$c_{vd}(a, \varepsilon) = \hat{c}(a) + \mathcal{O}(\varepsilon) \quad (5.2.37)$$

and satisfying  $\lim_{\xi \rightarrow -\infty} (u_{vd}, v_{vd})(\xi; a, \varepsilon) = (U_2, V_2)$  and  $\lim_{\xi \rightarrow \infty} (u_{vd}, v_{vd})(\xi; a, \varepsilon) = (U_0, V_0)$ .

**Remark 5.2.12.** *We recall that the case  $b = 0$  corresponds to the original Klausmeier model [95]; see Remark 5.1.1. From the geometry of the critical manifold (see Figure 5.5), the degeneracy of the limit  $b \rightarrow 0$  becomes apparent. In particular, the branch  $\mathcal{M}_0^r$  of the critical manifold is sent to infinity, and the left branch  $\mathcal{M}_0^l$  coincides with the hyperbola  $v = m/u$  in the plane  $q = 0$ . In the current analysis, we consider only the case  $b > 0$ . However, we note that under appropriate rescalings, it is possible to unfold the degenerate case  $b = 0$  and construct traveling wave solutions. Additional complications arise in the singular perturbation analysis due to loss of normal hyperbolicity along the critical manifold, for which blow up desingularization techniques are needed. We refer to [23] for the details.*

## 5.3 Persistence of solutions for $0 < \varepsilon \ll 1$

In this section, we prove that the singular orbits constructed in section 5.2.4 perturb to solutions of (5.1.7) for sufficiently small  $\varepsilon > 0$  using methods of geometric singular perturbation theory. In section 5.3.1, we prove technical lemmata regarding the transversality of the fast connections  $\phi_{\dagger, \diamond}$ , and we discuss the proofs of Theorems 5.2.8–5.2.11 in section 5.3.2.

### 5.3.1 Transversality along singular orbits

We consider the layer system (5.2.1)

$$\begin{cases} u' &= 0 \\ v' &= q \\ q' &= mv - (1 - bv)uv^2 - cq. \end{cases} \quad (5.3.1)$$

As outlined in section 5.2.2, this system possesses heteroclinic connections  $\phi_{\diamond, \dagger} = (v_{\diamond, \dagger}, q_{\diamond, \dagger})$  between the left and right critical manifolds  $\mathcal{M}_0^{\ell, r}$ , where the speed  $c$  for a given heteroclinic orbit depends on the value of  $u$  (as well as the other parameters). We define the stable and unstable manifolds,  $\mathcal{W}^s(\mathcal{M}_0^j)$  and  $\mathcal{W}^u(\mathcal{M}_0^j)$ , of a critical manifold  $\mathcal{M}_0^j$ ,  $j = \ell, r$ , as the union of the stable and unstable manifolds, respectively, of the corresponding equilibria of the layer problem (5.3.1).

Then an orbit  $\phi_{\dagger}$  lies in the intersection of  $\mathcal{W}^u(\mathcal{M}_0^l)$  and  $\mathcal{W}^s(\mathcal{M}_0^r)$ , while an orbit  $\phi_{\diamond}$  lies in the intersection of  $\mathcal{W}^u(\mathcal{M}_0^r)$  and  $\mathcal{W}^s(\mathcal{M}_0^l)$ . For a given orbit  $\phi_{\dagger}$ , which we suppose exists for some values of  $(c, u) = (c_0, u_0)$ , we aim to determine how this connection breaks as  $(c, u)$  varies near  $(c_0, u_0)$ ; that is, we determine the transversality of the intersection of  $\mathcal{W}^u(\mathcal{M}_0^l)$  and  $\mathcal{W}^s(\mathcal{M}_0^r)$  with respect to  $(c, u)$ . We find the following.



**Lemma 5.3.1.** *Consider a heteroclinic orbit  $\phi_{\dagger}$  which lies in the intersection of  $\mathcal{W}^u(\mathcal{M}_0^{\ell})$  and  $\mathcal{W}^s(\mathcal{M}_0^r)$  for some  $(c, u) = (c_0, u_0)$ . Then this intersection is transverse in  $(c, u)$ , and we compute the splitting of  $\mathcal{W}^u(\mathcal{M}_0^{\ell})$  and  $\mathcal{W}^s(\mathcal{M}_0^r)$  along  $\phi_{\dagger}$  via the distance function*

$$D_{\dagger}(\tilde{c}, \tilde{u}) = M_{\dagger}^c \tilde{c} + M_{\dagger}^u \tilde{u} + \mathcal{O}(\tilde{c}^2 + \tilde{u}^2) \quad (5.3.2)$$

where  $\tilde{c} := c - c_0$ ,  $\tilde{u} := u - u_0$ , and

$$\begin{aligned} M_{\dagger}^c &= \int_{-\infty}^{\infty} e^{c_0 \xi} q_{\dagger}(\xi)^2 d\xi > 0, \\ M_{\dagger}^u &= \int_{-\infty}^{\infty} e^{c_0 \xi} (1 - bv_{\dagger}(\xi)) v_{\dagger}(\xi)^2 q_{\dagger}(\xi) d\xi > 0. \end{aligned} \quad (5.3.3)$$

*Proof.* We use Melnikov theory to compute the distance between the unstable manifold  $\mathcal{W}^u(\mathcal{M}_0^{\ell})$  and the stable manifold  $\mathcal{W}^s(\mathcal{M}_0^r)$  to first order in  $|c - c_0|$  and  $|u - u_0|$ . We consider the adjoint equation of the linearization of (5.3.1) about the front  $\phi_{\dagger}$  given by

$$\psi' = \begin{pmatrix} 0 & -m + uv_{\dagger}(\xi)(2 - 3bv_{\dagger}(\xi)) \\ -1 & c \end{pmatrix} \psi. \quad (5.3.4)$$

The space of bounded solutions is one-dimensional and spanned by

$$\begin{aligned} \psi_{\dagger}(\xi) &:= e^{c_0 \xi} \begin{pmatrix} q'_{\dagger}(\xi) \\ -v'_{\dagger}(\xi) \end{pmatrix} \\ &= e^{c_0 \xi} \begin{pmatrix} q'_{\dagger}(\xi) \\ -q_{\dagger}(\xi) \end{pmatrix} \end{aligned} \quad (5.3.5)$$

Let  $F_0$  denote the right hand side of (5.3.1), and define the Melnikov integrals

$$M_{\dagger}^{\nu} := \int_{-\infty}^{\infty} D_{\nu} F_0(\phi_{\dagger}(\xi)) \cdot \psi_{\dagger}(\xi) d\xi, \quad (5.3.6)$$

for  $\nu = c, u$ . The quantities  $M_{\dagger}^c, M_{\dagger}^u$  measure the distance between  $\mathcal{W}^u(\mathcal{M}_0^{\ell})$  and  $\mathcal{W}^s(\mathcal{M}_0^r)$  to first order in  $|c - c_0|$  and  $|u - u_0|$ , respectively. We compute

$$\begin{aligned} M_{\dagger}^c &= \int_{-\infty}^{\infty} e^{c_0 \xi} q_{\dagger}(\xi)^2 d\xi > 0, \\ M_{\dagger}^u &= \int_{-\infty}^{\infty} e^{c_0 \xi} (1 - bv_{\dagger}(\xi)) v_{\dagger}(\xi)^2 q_{\dagger}(\xi) d\xi > 0. \end{aligned}$$

As these are nonzero, we deduce that the intersection of  $\mathcal{W}^u(\mathcal{M}_0^{\ell})$  and  $\mathcal{W}^s(\mathcal{M}_0^r)$  along  $\phi_{\dagger}$  is transverse in both  $c$  and  $u$ , and we arrive at the distance function (5.3.2).  $\square$

Analogously, we can determine the transversality of the intersection of  $\mathcal{W}^u(\mathcal{M}_0^r)$  and  $\mathcal{W}^s(\mathcal{M}_0^{\ell})$  along an orbit  $\phi_{\diamond}$ . We have the following lemma, which follows from a similar computation as in the proof Lemma 5.3.1

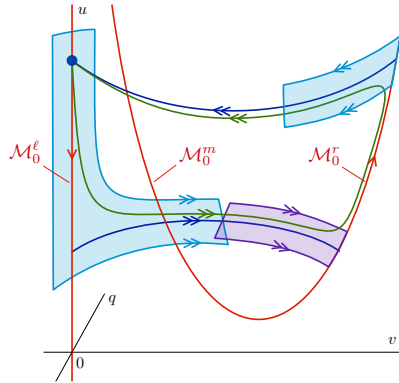


**Figure 5.10** – The traveling pulse solution of Theorem 5.2.8 is obtained for  $0 < \varepsilon \ll 1$  as a perturbation of the singular homoclinic orbit  $\mathcal{H}_d(a)$ .

**Lemma 5.3.2.** *Consider a heteroclinic orbit  $\phi_\diamond$  which lies in the intersection of  $\mathcal{W}^u(\mathcal{M}_0^r)$  and  $\mathcal{W}^s(\mathcal{M}_0^\ell)$  for some  $(c, u) = (c_0, u_0)$ . Then this intersection is transverse in  $(c, u)$ , and we compute the splitting of  $\mathcal{W}^u(\mathcal{M}_0^r)$  and  $\mathcal{W}^s(\mathcal{M}_0^\ell)$  along  $\phi_\diamond$  via the distance function*

$$D_\diamond(\tilde{c}, \tilde{u}) = M_\diamond^c \tilde{c} + M_\diamond^u \tilde{u} + \mathcal{O}(\tilde{c}^2 + \tilde{u}^2), \quad (5.3.7)$$

where  $\tilde{c} := c - c_0$ ,  $\tilde{u} := u - u_0$ , and

$$\begin{aligned} M_\diamond^c &= \int_{-\infty}^{\infty} e^{c_0 \xi} q_\diamond(\xi)^2 d\xi > 0, \\ M_\diamond^u &= \int_{-\infty}^{\infty} e^{c_0 \xi} (1 - b v_\diamond(\xi)) v_\diamond(\xi)^2 q_\diamond(\xi) d\xi < 0. \end{aligned} \quad (5.3.8)$$

### 5.3.2 Proof of existence results

In this section, we conclude the proof of Theorem 5.2.8. The proof of Theorem 5.2.9 is similar. The proofs of Theorems 5.2.10 and 5.2.11 also follow a similar argument – albeit less involved – and we omit the details.

*Proof of Theorem 5.2.8.* Based on the analysis in section 5.2, we obtain a traveling pulse solution of (5.1.2) as a perturbation from the singular homoclinic orbit  $\mathcal{H}_d(a)$  (see (5.2.24) and Figure 5.10) within the traveling wave ODE (5.1.7) for a speed  $c \approx c^*(a)$ . We will construct a homoclinic orbit for  $0 < \varepsilon \ll 1$  as an intersection of the stable and unstable manifolds  $\mathcal{W}^s(p_0(a))$  and  $\mathcal{W}^u(p_0(a))$  of the equilibrium  $p_0(a)$  corresponding to the desert state.

For  $\varepsilon_0 > 0$  sufficiently small, from standard methods of geometric singular perturbation theory, as the left branch  $\mathcal{M}_0^\ell$  of the critical manifold is normally hyperbolic, it persists for  $\varepsilon \in (0, \varepsilon_0)$  as a one-dimensional locally invariant slow manifold  $\mathcal{M}_\varepsilon^\ell$ . Similarly, away from the fold  $\mathcal{F}$ , the right branch  $\mathcal{M}_0^r$  of the critical manifold is normally hyperbolic and persists for  $\varepsilon \in (0, \varepsilon_0)$  as a one-dimensional locally invariant slow manifold  $\mathcal{M}_\varepsilon^r$ . The two-dimensional (un)stable manifolds  $\mathcal{W}^u(\mathcal{M}_0^j)$  and  $\mathcal{W}^s(\mathcal{M}_0^j)$ ,  $j = \ell, r$ , persist for  $\varepsilon \in (0, \varepsilon_0)$  as two-dimensional locally invariant manifolds  $\mathcal{W}^u(\mathcal{M}_\varepsilon^j)$  and  $\mathcal{W}^s(\mathcal{M}_\varepsilon^j)$ ,  $j = \ell, r$ .

As the equilibrium  $p_0(a)$  is repelling with respect to the reduced flow on  $\mathcal{M}_0^\ell$  (see section 5.2.3), for sufficiently small  $\varepsilon > 0$ , the two-dimensional unstable manifold  $\mathcal{W}^u(p_0(a))$  of  $p_0(a)$  coincides with  $\mathcal{W}^u(\mathcal{M}_\varepsilon^\ell)$ . The equilibrium  $p_0(a)$  also admits a one-dimensional stable manifold  $\mathcal{W}^s(p_0(a))$  which precisely corresponds the strong stable fiber of  $\mathcal{W}^s(\mathcal{M}_\varepsilon^\ell)$  with basepoint  $p_0(a)$ . We note that for  $\varepsilon = 0$  and  $c = c^*(a)$ , the manifold  $\mathcal{W}^s(p_0(a))$  is precisely the singular front  $\phi_\diamond(a)$ .

Using the results of Lemma 5.3.1 for  $c_0 = c^*(a)$ ,  $u_0 = u^*(a)$ , for each fixed  $c \approx c^*(a)$  the two-dimensional manifolds  $\mathcal{W}^u(\mathcal{M}_0^r)$  and  $\mathcal{W}^s(\mathcal{M}_0^r)$  intersect transversely along the front  $\phi_\dagger(u^*(a))$ . This transversality persists for sufficiently small  $\varepsilon > 0$ , and using the fact that  $\mathcal{W}^u(p_0(a)) = \mathcal{W}^u(\mathcal{M}_\varepsilon^\ell)$ , we deduce the transverse intersection of  $\mathcal{W}^u(p_0(a))$  and  $\mathcal{W}^s(\mathcal{M}_\varepsilon^r)$  for each  $c \approx c^*(a)$  and each sufficiently small  $\varepsilon > 0$ . We now track  $\mathcal{W}^u(p_0(a))$  as it passes near  $\mathcal{M}_\varepsilon^r$ ; by the exchange lemma [87, 143], there is a constant  $\eta > 0$  such that  $\mathcal{W}^u(p_0(a))$  aligns  $C^1$ - $\mathcal{O}(e^{-\eta/\varepsilon})$ -close to  $\mathcal{W}^u(\mathcal{M}_\varepsilon^r)$  upon exiting a neighborhood of  $\mathcal{M}_\varepsilon^r$  near the front  $\phi_\diamond(a)$ .

Using Lemma 5.3.2 for  $c_0 = c^*(a)$ ,  $u_0 = a$ , we can compute the distance between  $\mathcal{W}^u(\mathcal{M}_\varepsilon^r)$  and  $\mathcal{W}^s(p_0(a))$  along the singular front  $\phi_\diamond(a)$  using the distance function (5.3.7). In order to find a homoclinic orbit, we are interested in intersections of  $\mathcal{W}^u(p_0(a))$  and  $\mathcal{W}^s(p_0(a))$ . By the  $C^1$ - $\mathcal{O}(e^{-\eta/\varepsilon})$ -closeness of  $\mathcal{W}^u(p_0(a))$  and  $\mathcal{W}^u(\mathcal{M}_\varepsilon^r)$ , the resulting distance function differs only by  $\mathcal{O}(e^{-\eta/\varepsilon})$  terms. Hence we compute the distance between  $\mathcal{W}^u(p_0(a))$  and  $\mathcal{W}^s(p_0(a))$  along  $\phi_\diamond(a)$  as

$$D(\tilde{c}, \tilde{u}, \varepsilon) = M_\diamond^c \tilde{c} + \mathcal{O}(\varepsilon + \tilde{c}^2), \quad (5.3.9)$$

where  $M_\diamond^c \neq 0$  and  $\tilde{c} = c - c^*(a)$ . We solve for  $D(\tilde{c}, \tilde{u}, \varepsilon) = 0$  when

$$c = c_d(a, \varepsilon) = c^*(a) + \mathcal{O}(\varepsilon), \quad (5.3.10)$$

which corresponds to an intersection of  $\mathcal{W}^u(p_0(a))$  and  $\mathcal{W}^s(p_0(a))$  along a homoclinic orbit of (5.1.7).  $\square$

## 5.4 Stability

In the previous sections we have constructed several different localized solutions to the model (5.1.6): homoclinics to the desert state  $(u, v) = (U_0, V_0) = (a, 0)$ , homoclinics to the vegetated state  $(u, v) = (U_2, V_2)$  – see (5.1.5) – and heteroclinics connecting these states. In this section we study the linear stability of these solutions using formal arguments; rigorous proofs follows in section 5.5. We denote a steady state solution to (5.1.6) by  $(u_s, v_s)$  – without specifying yet which steady state solution – and we linearize around this state by setting  $(u, v)(\xi, t) = (u_s, v_s)(\xi) + e^{\lambda t + i\ell y}(\bar{u}, \bar{v})(\xi)$ . The linear stability problem then reads

$$\begin{cases} \lambda \bar{u} &= \frac{1+\varepsilon c_s}{\varepsilon} \bar{u}_\xi - (1 + v_s^2) \bar{u} - 2u_s v_s \bar{v}, \\ \lambda \bar{v} &= \bar{v}_\xi \xi + c_s \bar{v}_\xi + (-m - \ell^2 + (2 - 3bv_s)u_s v_s) \bar{v} + (1 - bv_s)v_s^2 \bar{u}. \end{cases} \quad (5.4.1)$$

Here,  $c_s$  denotes the speed of the steady state under consideration. With the introduction of  $\bar{q} := \bar{v}_\xi$  we can write this stability problem in matrix form as

$$\begin{pmatrix} \bar{u}_\xi \\ \bar{v}_\xi \\ \bar{q}_\xi \end{pmatrix} = A \begin{pmatrix} \bar{u} \\ \bar{v} \\ \bar{q} \end{pmatrix}, \quad (5.4.2)$$

where

$$A = \begin{pmatrix} \frac{\varepsilon}{1+\varepsilon c_s} [1 + \lambda + v_s^2] & \frac{\varepsilon}{1+\varepsilon c_s} 2u_s v_s & 0 \\ 0 & 0 & 1 \\ -(1 - bv_s)v_s^2 & m + \ell^2 + \lambda - (2 - 3bv_s)u_s v_s & -c_s \end{pmatrix}. \quad (5.4.3)$$

The rest of this section is devoted to finding the spectrum  $\Sigma$  of this eigenvalue problem for the different stationary solutions to (5.1.6), using formal computations. The spectrum consists of an essential spectrum  $\Sigma_{\text{ess}}$  and a point spectrum  $\Sigma_{\text{pt}}$ , which can each be interpreted in relation to the eigenvalue problem (4.3.10). The essential spectrum, which we consider in section 5.4.1, can be determined from properties of the asymptotic matrices obtained by taking the limit  $\xi \rightarrow \pm\infty$  in (4.3.10). We then study the point spectrum in section 5.4.2, which consists of eigenvalues for which (4.3.10) admits exponentially localized eigenfunctions. In section 5.4.4 we formulate theorems based on our findings, the proofs of which are given in section 5.5.

### 5.4.1 Essential spectrum

The essential spectrum consists of all eigenvalues  $\lambda$  such that an asymptotic matrix of (5.4.2) has a spatial eigenvalue with real part zero. Depending on the type of steady state solution we are inspecting, the asymptotic matrix or matrices might be different. However, since we are only considering steady state solutions that limit to either the desert state  $(u, v) = (a, 0)$  or the vegetated state  $(u, v) = (U_2, V_2)$ , there are only two possible asymptotic matrices; when  $(u_s, v_s)$  limits to  $(a, 0)$  (for either  $\xi \rightarrow \infty$  or  $\xi \rightarrow -\infty$ ) we have  $A_d$  as asymptotic matrix and when  $(u_s, v_s)$  limits to  $(U_2, V_2)$  we have  $A_v$ , where these matrices are given by

$$A_d(\lambda; \ell) = \begin{pmatrix} \frac{\varepsilon}{1+\varepsilon c_s} [1 + \lambda] & 0 & 0 \\ 0 & 0 & 1 \\ 0 & m + \ell^2 + \lambda & -c_s \end{pmatrix} \quad (5.4.4)$$

$$A_v(\lambda; \ell) = \begin{pmatrix} \frac{\varepsilon}{1+\varepsilon c_s} [1 + \lambda + V_2^2] & \frac{\varepsilon}{1+\varepsilon c_s} 2U_2 V_2 & 0 \\ 0 & 0 & 1 \\ -(1 - bV_2)V_2^2 & m + \ell^2 + \lambda - (2 - 3bV_2)U_2 V_2 & -c_s \end{pmatrix}, \quad (5.4.5)$$

where the values for  $U_2$  and  $V_2$  are given in (5.1.5).

**Lemma 5.4.1.** *Concerning the asymptotic matrices  $A_d, A_v$  defined in (5.4.4)–(5.4.5), we have the following.*

(i) *The matrix  $A_d$  is hyperbolic for all  $\lambda \in \mathbb{C}$  satisfying*

$$\text{Re}\lambda > -\min\{m + \ell^2, 1\}. \quad (5.4.6)$$

(ii) *For values of  $a, m, b > 0$  satisfying  $\frac{a}{m} > 4b + \frac{1}{b}$ , the matrix  $A_v$  is hyperbolic for all  $\lambda \in \mathbb{C}$  satisfying*

$$\text{Re}\lambda > -\min \left\{ 1 + \frac{1}{4b^2}, \frac{2m \left( b\sqrt{a^2 - 4m(m+ab)} - m \right)}{2m + ab - b\sqrt{a^2 - 4m(m+ab)}} + \ell^2 \right\} < 0. \quad (5.4.7)$$

*Proof.* For (i), a straightforward computation reveals that  $A_d$  is non-hyperbolic when  $\lambda \in \{\lambda \in \mathbb{C} : \text{Re}\lambda = -1\} \cup \{\lambda = -m - \ell^2 - k^2 + ic_s k; k \in \mathbb{R}\}$ ; see Figure 5.11.

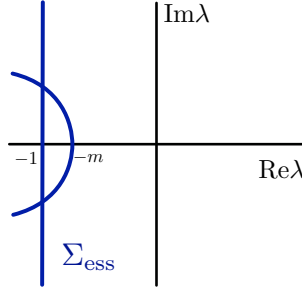


**Figure 5.11** – Shown is the essential spectrum  $\Sigma_{\text{ess}}$  associated with the desert state  $(u, v) = (a, 0)$  in the case  $\ell = 0$ .

For (ii), we compute that  $A_v$  is non-hyperbolic when

$$\left( \frac{\varepsilon}{1 + \varepsilon c_s} (1 + \lambda + V_2^2) - i\nu \right) (i\nu c_s - \nu^2 - m - \ell^2 - \lambda + (2 - 3bV_2)U_2V_2) - \frac{\varepsilon}{1 + \varepsilon c_s} 2U_2V_2(1 - bV_2)V_2^2 = 0, \quad (5.4.8)$$

for some  $\nu \in \mathbb{R}$ . We note that

$$\text{Re} (i\nu c_s - \nu^2 - m - \ell^2 - \lambda + (2 - 3bV_2)U_2V_2) < 0 \quad (5.4.9)$$

whenever

$$\text{Re}\lambda > -m - \ell^2 + (2 - 3bV_2)U_2V_2. \quad (5.4.10)$$

Furthermore, using the expressions (5.1.5), when  $\frac{a}{m} > 4b + \frac{1}{b}$ , we have that  $V_2 > \frac{1}{2b}$  and

$$\begin{aligned} -m - \ell^2 + (2 - 3bV_2)U_2V_2 &= -\frac{2m \left( b\sqrt{a^2 - 4m(m+ab)} - m \right)}{2m + ab - b\sqrt{a^2 - 4m(m+ab)}} - \ell^2 \\ &< 0. \end{aligned}$$

for all  $\ell \in \mathbb{R}$ . By rearranging (5.4.8), we deduce that  $A_v$  is non-hyperbolic when

$$\lambda = -1 - V_2^2 + \frac{2U_2V_2(1 - bV_2)V_2^2}{(i\nu c_s - \nu^2 - m - \ell^2 - \lambda + (2 - 3bV_2)U_2V_2)} + i\nu \frac{1 + \varepsilon c_s}{\varepsilon}. \quad (5.4.11)$$

Taking real parts of (5.4.11) in the region

$$\text{Re}\lambda > -\frac{2m \left( b\sqrt{a^2 - 4m(m+ab)} - m \right)}{2m + ab - b\sqrt{a^2 - 4m(m+ab)}} - \ell^2, \quad (5.4.12)$$

we have that  $\text{Re}\lambda < -1 - V_2^2$ , and noting  $V_2 > \frac{1}{2b}$ , the result follows.  $\square$

Thus, since both  $A_d$  and  $A_v$  stay hyperbolic for all  $\lambda$  with  $\text{Re}\lambda \geq 0$  for the relevant parameter values, the essential spectrum of all of the types of steady state solutions found in Section 5.2 is located in the left half-plane.

## 5.4.2 Point spectrum

In this section we study the point spectrum  $\Sigma_{\text{pt}}$  using formal perturbation theory. Here we focus on 1D stability, that is  $\ell = 0$ . Rigorous proofs of the statements in this section, and the extension to all  $\ell \in \mathbb{R}$ , follow in section 5.5.

We observe that the slow manifolds  $\mathcal{M}_0^{\ell,r}$  are hyperbolic (away from the fold point  $\mathcal{F}$ ) and consist entirely of saddle equilibria of the fast layer problem (5.2.1). Hence, these slow manifolds should not contribute any eigenvalues; the only eigenvalues come from the contribution of the fast fronts  $\phi_{\dagger}$  and  $\phi_{\diamond}$ . That is, eigenvalues in the point spectrum lie close to the eigenvalues of the fast-reduced subsystem (5.2.1). Since  $\phi_{\dagger}$  and  $\phi_{\diamond}$  are fronts and (5.2.1) is translational invariant, standard Sturm-Liouville theory indicates that they carry an eigenvalue  $\lambda = 0$  and possibly several other eigenvalues that are all real and negative. Therefore, if there are potentially unstable eigenvalues in the point spectrum  $\Sigma_{\text{pt}}$  they need to lie close to  $\lambda = 0$ . Specifically, there are as many eigenvalues close to 0 as there are fronts in the steady state solution  $(u_s, v_s)$  under consideration.

Because the full system (5.1.6) is translational invariant,  $\lambda = 0$  is an eigenvalue of the full system. When we study the stability of a heteroclinic connection (connecting the desert state  $p_0(a)$  to the vegetated state  $p_+(u_2)$  or vice-versa) this is the only eigenvalue close to 0; in particular  $\Sigma_{\text{pt}} \setminus \{0\} \subset \{\lambda \in \mathbb{C} : \text{Re}\lambda < 0\}$ . On the other hand, when we study the stability of a homoclinic connection (connecting either the desert state  $p_0(a)$  or the vegetated state  $p_+(u_2)$  to itself), there is an additional eigenvalue close to 0. This eigenvalue – of the homoclinic steady state solutions – can, in principle, move either to the left or to the right (making the steady state unstable). In this section, we use perturbation theory to track this movement and pinpoint the location of the second eigenvalue formally.

## 5.4.3 Formal computation of small eigenvalues

Let  $(u_s, v_s)$  be an exact solution to (5.1.6). The linearized stability problem (5.4.1) can be recast to the following form

$$\mathcal{L}(\ell) \begin{pmatrix} \bar{u} \\ \bar{v} \end{pmatrix} = \lambda \begin{pmatrix} \bar{u} \\ \bar{v} \end{pmatrix}, \quad (5.4.13)$$

where

$$\mathcal{L}(\ell) := \begin{pmatrix} \varepsilon^{-1}(1 + \varepsilon c_s) \partial_{\xi} - (1 + v_s^2) & -2u_s v_s \\ (1 - b v_s) v_s^2 & \partial_{\xi}^2 + c_s \partial_{\xi} - m - \ell^2 + (2 - 3b v_s) u_s v_s \end{pmatrix}. \quad (5.4.14)$$

For simplicity, we focus on the operator  $\mathcal{L}(0)$  corresponding to the case  $\ell = 0$ ; the case of  $\ell \in \mathbb{R}$  is similar and is carried out in detail in section 5.5.

Since we are looking for a small (order  $\mathcal{O}(\varepsilon)$ ) eigenvalue closely related to the derivatives of the fast fronts  $(u_{\dagger}, v_{\dagger})^T$  and  $(u_{\diamond}, v_{\diamond})^T$ , in particular at leading order, (5.4.13) is satisfied in the fast  $\xi$ -fields by any linear combination of  $(u'_{\dagger}, v'_{\dagger})^T$  and  $(u'_{\diamond}, v'_{\diamond})^T$ . We denote the fast region with the front  $(u_{\dagger}, v_{\dagger})$  by  $I_{\dagger}$  and the fast region with the front  $(u_{\diamond}, v_{\diamond})$  by  $I_{\diamond}$ . Then, to find the small eigenvalues we therefore use regular expansion and determine the eigenvalues with a Fredholm solvability condition. In particular, we first focus on the fast fields and we expand the eigenvalue and  $(\bar{u}, \bar{v})^T$

in these fast regions as

$$\begin{pmatrix} \bar{u} \\ \bar{v} \end{pmatrix} = \alpha_j \phi'_j + \varepsilon \begin{pmatrix} \bar{u}_{j,1} \\ \bar{v}_{j,1} \end{pmatrix} + \mathcal{O}(\varepsilon^2), \quad (\xi \in I_j, j = \dagger, \diamond) \quad (5.4.15)$$

$$\lambda = 0 + \varepsilon \tilde{\lambda} + \mathcal{O}(\varepsilon^2), \quad (5.4.16)$$

where  $\alpha_{\dagger, \diamond}$  are constants to be determined. Moreover, we also need to expand the exact solution  $(u_s, v_s)^T$  as well as the speed  $c_s$ :

$$\begin{pmatrix} u_s \\ v_s \end{pmatrix} = \begin{pmatrix} u_j \\ v_j \end{pmatrix} + \varepsilon \begin{pmatrix} u_{j,1} \\ v_{j,1} \end{pmatrix} + \mathcal{O}(\varepsilon^2), \quad (\xi \in I_j, j = \dagger, \diamond) \quad (5.4.17)$$

$$c_s = c_0 + \varepsilon c_1 + \mathcal{O}(\varepsilon^2), \quad (5.4.18)$$

where  $(u_j, v_j)^T$  ( $j = \dagger, \diamond$ ) and  $c_0$  are the leading order approximations of the exact solutions as constructed in section 5.2.5, Theorems 5.2.8 and 5.2.9. Substitution in (5.4.13) leads at order  $\mathcal{O}(\varepsilon)$  to the following equation (the  $\mathcal{O}(1)$  equations are automatically satisfied):

$$\begin{cases} \bar{u}'_{j,1} &= 2\alpha_j u_j v_j v'_j, \\ \mathcal{L}_j^r \bar{v}_{j,1} &= \left( \tilde{\lambda} - c_1 \partial_\xi - [2 - 6bv_j] u_j v_{j,1} - [2 - 3bv_j] v_j u_{j,1} \right) \alpha_j v'_j - [1 - bv_j] v_j^2 \bar{u}_{j,1}, \end{cases} \quad (5.4.19)$$

(for  $\xi \in I_j$ ,  $j = \dagger, \diamond$ ), where

$$\mathcal{L}_j^r := \partial_\xi^2 + c_0 \partial_\xi - m + (2 - 3bv_j) u_j v_j. \quad (5.4.20)$$

In (5.4.19) terms with  $c_1$ ,  $v_{j,1}$  and  $u_{j,1}$  appear, and to determine these, we expand the existence problem (5.1.7) in  $\varepsilon$  as well. In the fast fields the order  $\mathcal{O}(\varepsilon)$  terms read

$$\begin{cases} u'_{j,1} &= u_j - a + u_j v_j^2, \\ \mathcal{L}_j^r v_{j,1} &= -(1 - bv_j) v_j u_{j,1} - c_1 v'_j. \end{cases} \quad (\xi \in I_j, j = \dagger, \diamond) \quad (5.4.21)$$

Taking the derivative with respect to  $\xi$  of the second equation then yields

$$\mathcal{L}_j^r v'_{j,1} = (-c_1 \partial_\xi - [2 - 6bv_j] u_j v_{j,1} - [2 - 3bv_j] v_j u_{j,1}) v'_j - [1 - bv_j] v_j^2 u'_{j,1} \quad (5.4.22)$$

Substitution in (5.4.19) then reduces the core stability problem to

$$\begin{cases} \bar{u}'_{j,1} &= 2\alpha_j u_j v_j v'_j, \\ \mathcal{L}_j^r \bar{v}_{j,1} &= \alpha_j \mathcal{L}_j^r v'_{j,1} + \tilde{\lambda} \alpha_j v'_j + [1 - bv_j] v_j^2 (\alpha_j u'_{j,1} - \bar{u}_{j,1}). \end{cases} \quad (\xi \in I_j, j = \dagger, \diamond) \quad (5.4.23)$$

From this equation it is clear that  $\bar{u}_{j,1}$  can be found by integration (regardless of the value of  $\tilde{\lambda}$ ,  $\alpha_{\dagger}$  and  $\alpha_{\diamond}$ ). However, since  $\mathcal{L}_j^r$  has a non-trivial kernel, we have to impose a solvability condition on  $\bar{v}_{j,1}$ . We define  $v_j^*$  as a solution to the adjoint equation  $(\mathcal{L}_j^r)^* v_j^* = 0$  and note that

$$v_j^*(\xi) = e^{c_0 \xi} v'_j(\xi), \quad (\xi \in I_j, j = \dagger, \diamond). \quad (5.4.24)$$

Thus we obtain the following Fredholm solvability condition

$$0 = \alpha_j \tilde{\lambda} \int_{-\infty}^{\infty} (v'_j)^2 e^{c_0 \xi} d\xi + \int_{-\infty}^{\infty} [1 - bv_j] v_j^2 e^{c_0 \xi} v'_j (\alpha_j u'_{j,1} - \bar{u}_{j,1}) d\xi \quad (j = \dagger, \diamond) \quad (5.4.25)$$

We observe from (5.4.19) and (5.4.21) that  $\alpha_j u'_{j,1} - \bar{u}_{j,1}$  is constant in the fast fields  $I_j$  ( $j = \dagger, \diamond$ ). Thus the Fredholm condition reduces to

$$0 = \alpha_j \tilde{\lambda} \int_{-\infty}^{\infty} (v'_j)^2 e^{c_0 \xi} d\xi + (\alpha_j u'_{j,1} - \bar{u}_{j,1}) \int_{-\infty}^{\infty} [1 - bv_j] v_j^2 e^{c_0 \xi} v'_j d\xi \quad (j = \dagger, \diamond) \quad (5.4.26)$$

Note that we thus have two solvability conditions. Only when both are satisfied simultaneously, it is possible to find  $(\bar{u}, \bar{v})^T$  that solve (5.4.13). The terms in (5.4.26) change depending on the type of steady state solution we are considering, and in particular, to which equilibrium state these solutions are homoclinic, as this determines the value of  $\alpha_j u'_{j,1} - \bar{u}_{j,1}$ .

**Homoclinics to desert state** In this situation,  $u'_{\diamond,1}(\xi) \rightarrow 0$  for  $\xi \rightarrow \infty$  in  $I_{\diamond}$ , since the jump here is onto the fixed point. Moreover,  $\bar{u}_{\diamond,1}(\xi) \rightarrow 0$  for  $\xi \rightarrow \infty$  in  $I_{\diamond}$  to ensure integrability of the eigenfunction. Thus, the condition in  $I_{\diamond}$  is

$$\alpha_{\diamond} \tilde{\lambda} M_{\diamond, \lambda}^d = 0, \quad (5.4.27)$$

where

$$M_{\diamond, \lambda}^d := \int_{-\infty}^{\infty} v'_{\diamond}(\xi)^2 e^{c^*(a)\xi} d\xi > 0. \quad (5.4.28)$$

Therefore, either  $\tilde{\lambda} = 0$  or  $\alpha_{\diamond} = 0$ . The former gives us back the translational invariant eigenvalue (with eigenfunction  $(\bar{u}, \bar{v})^T = (u'_s, v'_s)^T$ ), so we focus on the latter possibility. Note that  $\alpha_{\diamond} = 0$  implies that  $\bar{u}_{\diamond,1} = 0$  in the fast field  $I_{\diamond}$ . Thus, this provides a matching condition for the equations in the slow field between the fast fields  $I_{\dagger}$  and  $I_{\diamond}$ . By expanding the slow field equation in the slow variable, it immediately follows, from this fact, that the eigenfunction must be 0 in the slow field between  $I_{\dagger}$  and  $I_{\diamond}$  as well. Hence we conclude that  $\bar{u}_{\dagger,1}(\xi) \rightarrow 0$  for  $\xi \rightarrow \infty$  in  $I_{\dagger}$  as well. Moreover,  $u_{\dagger,1}(\xi) \rightarrow u_{\dagger} - a - u_{\dagger} v_+(u_{\dagger})^2 = u^*(a) - a + u^*(a) v_+(u^*(a))^2$  for  $\xi \rightarrow \infty$  in  $I_{\dagger}$  – see equation (5.4.21) and Theorem 5.2.8. Thus the second solvability condition becomes

$$\alpha_{\dagger} \left[ \tilde{\lambda} M_{\dagger, \lambda}^d + M_{\dagger, \varepsilon}^d \right] = 0, \quad (5.4.29)$$

where

$$M_{\dagger, \lambda}^d := \int_{-\infty}^{\infty} v'_{\dagger}(\xi)^2 e^{c^*(a)\xi} d\xi > 0, \quad (5.4.30)$$

$$M_{\dagger, \varepsilon}^d := \left[ u^*(a) - a + u^*(a) v_+(u^*(a))^2 \right] \int_{-\infty}^{\infty} (1 - bv_{\dagger}(\xi)) v_{\dagger}(\xi)^2 e^{c^*(a)\xi} v'_{\dagger}(\xi) d\xi > 0. \quad (5.4.31)$$

The signs of these expressions are positive, since  $v_{\dagger}$  is increasing with  $\xi$ , and the quantity  $(u^*(a) - a + u^*(a) v_+(u^*(a))^2)$  is positive per construction. Because taking  $\alpha_{\dagger} = 0$  leads to the trivial solution (on  $\mathbb{R}$ ), we therefore obtain the additional eigenvalue  $\lambda = \varepsilon \tilde{\lambda} = -\varepsilon \frac{M_{\dagger, \varepsilon}^d}{M_{\dagger, \lambda}^d} < 0$ , which indicates that the eigenvalue  $\lambda$  close to zero has moved into the stable half-plane  $\{\lambda \in \mathbb{C} : \text{Re} \lambda < 0\}$ . A plot of the corresponding eigenfunction, computed numerically, is given in Figure 5.13b.



**Homoclinics to the vegetated state** This case is very similar. However, now the solution in  $I_{\dagger}$  limits to the fixed point of (5.1.7). Using similar arguments, we then find the following condition in  $I_{\dagger}$ :

$$\alpha_{\dagger} \tilde{\lambda} M_{\dagger, \lambda}^{\vee} = 0, \quad (5.4.32)$$

where

$$M_{\dagger, \lambda}^{\vee} := \int_{-\infty}^{\infty} v'_{\dagger}(\xi)^2 e^{\hat{c}(a)\xi} d\xi > 0. \quad (5.4.33)$$

This time we need to take  $\alpha_{\dagger} = 0$ . Similar to before, matching through the slow field yields  $\bar{u}_{\dagger, 1}(\xi) \rightarrow 0$  and  $u_{\diamond, 1} \rightarrow u_{\diamond} - a = \hat{u}_2(a) - a$  for  $\xi \rightarrow \infty$  in  $I_{\diamond}$ . Therefore the second condition for this steady state reads

$$\alpha_{\diamond} \left[ \tilde{\lambda} M_{\diamond, \lambda}^{\vee} + M_{\diamond, \varepsilon}^d \right] = 0, \quad (5.4.34)$$

where

$$M_{\diamond, \lambda}^{\vee} := \int_{-\infty}^{\infty} v'_{\diamond}(\xi)^2 e^{\hat{c}(a)\xi} d\xi > 0, \quad (5.4.35)$$

$$M_{\diamond, \varepsilon}^d := [\hat{u}_2(a) - a] \int_{-\infty}^{\infty} (1 - bv_{\diamond}(\xi)) v_{\diamond}(\xi)^2 e^{\hat{c}(a)\xi} v'_{\diamond}(\xi) d\xi > 0. \quad (5.4.36)$$

Because  $\hat{u}_2(a) - a < 0$  and  $v_{\diamond}$  is decreasing with  $\xi$ , the sign of all these terms are positive again. Therefore we obtain the additional eigenvalue  $\lambda = \varepsilon \tilde{\lambda} = -\varepsilon \frac{M_{\diamond, \varepsilon}^d}{M_{\diamond, \lambda}^{\vee}} < 0$ , and again the eigenvalue has moved into the stable half-plane.

## 5.4.4 Main stability results

In the previous sections we have formally determined the spectrum of the various steady state solutions to (5.1.6). The computations in these sections hold for 1D perturbations of the steady state in question. We do, however, also want to understand the stability of these steady states under 2D perturbations. For that, we linearize around this state by setting  $(u, v)(\xi, y, t) = (u_s, v_s)(\xi) + e^{\lambda t + i\ell y} (\bar{u}, \bar{v})(\xi)$ , where  $\ell \in \mathbb{R}$  is the transverse wavenumber, which results in the family of linearized PDE operators

$$\mathcal{L}(\ell) := \begin{pmatrix} \varepsilon^{-1}(1 + \varepsilon c_s) \partial_{\xi} - 1 - v_s^2 & -2u_s v_s \\ (1 - bv_s) v_s^2 & \partial_{\xi}^2 + \ell^2 + c_s \partial_{\xi} - m + (2 - 3bv_s) u_s v_s \end{pmatrix}. \quad (5.4.37)$$

Linear stability is then determined by the corresponding family of eigenvalue problems

$$\mathcal{L}(\ell) \begin{pmatrix} U \\ V \end{pmatrix} = \lambda \begin{pmatrix} U \\ V \end{pmatrix}, \quad \ell \in \mathbb{R}. \quad (5.4.38)$$

Introducing  $\Psi := (\bar{u}, \bar{v}, \bar{v}')^T$  we write the eigenvalue problem (5.4.38) as the first order nonautonomous ODE

$$\Psi' = A(\xi; \lambda, \ell, \varepsilon) \Psi \quad (5.4.39)$$

where

$$A(\xi; \lambda, \ell, \varepsilon) = \begin{pmatrix} \frac{\varepsilon}{1 + \varepsilon c_s} [1 + \lambda + v_s^2] & \frac{\varepsilon}{1 + \varepsilon c_s} 2u_s v_s & 0 \\ 0 & 0 & 1 \\ -(1 - bv_s) v_s^2 & m + \lambda + \ell^2 - (2 - 3bv_s) u_s v_s & -c_s \end{pmatrix}. \quad (5.4.40)$$

The essential spectrum associated with this problem was treated in section 5.4.1. By introducing  $\hat{\lambda} = \lambda - \ell^2$  the previous formal computations for the point spectrum in section 5.4.2 still hold up to leading order by replacing  $\lambda$  with  $\hat{\lambda}$ . To summarize our findings, we formulate several stability theorems for the various types of steady state solutions; these are proved rigorously in section 5.5.

**Theorem 5.4.2** (Spectrum of traveling front solutions). *Let  $a, b, m, \varepsilon$  as in Theorem 5.2.10 or 5.2.11 and let  $\phi_h$  denote a traveling front solution as in the same theorem. Then, the following hold.*

- (i) *The spectrum of the operator  $\mathcal{L}(0)$  is contained in the set  $\{\lambda \in \mathbb{C} : \text{Re}\lambda < 0\} \cup \{0\}$ , and the spectrum of the operator  $\mathcal{L}(\ell), \ell \neq 0$  is contained in the set  $\{\lambda \in \mathbb{C} : \text{Re}\lambda < 0\}$ .*
- (ii) *The eigenvalue  $\lambda_0(0) = 0$  of  $\mathcal{L}(0)$  is simple and continues to an eigenvalue of  $\mathcal{L}(\ell), |\ell| \leq L_M$  for some  $L_M \gg 1$ , satisfying  $\lambda'_0(0) = 0$  and*

$$\lambda_0(\ell) = -\ell^2 + \mathcal{O}(|\varepsilon \log \varepsilon|^2), \quad \lambda''_0(\ell) = -2 + \mathcal{O}(|\varepsilon \log \varepsilon|^2), \quad |\ell| \leq L_M. \quad (5.4.41)$$

- (iii) *The remaining spectrum of  $\mathcal{L}(\ell)$  is bounded away from the imaginary axis uniformly in  $\varepsilon > 0$  sufficiently small and  $\ell \in \mathbb{R}$ .*

**Theorem 5.4.3** (Spectrum of vegetation stripe solutions). *Let  $a, b, m, \varepsilon$  as in Theorem 5.2.8 and let  $\phi_d$  be a traveling pulse ‘stripe’ solution as in Theorem 5.2.8. Then, the following hold.*

- (i) *The spectrum of the operator  $\mathcal{L}(0)$  is contained in the set  $\{\lambda \in \mathbb{C} : \text{Re}\lambda < 0\} \cup \{0\}$ , and the spectrum of the operator  $\mathcal{L}(\ell), \ell \neq 0$  is contained in the set  $\{\lambda \in \mathbb{C} : \text{Re}\lambda < 0\}$ .*
- (ii) *The eigenvalue  $\lambda_0(0) = 0$  of  $\mathcal{L}(0)$  is simple and continues to an eigenvalue of  $\mathcal{L}(\ell), |\ell| \leq L_M$  for some  $L_M \gg 1$ , satisfying  $\lambda'_0(0) = 0$  and*

$$\lambda_0(\ell) = -\ell^2 + \mathcal{O}(|\varepsilon \log \varepsilon|^2), \quad \lambda''_0(\ell) = -2 + \mathcal{O}(|\varepsilon \log \varepsilon|^2), \quad |\ell| \leq L_M. \quad (5.4.42)$$

- (iii) *The operator  $\mathcal{L}(\ell), |\ell| \leq L_M$  admits an additional critical eigenvalue*

$$\lambda_c(\ell) = -\ell^2 - \frac{M_{\dagger, \varepsilon}^d}{M_{\dagger, \lambda}^d} \varepsilon + \mathcal{O}(|\varepsilon \log \varepsilon|^2), \quad |\ell| \leq L_M, \quad (5.4.43)$$

where  $M_{\dagger, \lambda}^d$  and  $M_{\dagger, \varepsilon}^d$  are as defined in (5.4.30) and (5.4.31).

- (iv) *The remaining spectrum of  $\mathcal{L}(\ell)$  is bounded away from the imaginary axis uniformly in  $\varepsilon > 0$  sufficiently small and  $\ell \in \mathbb{R}$ .*

**Theorem 5.4.4** (Spectrum of vegetation gap solutions). *Let  $a, b, m, \varepsilon$  as in Theorem 5.2.9 and let  $\phi_v$  be a travelling pulse ‘gap’ solution as in Theorem 5.2.9. Then, the following hold.*

- (i) *The spectrum of the operator  $\mathcal{L}(0)$  is contained in the set  $\{\lambda \in \mathbb{C} : \text{Re}\lambda < 0\} \cup \{0\}$ , and the spectrum of the operator  $\mathcal{L}(\ell), \ell \neq 0$  is contained in the set  $\{\lambda \in \mathbb{C} : \text{Re}\lambda < 0\}$ .*

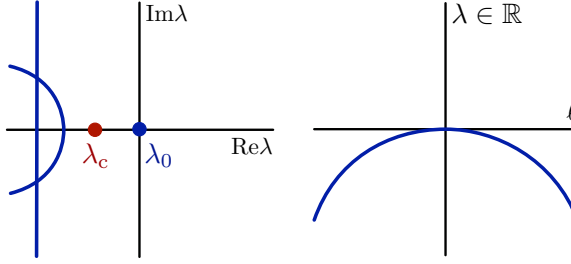


**Figure 5.12** – Shown are the results of Theorem 5.4.3. The left panel depicts the spectrum of the  $\ell = 0$  operator  $\mathcal{L}(0)$ , corresponding to  $1D$  stability. The point spectrum contains two critical eigenvalues  $\lambda_0, \lambda_c$  close to the origin, while the remainder of the spectrum is bounded away from the imaginary axis in the left half plane. The right panel depicts a schematic of the continuation of the critical eigenvalue  $\lambda_0$  for  $|\ell| > 0$ .

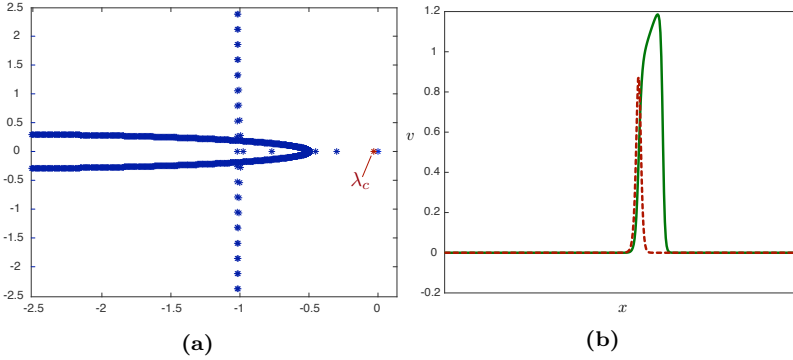


**Figure 5.13** – Shown is the numerically computed  $1D$  spectrum (left panel) associated with a traveling pulse solution of (5.1.2) found for  $a = 1.61, b = 0.6, m = 0.5, \varepsilon = 0.003$ . The  $v$  profile of the solution is shown in the right panel, along with the eigenfunction corresponding to the critical eigenvalue  $\lambda_c$ .

(ii) The eigenvalue  $\lambda_0(0) = 0$  of  $\mathcal{L}(0)$  is simple and continues to an eigenvalue of  $\mathcal{L}(\ell), |\ell| \leq L_M$  for some  $L_M \gg 1$ , satisfying  $\lambda_0'(0) = 0$  and

$$\lambda_0(\ell) = -\ell^2 + \mathcal{O}(|\varepsilon \log \varepsilon|^2), \quad \lambda_0''(\ell) = -2 + \mathcal{O}(|\varepsilon \log \varepsilon|^2), \quad |\ell| \leq L_M. \quad (5.4.44)$$

(iii) The operator  $\mathcal{L}(\ell), |\ell| \leq L_M$  admits an additional critical eigenvalue

$$\lambda_c(\ell) = -\ell^2 - \frac{M_{\diamond, \varepsilon}^v}{M_{\diamond, \lambda}^v} \varepsilon + \mathcal{O}(|\varepsilon \log \varepsilon|^2), \quad |\ell| \leq L_M, \quad (5.4.45)$$

where  $M_{\diamond, \lambda}^v$  and  $M_{\diamond, \varepsilon}^v$  are as defined in (5.4.35) and (5.4.36).

(iv) The remaining spectrum of  $\mathcal{L}(\ell)$  is bounded away from the imaginary axis uniformly in  $\varepsilon > 0$  sufficiently small and  $\ell \in \mathbb{R}$ .

## 5.5 Rigorous proof for stability theorems

The theorems in section 5.4.4 are based on computations of the essential spectrum in section 5.4.1 and a formal computation of the point spectrum in section 5.4.2. The former directly provides proof for the theorem statements concerning the essential spectrum. The latter, however, does not provide a rigorous proof for the theorem statements concerning the point spectrum; to that end, in this section we provide the rigorous justification for the formal point spectrum computations in section 5.4.2. We restrict ourselves to the study of the traveling pulse ‘stripe’ solution  $\phi_d$  as in Theorem 5.2.8 and Theorem 5.4.3. The setup and proof for the traveling ‘gap’ solution  $\phi_v$  as in Theorem 5.2.9 and Theorem 5.4.4 is similar; the setup and proofs for the traveling heteroclinic orbits  $\phi_{vd}$  and  $\phi_{dv}$  as in Theorem 5.2.10, Theorem 5.2.11 and Theorem 5.4.2 are also very similar, though less involved. Therefore, the details of these are omitted.

To analyze the point spectrum, we search for exponentially localized solutions to the family of eigenvalue problems (5.4.40) parametrized by the transverse wavenumber  $\ell \in \mathbb{R}$ . To this end, we use exponential dichotomies/trichotomies and Lin’s method to construct potential eigenfunctions, based on similar techniques used in the study of stability of traveling pulses in the FitzHugh–Nagumo equation [22]. We briefly review the notions of exponential dichotomies/trichotomies in section 5.5.1.

To determine eigenvalues of (5.4.40), it is useful to split the complex plane in several regions. For  $M \gg 1$  and  $\delta \ll 1$  fixed independent of  $\varepsilon$ , we define the following regions (see Figure 5.14)

$$\begin{aligned} R_1(\delta) &:= \{\zeta \in \mathbb{C} : |\zeta| \leq \delta\} \\ R_2(\delta, M) &:= \{\zeta \in \mathbb{C} : \delta < |\zeta| < M, \operatorname{Re}\zeta > -\delta\} \\ R_3(M) &:= \{\zeta \in \mathbb{C} : |\zeta| > M, |\arg(\zeta)| < 2\pi/3\}. \end{aligned} \tag{5.5.1}$$

In section 5.5.2, we first show that large wavenumbers  $\ell$  do not contribute eigenvalues, and hence it suffices to restrict to a region of bounded  $\ell$ . We then set  $\tilde{\lambda}(\ell) := \lambda - \ell^2$  and study the behavior of solutions to (5.4.40) for  $\tilde{\lambda}$  in the various regions (5.5.1). The region  $R_3$  is considered in section 5.5.3. In section 5.5.4, we collect preliminary results in order to set up the analysis for  $\tilde{\lambda}(\ell)$  in the regions  $R_1$  and  $R_2$ , which are analyzed in section 5.5.5 and 5.5.6, respectively. We briefly conclude the proof of Theorem 5.4.3 in section 5.5.7.

### 5.5.1 Exponential dichotomies/trichotomies

Exponential dichotomies extend the notion of hyperbolicity to nonautonomous linear systems such as (5.4.40) by separating the dynamics into subspaces of solutions which satisfy exponential growth/decay estimates. Consider a linear system

$$\Psi_\xi = A(\xi)\Psi, \quad \Psi \in \mathbb{C}^n \tag{5.5.2}$$

and let  $T(\xi, \hat{\xi})$  denote the corresponding evolution operator. Let  $I \subseteq \mathbb{R}$  denote an interval. The system (5.5.2) is said to admit an exponential dichotomy on  $I$  with

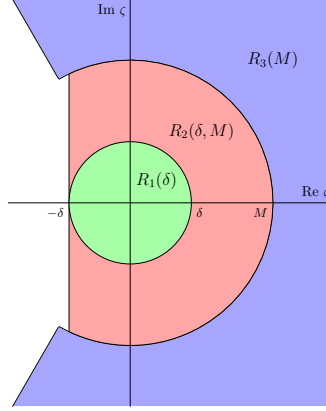


**Figure 5.14** – Sketch of the regions  $R_1(\delta)$ ,  $R_2(\delta, M)$  and  $R_3(M)$  as considered in the analysis of the point spectrum.

constants  $C, \mu > 0$  and projections  $P^{u,s}(\xi), \xi \in I$  if the following hold for all  $\xi, \hat{\xi} \in I$

$$\begin{aligned} P^u(\xi) + P^s(\xi) &= 1 \\ T(\xi, \hat{\xi})P^{u,s}(\hat{\xi}) &= P^{u,s}(\xi)T(\xi, \hat{\xi}) \\ |T(\xi, \hat{\xi})P^s(\hat{\xi})|, |T(\hat{\xi}, \xi)P^u(\xi)| &\leq Ce^{-\mu(\xi - \hat{\xi})}, \quad \xi \geq \hat{\xi}. \end{aligned}$$

We will sometimes write  $T^{u,s}(\xi, \hat{\xi}) := T(\xi, \hat{\xi})P^{u,s}(\hat{\xi})$  to denote the corresponding stable/unstable evolution operators.

Exponential trichotomies allow for a ‘center’ subspace which does not satisfy the same exponential decay estimates required for an exponential dichotomy. The system (5.5.2) is said to admit an exponential trichotomy on  $I$  with constants  $C > 0$  and  $\mu_1 > \mu_2 > 0$  and projections  $P^{u,c,s}(\xi), \xi \in I$  if the following hold for all  $\xi, \hat{\xi} \in I$

$$\begin{aligned} P^u(\xi) + P^c(\xi) + P^s(\xi) &= 1 \\ T(\xi, \hat{\xi})P^{u,c,s}(\hat{\xi}) &= P^{u,c,s}(\xi)T(\xi, \hat{\xi}) \\ |T(\xi, \hat{\xi})P^s(\hat{\xi})|, |T(\hat{\xi}, \xi)P^u(\xi)| &\leq Ce^{-\mu_1(\xi - \hat{\xi})}, \quad \text{if } \xi \geq \hat{\xi} \\ |T(\xi, \hat{\xi})P^c(\hat{\xi})| &\leq Ce^{\mu_2|\xi - \hat{\xi}|}. \end{aligned}$$

Our analysis will make use of exponential di-/trichotomies in order to build exponentially localized eigenfunctions, and in particular we will make use roughness properties, which guarantee that exponential di-/trichotomies persist under small perturbations of the linear system (5.5.2). For more information on dichotomies and their properties, as well as their applications to stability analysis, see [31, 126, 142].

### 5.5.2 Reduction to region of bounded $|\ell|$

In this section, we show that it suffices to consider bounded wavenumbers  $|\ell| \leq L_M$  for some  $L_M \gg 1$ .

The region  $|\ell| \gg 1$

We first consider the region of large transverse wavenumber, that is we consider  $(\lambda, \ell)$  such that  $\lambda \in R_1(\delta) \cup R_2(\delta, M) \cup R_3(M)$  and  $|\ell| \geq L_M$  for a fixed constant  $1 \ll L_M \ll M$  independent of  $\varepsilon$ . In this region, we perform a rescaling of the stability problem (5.4.40) and show that the rescaled problem is a small perturbation of a constant coefficient problem which admits exponential di/trichotomies and no exponentially localized solutions.

We rescale  $\bar{\xi} = \sqrt{\lambda + \ell^2}\xi$ ,  $\bar{q} = q/\sqrt{\lambda + \ell^2}$ , which results in the system

$$\frac{d\Psi}{d\bar{\xi}} = \bar{A}(\bar{\xi}; \lambda, \ell, \varepsilon)\Psi, \quad \bar{A}(\bar{\xi}; \lambda, \ell, \varepsilon) = \bar{A}_1(\lambda, \ell, \varepsilon) + \bar{A}_2(\bar{\xi}; \ell, \varepsilon) \quad (5.5.3)$$

where  $\bar{A}_1(\lambda, \ell, \varepsilon)$  is the constant coefficient matrix

$$\bar{A}_1(\lambda, \ell, \varepsilon) = \begin{pmatrix} \frac{\varepsilon}{1+\varepsilon c_s} \frac{\lambda}{\sqrt{\lambda+\ell^2}} & 0 & 0 \\ 0 & 0 & 1 \\ 0 & \frac{\lambda+\ell^2}{|\lambda+\ell^2|} & 0 \end{pmatrix}$$

and

$$\bar{A}_2(\bar{\xi}; \ell, \varepsilon) = \mathcal{O}\left(\frac{1}{\sqrt{\lambda + \ell^2}}\right)$$

uniformly in  $\bar{\xi}, \varepsilon$ . We consider  $|\ell| \geq L_M$  for some sufficiently large, fixed constant  $L_M$ . We can compute the eigenvalues of  $\bar{A}_1(\lambda, \ell, \varepsilon)$  explicitly as

$$\nu_{\pm} = \pm \sqrt{\frac{\lambda + \ell^2}{|\lambda + \ell^2|}}, \quad \nu_{\varepsilon} = \frac{\varepsilon}{1 + \varepsilon c_d} \frac{\lambda}{\sqrt{\lambda + \ell^2}}.$$

For  $\lambda \in R_1(\delta) \cup R_2(\delta, M) \cup R_3(M)$  and for any  $\delta \ll 1$  and  $M \gg L_M$ , we note that the pair of eigenvalues  $\nu_{\pm}$  must have absolute real part greater than  $1/2$ , since  $|\arg \sqrt{(\lambda + \ell^2)/|\lambda + \ell^2|}| < \pi/3$ . One of these eigenvalues has negative real part and the other positive real part.

For the third eigenvalue,  $\nu_{\varepsilon}$ , there are three cases:  $\text{Re}\nu_{\varepsilon} > 1/4$ ,  $|\text{Re}\nu_{\varepsilon}| \leq 1/4$ , and  $\text{Re}\nu_{\varepsilon} < -1/4$ . If  $\text{Re}\nu_{\varepsilon} > 1/4$ , then, by roughness, (5.5.3) admits exponential dichotomies and hence no exponentially localized solutions. If  $|\text{Re}\nu_{\varepsilon}| \leq 1/4$ , by roughness (5.5.3) admits exponential trichotomies with one-dimensional center subspace. Any bounded solution must lie entirely in this center subspace. By continuity, the eigenvalues of the asymptotic matrix  $\bar{A}^{\pm\infty}(\lambda, \ell, \varepsilon) = \lim_{\bar{\xi} \rightarrow \pm\infty} \bar{A}(\bar{\xi}; \lambda, \ell, \varepsilon)$  are separated so that only the eigenvalue  $\nu_{\varepsilon}$  has absolute real part less than  $1/4 + \kappa$  for some small  $\kappa > 0$ . For  $\lambda$  to the right of the essential spectrum, we have that  $\text{Re}\nu_{\varepsilon} > 0$ . Let  $\Psi_c$  be the corresponding eigenvector. Any solution  $\Psi(\xi)$  in the center subspace satisfies  $\lim_{\bar{\xi} \rightarrow \pm\infty} \Psi(\bar{\xi})e^{-\nu_{\varepsilon}\bar{\xi}} = \zeta_{\pm}\Psi_c$  for some  $\zeta_{\pm} \in \mathbb{C} \setminus \{0\}$ , which contradicts the fact that  $\Psi(\bar{\xi})$  is bounded. Finally we note that the case  $\text{Re}\nu_{\varepsilon} < -1/4$  cannot occur for  $\lambda$  to the right of the essential spectrum since in this region the asymptotic matrix  $\bar{A}^{\pm\infty}(\lambda, \ell, \varepsilon)$  has two eigenvalues of positive real part and one of negative real part.

Thus we conclude that for  $|\ell| \geq L_M$  and any  $\lambda \in R_1(\delta) \cup R_2(\delta, M) \cup R_3(M)$  to the right of the essential spectrum, (5.4.40) admits no exponentially localized solutions.

Setup for  $|\ell| \leq L_M$

In the following sections, we will consider the region where  $|\ell|$  is bounded. We begin by setting  $\tilde{\lambda} = \tilde{\lambda}(\ell) := \lambda + \ell^2$ . Under this transformation, (5.4.40) becomes

$$\Psi' = \tilde{A}(\xi; \tilde{\lambda}, \ell, \varepsilon)\Psi, \quad (5.5.4)$$

where

$$\tilde{A}(\xi; \tilde{\lambda}, \ell, \varepsilon) := A(\xi; \tilde{\lambda} - \ell^2, \ell, \varepsilon) \quad (5.5.5)$$

$$= \begin{pmatrix} \frac{\varepsilon}{1+\varepsilon c_s} \left[ 1 + \tilde{\lambda} - \ell^2 + v_s^2 \right] & \frac{\varepsilon}{1+\varepsilon c_s} 2u_s v_s & 0 \\ 0 & 0 & 1 \\ -(1 - bv_s)v_s^2 & m + \tilde{\lambda} - (2 - 3bv_s)u_s v_s & -c_s \end{pmatrix}. \quad (5.5.6)$$

In the following we characterize all eigenvalues  $\lambda \in \mathbb{C}$  such that

$$(\tilde{\lambda}, \ell) \in R_1(\delta) \cup R_2(\delta, M) \cup R_3(M) \times [-L_M, L_M]. \quad (5.5.7)$$

This characterizes all eigenvalues  $\lambda \in \mathbb{C}$  with  $\operatorname{Re}\lambda > -\ell^2 - \delta$  and thus all eigenvalues  $\lambda \in \mathbb{C}$  with  $\operatorname{Re}\lambda > -\delta$ . In particular, all unstable eigenvalues with  $\operatorname{Re}\lambda \geq 0$  are found this way.

### 5.5.3 The region $(\tilde{\lambda}(\ell), \ell) \in R_3(M) \times [-L_M, L_M]$

In this region, we follow a similar strategy to that in section 5.5.2 and perform the rescaling  $\hat{\xi} = \sqrt{|\tilde{\lambda}|}\xi, \hat{q} = q/\sqrt{|\tilde{\lambda}|}$ , which results in the system

$$\frac{d\Psi}{d\hat{\xi}} = \hat{A}(\hat{\xi}; \tilde{\lambda}, \ell, \varepsilon)\Psi, \quad \hat{A}(\hat{\xi}; \tilde{\lambda}, \ell, \varepsilon) = \hat{A}_1(\tilde{\lambda}, \ell, \varepsilon) + \hat{A}_2(\hat{\xi}; \tilde{\lambda}, \ell, \varepsilon) \quad (5.5.8)$$

where  $\hat{A}_1(\tilde{\lambda}, \ell, \varepsilon)$  is the constant coefficient matrix

$$\hat{A}_1(\tilde{\lambda}, \ell, \varepsilon) = \begin{pmatrix} \frac{\varepsilon}{1+\varepsilon c_s} \frac{\tilde{\lambda}}{\sqrt{|\tilde{\lambda}|}} & 0 & 0 \\ 0 & 0 & 1 \\ 0 & \frac{\tilde{\lambda}}{|\tilde{\lambda}|} & 0 \end{pmatrix}$$

and

$$\hat{A}_2(\hat{\xi}; \tilde{\lambda}, \ell, \varepsilon) = \mathcal{O}\left(\frac{1}{\sqrt{|\tilde{\lambda}|}}\right),$$

uniformly in  $\hat{\xi}, \varepsilon$ , and  $|\ell| \leq L_M$ , where we recall that  $1 \ll L_M \ll M$ . The remainder of the argument follows analogously as in section 5.5.2, and we conclude that for any fixed  $L_M$ , any sufficiently large  $M$  and any  $(\tilde{\lambda}(\ell), \ell) \in R_3(M) \times [-L_M, L_M]$  with  $\lambda = \tilde{\lambda} - \ell^2$  to the right of the essential spectrum, (5.4.40) admits no exponentially localized solutions.

### 5.5.4 Setup for the region $(\tilde{\lambda}(\ell), \ell) \in R_1(\delta) \cup R_2(\delta, M) \times [-L_M, L_M]$

In the previous section we have deduced that all eigenvalues need to be located in the region  $(\tilde{\lambda}(\ell), \ell) \in R_1(\delta) \cup R_2(\delta, M) \times [-L_m, L_m]$ . The analysis in this region is more involved and we need a specific set-up for this region, the details of which are explained in the next subsections.

### Estimates from the existence analysis

To study the stability of the traveling pulse solution  $\phi_d$ , we need to be able to approximate it pointwise by its singular limit, and bound the resulting error terms. The following theorem establishes these estimates.

**Theorem 5.5.1.** *For each  $\nu > 0$  sufficiently large, there exists  $\varepsilon_0 > 0$  such that the following holds. Let  $\phi_d(\xi) = (u_d(\xi), v_d(\xi))^t$  be a traveling-pulse solution as in Theorem 5.2.8 for  $0 < \varepsilon < \varepsilon_0$ , and define  $L_\varepsilon := -\nu \log \varepsilon$  and  $\Phi_d(\xi) := (u_d(\xi), v_d(\xi), v'_d(\xi))^T$ . There exists  $0 < Z_\varepsilon = \mathcal{O}(1/\varepsilon)$  such that:*

(i) *For  $\xi \in I_\ell := (-\infty, -L_\varepsilon]$ ,  $\Phi_d(\xi)$  is approximated by the left slow manifold  $\mathcal{M}_0^\ell$  with*

$$d(\Phi_d(\xi), \mathcal{M}_0^\ell) = \mathcal{O}(\varepsilon).$$

(ii) *For  $\xi \in I_\dagger := [-L_\varepsilon, L_\varepsilon]$ ,  $\Phi_d(\xi)$  is approximated by the front  $\phi_\dagger(\xi) = (v_\dagger(\xi), q_\dagger(\xi))^T$  with*

$$\left| \Phi_d(\xi) - \begin{pmatrix} u^*(a) \\ \phi_\dagger(\xi) \end{pmatrix} \right| = \mathcal{O}(\varepsilon \log \varepsilon), \quad \left| \Phi'_d(\xi) - \begin{pmatrix} 0 \\ \phi'_\dagger(\xi) \end{pmatrix} \right| = \mathcal{O}(\varepsilon \log \varepsilon).$$

(iii) *For  $\xi \in I_r := [L_\varepsilon, Z_{a,\varepsilon} - L_\varepsilon]$ ,  $\Phi_d(\xi)$  is approximated by the right slow manifold  $\mathcal{M}_0^r$  with*

$$d(\Phi_d(\xi), \mathcal{M}_0^r) = \mathcal{O}(\varepsilon).$$

(iv) *For  $\xi \in I_\diamond := [Z_{a,\varepsilon} - L_\varepsilon, \infty)$ ,  $\Phi_d(\xi)$  is approximated by the front  $\phi_\diamond(\xi) = (v_\diamond(\xi), q_\diamond(\xi))^T$  with*

$$\left| \Phi_d(\xi) - \begin{pmatrix} a \\ \phi_\diamond(\xi - Z_{a,\varepsilon}) \end{pmatrix} \right| = \mathcal{O}(\varepsilon \log \varepsilon)$$

and

$$\left| \Phi'_d(\xi) - \begin{pmatrix} 0 \\ \phi'_\diamond(\xi - Z_{a,\varepsilon}) \end{pmatrix} \right| = \mathcal{O}(\varepsilon \log \varepsilon)$$

*Proof.* The proof is similar to Theorem 4.3 in [22]. The estimates are based on the proximity of the solution to the singular limit; along each of the slow manifolds, and along each of the fast jumps outside small neighborhoods of the slow manifolds, these estimates follow directly from the existence analysis, and  $\Phi_d(\xi)$  is within  $\mathcal{O}(\varepsilon)$  of the corresponding singular profile. The regions in between, i.e. where  $\Phi_d(\xi)$  transitions from a fast jump to a slow manifold or vice versa, are more delicate and require corner-type estimates, which result in the  $\mathcal{O}(\varepsilon \log \varepsilon)$  errors; see, e.g. [22, Theorem 4.5] or [60, 83].  $\square$

### Weighted eigenvalue problem

In this section we introduce a small exponential weight to the stability problem (5.5.4). This weight is introduced to deal with the inconvenience that arises due to the fact that when  $\varepsilon = 0$ , along the critical manifolds  $\mathcal{M}_0^\ell, \mathcal{M}_0^r$  the matrix  $A$  admits three



spatial eigenvalues: one negative, one positive, and a zero eigenvalue which corresponds to the slow direction. On the other hand, for  $\varepsilon > 0$  the asymptotic matrix  $\mathcal{A}_d$  is hyperbolic with two positive spatial eigenvalues and one negative eigenvalue. In the following, we will construct exponential dichotomies for (5.5.4) along each of the slow manifolds  $\mathcal{M}_\varepsilon^\ell, \mathcal{M}_\varepsilon^r$  and each of the fast jumps, and for the following computations it will be convenient to preserve this dichotomy splitting at  $\varepsilon = 0$  and preserve the exponential decay in forward (resp. backward) time within the corresponding stable (resp. unstable) dichotomy subspaces. To this end, for each  $\eta \geq 0$  we consider the weighted eigenvalue problem

$$\Psi' = A_\eta(\xi; \tilde{\lambda}, \ell, \varepsilon)\Psi, \tag{5.5.9}$$

where

$$\begin{aligned} A_\eta(\xi; \tilde{\lambda}, \ell, \varepsilon) &:= \tilde{A}(\xi; \tilde{\lambda}, \ell, \varepsilon) + \eta I \\ &= \begin{pmatrix} \frac{\varepsilon}{1+\varepsilon c} \left[ 1 + \tilde{\lambda} - \ell^2 + v_d^2 \right] + \eta & \frac{\varepsilon}{1+\varepsilon c} 2u_d v_d & 0 \\ 0 & \eta & 1 \\ -(1 - bv_d)v_d^2 & m + \tilde{\lambda} - (2 - 3bv_d)u_d v_d & \eta - c \end{pmatrix}. \end{aligned}$$

The effect of introducing the weight  $\eta$  is to shift the spectrum (i.e. the spatial eigenvalues) of the matrix  $\tilde{A}(\xi; \tilde{\lambda}, \ell, \varepsilon)$  to the right. For any  $\tilde{\lambda}$  chosen so that  $\lambda = \tilde{\lambda} - \ell^2$  lies to the right of the essential spectrum of  $\mathcal{L}$ , the asymptotic matrix  $\tilde{A}^{\pm\infty}(\tilde{\lambda}, \ell, \varepsilon) = \lim_{\xi \rightarrow \infty} \tilde{A}(\xi; \tilde{\lambda}, \ell, \varepsilon)$  admits two eigenvalues of positive real part and one of negative real part. Provided  $\eta$  is chosen so that  $A_\eta^{\pm\infty}(\tilde{\lambda}, \ell, \varepsilon) = \lim_{\xi \rightarrow \infty} A_\eta(\xi; \tilde{\lambda}, \ell, \varepsilon)$  retains this spectral splitting, the original eigenvalue problem (5.4.40) admits a nontrivial exponentially localized solution  $\Psi(\xi)$  if and only if the weighted problem (5.5.9) admits a solution given by  $e^{\eta\xi}\Psi(\xi)$ .

We proceed by determining  $\eta, \nu > 0$  such that the spectrum of the coefficient matrix  $A_\eta(\xi; \tilde{\lambda}, \ell, \varepsilon)$  of (5.5.9) has a consistent splitting into one unstable and two stable eigenvalues for any  $\tilde{\lambda} \in R_1(\delta) \cup R_2(\delta, M)$  such that  $\lambda = \tilde{\lambda} - \ell^2$  lies to the right of the essential spectrum of  $\mathcal{L}$  and any  $\xi \in I_\ell \cup I_r$ , where  $I_\ell, I_r$  are as in Theorem 5.5.1. This consistent splitting will be used to construct exponential dichotomies for (5.5.9) on the intervals  $I_\ell, I_r$ . This is the content of the following proposition.

**Proposition 5.5.2.** *There exists  $C, \mu, \eta, \varepsilon_0 > 0$  such that for  $\varepsilon \in (0, \varepsilon_0)$ , (5.5.9) admits exponential dichotomies on the intervals  $I_\ell = (-\infty, -L_\varepsilon]$  and  $I_r = [L_\varepsilon, Z_\varepsilon - L_\varepsilon]$  with constants  $C, \mu > 0$ , and the associated projections  $\mathcal{Q}_{\ell,r}^{u,s}(\xi; \tilde{\lambda}, \varepsilon)$  are analytic in  $\tilde{\lambda} \in R_1(\delta) \cup R_2(\delta, M)$  and satisfy*

$$\begin{aligned} \left\| [\mathcal{Q}_\ell^s - \mathcal{P}](-L_\varepsilon; \tilde{\lambda}, \varepsilon) \right\| &\leq C|\varepsilon \log \varepsilon|, \\ \left\| [\mathcal{Q}_r^s - \mathcal{P}](L_\varepsilon; \tilde{\lambda}, \varepsilon) \right\| &\leq C|\varepsilon \log \varepsilon|, \\ \left\| [\mathcal{Q}_r^s - \mathcal{P}](Z_\varepsilon - L_\varepsilon; \tilde{\lambda}, \varepsilon) \right\| &\leq C|\varepsilon \log \varepsilon|, \end{aligned}$$

where  $\mathcal{P}(\xi; \tilde{\lambda}, \varepsilon)$  denotes the spectral projection onto the stable eigenspace of the coefficient matrix  $A_\eta(\xi; \tilde{\lambda}, \ell, \varepsilon)$  in (5.5.9).

*Proof.* By Theorem 5.5.1, for  $\xi \in I_\ell \cup I_r$ , the pulse solution is  $\mathcal{O}(\varepsilon)$ -close to the slow manifolds  $\mathcal{M}_\varepsilon^\ell$  and  $\mathcal{M}_\varepsilon^r$ , respectively. For  $|\ell| \leq L_M$  bounded and any  $\tilde{\lambda} \in R_1(\delta) \cup$

$R_2(\delta, M)$ , on  $I_\ell$  the matrix  $A_\eta(\xi; \tilde{\lambda}, \ell, \varepsilon)$  has slowly varying coefficients and is an  $\mathcal{O}(\varepsilon)$  perturbation of the constant-coefficient matrix

$$A_\eta^\ell(\xi; \tilde{\lambda}, \ell, \varepsilon) = \begin{pmatrix} \eta & 0 & 0 \\ 0 & \eta & 1 \\ 0 & m + \tilde{\lambda} & \eta - c^*(a) \end{pmatrix}. \quad (5.5.10)$$

For any sufficiently small  $\eta > 0$  fixed independently of  $\varepsilon$  and  $\tilde{\lambda} \in R_1(\delta) \cup R_2(\delta, M)$ , this matrix is hyperbolic with two eigenvalues with positive real part and one with negative real part and a spectral gap with lower bound independent of  $\tilde{\lambda} \in R_1(\delta) \cup R_2(\delta, M)$ . By continuity this also holds for  $A_\eta(\xi; \tilde{\lambda}, \ell, \varepsilon)$  for  $\xi \in I_\ell$ , and since  $A_\eta(\xi; \tilde{\lambda}, \ell, \varepsilon)$  has slowly varying coefficients on this interval (see [31, Proposition 6.1]), as in the proof of [22, Proposition 6.5], we can construct exponential dichotomies for (5.5.9) on  $I_\ell$  with constants  $C, \mu$  independent of  $\tilde{\lambda} \in R_1(\delta) \cup R_2(\delta, M)$  and all sufficiently small  $\varepsilon$ .

We proceed similarly along  $I_r$ , noting that here the matrix  $A_\eta(\xi; \tilde{\lambda}, \ell, \varepsilon)$  again has slowly varying coefficients but is now an  $\mathcal{O}(\varepsilon)$  perturbation of the matrix

$$A_\eta^r(\xi; \tilde{\lambda}, \ell, \varepsilon) = \begin{pmatrix} \eta & 0 & 0 \\ 0 & \eta & 1 \\ -(1 - bv_d)v_d & m + \tilde{\lambda} - (2 - 3bv_d)u_dv_d & \eta - c^*(a) \end{pmatrix}. \quad (5.5.11)$$

where  $(u_d, v_d)$  lies within  $\mathcal{O}(\varepsilon)$  of the set  $\{(u, v) = (u, v_+(u)) : u \in [u^*(a), a]\}$  where  $v_+$  is as in (5.2.3). On this set, we note that since  $m = (1 - bv_+(u))uv_+(u)$ ,  $u > 0$  and  $v_+(u) \geq \frac{1}{2b}$ , we have that

$$m - (2 - 3bv_+(u))uv_+(u) = (-1 + 2bv_+(u))uv_+(u) \geq 0. \quad (5.5.12)$$

Hence for  $\delta > 0$  sufficiently small  $A_\eta^r(\xi; \tilde{\lambda}, \ell, \varepsilon)$  is hyperbolic with two eigenvalues with positive real part and one with negative real part and a spectral gap with lower bound independent of  $\tilde{\lambda} \in R_1(\delta) \cup R_2(\delta, M)$ . The existence of exponential dichotomies for  $A_\eta(\xi; \tilde{\lambda}, \ell, \varepsilon)$  on  $I_r$  then proceeds similarly to the case of  $I_\ell$  above.  $\square$

### 5.5.5 The region $(\tilde{\lambda}(\ell), \ell) \in R_1(\delta) \times [-L_M, L_M]$

The argument below is based on the analysis in [22] regarding the stability of traveling pulse solutions in the FitzHugh–Nagumo equation. The fundamental idea is to construct potential eigenfunctions as solutions to (5.4.40) using Lin’s method: the solutions are constructed along three separate intervals which form a partition of the real line and are matched at two locations corresponding to the two fast jumps in the layer problem; see Figure 5.15. The resulting matching conditions give bifurcation equations which can be solved using the eigenvalue  $\lambda$  as a free parameter, and to leading order these conditions correspond to the Fredholm conditions (5.4.27) and (5.4.29).

#### Reduced eigenvalue problems along fast jumps

We consider the reduced eigenvalue problems

$$\Psi' = A_{j,\eta}(\xi)\Psi, \quad j = \dagger, \diamond, \quad (5.5.13)$$

where

$$A_{j,\eta}(\xi) := \begin{pmatrix} \eta & 0 & 0 \\ 0 & \eta & 1 \\ -(1 - bv_j(\xi))v_j(\xi)^2 & m - (2 - 3bv_j(\xi))u_jv_j(\xi) & \eta - c^*(a) \end{pmatrix}, \quad (5.5.14)$$

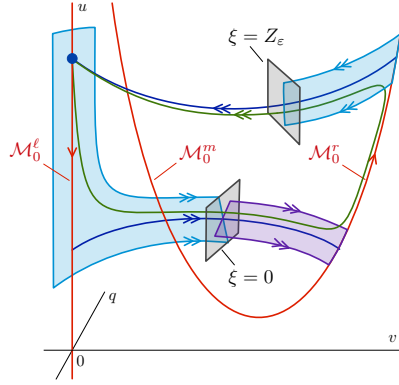


**Figure 5.15** – Shown is the geometric setup for the construction of potential eigenfunctions using Lin’s method. The solutions are constructed along the three intervals  $(-\infty, 0]$ ,  $[0, Z_\varepsilon]$ ,  $[Z_\varepsilon, \infty)$  and are then matched at  $\xi = 0$  and  $\xi = Z_\varepsilon$  corresponding to the two fast jumps in the layer problem (5.2.2).

(for  $j = \dagger, \diamond$ ). These are obtained by considering (5.5.9) with  $\varepsilon = \tilde{\lambda} = 0$  and approximating  $\phi_d$  by the fast front solutions  $\phi_j$ ,  $j = \dagger, \diamond$ . We denote the corresponding evolutions by  $T_j(\xi, \hat{\xi})$  for  $j = \dagger, \diamond$ . In (5.5.13),  $v_j(\xi)$  denotes the  $v$ -component of  $\phi_j(\xi)$ , and  $u_\dagger = u^*(a)$ ,  $u_\diamond = a$ . Hence, for  $\xi \in I_\dagger = [-L_\varepsilon, L_\varepsilon]$ , (5.5.9) can be written as the perturbation

$$\Psi' = \left( A_{\dagger, \eta}(\xi) + B_{\dagger}(\xi; \tilde{\lambda}, \ell, \varepsilon) \right) \Psi, \quad B_{\dagger}(\xi; \tilde{\lambda}, \ell, \varepsilon) := A_\eta(\xi; \tilde{\lambda}, \ell, \varepsilon) - A_{\dagger, \eta}(\xi) \quad (5.5.15)$$

and for  $\xi \in [-L_\varepsilon, \infty)$ , (5.5.9) can be written as the perturbation

$$\Psi' = \left( A_{\diamond, \eta}(\xi) + B_{\diamond}(\xi; \tilde{\lambda}, \ell, \varepsilon) \right) \Psi, \quad B_{\diamond}(\xi; \tilde{\lambda}, \ell, \varepsilon) := A_\eta(\xi + Z_\varepsilon; \tilde{\lambda}, \ell, \varepsilon) - A_{\diamond, \eta}(\xi). \quad (5.5.16)$$

We note by Theorem 5.5.1 (ii) and (iv) that the perturbation matrices  $B_{\dagger}, B_{\diamond}$  satisfy

$$\begin{aligned} \|B_{\dagger}(\xi; \tilde{\lambda}, \ell, \varepsilon)\| &\leq C(\varepsilon|\log \varepsilon| + |\tilde{\lambda}|), & \xi \in [-L_\varepsilon, L_\varepsilon], \\ \|B_{\diamond}(\xi; \tilde{\lambda}, \ell, \varepsilon)\| &\leq C(\varepsilon|\log \varepsilon| + |\tilde{\lambda}|), & \xi \in [-L_\varepsilon, \infty). \end{aligned} \quad (5.5.17)$$

Next, we note that (5.5.13) has a lower triangular block structure and leaves the two-dimensional subspace  $\{0\} \times \mathbb{C}^2 \subset \mathbb{C}^3$  invariant, the dynamics on which are given by

$$\psi' = C_{j, \eta}(\xi)\psi, \quad C_{j, \eta}(\xi) := \begin{pmatrix} \eta & 1 \\ m - (2 - 3bv_j(\xi))u_jv_j(\xi) & \eta - c^*(a) \end{pmatrix}, \quad j = \dagger, \diamond. \quad (5.5.18)$$

The space of bounded solutions of (5.5.18) is one-dimensional and spanned by

$$\psi_j(\xi) := e^{\eta\xi}\phi'_j(\xi), \quad j = \dagger, \diamond. \quad (5.5.19)$$

Likewise, the associated adjoint system

$$\psi' = -C_{j, \eta}(\xi)^*\psi, \quad j = \dagger, \diamond, \quad (5.5.20)$$

has a one-dimensional space of bounded solutions spanned by

$$\psi_{j,\text{ad}}(\xi) := \begin{pmatrix} q'_j(\xi) \\ -v'_j(\xi) \end{pmatrix} e^{(c^*(a)-\eta)\xi}, \quad j = \dagger, \diamond. \quad (5.5.21)$$

Note the similarities with (5.4.24) in the formal computation. The system (5.5.18) admits exponential dichotomies on both half-lines, which can be extended to the full system (5.5.13) by exploiting the lower triangular block structure and using variation of constants formulae. This is the content of the following proposition.

**Proposition 5.5.3.** *There exist  $C, \mu > 0$  such that the following hold.*

- (i) *The system (5.5.18) admits exponential dichotomies on  $\mathbb{R}_\pm$  with constants  $C, \mu > 0$ , projections  $\Pi_{j,\pm}^{\text{u,s}}(\xi)$ , and corresponding (un)stable evolutions  $S_{j,\pm}^{\text{u,s}}$ ,  $j = \dagger, \diamond$ . The projections can be chosen so that*

$$R(\Pi_{j,+}^{\text{s}}(0)) = \text{Span}(\psi_j(0)) = R(\Pi_{j,-}^{\text{u}}(0)), \quad (j = \dagger, \diamond) \quad (5.5.22)$$

$$R(\Pi_{j,+}^{\text{u}}(0)) = \text{Span}(\psi_{j,\text{ad}}(0)) = R(\Pi_{j,-}^{\text{s}}(0)), \quad (j = \dagger, \diamond). \quad (5.5.23)$$

- (ii) *The system (5.5.13) admits exponential dichotomies on  $\mathbb{R}_\pm$  with constants  $C, \mu > 0$ , projections  $Q_{j,\pm}^{\text{u,s}}(\xi)$ , ( $j = \dagger, \diamond$ ), and (un)stable evolution operators  $T_{j,\pm}^{\text{u,s}}(\xi, \hat{\xi})$ . We have that for  $\xi \geq 0$ ,*

$$Q_{j,+}^{\text{s}}(\xi) = \begin{pmatrix} 0 & 0 \\ -\int_0^\xi e^{-\eta(\xi-\hat{\xi})} S_{j,+}^{\text{s}}(\xi, \hat{\xi}) F_j(\hat{\xi}) d\hat{\xi} & \Pi_{j,+}^{\text{s}}(\xi) \end{pmatrix} = 1 - Q_{j,+}^{\text{u}}(\xi), \quad (5.5.24)$$

and for  $\xi \leq 0$ ,

$$Q_{j,-}^{\text{s}}(\xi) = \begin{pmatrix} 0 & 0 \\ -\int_{-\infty}^\xi e^{-\eta(\xi-\hat{\xi})} S_{j,-}^{\text{s}}(\xi, \hat{\xi}) F_j(\hat{\xi}) d\hat{\xi} & \Pi_{j,-}^{\text{s}}(\xi) \end{pmatrix} = 1 - Q_{j,-}^{\text{u}}(\xi), \quad (5.5.25)$$

where  $F_j(\xi) := (0, -(1 - bv_j(\xi))v_j(\xi)^2)^T$ . Furthermore, the projections satisfy

$$\begin{aligned} R(Q_{j,+}^{\text{u}}(0)) &= \text{Span}(\omega_{j,\text{ad}}(0), \Psi_0), & R(Q_{j,+}^{\text{s}}(0)) &= \text{Span}(\omega_j(0)), \\ R(Q_{j,-}^{\text{u}}(0)) &= \text{Span}(\omega_j(0), \Psi_{j,\infty}), & R(Q_{j,-}^{\text{s}}(0)) &= \text{Span}(\omega_{j,\text{ad}}(0)), \end{aligned} \quad (5.5.26)$$

where

$$\omega_j(\xi) := \begin{pmatrix} 0 \\ \psi_j(\xi) \end{pmatrix}, \quad \omega_{j,\text{ad}}(\xi) := \begin{pmatrix} 0 \\ \psi_{j,\text{ad}}(\xi) \end{pmatrix}, \quad j = \dagger, \diamond, \quad (5.5.27)$$

and

$$\Psi_0 := \begin{pmatrix} 1 \\ 0 \\ 0 \end{pmatrix}, \quad \Psi_{j,\infty} := Q_{j,-}^{\text{u}}(0)\Psi_0, \quad j = \dagger, \diamond, \quad (5.5.28)$$

with  $\psi_j(\xi)$  and  $\psi_{j,\text{ad}}(\xi)$  defined in (5.5.19) and (5.5.21), respectively.

*Proof.* For (i), we refer to [22, Proposition 6.6]. The exponential dichotomies in (ii) can be constructed from those in (i) using variation of constants formulae, by exploiting the block triangular structure in (5.5.13); see [22, Corollary 6.7].  $\square$

## Construction of eigenfunctions

In this section, we use the exponential dichotomies from Proposition 5.5.3, variation of constants formulae, and the estimates from Theorem 5.5.1 to construct potential eigenfunctions. These eigenfunctions are constructed in three pieces along the intervals  $(-\infty, 0]$ ,  $[0, Z_\varepsilon]$ ,  $[Z_\varepsilon, \infty)$  (see Figure 5.15), and then matched together at  $\xi = 0, Z_\varepsilon$ ; the associated matching conditions can then be solved to find eigenvalues  $\tilde{\lambda}$ . We begin with the following proposition, which describes potential eigenfunctions along each of the three intervals.

**Proposition 5.5.4.** *Let  $B_j$  be as in (5.5.15) and (5.5.16), and  $\omega_j, \Psi_0, \Psi_{j,\infty}$  as in (5.5.27) and (5.5.28) for  $j = \dagger, \diamond$ . There exists  $\delta, \varepsilon_0, C, q > 0$  such that for  $\tilde{\lambda} \in R_1(\delta)$  and  $\varepsilon \in (0, \varepsilon_0)$  the following hold.*

- (i) *Any solution  $\Psi_{\dagger,-}(\xi, \tilde{\lambda})$  to (5.5.9), which decays exponentially in backward time, satisfies*

$$\begin{aligned} \Psi_{\dagger,-}(0, \tilde{\lambda}) &= \beta_{\dagger,-}\omega_{\dagger}(0) + \zeta_{\dagger,-}\Psi_{\dagger,\infty} \\ &+ \beta_{\dagger,-} \int_{-L_\varepsilon}^0 T_{\dagger,-}^s(0, \hat{\xi}) B_{\dagger}(\hat{\xi}; \tilde{\lambda}, \ell, \varepsilon) \omega_{\dagger}(\hat{\xi}) d\hat{\xi} + \mathcal{H}_{\dagger,-}(\beta_{\dagger,-}, \zeta_{\dagger,-}), \end{aligned} \quad (5.5.29)$$

for some  $\beta_{\dagger,-}, \zeta_{\dagger,-} \in \mathbb{C}$ , where  $\mathcal{H}_{\dagger,-}$  is a linear map satisfying

$$\|\mathcal{H}_{\dagger,-}(\beta_{\dagger,-}, \zeta_{\dagger,-})\| \leq C \left( (\varepsilon |\log \varepsilon| + |\tilde{\lambda}|) |\zeta_{\dagger,-}| + (\varepsilon |\log \varepsilon| + |\tilde{\lambda}|)^2 |\beta_{\dagger,-}| \right).$$

- (ii) *Any solution  $\Psi_{\text{sl}}(\xi, \tilde{\lambda})$  to (5.5.9) which is bounded along the slow manifold  $\mathcal{M}_\varepsilon^r$  satisfies*

$$\Psi_{\text{sl}}(0, \tilde{\lambda}) = \beta_{\dagger}\omega_{\dagger}(0) + \beta_{\dagger} \int_{L_\varepsilon}^0 T_{\dagger,+}^u(0, \hat{\xi}) B_{\dagger}(\hat{\xi}; \tilde{\lambda}, \ell, \varepsilon) \omega_{\dagger}(\hat{\xi}) d\hat{\xi} + \mathcal{H}_{\dagger}(\beta_{\dagger}, \beta_{\diamond}, \zeta_{\diamond}), \quad (5.5.30)$$

$$\begin{aligned} \Psi_{\text{sl}}(Z_\varepsilon, \tilde{\lambda}) &= \beta_{\diamond}\omega_{\diamond}(0) + \zeta_{\diamond}\Psi_{\diamond,\infty} \\ &+ \beta_{\diamond} \int_{-L_\varepsilon}^0 T_{\diamond,-}^s(0, \hat{\xi}) B_{\diamond}(\hat{\xi}; \tilde{\lambda}, \ell, \varepsilon) \omega_{\diamond}(\hat{\xi}) d\hat{\xi} + \mathcal{H}_{\diamond}(\beta_{\dagger}, \beta_{\diamond}, \zeta_{\diamond}), \end{aligned} \quad (5.5.31)$$

for some  $\beta_{\dagger}, \beta_{\diamond}, \zeta_{\diamond} \in \mathbb{C}$ , where  $\mathcal{H}_{\dagger}$  and  $\mathcal{H}_{\diamond}$  are linear maps satisfying

$$\begin{aligned} \|\mathcal{H}_{\dagger}(\beta_{\dagger}, \beta_{\diamond}, \zeta_{\diamond})\| &\leq C \left( (\varepsilon |\log \varepsilon| + |\tilde{\lambda}|)^2 |\beta_{\dagger}| + e^{-q/\varepsilon} (|\beta_{\diamond}| + |\zeta_{\diamond}|) \right), \\ \|\mathcal{H}_{\diamond}(\beta_{\dagger}, \beta_{\diamond}, \zeta_{\diamond})\| &\leq C \left( (\varepsilon |\log \varepsilon| + |\tilde{\lambda}|) |\zeta_{\diamond}| + (\varepsilon |\log \varepsilon| + |\tilde{\lambda}|)^2 |\beta_{\diamond}| + e^{-q/\varepsilon} |\beta_{\dagger}| \right). \end{aligned}$$

- (iii) *Any solution  $\Psi_{\diamond,+}(\xi, \tilde{\lambda})$  to (5.5.9) which decays exponentially in forward time satisfies*

$$\begin{aligned} \Psi_{\diamond,+}(Z_\varepsilon, \tilde{\lambda}) &= \beta_{\diamond,+}\omega_{\diamond}(0) \\ &+ \beta_{\diamond,+} \int_{\infty}^0 T_{\diamond,+}^u(0, \hat{\xi}) B_{\diamond}(\hat{\xi}; \tilde{\lambda}, \ell, \varepsilon) \omega_{\diamond}(\hat{\xi}) d\hat{\xi} + \mathcal{H}_{\diamond,+}(\beta_{\diamond,+}), \end{aligned} \quad (5.5.32)$$

for some  $\beta_{\diamond,+} \in \mathbb{C}$ , where  $\mathcal{H}_{\diamond,+}$  is a linear map satisfying

$$\|\mathcal{H}_{\diamond,+}(\beta_{\diamond,+})\| \leq C(\varepsilon |\log \varepsilon| + |\tilde{\lambda}|)^2 |\beta_{\diamond,+}|,$$

Moreover, the functions  $\psi_{\dagger,-}(\xi, \tilde{\lambda})$ ,  $\psi^{\text{sl}}(\xi, \tilde{\lambda})$ , and  $\psi_{\diamond,+}(\xi, \tilde{\lambda})$  are analytic in  $\tilde{\lambda}$ .

*Proof.* Using the exponential dichotomies from Propositions 5.5.2 and 5.5.3(ii), the proof is nearly identical to the proofs of Propositions 6.8–6.10 in [22].  $\square$

It remains to solve the matching conditions which arise when attempting to glue together the three solutions from Proposition 5.5.4 (i)–(iii) at  $\xi = 0$  and  $\xi = Z_\varepsilon$ , in order to construct an exponentially localized eigenfunction.

**Theorem 5.5.5.** *There exists  $\delta, \varepsilon_0 > 0$  such that for  $\varepsilon \in (0, \varepsilon_0)$  and  $|\ell| \leq L_M$ , the eigenvalue problem (5.5.9) has precisely two eigenvalues  $\tilde{\lambda}_0(\ell), \tilde{\lambda}_c(\ell) \in R_1(\delta)$  given by*

$$\tilde{\lambda}_0(\ell) = \mathcal{O}(|\varepsilon \log \varepsilon|^2), \quad \tilde{\lambda}_c(\ell) = -\frac{M_{\dagger,\varepsilon}^{\text{d}}}{M_{\dagger,\tilde{\lambda}}^{\text{d}}} \varepsilon + \mathcal{O}\left(|\varepsilon \log \varepsilon|^2\right),$$

where

$$M_{\dagger,\tilde{\lambda}}^{\text{d}} := \int_{-\infty}^{\infty} v_{\dagger}'(\xi; a)^2 e^{c^*(a)\xi} d\xi > 0, \quad (5.5.33)$$

$$M_{\dagger,\varepsilon}^{\text{d}} := [u^*(a) - a + u^*(a)v_+(u^*(a))]^2 \int_{-\infty}^{\infty} (1 - bv_{\dagger}(\xi))v_{\dagger}(\xi)^2 e^{c^*(a)\xi} v_{\dagger}'(\xi) d\xi > 0. \quad (5.5.34)$$

The derivatives of  $\tilde{\lambda}_0(\ell)$  with respect to  $\ell$  satisfy the same estimates, and  $\tilde{\lambda}_0(0) = \tilde{\lambda}'_0(0) = 0$ .

*Proof.* We recall from Proposition 5.5.4 that any exponentially localized solution must satisfy the conditions (5.5.29)–(5.5.32) at  $\xi = 0, Z_\varepsilon$  for some  $\beta_{\dagger,-}, \zeta_{\dagger,-}, \beta_{\dagger}, \beta_{\diamond}, \zeta_{\diamond}, \beta_{\diamond,+} \in \mathbb{C}$ . Therefore, to obtain an exponentially localized solution to (5.5.9) we match the solutions  $\Psi_{\dagger,-}, \Psi_{\text{sl}}$  at  $\xi = 0$  and the solutions  $\Psi_{\text{sl}}, \Psi_{\diamond,+}$  at  $\xi = Z_{a,\varepsilon}$ , which results in matching conditions which must be satisfied by  $\tilde{\lambda}$  and  $\varepsilon$  which can be solved to find eigenfunctions. Since the projections  $Q_{j,+}^{\text{u,s}}(0)$  associated with the exponential dichotomy of (5.5.13) established in Proposition 5.5.3(ii) satisfy

$$Q_{j,+}^{\text{u}}(0) + Q_{j,+}^{\text{s}}(0) = I, \quad j = \dagger, \diamond,$$

this is equivalent to ensuring the differences  $\Psi_{\dagger,-}(0, \tilde{\lambda}) - \Psi_{\text{sl}}(0, \tilde{\lambda})$  and  $\Psi_{\text{sl}}(Z_\varepsilon, \tilde{\lambda}) - \Psi_{\diamond,+}(Z_\varepsilon, \tilde{\lambda})$  vanish under the projections  $Q_{\dagger,+}^{\text{u,s}}(0)$  and  $Q_{\diamond,+}^{\text{u,s}}(0)$ , respectively.

We first note that we must have  $\beta_{\dagger} = \beta_{\dagger,-}$  and  $\beta_{\diamond} = \beta_{\diamond,+}$ . This can be seen by applying  $Q_{j,+}^{\text{s}}(0)$ ,  $j = \dagger, \diamond$ , to the differences  $\Psi_{\dagger,-}(0, \tilde{\lambda}) - \Psi_{\text{sl}}(0, \tilde{\lambda})$  and  $\Psi_{\text{sl}}(Z_\varepsilon, \tilde{\lambda}) - \Psi_{\diamond,+}(Z_\varepsilon, \tilde{\lambda})$ , respectively, using the expressions (5.5.29)–(5.5.32).

We next recall the vectors  $\omega_{j,\text{ad}}(0)$  and  $\Psi_0$  defined in (5.5.27). By (5.5.26) the vectors  $\Psi_0$  and

$$\begin{aligned} \Psi_{j,\perp} &:= \omega_{j,\text{ad}}(0) - \left( \int_{-\infty}^0 e^{\eta\xi} \langle \psi_{j,\text{ad}}(\xi), F_j(\xi) \rangle d\xi \right) \Psi_0, & j = \dagger, \diamond, \\ F_j(\xi) &= \begin{pmatrix} 0 \\ -(1 - bv_j(\xi))v_j(\xi)^2 \end{pmatrix}, & j = \dagger, \diamond, \end{aligned}$$

span  $R(Q_{j,+}^{\text{u}}(0))$ . Hence we aim to show that the inner products of the differences  $\Psi_{\dagger,-}(0, \tilde{\lambda}) - \Psi_{\text{sl}}(0, \tilde{\lambda})$  and  $\Psi_{\text{sl}}(Z_\varepsilon, \tilde{\lambda}) - \Psi_{\diamond,+}(Z_\varepsilon, \tilde{\lambda})$  with  $\Psi_0$  and  $\Psi_{j,\perp}$  vanish for  $j = \dagger, \diamond$ ,

respectively. Using (5.5.29)–(5.5.32) we first project along  $\Psi_0$ , whereby

$$\begin{aligned} 0 &= \left\langle \Psi_0, \Psi_{\dagger,-}(0, \tilde{\lambda}) - \Psi_{\text{sl}}(0, \tilde{\lambda}) \right\rangle \\ &= \zeta_{\dagger,-} + \mathcal{O} \left( \left( \varepsilon |\log \varepsilon| + |\tilde{\lambda}| \right) (|\beta_{\dagger}| + |\zeta_{\dagger,-}|) + e^{-q/\varepsilon} (|\beta_{\diamond}| + |\zeta_{\diamond}|) \right), \\ 0 &= \left\langle \Psi_0, \Psi_{\text{sl}}(Z_\varepsilon, \tilde{\lambda}) - \Psi_{\diamond,+}(Z_\varepsilon, \tilde{\lambda}) \right\rangle \\ &= \zeta_{\diamond} + \mathcal{O} \left( \left( \varepsilon |\log \varepsilon| + |\tilde{\lambda}| \right) (|\beta_{\diamond}| + |\zeta_{\diamond}|) + e^{-q/\varepsilon} |\beta_{\dagger}| \right), \end{aligned} \quad (5.5.35)$$

where we used Theorem 5.5.1 (ii) and (iv), and (5.5.17). Provided  $|\tilde{\lambda}|, \varepsilon > 0$  are sufficiently small, we can solve (5.5.35) for  $\zeta_{\dagger,-}$  and  $\zeta_{\diamond}$  to obtain

$$\begin{aligned} \zeta_{\dagger,-} &= \mathcal{O} \left( \left( \varepsilon |\log \varepsilon| + |\tilde{\lambda}| \right) |\beta_{\dagger}| + e^{-q/\varepsilon} |\beta_{\diamond}| \right) \\ \zeta_{\diamond} &= \mathcal{O} \left( \left( \varepsilon |\log \varepsilon| + |\tilde{\lambda}| \right) |\beta_{\diamond}| + e^{-q/\varepsilon} |\beta_{\dagger}| \right). \end{aligned} \quad (5.5.36)$$

We substitute (5.5.36) into (5.5.29)–(5.5.32) and noting  $\Psi_{j,\perp} \in \ker(Q_{j,-}^{\text{u}}(0)^*) = R(Q_{j,-}^{\text{s}}(0)^*) \subset R(Q_{j,+}^{\text{u}}(0)^*)$  for  $j = \dagger, \diamond$ , we obtain the final conditions by projecting with  $\Psi_{j,\perp}, j = \dagger, \diamond$ , whereby

$$\begin{aligned} 0 &= \left\langle \Psi_{\dagger,\perp}, \Psi_{\dagger,-}(0, \tilde{\lambda}) - \Psi_{\text{sl}}(0, \tilde{\lambda}) \right\rangle \\ &= \beta_{\dagger} \underbrace{\int_{-L_\varepsilon}^{L_\varepsilon} \left\langle T_{\dagger}(0, \xi)^* \Psi_{\dagger,\perp}, B_{\dagger}(\xi; \tilde{\lambda}, \ell, \varepsilon) \omega_{\dagger}(\xi) \right\rangle d\xi}_{=: \mathcal{I}_{\dagger}} \\ &\quad + \mathcal{O} \left( \left( \varepsilon |\log \varepsilon| + |\tilde{\lambda}| \right)^2 |\beta_{\dagger}| + e^{-q/\varepsilon} |\beta_{\diamond}| \right), \end{aligned} \quad (5.5.37)$$

$$\begin{aligned} 0 &= \left\langle \Psi_{\diamond,\perp}, \Psi_{\text{sl}}(Z_\varepsilon, \tilde{\lambda}) - \Psi_{\diamond,+}(Z_\varepsilon, \tilde{\lambda}) \right\rangle \\ &= \beta_{\diamond} \underbrace{\int_{-L_\varepsilon}^{\infty} \left\langle T_{\diamond}(0, \xi)^* \Psi_{\diamond,\perp}, B_{\diamond}(\xi; \tilde{\lambda}, \ell, \varepsilon) \omega_{\diamond}(\xi) \right\rangle d\xi}_{=: \mathcal{I}_{\diamond}} \\ &\quad + \mathcal{O} \left( \left( \varepsilon |\log \varepsilon| + |\tilde{\lambda}| \right)^2 |\beta_{\diamond}| + e^{-q/\varepsilon} |\beta_{\dagger}| \right). \end{aligned} \quad (5.5.38)$$

where we recall that  $T_j(\xi, \hat{\xi})$  denotes the evolution for the reduced system (5.5.13).

To estimate the integrals  $\mathcal{I}_j$  for  $j = \dagger, \diamond$  appearing in (5.5.37)–(5.5.38), we note that  $T_j(0, \xi)^* \Psi_{j,\perp}$  is the solution to the adjoint equation

$$\Psi' = -A_{j,\eta}^* \Psi \quad (5.5.39)$$

of (5.5.13) satisfying  $\Psi(0) = \Psi_{j,\perp}$ ; hence we calculate

$$T_j(0, \xi)^* \Psi_{j,\perp} = \begin{pmatrix} -\int_{-\infty}^{\xi} \left\langle \psi_{j,\text{ad}}(\hat{\xi}), F_j(\hat{\xi}) \right\rangle d\hat{\xi} \\ \psi_{j,\text{ad}}(\xi) \end{pmatrix} \quad (5.5.40)$$

$$= \begin{pmatrix} -\int_{-\infty}^{\xi} e^{(c^*(a)-\eta)\hat{\xi}} (1 - bv_j(\hat{\xi})) v_j(\hat{\xi})^2 v_j'(\hat{\xi}) d\hat{\xi} \\ e^{(c^*(a)-\eta)\xi} q_j'(\xi) \\ -e^{(c^*(a)-\eta)\xi} v_j'(\xi) \end{pmatrix}, \quad (5.5.41)$$

for  $\xi \in \mathbb{R}$  and  $j = \dagger, \diamond$ . We now approximate  $\mathcal{I}_j$  by first extracting the leading order  $\tilde{\lambda}$  contribution, whereby we obtain

$$\mathcal{I}_\dagger = \underbrace{\int_{-L_\varepsilon}^{L_\varepsilon} \langle e^{\eta\xi} T_\dagger(0, \xi)^* \Psi_{\dagger, \perp}, B_\dagger(\xi; 0, \ell, \varepsilon) \phi'_d(\xi) \rangle d\xi}_{=:\mathcal{J}_\dagger} - M_{\dagger, \tilde{\lambda}}^d \tilde{\lambda} + \mathcal{O}\left(|\varepsilon \log \varepsilon|(|\tilde{\lambda}| + |\varepsilon \log \varepsilon|)\right) \quad (5.5.42)$$

$$\mathcal{I}_\diamond = \underbrace{\int_{-L_\varepsilon}^{\infty} \langle e^{\eta\xi} T_\diamond(0, \xi)^* \Psi_{\diamond, \perp}, B_\diamond(\xi; 0, \ell, \varepsilon) \phi'_d(\xi + Z_\varepsilon) \rangle d\xi}_{=:\mathcal{J}_\diamond} - M_{\diamond, \tilde{\lambda}}^d \tilde{\lambda} + \mathcal{O}\left(|\varepsilon \log \varepsilon|(|\tilde{\lambda}| + |\varepsilon \log \varepsilon|)\right), \quad (5.5.43)$$

where

$$M_{\dagger, \tilde{\lambda}}^d := \int_{-\infty}^{\infty} e^{c^*(a)\xi} (v'_\dagger(\xi))^2 d\xi = \int_{-L_\varepsilon}^{L_\varepsilon} e^{c^*(a)\xi} (v'_\dagger(\xi))^2 d\xi + \mathcal{O}(\varepsilon) \quad (5.5.44)$$

$$M_{\diamond, \tilde{\lambda}}^d := \int_{-\infty}^{\infty} e^{c^*(a)\xi} (v'_\diamond(\xi))^2 d\xi = \int_{-L_\varepsilon}^{\infty} e^{c^*(a)\xi} (v'_\diamond(\xi))^2 d\xi + \mathcal{O}(\varepsilon), \quad (5.5.45)$$

where we used the fact that the integrands decay exponentially to estimate the tails of the integrals. Finally, in order to obtain the leading order  $\varepsilon$  contribution, it remains to estimate the integrals  $\mathcal{J}_j$  for  $j = \dagger, \diamond$  which appear in the expressions (5.5.42)–(5.5.43). To do this, we note that the derivative  $\Phi'_d(\xi) = (u'_d(\xi), v'_d(\xi), q'_d(\xi))^T$  of the pulse solution solves the linearized equations when  $\ell = 0$ , and therefore satisfies

$$\Phi''_d(\xi) = (A_{\dagger, 0}(\xi) + B_\dagger(\xi; 0, 0, \varepsilon)) \Phi'_d(\xi), \quad \xi \in [-L_\varepsilon, L_\varepsilon] \quad (5.5.46)$$

and

$$\Phi''_d(\xi + Z_\varepsilon) = (A_{\diamond, 0}(\xi) + B_\diamond(\xi; 0, 0, \varepsilon)) \Phi'_d(\xi + Z_\varepsilon), \quad \xi \in [-L_\varepsilon, \infty). \quad (5.5.47)$$

In particular, for  $\xi \in [-L_\varepsilon, L_\varepsilon]$ , we obtain

$$\begin{aligned} B_\dagger(\xi; 0, \ell, \varepsilon) \Phi'_d(\xi) &= [\partial_\xi - A_{\dagger, 0}(\xi) + B_\dagger(\xi; 0, \ell, \varepsilon) - B_\dagger(\xi; 0, 0, \varepsilon)] \Phi'_d(\xi) \\ &= \begin{pmatrix} 0 \\ [\partial_\xi - C_{\dagger, 0}(\xi)] \begin{pmatrix} v'_d(\xi) \\ q'_d(\xi) \end{pmatrix} \end{pmatrix} + \begin{pmatrix} u''_d(\xi) - \frac{\varepsilon \ell^2}{1 + \varepsilon c_d} u'_d(\xi) \\ 0 \\ (1 - bv_\dagger(\xi)) v_\dagger(\xi)^2 u'_d(\xi) \end{pmatrix} \end{aligned}$$

and similarly

$$\begin{aligned} B_\diamond(\xi; 0, \ell, \varepsilon) \Phi'_d(\xi + Z_\varepsilon) &= [\partial_\xi - A_{\diamond, 0}(\xi) + B_\diamond(\xi; 0, \ell, \varepsilon) - B_\diamond(\xi; 0, 0, \varepsilon)] \Phi'_d(\xi + Z_\varepsilon) \\ &= \begin{pmatrix} 0 \\ [\partial_\xi - C_{\diamond, 0}(\xi)] \begin{pmatrix} v'_d(\xi + Z_\varepsilon) \\ q'_d(\xi + Z_\varepsilon) \end{pmatrix} \end{pmatrix} + \begin{pmatrix} u''_d(\xi + Z_\varepsilon) - \frac{\varepsilon \ell^2}{1 + \varepsilon c_d} u'_d(\xi + Z_\varepsilon) \\ 0 \\ (1 - bv_\diamond(\xi)) v_\diamond(\xi)^2 u'_d(\xi + Z_\varepsilon) \end{pmatrix} \end{aligned}$$

for  $\xi \in [-L_\varepsilon, \infty)$ . Using the fact that  $\psi_{j, \text{ad}}(\xi)$  solves (5.5.20), we have

$$[\partial_\xi - C_{j, 0}(\xi)]^* (e^{\eta\xi} \psi_{j, \text{ad}}(\xi)) = 0, \quad j = \dagger, \diamond, \quad (5.5.48)$$



and we therefore obtain

$$\begin{aligned}
 \mathcal{J}_\dagger &= \int_{-L_\varepsilon}^{L_\varepsilon} \left\langle e^{\eta\xi} T_\dagger(0, \xi)^* \Psi_{\dagger, \perp}, \begin{pmatrix} u_d''(\xi) - \frac{\varepsilon\ell^2}{1+\varepsilon c_d} u_d'(\xi) \\ 0 \\ (1 - bv_\dagger(\xi))v_\dagger(\xi)^2 u_d'(\xi) \end{pmatrix} \right\rangle d\xi \\
 &= - \int_{-L_\varepsilon}^{L_\varepsilon} \left( e^{c^*(a)\xi} v_\dagger'(\xi) (1 - bv_\dagger(\xi))v_\dagger(\xi)^2 u_d'(\xi) \right. \\
 &\quad \left. + u_d''(\xi) \int_{-\infty}^{\xi} e^{c^*(a)\hat{\xi}} (1 - bv_\dagger(\hat{\xi}))v_\dagger(\hat{\xi})^2 v_\dagger'(\hat{\xi}) d\hat{\xi} \right) d\xi \\
 &\quad + \frac{\varepsilon\ell^2}{1 + \varepsilon c_d} \int_{-L_\varepsilon}^{L_\varepsilon} \left( u_d'(\xi) \int_{-\infty}^{\xi} e^{c^*(a)\hat{\xi}} (1 - bv_\dagger(\hat{\xi}))v_\dagger(\hat{\xi})^2 v_\dagger'(\hat{\xi}) d\hat{\xi} \right) d\xi + \mathcal{O}(\varepsilon^2),
 \end{aligned}$$

where we used the fact that the integrands decay exponentially. Integrating by parts, we have that

$$\begin{aligned}
 \mathcal{J}_\dagger &= - \int_{-L_\varepsilon}^{L_\varepsilon} \frac{d}{d\xi} \left( u_d'(\xi) \int_{-\infty}^{\xi} e^{c^*(a)\hat{\xi}} (1 - bv_\dagger(\hat{\xi}))v_\dagger(\hat{\xi})^2 v_\dagger'(\hat{\xi}) d\hat{\xi} \right) d\xi \\
 &\quad + \frac{\varepsilon\ell^2}{1 + \varepsilon c_d} \left[ u_d(\xi) \int_{-\infty}^{\xi} e^{c^*(a)\hat{\xi}} (1 - bv_\dagger(\hat{\xi}))v_\dagger(\hat{\xi})^2 v_\dagger'(\hat{\xi}) d\hat{\xi} \right]_{-L_\varepsilon}^{L_\varepsilon} \\
 &\quad - \frac{\varepsilon\ell^2}{1 + \varepsilon c_d} \int_{-L_\varepsilon}^{L_\varepsilon} u_d(\xi) e^{c^*(a)\xi} (1 - bv_\dagger(\xi))v_\dagger(\xi)^2 v_\dagger'(\xi) d\xi + \mathcal{O}(\varepsilon^2) \\
 &= -u_d'(L_\varepsilon) \int_{-\infty}^{L_\varepsilon} e^{c^*(a)\xi} (1 - bv_\dagger(\xi))v_\dagger(\xi)^2 v_\dagger'(\xi) d\xi + \mathcal{O}(\varepsilon^2 |\log \varepsilon|) \\
 &= -\varepsilon [u^*(a) - a + u^*(a)v_+(u^*(a))^2] \int_{-\infty}^{\infty} e^{c^*(a)\xi} (1 - bv_\dagger(\xi))v_\dagger(\xi)^2 v_\dagger'(\xi) d\xi \\
 &\quad + \mathcal{O}(\varepsilon^2 |\log \varepsilon|),
 \end{aligned}$$

where we again used the fact that the integrands decay exponentially, and we estimated  $u_d(\xi) = u^*(a) + \mathcal{O}(\varepsilon \log \varepsilon)$  for  $\xi \in [-L_\varepsilon, L_\varepsilon]$  and

$$\begin{aligned}
 u_d'(L_\varepsilon) &= \varepsilon [u_d(L_\varepsilon) - a + u_d(L_\varepsilon)v_d'(L_\varepsilon)^2] \\
 &= \varepsilon [u^*(a) - a + u^*(a)v_+(u^*(a))^2 + \mathcal{O}(|\varepsilon \log \varepsilon|)],
 \end{aligned}$$

using Theorem 5.5.1. Hence we have that

$$\mathcal{J}_\dagger = -M_{\dagger, \varepsilon}^d \varepsilon + \mathcal{O}(\varepsilon^2 |\log \varepsilon|), \tag{5.5.49}$$

where

$$M_{\dagger, \varepsilon}^d := [u^*(a) - a + u^*(a)v_+(u^*(a))^2] \int_{-\infty}^{\infty} e^{c^*(a)\xi} (1 - bv_\dagger(\xi))v_\dagger(\xi)^2 v_\dagger'(\xi) d\xi > 0. \tag{5.5.50}$$

Performing a similar computation for  $\mathcal{J}_\circ$ , we arrive at

$$\mathcal{J}_\circ = - \lim_{\xi \rightarrow \infty} u_d'(Z_\varepsilon + \xi) \int_{-\infty}^{\infty} e^{c^*(a)\xi} (1 - bv_\dagger(\xi))v_\dagger(\xi)^2 v_\dagger'(\xi) d\xi + \mathcal{O}(\varepsilon^2) = \mathcal{O}(\varepsilon^2), \tag{5.5.51}$$

due to the fact that  $u'_d(Z_\varepsilon + \xi) \rightarrow 0$  as  $\xi \rightarrow \infty$ .

Substituting the expressions for  $\mathcal{I}_j, \mathcal{J}_j, j = \dagger, \diamond$ , into the remaining conditions (5.5.37)–(5.5.38), we find the following linear system of equations for  $(\beta_\dagger, \beta_\diamond)$ , solutions of which correspond to eigenfunctions of (5.5.9):

$$\mathcal{M}(\tilde{\lambda}, \varepsilon) \begin{pmatrix} \beta_\dagger \\ \beta_\diamond \end{pmatrix} = 0, \quad (5.5.52)$$

where

$$\mathcal{M}(\tilde{\lambda}, \varepsilon) := \begin{pmatrix} -\tilde{\lambda}M_{\dagger, \tilde{\lambda}}^d - M_{\dagger, \varepsilon}^d + \mathcal{O}((\varepsilon|\log \varepsilon| + |\tilde{\lambda}|)^2) & \mathcal{O}(e^{-q/\varepsilon}) \\ \mathcal{O}(e^{-q/\varepsilon}) & -\tilde{\lambda}M_{\diamond, \tilde{\lambda}}^d + \mathcal{O}((\varepsilon|\log \varepsilon| + |\tilde{\lambda}|)^2) \end{pmatrix}. \quad (5.5.53)$$

Since the solutions  $\Psi_{\dagger, -}, \Psi_{\text{sl}}, \Psi_{\diamond, +}$  from Proposition 5.5.4 and the matrices  $B_j$  are analytic in  $\tilde{\lambda}$ , all entries in the matrix  $\mathcal{M}(\tilde{\lambda}, \varepsilon)$  (5.5.53), and furthermore its determinant  $D(\tilde{\lambda}, \varepsilon)$ , are analytic in  $\tilde{\lambda}$ . Note that the quantities  $M_{\dagger, \varepsilon}^d$  and  $M_{j, \tilde{\lambda}}^d, j = \dagger, \diamond$  are nonzero and independent of  $\tilde{\lambda}, \varepsilon$ . Hence, provided  $\delta, \varepsilon > 0$  are sufficiently small, we have

$$|D(\tilde{\lambda}, \varepsilon) - \tilde{\lambda}M_{\diamond, \tilde{\lambda}}^d(\tilde{\lambda}M_{\dagger, \tilde{\lambda}}^d + \varepsilon M_{\dagger, \varepsilon}^d)| < |\tilde{\lambda}M_{\diamond, \tilde{\lambda}}^d(\tilde{\lambda}M_{\dagger, \tilde{\lambda}}^d + \varepsilon M_{\dagger, \varepsilon}^d)|.$$

for  $\tilde{\lambda} \in \partial R_1(\delta) = \{\tilde{\lambda} \in \mathbb{C} : |\tilde{\lambda}| = \delta\}$ , and by Rouché's Theorem  $D(\tilde{\lambda}, \varepsilon)$  has precisely two roots  $\tilde{\lambda}_0, \tilde{\lambda}_1$  in  $R_1(\delta)$  which are  $\mathcal{O}(|\varepsilon \log \varepsilon|^2)$ -close to the roots

$$\tilde{\lambda} = 0, \quad \tilde{\lambda} = -\frac{M_{\dagger, \varepsilon}^d}{M_{\dagger, \tilde{\lambda}}^d} \varepsilon$$

of  $\tilde{\lambda}M_{\diamond, \tilde{\lambda}}^d(\tilde{\lambda}M_{\dagger, \tilde{\lambda}}^d + \varepsilon M_{\dagger, \varepsilon}^d)$ . We deduce that (5.5.9) has two real eigenvalues in the region  $R_1(\delta)$  given by

$$\tilde{\lambda}_0(\ell) = \mathcal{O}(|\varepsilon \log \varepsilon|^2), \quad \tilde{\lambda}_c(\ell) = -\frac{M_{\dagger, \varepsilon}^d}{M_{\dagger, \tilde{\lambda}}^d} \varepsilon + \mathcal{O}(|\varepsilon \log \varepsilon|^2),$$

and by implicitly differentiating the characteristic equation of (5.5.53), we furthermore obtain that the derivatives of  $\tilde{\lambda}_0(\ell)$  with respect to  $\ell$  satisfy the same estimates. We note that the derivative  $\Phi'_d$  of the pulse solution is an eigenfunction with eigenvalue 0 when  $\ell = 0$  due to translation invariance, hence  $\lambda_0(0) = 0$ . Furthermore, since (5.5.53) depends on  $\ell$  only via the quantity  $\ell^2$ , we obtain that  $\tilde{\lambda}'_0(0) = 0$ .  $\square$

### 5.5.6 The region $(\tilde{\lambda}(\ell), \ell) \in R_2(\delta, M) \times [-L_M, L_M]$

We now consider the final remaining region,  $\tilde{\lambda}(\ell) \in R_2(\delta, M)$  for  $|\ell|$  bounded. The fundamental idea is the same as for the region  $R_1(\delta)$ ; using exponential dichotomies along the fast jumps and the slow manifolds, we attempt to construct potential eigenfunctions. However, in this region it is possible to construct exponential dichotomies along each of the intervals  $I_\ell, I_\dagger, I_r, I_\diamond$ , and by comparing their projections at the endpoints of these intervals we obtain estimates which preclude the existence of a nontrivial exponentially localized eigenfunction. We note that the exponential dichotomies along  $I_r$

and  $I_\ell$  are guaranteed by Proposition 5.5.2. The existence of exponential dichotomies along  $I_\dagger$  and  $I_\diamond$  is due to the fact that the associated reduced problems along each of the fast jumps admit no eigenvalues for  $\tilde{\lambda}(\ell) \in R_2(\delta, M)$ .

To see this, proceeding in a similar fashion as in section 5.5.5, we consider the following reduced problems along  $I_\dagger$  and  $I_\diamond$  obtained for  $\varepsilon = 0$  and  $\tilde{\lambda} \in R_2(\delta, M)$ .

$$\psi_\xi = A_{j,\eta}(\xi; \tilde{\lambda})\psi, \quad (5.5.54)$$

$$A_{j,\eta}(\xi; \tilde{\lambda}) := \begin{pmatrix} \eta & 0 & 0 \\ 0 & \eta & 1 \\ -(1 - bv_j(\xi))v_j(\xi)^2 & m + \tilde{\lambda} - (2 - 3bv_j(\xi))u_jv_j(\xi) & \eta - c^*(a) \end{pmatrix}, \quad (5.5.55)$$

Here  $j = \dagger, \diamond$ , where again  $v_j(\xi)$  denotes the  $v$ -component of  $\phi_j(\xi)$ , and  $u_\dagger = u^*(a)$ , respectively  $u_\diamond = a$ . As in section 5.5.5, the lower triangular structure allows us to restrict to a two-dimensional invariant subspace with dynamics

$$\psi' = C_{j,\eta}(\xi; \tilde{\lambda})\psi, \quad j = \dagger, \diamond \quad (5.5.56)$$

$$C_{j,\eta}(\xi; \tilde{\lambda}) := \begin{pmatrix} \eta & 1 \\ m + \tilde{\lambda} - (2 - 3bv_j(\xi))u_jv_j(\xi) & \eta - c^*(a) \end{pmatrix}, \quad j = \dagger, \diamond. \quad (5.5.57)$$

We note that the front profiles  $v_\dagger(\xi)$  and  $v_\diamond(\xi)$  are solutions to the scalar equations

$$v_t = v_\xi\xi + c^*(a)v_\xi - mv + (1 - bv)u_jv^2, \quad j = \dagger, \diamond,$$

and critically, the linear system (5.5.56) is precisely the (weighted) eigenvalue problem one obtains by considering their stability with eigenvalue parameter  $\tilde{\lambda}$ . Since the derivatives  $v'_j(\xi), j = \dagger, \diamond$  define exponentially localized eigenfunctions with no zeros when  $\tilde{\lambda} = 0$ , Sturm-Liouville theory precludes the existence of eigenvalues in  $R_2(\delta, M)$ , provided  $\delta$  is sufficiently small. Thus (5.5.56) admits exponential dichotomies, which can be extended to the full system (5.5.54) using variation of constants formulae. Finally, these exponential dichotomies can be extended to the stability problem (5.5.9) on the intervals  $I_\dagger$  and  $I_\diamond$  using roughness results.

Once exponential dichotomies are established along each of the intervals  $I_\ell, I_\dagger, I_r$  and  $I_\diamond$ , it remains to compare their projections at the endpoints of each interval. Using the estimates in Theorem 5.5.1 combined with repeated use of a technical lemma [83, Lemma 6.10], it is possible to show that each pair of projections is sufficiently close at each endpoint, and further that any exponentially localized solution to (5.5.9) must be trivial. This is summarized in the following proposition.

**Proposition 5.5.6.** *Fix  $M > 0$ . There exists  $\delta > 0$  such that for each sufficiently small  $\varepsilon > 0$  and each  $\tilde{\lambda} \in R_2(\delta, M)$ , the eigenvalue problem (5.5.9) admits no nontrivial exponentially localized solution.*

The proof of Proposition 5.5.6 follows the argument as outlined above, and is similar to the proof of [22, Proposition 6.20]. For completeness, we include this in Appendix 5.B.

### 5.5.7 Proof of Theorem 5.4.3

*Proof of Theorem 5.4.3.* This is a direct consequence of the analysis in section 5.4.1, section 5.5.2, section 5.5.3, in combination with Theorem 5.5.5 and Proposition 5.5.6. The fact that the translational eigenvalue  $\tilde{\lambda}_0(0) = 0$  is simple follows from a similar argument as in [22, Proposition 6.14].  $\square$

## 5.6 Defects and curved vegetation pattern solutions

In this section we consider (5.1.2) with a small diffusion term added to the water component.

$$\begin{cases} u_t &= D\Delta u + \frac{1}{\varepsilon}u_x + a - u - G(u, v)v, \\ v_t &= \Delta v - mv + R(v)G(u, v)v, \end{cases} \quad (5.6.1)$$

where  $D \ll 1$ . The reason for this is mainly technical, in order to draw on results concerning planar interface propagation in parabolic equations. However, to accurately describe water movement on flat terrains a diffusion term is necessary [170] – see also the upcoming discussion section, section 5.8.

The results of Theorems 5.2.8–5.2.11 and Theorems 5.4.2–5.4.4 concern the existence and stability of straight stripe, gap, and front solutions; that is, the traveling patterns are constant in the direction transverse to the slope and are essentially one-dimensional patterns. We reiterate that these patterns are, however, stable to perturbations in two spatial dimensions.

We now consider the system (5.6.1) for which, by a perturbation argument, the results of Theorems 5.2.8–5.2.11, and furthermore the results of Theorems 5.4.2–5.4.4, are expected to hold for sufficiently small  $D > 0$ . Within this system, we are able to call on general results on the existence and stability of corner defects in planar wave propagation [76, 77]. In essence, considering a straight vegetation stripe, gap, or front solution satisfying certain hypotheses (see below), for nearby wave speeds there exist stripe solutions at slightly offset angles. Two oppositely angled such stripes can meet at a corner defect, forming a “curved” stripe solution, which can be oriented convex upslope (exterior corner) or downslope (interior corner). Further, some of these solutions can be shown to be stable. In particular, we will argue using the results of [76, 77] that nearby vegetation stripe, gap, or front solutions of (5.6.1), there exist stable interior corner defects, and in the case of certain front solutions, there exist stable exterior corner defects.

Consider a traveling wave solution  $(u, v)(x, y, t) = (u_s, v_s)(\xi)$  of (5.6.1) with speed  $c = c_s$ , and  $\xi = x - ct$ . An almost planar interface  $\sigma$ -close to  $(u_s, v_s)(\xi)$  with speed  $c$  is a solution of the form

$$(u, v)(x, y, t) = (u_s, v_s)(\xi + h(y)) + (\tilde{u}, \tilde{v})(\xi, y), \quad (5.6.2)$$

where  $h \in C^2(\mathbb{R})$  and

$$\sup_{y \in \mathbb{R}} |h'(y)| < \sigma, \quad \sup_{y \in \mathbb{R}} \|(\tilde{u}, \tilde{v})(\cdot, y)\|_{H^1(\mathbb{R}, \mathbb{R}^2)} < \sigma, \quad |c - c_s| < \sigma \quad (5.6.3)$$

This solution is a planar interface if  $h'' = 0$  and a corner defect if  $h'' \neq 0$ , and  $h'(y) \rightarrow \eta_{\pm}$  as  $y \rightarrow \infty$ . A corner defect can be classified depending on the asymptotic orientations  $\eta_{\pm}$  as an (i) interior corner ( $\eta_+ < \eta_-$ ), (ii) exterior corner ( $\eta_- < \eta_+$ ), (iii) step ( $\eta_+ = \eta_- \neq 0$ ), or (iv) hole ( $\eta_+ = \eta_- = 0$ ).

Depending on the original traveling wave solution  $(u_s, v_s)(\xi)$ , it may be possible to determine which type(s) of defects can arise. As stated above, a corner defect is essentially composed of slightly angled stripe solutions meeting along an interface. An angled stripe solution can be written as a traveling wave

$$(u, v)(x, y, t) = (u, v)(\xi), \quad \xi = x \cos \varphi + y \sin \varphi - ct \quad (5.6.4)$$

where the case  $\varphi = 0$  corresponds to a solution which is constant in the direction transverse to the slope as before. Substituting this ansatz into (5.6.1) results in the traveling wave ODE

$$\begin{cases} -cu_\xi &= Du_{\xi\xi} + \frac{\cos\varphi}{\varepsilon}u_\xi + a - u - G(u, v)v, \\ -cv_\xi &= v_{\xi\xi} - mv + R(v)G(u, v)v. \end{cases} \quad (5.6.5)$$

By setting  $\tilde{\varepsilon} = \varepsilon/\cos\varphi$ , we see that (5.6.5) is the same traveling wave equation one obtains in the case of  $\varphi = 0$ , except with  $\varepsilon$  replaced by  $\tilde{\varepsilon}$ . For small values of  $\varphi$ , we have that

$$\tilde{\varepsilon} = \varepsilon(1 + \mathcal{O}(\varphi^2)) \quad (5.6.6)$$

and (5.6.5) can therefore be solved to find an angled traveling wave solution when

$$c = c(\varphi) = c_s + \mathcal{O}(\varepsilon\varphi^2). \quad (5.6.7)$$

The quantity  $c(\varphi)$  is called the nonlinear dispersion relation and relates the speed of propagation and angle of the traveling wave solution. A related quantity

$$d(\varphi) := \frac{c(\varphi)}{\cos(\varphi)} \quad (5.6.8)$$

called the directional dispersion, or flux, relates the angle to the speed of propagation in the direction of the original traveling wave  $(u_s, v_s)$ , i.e. the  $x$ -direction. The flux near  $\varphi = 0$  is said to be convex if  $d'' > 0$ , concave if  $d'' < 0$ , and flat if  $d'' \equiv 0$  for small  $|\varphi|$ . In [76], the authors related the convexity of the flux to the type of corner defect which is selected: in particular when  $d$  is convex, there exist interior corner defects for nearby speeds  $c > c_s$ , while for  $d$  concave there exist exterior corner defects for speeds  $c < c_s$ .

In the case of (5.6.5), the directional dispersion is computed as

$$d(\varphi) := c_s \left( 1 + \frac{\varphi^2}{2} \right) + \mathcal{O}(\varepsilon\varphi^2, \varphi^4), \quad (5.6.9)$$

from which we find that

$$d''(\varphi) := c_s + \mathcal{O}(\varepsilon, \varphi^2), \quad (5.6.10)$$

that is, to leading order the convexity is determined by the speed of propagation of the original traveling wave  $(u_s, v_s)$ . In particular, for sufficiently small  $\varepsilon$ , the directional dispersion is convex for  $c_s > 0$  and concave for  $c_s < 0$ . Hence in the setting of Theorems 5.2.8, 5.2.9, or 5.2.10, one expects to see nearby interior corner solutions, but *not* exterior corner solutions. That is, the resulting curved vegetation stripe, gap, or front is oriented convex downslope. However, in the setting of Theorem 5.2.11, the convexity depends on the value of  $a/m$  as the speed  $c_s$  can be negative if  $a$  is large enough. In particular, one expects interior corner solutions if  $\frac{a}{m} < \frac{9b}{2} + \frac{2}{b}$ , but exterior corners (oriented convex upslope) if  $\frac{a}{m} > \frac{9b}{2} + \frac{2}{b}$ .

## 5.7 Numerics

In this section we present numerical results related to Theorems 5.2.8–5.2.11 and Theorems 5.4.2–5.4.4 regarding the existence and stability of front, stripe, and gap pattern

solutions of (5.1.2). In particular, we discuss the results of numerical continuation of stripe and gap traveling wave solutions, and direct numerical simulation of planar stripe, gap, and front solutions, as well as corner defect solutions as discussed in section 5.6.

### 5.7.1 Continuation of traveling stripes and gaps

Theorems 5.2.8–5.2.9 predict the existence of traveling stripe and gap solutions to (5.1.2) which solve the traveling wave ODE (5.1.7). These solutions were constructed as perturbations of singular homoclinic orbits, organized by the singular bifurcations diagrams in Figures 5.8a and 5.8b, corresponding to the cases of  $b < 2/3$  and  $b > 2/3$ , respectively. Figure 5.16 depicts the results of numerical continuation of speed  $c$  versus  $a$  for traveling stripes and gaps, conducted in AUTO for the parameter values  $\varepsilon = 3 \cdot 10^{-4}$ ,  $m = 0.5$ , and values of  $b = 0.6, 0.7$  on either side of the critical value  $b = 2/3$ . The continuation curves corresponding to vegetation stripe solutions are depicted in green, while those corresponding to gap solutions are in purple, with the relevant singular bifurcation curves depicted as dashed lines.

We note that the upper branches of the bifurcation curves for both stripes and gaps continue towards  $c = 0$  and eventually turn back onto lower branches which persist for a range of  $a$  values and small speeds  $c \ll 1$ . These waves arise as perturbations of a family of fast planar homoclinic orbits, as discussed in Remark 5.2.4, and we expect they are unstable (even to 1D perturbations) as traveling wave solutions of (5.1.2). Interestingly, the lower branch of stripe solutions continues for increasing  $a$ , while the lower branch of gap solutions eventually turns back near the canard value  $\frac{a}{m} = 4b + 1/b$  due to interaction of the equilibrium  $p_+(u_2)$  with the fold point  $\mathcal{F}$ .

**Remark 5.7.1.** *We also remark that in the case of  $b < 2/3$ , depicted in the left panel of Figure 5.16, that the upper branch of gap solutions also approaches the canard point. Here this branch transitions into a “double-gap” solution, resembling two copies of the primary homoclinic orbit. This transition is similar to canard transitions observed in systems such as the FitzHugh–Nagumo equation [26, 27, 73], albeit with a somewhat different mechanism due to the presence of the additional equilibrium  $p_0(a)$ .*

We also depict the results of continuation of both stripe and gap solutions for fixed values of rainfall  $a = 1.2$  (stripes) and  $a = 2$  (gaps), with  $m = 0.45, b = 0.5$ , and  $\varepsilon = 0.01$ . As discussed in section 5.2.4, it is expected that nearby the single traveling stripe or gap solutions are periodic wave train solutions corresponding to repeating vegetation patterns which exist for a range of wave speeds, and that these patterns can similarly be constructed by perturbing from singular periodic orbits in the traveling wave equation (5.1.7). We verify this prediction by numerically continuing the stripe (and gap) solutions as periodic orbits for decreasing period, the results of which are depicted in Figure 5.17. We observe that in general the wave speed  $c$  decreases as the period  $T$  decreases, as do the total biomass  $B := \int_0^T v \, dx$  and the maximum value of  $v$  over one period, denoted by  $v_{\max}$ . Lastly the results of continuation of periodic orbits in  $(a, k)$ -space for fixed wave speeds  $c = \{0.15, 0.2, 0.25, 0.3, 0.35\}$  are depicted in Figure 5.18; here  $k$  denotes the wavenumber of the corresponding pattern.

These numerical results align with previous work on (similar) ecosystem models; similar trends are found in, for instance, studies on the Klausmeier vegetation model [152], on extended Klausmeier models [8, 9, 158], on the Klausmeier–Gray–Scott model [148] and the Rietkerk model [36]. Moreover, measurements on the speed of migrating vegetation patterns, indeed, show vegetation patterns with higher wavelength

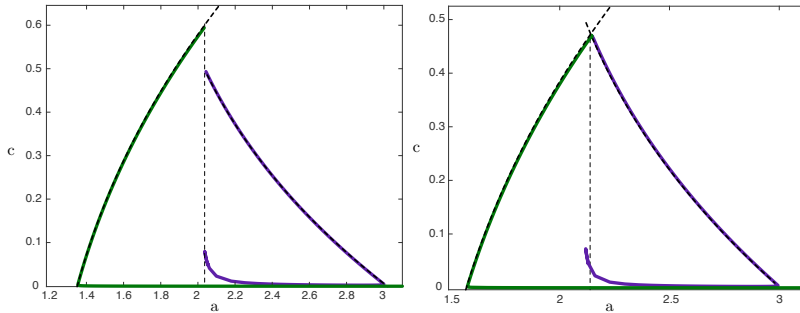


**Figure 5.16** – Shown are numerically computed bifurcation diagrams of vegetation stripes (green curves) and gaps (purple curves) for the parameter values  $m = 0.5$ ,  $\varepsilon = 0.0003$ , and  $b = 0.6$  (left panel),  $b = 0.74$  (right panel). The solutions were obtained via parameter continuation in AUTO for the traveling wave equation (5.1.7). Also plotted in dashed black are the curves  $c = c^*(a)$  and  $c = \hat{c}(a)$ . The vertical dashed curve denotes the location of  $\bar{a}$  in each panel.

move faster [9, 41]. Finally, recent in-situ measurement on the above ground biomass in the Horn of Africa corroborate displayed trends in biomass [9].

## 5.7.2 Direct simulations

In this section we present direct numerical simulations of the various traveling wave solutions predicted by Theorems 5.2.8–5.2.11. To that end, we have spatially discretized the PDE (5.1.2) with a uniformly spaced grid in both  $x$  and  $y$  directions, which was integrated using a Runge–Kutta solver. In all simulations, the initial conditions were constructed using the approximate expressions derived in the previous sections of this article.

First, we have tested the existence and 2D stability of straight (i.e. non-curved) patterns. The results for  $b = 0.5 < 2/3$  are given in Figure 5.19 and for  $b = 0.75 > 2/3$  in Figure 5.20. In both cases, all solutions from Theorems 5.2.8–5.2.11 could be obtained easily and were (2D) stable in our simulations (and in fact all seem to have a quite large domain of attraction).

Moreover, we numerically inspected corner solutions as described in section 5.6. Again, numerical simulations corroborate theoretical predictions – see Figure 5.21. In fact, we were able to find corner-type solutions for each front or pulse in Theorems 5.2.8–5.2.11. When the speed of the straight pattern is positive, i.e.  $c_s > 0$ , it is possible to find curved patterns which are oriented convex downslope (interior defect) and when  $c_s < 0$  the curved pattern is oriented convex upslope (exterior defect); recall that upslope corresponds to the direction of increasing  $x$ . This matches the prediction given by the directional dispersion, as outlined in section 5.6.

## 5.8 Discussion

In this paper we constructed planar traveling stripes, gaps and front-type solutions to the modified Klausmeier model (5.1.2). We proved their existence rigorously using geometric singular perturbation methods for a wide range of system parameters  $a, b, m$  in the large advection limit  $\varepsilon \rightarrow 0$ . We showed that vegetation stripes exist for smaller

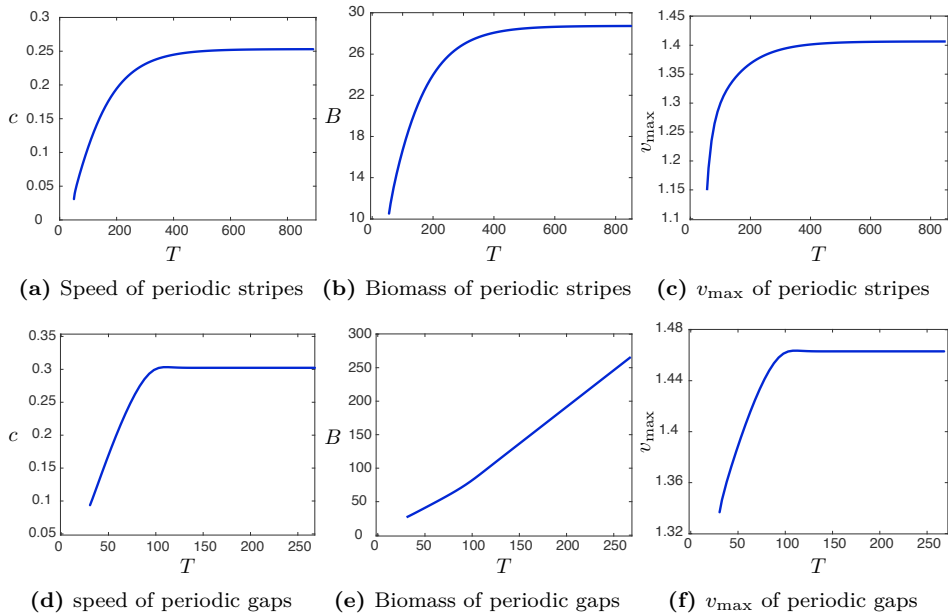


**Figure 5.17** – Results of numerical continuation of periodic stripe (a-c) and gap (d-f) pattern solutions for decreasing wavelength for the parameter values  $m = 0.45$ ,  $b = 0.5$ ,  $\varepsilon = 0.01$  and  $a = 1.2$  (stripes),  $a = 2$  (gaps). Shown are plots of speed  $c$  of the pattern vs. period  $T$  (left panels), biomass  $B := \int_0^T v \, dx$  vs. period  $T$  (middle panels), and  $v_{\max}$  versus the period  $T$ , where  $v_{\max}$  denotes the maximum of  $v$  over one period (right panels).

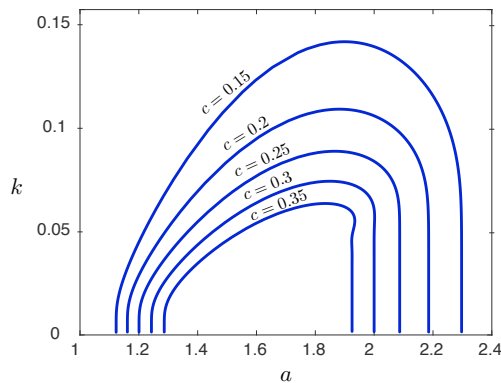


**Figure 5.18** – Results of numerical continuation of periodic stripe/gap patterns for spatial wavenumber  $k$  versus  $a$  for fixed  $b = 0.5$ ,  $m = 0.45$ ,  $\varepsilon = 0.01$  and wave speeds  $c = \{0.15, 0.2, 0.25, 0.3, 0.35\}$ .



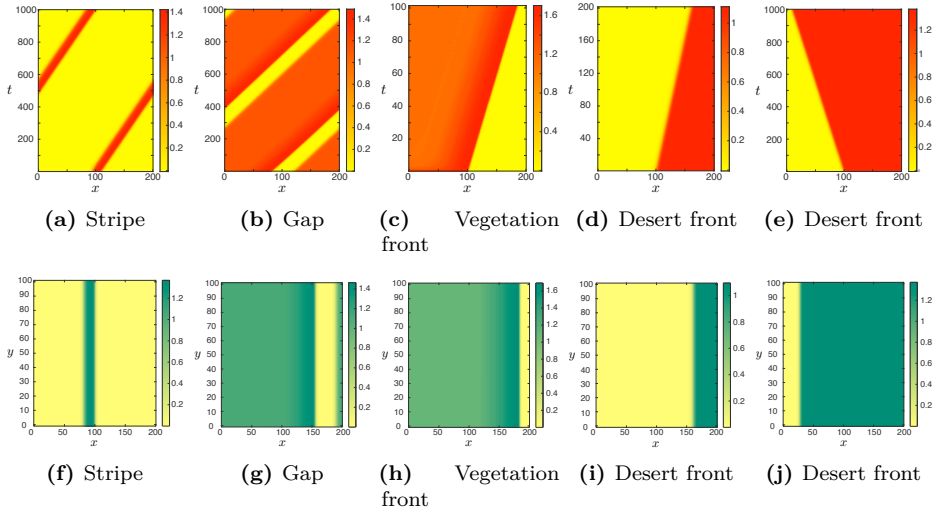


**Figure 5.19** – Results of direct numerical simulation of the PDE (5.1.2) for  $b = 0.5$ ,  $m = 0.45$ ,  $\varepsilon = 0.01$  and  $a = 1.2$  (a,f),  $a = 2.0$  (b–d,g–i) or  $a = 3.0$  (e,j). Figures a–e show the evolution of a cross section of  $v$ , i.e. for constant  $y$  and figures f–j show the  $v(x, y)$  pattern at a specific time. Simulations are run on a finite grid of size  $L_x = 200$ ,  $L_y = 100$ , accompanied with Neumann boundary conditions for the  $y$ -direction and either periodic (a–b,f–g) or Neumann (c–e,h–j) boundary conditions in the  $x$ -direction.

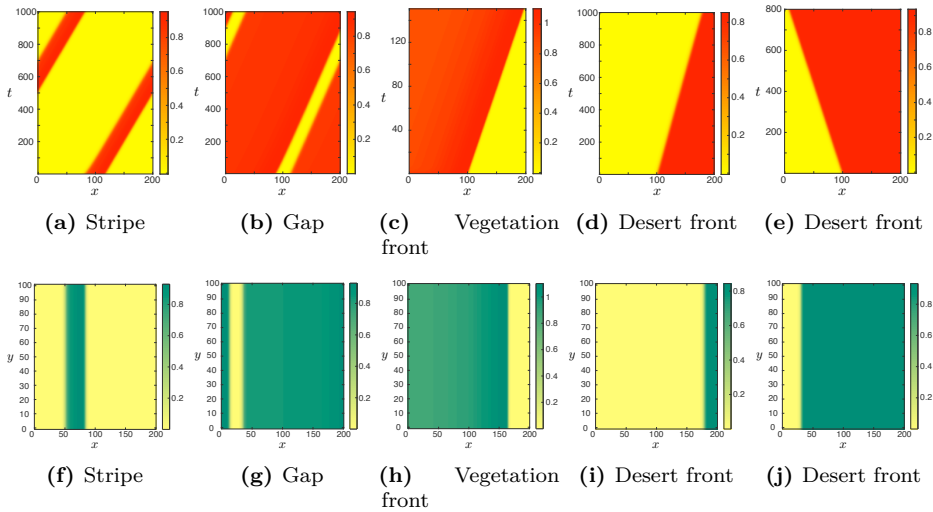


**Figure 5.20** – Results of direct numerical simulation of the PDE (5.1.2) for  $b = 0.75$ ,  $m = 0.45$ ,  $\varepsilon = 0.01$  and  $a = 1.75$  (a,f),  $a = 2.4$  (b,g),  $a = 2.5$  (c–d,h–i) or  $a = 3.0$  (e,j). Figures a–e show the evolution of a cross section of  $v$ , i.e. for constant  $y$  and figures f–j show the  $v(x, y)$  pattern at a specific time. Simulations are run on a finite grid of size  $L_x = 200$ ,  $L_y = 100$ , accompanied with Neumann boundary conditions for the  $y$ -direction and either periodic (a–b,f–g) or Neumann (c–e,h–j) boundary conditions in the  $x$ -direction.

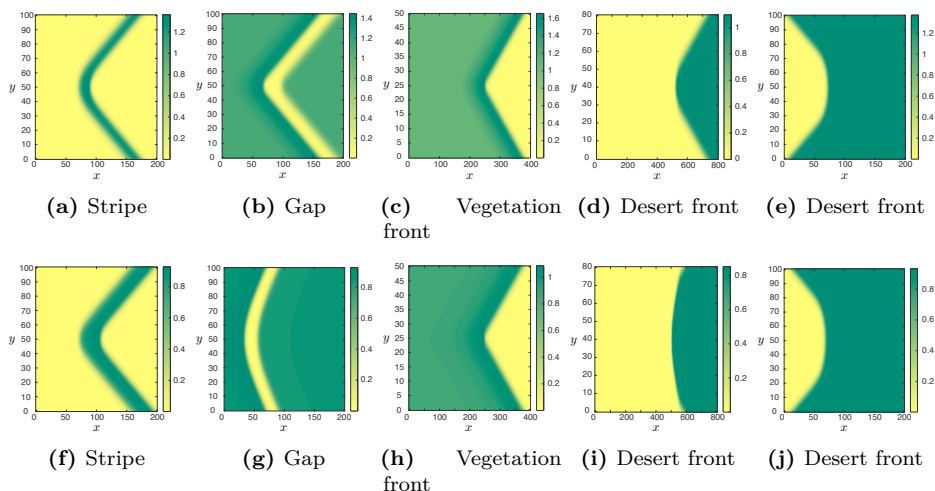


**Figure 5.21** –  $v(x, y)$  configuration of corner solutions in direct numerical simulations of the PDE (5.1.2) for  $m = 0.45$ ,  $\varepsilon = 0.01$ ,  $b = 0.5$  (a–e) or  $b = 0.75$  (f–j) and various  $a$ -values. Simulations are done on a finite grid of various sizes, accompanied with either periodic boundary conditions (a–b, f–g) or Neumann boundary conditions (c–e, h–j) in the  $x$ -direction and the boundary conditions  $v_y(x, L_y) - \alpha v_x(x, L_y) = 0$  and  $v_y(x, 0) + \alpha u_x(x, 0) = 0$  in the  $y$ -direction to accommodate corner solutions, with  $\alpha = -1$  (a–d, f, h–i),  $\alpha = -0.5$  (g)  $\alpha = +1$  (e, j)

$a/m$  values, while vegetation gap patterns and front solutions can be found for larger values of  $a/m$ . For the largest  $a/m$  values, stripes and gaps no longer persist, and we find only front-type solutions that correspond to invading vegetation. Contrary to the typical pulse patterns constructed in similar dryland models [8, 148], the stripes and gaps found in (5.1.2) are not thin, but have sizable widths – aligning better with observations of real dryland ecosystems [42, 64, 136, 176].

Furthermore, we showed that all such solutions are 2D spectrally stable, using exponential dichotomies and Lin’s method, based on similar stability analysis of traveling pulse solutions to the FitzHugh–Nagumo equations in [22]. We note that, to our knowledge, there are currently no direct results which guarantee nonlinear stability based on spectral stability of traveling wave solutions to (5.1.2). Multidimensional nonlinear stability of traveling wave solutions in reaction-diffusion systems, however, has been studied previously [90]. By adding a small diffusion term, as in (5.6.1), we obtain a system which fits into the framework of planar interface propagation studied in [76, 77]. We expect our results still hold for (5.6.1) using a perturbation argument, provided  $D \ll \varepsilon \ll 1$ . Further, results relating spectral and nonlinear stability have been found to hold in mixed parabolic-hyperbolic equations such as (5.1.2) for perturbations in one spatial dimension [140], and we expect that similar results may hold in higher dimensions.

As far as we are aware, ours is the first construction of 2D linearly stable traveling stripes in a reaction-diffusion-advection model of vegetation pattern formation. Typically in this class of models, one finds that stripe solutions are stable in 1D, but destabilize for some range of (small) wavenumbers in 2D [54, 120, 148, 155]. We attribute this phenomenon to the stabilizing effect of the large advection term, as well

as the destabilizing effect of water diffusion. By ignoring the diffusion of water and allowing the advection to dominate, the lateral competition for water resources is diminished, and 2D stability can essentially be reduced to 1D stability. This is reflected in our stability analysis in which the critical part of the 2D spectrum is bounded to the left of the 1D spectrum: In order to compute the 2D spectrum, a Fourier decomposition in the transverse variable  $y$  results in a family of 1D eigenvalue problems parameterized by the transverse wavenumber  $\ell$ . These eigenvalue problems can then be solved using the methods of [22], and we find that eigenvalues occurring for  $\ell \neq 0$  can be bounded to the left of those occurring for  $\ell = 0$ , corresponding to the 1D spectrum. In fact we find that the correspondence is approximately  $\lambda \rightarrow \lambda - \ell^2$ .

An important question is how and why the addition of water diffusion and reduction in the magnitude of the advection term results in instabilities in the resulting patterns. This matches intuition, as water diffusion allows for lateral competition for water resources, which – if sufficiently large – could manifest in lateral instabilities. From the mathematical point of view, the onset of these instabilities is not well understood, though we note that one indeed finds lateral instabilities, both numerically and analytically, in similar models where both advection and diffusion are present [54, 120, 148, 155]. A natural direction for future research lies in understanding this transition, and in particular the precise relation between the water diffusion and advection which determines the boundary for stability. This is likely to be challenging, given that the singular geometries in the advection-dominant case (as in this paper) versus the diffusion-dominant case are wholly distinct. The traveling wave solutions constructed in this work are all based off of singular fast front-type jumps between one-dimensional slow manifolds, much like one finds in the classic FitzHugh–Nagumo equation. However, typically in the diffusion-dominant regime traveling stripe solutions are constructed as perturbations of fast homoclinic orbits which depart and return to the same two-dimensional slow manifold in a four-dimensional singularly perturbed traveling wave equation [56, 148]. Hence, even the existence of stripe solutions in an intermediate regime is far from clear, as one must understand how the transition between these two geometries occurs.

Also novel to our results are the implications for the appearance of curved solutions, even in the absence of terrain curvature. These arise as corner defect solutions [76, 77], which resemble two angled planar traveling wave solutions which meet along an interface. We find that the speed of the straight planar traveling wave predicts whether the associated corner solutions are oriented convex upslope or downslope. In particular, since all of the traveling stripe and gap solutions we constructed travel in the uphill direction, the corresponding curved stripes and gaps are oriented convex downslope. The planar front solutions, however, can be oriented either convex downslope or upslope depending on parameters. An interesting direction for future research lies in determining the effect of alternative topographies, in particular topographies which can be viewed as perturbations of constantly sloped terrain, which we expect can be studied using similar methods. A natural question is whether such topographies can destabilize stripe patterns or affect the curvature of these patterns. There are several numerical and observational results in this direction [64], but little is known analytically. A first analytical step towards this can be found in [7], in which the impact of non-trivial topographies on 1D stripe patterns is studied.

Finally, we remark on the implications of our results for Klausmeier’s original equation [95], which corresponds to infinite carrying capacity, or setting  $b = 0$  in (5.1.2). As discussed in section 5.2.1 (see Remark 5.2.12), the limit  $b \rightarrow 0$  is highly singular,

and our results no longer hold in this regime. Existence of traveling stripes in this case has been obtained in [23] using geometric singular perturbation theory and blow-up methods to account for passage near a nonhyperbolic slow manifold. Pulse solutions in that setting consist of portions of two slow manifolds, along with a single fast jump. Stability, however, is not known; this is due to the fact that several rescalings and coordinate transformations are required to recover a slow-fast structure in the corresponding traveling wave equation. The result is that the associated reduced eigenvalue problem across the fast jump can no longer be interpreted in terms of the simpler scalar problem for the corresponding front as in section 5.5.6, which precludes the application of Sturm-Liouville theory. However, we expect stability to continue to hold in this regime. In particular, the existence of a single fast jump should result in one matching condition, and hence a single critical eigenvalue  $\lambda = 0$  due to translation invariance. This intuition is supported by the fact that the second critical eigenvalue  $\tilde{\lambda}_c$  of Theorem 5.5.5 satisfies  $\tilde{\lambda}_c \rightarrow -\infty$ , when naively taking the limit  $b \rightarrow 0$  for fixed  $\varepsilon$ . Rigorous verification of the stability of traveling stripes in the Klausmeier equation is the subject of ongoing work.

## Acknowledgments

Robbin Bastiaansen was supported by the Mathematics of Planet Earth program of the Netherlands Organization of Scientific Research (NWO). Paul Carter gratefully acknowledges support through NSF grant DMS-1815315.

## Appendices

### 5.A Stability of steady states

To understand the stability of steady states, (5.1.4) and (5.1.5), against homogeneous perturbations, we linearize (5.1.2) around the steady states by setting  $(U, V)(x, t) = (U^*, V^*) + e^{\lambda t}(\bar{U}, \bar{V})$ , where  $(U^*, V^*)$  is the steady state solution. For the desert-state  $(U_0, V_0) = (a, 0)$  this gives the linearized system

$$\lambda \begin{pmatrix} \bar{U} \\ \bar{V} \end{pmatrix} = \begin{pmatrix} -1 & 0 \\ 0 & -m \end{pmatrix} \begin{pmatrix} \bar{U} \\ \bar{V} \end{pmatrix}.$$

Thus the corresponding eigenvalues are  $\lambda = -1 < 0$  and  $\lambda = -m < 0$ . Both eigenvalues are negative and thus the desert-state  $(U_0, V_0) = (a, 0)$  is stable against homogeneous perturbations for all parameter values.

Linearization around the other steady states  $(U_{1,2}, V_{1,2})$  yields the eigenvalue problem

$$\lambda \begin{pmatrix} \bar{U} \\ \bar{V} \end{pmatrix} = M \begin{pmatrix} \bar{U} \\ \bar{V} \end{pmatrix}; M := \begin{pmatrix} -1 - V_{1,2}^2 & -2U_{1,2}V_{1,2} \\ (1 - bV_{1,2})V_{1,2}^2 & -m + (2 - 3bV_{1,2})U_{1,2}V_{1,2} \end{pmatrix}. \quad (5.A.1)$$

The determinant of the matrix on the right-hand side can be computed as

$$\det M = \frac{-1 + 2bV_{1,2} + V_{1,2}^2}{1 - bV_{1,2}} m.$$

From this, it can be found that the determinant is negative when  $V_{1,2} < -b + \sqrt{1 + b^2}$  and positive when  $V_{1,2} > -b + \sqrt{1 + b^2}$ . Using (5.1.5), one can readily obtain that  $V_1 < -b + \sqrt{1 + b^2}$  and  $V_2 > -b + \sqrt{1 + b^2}$ . Hence the uniform steady state  $(U_1, V_1)$  necessarily has a positive eigenvalue and therefore this steady state is unstable. To determine the stability for  $(U_2, V_2)$  we need to determine the trace of the matrix  $M$ . Straightforward computation using the expressions (5.1.5) yields:

$$\text{Tr } M = -1 - V_2^2 + m \frac{1 - 2bV_{1,2}}{1 - bV_2},$$

which we note is always negative if  $V_2 > \frac{1}{2b}$ , corresponding to the condition  $\frac{a}{m} > 4b + \frac{1}{b}$ , and hence the state  $(U_2, V_2)$  is stable to homogeneous perturbations in this regime.

### 5.B Absence of point spectrum in $R_2(\delta, M)$

In this section, we complete the proof of Proposition 5.5.6, and show that the region  $R_2(\delta, M)$  contains no eigenvalues  $\tilde{\lambda}$  of (5.5.9).

*Proof of Proposition 5.5.6.* Following the argument outlined in section 5.5.6, we note that the translated derivative  $e^{\eta\xi}\phi'_j(\xi)$  is an exponentially localized solution to (5.5.56) at  $\tilde{\lambda} = 0$ , which admits no zeros. Therefore, by Sturm-Liouville theory [91, Theorem 2.3.3], (5.5.56) admits no bounded solutions for  $\tilde{\lambda} \in R_2(\delta, M)$ . Thus, for  $\tilde{\lambda} \in R_2(\delta, M)$  (5.5.56) admits an exponential dichotomy on  $\mathbb{R}$  with constants  $C, \mu > 0$  independent of  $\tilde{\lambda} \in R_2(\delta, M)$ . Exploiting the lower triangular structure of system (5.5.54)

the exponential dichotomy of (5.5.56) can be extended to the system (5.5.54) using variation of constants formulae. We denote the corresponding projections by  $Q_j^{\text{u},\text{s}}(\xi; \tilde{\lambda})$  for  $j = \dagger, \diamond$ .

We now consider the eigenvalue problem (5.5.9) as a perturbation of (5.5.13). By Theorem 5.5.1, we have that

$$\begin{aligned} |A_\eta(\xi; \tilde{\lambda}, \ell, \varepsilon) - A_{\dagger, \eta}(\xi; \tilde{\lambda})| &= \mathcal{O}(\varepsilon |\log \varepsilon|), & \xi \in [-L_\varepsilon, L_\varepsilon], \\ |A_\eta(Z_\varepsilon + \xi; \tilde{\lambda}, \ell, \varepsilon) - A_{\diamond, \eta}(\xi; \tilde{\lambda})| &= \mathcal{O}(\varepsilon |\log \varepsilon|), & \xi \in [-L_\varepsilon, \infty). \end{aligned} \quad (5.B.1)$$

Denote by  $P_{j, \pm}^{\text{u},\text{s}}(\tilde{\lambda})$  the spectral projection onto the (un)stable eigenspace of the asymptotic matrices  $A_{j, \eta}^{\pm\infty}(\tilde{\lambda}) = \lim_{\xi \rightarrow \pm\infty} A_{j, \eta}(\xi; \tilde{\lambda})$  of (5.5.13). We note that  $A_{j, \eta}(\xi; \tilde{\lambda})$  converges at an exponential rate to the asymptotic matrix  $A_{j, \eta}^{\pm\infty}(\tilde{\lambda})$  as  $\xi \rightarrow \infty$ . Hence, the projections  $Q_j^{\text{u},\text{s}}(\pm\xi, \tilde{\lambda})$  satisfy

$$\|Q_j^{\text{u},\text{s}}(\pm\xi, \tilde{\lambda}) - P_{j, \pm}^{\text{u},\text{s}}(\tilde{\lambda})\| \leq C e^{-\tilde{\mu}\xi}, \quad j = \dagger, \diamond, \quad (5.B.2)$$

for  $\xi \geq 0$  for some  $\tilde{\mu} > 0$  (see for instance [126, Lemma 3.4]). Using (5.B.1) and roughness [32, Theorem 2], we obtain exponential dichotomies for (5.5.9) on  $I_\dagger$  and  $I_\diamond$  with constants  $C, \frac{\mu}{2} > 0$  independent of  $\tilde{\lambda} \in R_2(\delta, M)$  and projections  $Q_j^{\text{u},\text{s}}(\xi; \tilde{\lambda}, \varepsilon)$ , which satisfy

$$\begin{aligned} \|Q_j^{\text{u},\text{s}}(\xi; \tilde{\lambda}, \varepsilon) - Q_\dagger^{\text{u},\text{s}}(\xi, \tilde{\lambda})\| &\leq C\varepsilon |\log \varepsilon|, \\ \|Q_j^{\text{u},\text{s}}(Z_\varepsilon + \xi; \tilde{\lambda}, \varepsilon) - Q_\diamond^{\text{u},\text{s}}(\xi, \tilde{\lambda})\| &\leq C\varepsilon |\log \varepsilon|, \end{aligned} \quad (5.B.3)$$

for  $|\xi| \leq L_\varepsilon$ .

By Proposition 5.5.2 system (5.5.9) admits exponential dichotomies on the intervals  $I_\ell = (-\infty, L_\varepsilon]$  and  $I_r = [L_\varepsilon, Z_{a, \varepsilon} - L_\varepsilon]$  with projections  $Q_{r, \ell}^{\text{u},\text{s}}(\xi; \tilde{\lambda}, \varepsilon)$ , which satisfy

$$\begin{aligned} \left\| [Q_\ell^{\text{s}} - \mathcal{P}](-L_\varepsilon; \tilde{\lambda}, \varepsilon) \right\| &\leq C\varepsilon |\log \varepsilon|, \\ \left\| [Q_r^{\text{s}} - \mathcal{P}](L_\varepsilon; \tilde{\lambda}, \varepsilon) \right\| &\leq C\varepsilon |\log \varepsilon|, \\ \left\| [Q_r^{\text{s}} - \mathcal{P}](Z_{a, \varepsilon} - L_\varepsilon; \tilde{\lambda}, \varepsilon) \right\| &\leq C\varepsilon |\log \varepsilon|, \end{aligned} \quad (5.B.4)$$

where  $\mathcal{P}(\xi; \tilde{\lambda}, \varepsilon)$  denotes the spectral projection onto the stable eigenspace of the matrix  $A_\eta(\xi; \tilde{\lambda}, \ell, \varepsilon)$ .

We now compare the exponential dichotomies for (5.5.9) constructed on each of the intervals  $I_\ell, I_\dagger, I_r, I_\diamond$  at the endpoints of the intervals. Recall that  $A_{j, \eta}(\xi; \tilde{\lambda})$  converges at an exponential rate to the asymptotic matrix  $A_{j, \eta}^{\pm\infty}(\tilde{\lambda})$  as  $\xi \rightarrow \pm\infty$  for  $j = \dagger, \diamond$ . Recalling (5.B.1), we have that

$$|A_\eta(\pm L_\varepsilon; \tilde{\lambda}, \ell, \varepsilon) - A_{\dagger, \eta}^{\pm\infty}(\tilde{\lambda})|, |A_\eta(Z_\varepsilon - L_\varepsilon; \tilde{\lambda}, \ell, \varepsilon) - A_{\diamond, \eta}^{\infty}(\tilde{\lambda})| \leq C\varepsilon |\log \varepsilon|.$$

By continuity the same bound holds for the spectral projections associated with these matrices. Combining this with (5.B.2)–(5.B.4) we obtain

$$\begin{aligned} \left\| [Q_\ell^{\text{u},\text{s}} - Q_\dagger^{\text{u},\text{s}}](-L_\varepsilon; \tilde{\lambda}, \varepsilon) \right\| &\leq C\varepsilon |\log \varepsilon|, \\ \left\| [Q_r^{\text{u},\text{s}} - Q_\dagger^{\text{u},\text{s}}](L_\varepsilon; \tilde{\lambda}, \varepsilon) \right\| &\leq C\varepsilon |\log \varepsilon|, \\ \left\| [Q_r^{\text{u},\text{s}} - Q_\diamond^{\text{u},\text{s}}](Z_\varepsilon - L_\varepsilon; \tilde{\lambda}, \varepsilon) \right\| &\leq C\varepsilon |\log \varepsilon|. \end{aligned} \quad (5.B.5)$$

Let  $\psi(\xi)$  be an exponentially localized solution to (5.5.9) at some  $\tilde{\lambda} \in R_2(\delta, M)$ . This implies  $\mathcal{Q}_\ell^s(-L_\varepsilon; \tilde{\lambda}, \varepsilon)\psi(-L_\varepsilon) = 0$ . By for instance [83, Lemma 6.10] or [22, Lemma 6.19], we have that

$$|\mathcal{Q}_r^s(L_\varepsilon; \tilde{\lambda}, \varepsilon)\psi(L_\varepsilon)| \leq C\varepsilon|\log \varepsilon| |\mathcal{Q}_r^u(L_\varepsilon; \tilde{\lambda}, \varepsilon)\psi(L_\varepsilon)|, \quad (5.B.6)$$

using (5.B.5). Again using [22, Lemma 6.19] and (5.B.5) to obtain a similar inequality at the endpoint  $Z_{a,\varepsilon} - L_\varepsilon$ , we obtain

$$\begin{aligned} & |\mathcal{Q}_\diamond^s(Z_\varepsilon - L_\varepsilon; \tilde{\lambda}, \varepsilon)\psi(Z_{a,\varepsilon} - L_\varepsilon)| \\ & \leq C\varepsilon|\log \varepsilon| |\mathcal{Q}_\diamond^u(Z_\varepsilon - L_\varepsilon; \tilde{\lambda}, \varepsilon)\psi(Z_\varepsilon - L_\varepsilon)| \\ & = 0, \end{aligned}$$

since we assumed  $\psi(\xi)$  is exponentially localized. Hence, any exponentially localized solution  $\psi(\xi)$  to (5.5.9) is the trivial solution.  $\square$

## Bibliography

- [1] J. Alexander, R. Gardner, and C. Jones. A topological invariant arising in the stability analysis of travelling waves. *Journal für die reine und angewandte Mathematik*, 410(167-212):143, 1990.
- [2] D. Archer, A. Winguth, D. Lea, and N. Mahowald. What caused the glacial/interglacial atmospheric pCO<sub>2</sub> cycles? *Reviews of Geophysics*, 38(2):159–189, 2000.
- [3] D. Avitabile, V. F. Brenã, and M. J. Ward. Spot dynamics in a reaction-diffusion model of plant root hair initiation. *SIAM Journal on Applied Mathematics*, 78(1):291–319, 2018.
- [4] N. Barbier, P. Couteron, J. Lejoly, V. Deblauwe, and O. Lejeune. Self-organized vegetation patterning as a fingerprint of climate and human impact on semi-arid ecosystems. *Journal of Ecology*, 94(3):537–547, 2006.
- [5] N. Barbier, P. Couteron, O. Planchon, and A. Diouf. Multiscale comparison of spatial patterns using two-dimensional cross-spectral analysis: application to a semi-arid (gapped) landscape. *Landscape ecology*, 25(6):889–902, 2010.
- [6] R. Bastiaansen, P. Carter, and A. Doelman. Stable planar vegetation stripe patterns on sloped terrain in dryland ecosystems. *to appear in Nonlinearity*, 2019.
- [7] R. Bastiaansen, M. Chirilus-Bruckner, and A. Doelman. Pulse solutions for an extended Klausmeier model with spatially varying coefficients. *submitted*, 2018.
- [8] R. Bastiaansen and A. Doelman. The dynamics of disappearing pulses in a singularly perturbed reaction-diffusion system with parameters that vary in time and space. *Physica D: Nonlinear Phenomena*, 388:45–72, 2019.
- [9] R. Bastiaansen, O. Jaïbi, V. Debaluwe, M. Eppinga, K. Siteur, E. Siero, S. Mermozh, A. Bouvet, A. Doelman, and M. Rietkerk. Multistability of model and real dryland ecosystems through spatial self-organization. *Proceedings of the National Academy of Sciences*, 115(44):11256–11261, 2018.
- [10] M. Beck, C. K. R. T. Jones, D. Schaeffer, and M. Wechselberger. Electrical waves in a one-dimensional model of cardiac tissue. *SIAM Journal on Applied Dynamical Systems*, 7(4):1558–1581, 2008.
- [11] G. Bel, A. Hagberg, and E. Meron. Gradual regime shifts in spatially extended ecosystems. *Theoretical Ecology*, 5(4):591–604, 2012.
- [12] T. Bellsky, A. Doelman, T. J. Kaper, and K. Promislow. Adiabatic stability under semi-strong interactions: the weakly damped regime. *Indiana University Mathematics Journal*, 62(2):1809–1859, 2013.



- 
- [13] H. Berestycki, J. Wei, and M. Winter. Existence of symmetric and asymmetric spikes for a crime hotspot model. *SIAM Journal on Mathematical Analysis*, 46(1):691–719, 2014.
- [14] A. Bouvet, S. Mermoz, T. L. Toan, L. Villard, R. Mathieu, L. Naidoo, and G. P. Asner. An above-ground biomass map of African savannahs and woodlands at 25 m resolution derived from ALOS PALSAR. *Remote Sensing of Environment*, 206:156 – 173, 2018.
- [15] V. Brenã Medina, A. R. Champneys, C. Grierson, and M. J. Ward. Mathematical modeling of plant root hair initiation: dynamics of localized patches. *SIAM Journal on Applied Dynamical Systems*, 13(1):210–248, 2014.
- [16] V. F. Brenã Medina, D. Avitabile, A. R. Champneys, and M. J. Ward. Stripe to spot transition in a plant root hair initiation model. *SIAM Journal on Applied Mathematics*, 75(3):1090–1119, 2015.
- [17] J. Bruniquel and A. Lopes. Multi-variate optimal speckle reduction in SAR imagery. *International journal of remote sensing*, 18(3):603–627, 1997.
- [18] S. L. Brusatte, R. J. Butler, P. M. Barrett, M. T. Carrano, D. C. Evans, G. T. Lloyd, P. D. Mannion, M. A. Norell, D. J. Peppe, P. Upchurch, and T. E. Williamson. The extinction of the dinosaurs. *Biological Reviews*, 90(2):628–642.
- [19] F. Busse. Non-linear properties of thermal convection. *Reports on Progress in Physics*, 41(12):1929, 1978.
- [20] R. Canfield. Reproduction and life span of some perennial grasses of southern Arizona. *Rangeland Ecology & Management/Journal of Range Management Archives*, 10(5):199–203, 1957.
- [21] G. Carpenter. A geometric approach to singular perturbation problems with applications to nerve impulse equations. *Journal on Differential Equations*, 23(3):335–367, 1977.
- [22] P. Carter, B. de Rijk, and B. Sandstede. Stability of traveling pulses with oscillatory tails in the FitzHugh–Nagumo system. *Journal of Nonlinear Science*, 26(5):1369–1444, 2016.
- [23] P. Carter and A. Doelman. Traveling stripes in the klausmeier model of vegetation pattern formation. *SIAM Journal on Applied Mathematics*, 78(6):3213–3237, 2018.
- [24] P. Carter and A. Doelman. In preparation.
- [25] P. Carter and B. Sandstede. Fast pulses with oscillatory tails in the FitzHugh–Nagumo system. *SIAM Journal on Mathematical Analysis*, 47(5):3393–3441, 2015.
- [26] P. Carter and B. Sandstede. Unpeeling a homoclinic banana in the FitzHugh–Nagumo system. *SIAM Journal on Applied Dynamical Systems*, 17(1):236–349, 2018.
- [27] A. Champneys, V. Kirk, E. Knobloch, B. Oldeman, and J. Sneyd. When Shil’nikov meets Hopf in excitable systems. *SIAM Journal on Applied Dynamical Systems*, 6(4):663–693, 2007.
- [28] W. Chen and M. J. Ward. Oscillatory instabilities and dynamics of multi-spike patterns for the one-dimensional Gray-Scott model. *European Journal of Applied Mathematics*, 20(02):187–214, 2009.
- [29] W. Chen and M. J. Ward. The stability and dynamics of localized spot patterns in the two-dimensional Gray-Scott model. *SIAM Journal on Applied Dynamical Systems*, 10(2):582–666, 2011.

- [30] Y. Chen, T. Kolokolnikov, J. Tzou, and C. Gai. Patterned vegetation, tipping points, and the rate of climate change. *European Journal of Applied Mathematics*, 26(6):945–958, 2015.
- [31] W. Coppel. *Dichotomies in Stability Theory*, volume 629 of *Lecture Notes in Mathematics*. Springer-Verlag, Berlin-New York, 1978.
- [32] W. A. Coppel. Dichotomies and reducibility. *Journal of Differential Equations*, 3:500–521, 1967.
- [33] P. Couteron. Using spectral analysis to confront distributions of individual species with an overall periodic pattern in semi-arid vegetation. *Plant Ecology*, 156(2):229–243, 2001.
- [34] P. Couteron and O. Lejeune. Periodic spotted patterns in semi-arid vegetation explained by a propagation-inhibition model. *Journal of Ecology*, 89(4):616–628, 2001.
- [35] M. C. Cross and P. C. Hohenberg. Pattern formation outside of equilibrium. *Reviews of modern physics*, 65(3):851, 1993.
- [36] A. S. Dagbovie and J. A. Sherratt. Pattern selection and hysteresis in the Rietkerk model for banded vegetation in semi-arid environments. *Journal of The Royal Society Interface*, 11(99):20140465, 2014.
- [37] M. Davis, S. Faurby, and J. C. Svenning. Mammal diversity will take millions of years to recover from the current biodiversity crisis. *Proceedings of the National Academy of Sciences*, 2018.
- [38] B. de Rijk. Spectra and stability of spatially periodic pulse patterns II: the critical spectral curve. *SIAM Journal on Mathematical Analysis*, 50(2):1958–2019, 2018.
- [39] B. de Rijk, A. Doelman, and J. D. Rademacher. Spectra and stability of spatially periodic pulse patterns: Evans function factorization via Riccati transformation. *SIAM Journal on Mathematical Analysis*, 48(1):61–121, 2016.
- [40] V. Deblauwe, N. Barbier, P. Couteron, O. Lejeune, and J. Bogaert. The global biogeography of semi-arid periodic vegetation patterns. *Global Ecology and Biogeography*, 17(6):715–723, 2008.
- [41] V. Deblauwe, P. Couteron, J. Bogaert, and N. Barbier. Determinants and dynamics of banded vegetation pattern migration in arid climates. *Ecological Monographs*, 82(1):3–21, 2012.
- [42] V. Deblauwe, P. Couteron, O. Lejeune, J. Bogaert, and N. Barbier. Environmental modulation of self-organized periodic vegetation patterns in Sudan. *Ecography*, 34(6):990–1001, 2011.
- [43] V. Deblauwe, V. Droissart, R. Bose, B. Sonké, A. Blach-Overgaard, J. C. Svenning, J. J. Wieringa, B. R. Ramesh, T. Stévant, and T. L. P. Couvreur. Remotely sensed temperature and precipitation data improve species distribution modelling in the tropics. *Global Ecology and Biogeography*, 25(4):443–454, 2016.
- [44] V. Deblauwe, P. Kennel, and P. Couteron. Testing pairwise association between spatially autocorrelated variables: a new approach using surrogate lattice data. *PLOS ONE*, 7(11):e48766, 2012.
- [45] A. Doelman, W. Eckhaus, and T. J. Kaper. Slowly modulated two-pulse solutions in the Gray-Scott model I: asymptotic construction and stability. *SIAM Journal on Applied Mathematics*, 61(3):1080–1102, 2000.

- 
- [46] A. Doelman, W. Eckhaus, and T. J. Kaper. slowly modulated two-pulse solutions in the Gray-Scott model II: geometric theory, bifurcations, and splitting dynamics. *SIAM Journal on Applied Mathematics*, 61(6):2036–2062, 2001.
- [47] A. Doelman, R. A. Gardner, and T. J. Kaper. Stability analysis of singular patterns in the 1D Gray-Scott model: a matched asymptotics approach. *Physica D: Nonlinear Phenomena*, 122(1):1–36, 1998.
- [48] A. Doelman, R. A. Gardner, and T. J. Kaper. Large stable pulse solutions in reaction-diffusion equations. *Indiana University Mathematics Journal*, 50(1):443–507, 2001.
- [49] A. Doelman and T. J. Kaper. Semi-strong pulse interactions in a class of coupled reaction-diffusion equations. *SIAM Journal on Applied Dynamical Systems*, 2(1):53–96, 2003.
- [50] A. Doelman, T. J. Kaper, and K. Promislow. Nonlinear asymptotic stability of the semistrong pulse dynamics in a regularized Gierer–Meinhardt model. *SIAM Journal on Mathematical Analysis*, 38(6):1760–1787, 2007.
- [51] A. Doelman, T. J. Kaper, and P. A. Zegeling. Pattern formation in the one-dimensional Gray-Scott model. *Nonlinearity*, 10(2):523, 1997.
- [52] A. Doelman, J. Rademacher, B. de Rijk, and F. Veerman. Destabilization mechanisms of periodic pulse patterns near a homoclinic limit. *SIAM Journal on Applied Dynamical Systems*, 17(2):1833–1890, 2018.
- [53] A. Doelman, J. D. M. Rademacher, and S. van der Stelt. Hopf dances near the tips of Busse balloons. *Discrete and Continuous Dynamical Systems-Series S*, 5(1):61–92, 2012.
- [54] A. Doelman and H. van der Ploeg. Homoclinic stripe patterns. *SIAM Journal on Applied Dynamical Systems*, 1(1):65–104, 2002.
- [55] A. Doelman, P. van Heijster, and F. Xie. A geometric approach to stationary defect solutions in one space dimension. *SIAM Journal on Applied Dynamical Systems*, 15(2):655–712, 2016.
- [56] A. Doelman and F. Veerman. An explicit theory for pulses in two component, singularly perturbed, reaction–diffusion equations. *Journal of Dynamics and Differential Equations*, 27(3-4):555–595, 2015.
- [57] D. L. Dunkerley. Vegetation mosaics of arid Western New South Wales, Australia: considerations of their origin and persistence. In *Patterns of Land Degradation in Drylands*, pages 315–345. Springer, 2014.
- [58] J. Eddy, G. Humphreys, D. Hart, P. Mitchell, and P. Fanning. Vegetation arcs and litter dams: similarities and differences. *CATENA*, 37(1-2):57 – 73, 1999.
- [59] M. B. Eppinga, P. C. de Ruiter, M. J. Wassen, and M. Rietkerk. Nutrients and hydrology indicate the driving mechanisms of peatland surface patterning. *The American Naturalist*, 173(6):803–818, 2009. PMID: 19371168.
- [60] E. G. Eszter. *An Evans function analysis of the stability of periodic travelling wave solutions of the FitzHugh-Nagumo system*. PhD thesis, University of Massachusetts, 1999.
- [61] D. E. Fastovsky. The extinction of the dinosaurs in North America. *GSA Today*, 15(3):4–10, 2005.

- [62] N. Fenichel. Geometric singular perturbation theory for ordinary differential equations. *Journal of differential equations*, 31(1):53–98, 1979.
- [63] C. Funk, P. Peterson, M. Landsfeld, D. Pedreros, J. Verdin, S. Shukla, G. Husak, J. Rowland, L. Harrison, A. Hoell, and J. Michaelsen. The climate hazards infrared precipitation with stations—a new environmental record for monitoring extremes. *Scientific data*, 2:150066, 2015.
- [64] P. Gandhi, L. Werner, S. Iams, K. Gowda, and M. Silber. A topographic mechanism for arcing of dryland vegetation bands. *Journal of The Royal Society Interface*, 15(147), 2018.
- [65] R. Gardner and C. K. Jones. Stability of travelling wave solutions of diffusive predator-prey systems. *Transactions of the American Mathematical Society*, 327(2):465–524, 1991.
- [66] S. Gerschgorin. Über die Abgrenzung der Eigenwerte einer Matrix. *Bulletin de l'Académie des Sciences de l'URSS. Classe des sciences mathématiques et na*, pages 749–754, 1931.
- [67] E. Gilad, J. von Hardenberg, A. Provenzale, M. Shachak, and E. Meron. Ecosystem engineers: from pattern formation to habitat creation. *Physical Review Letters*, 93(9):098105, 2004.
- [68] K. Gowda, S. Iams, and M. Silber. Signatures of human impact on self-organized vegetation in the Horn of Africa. *Scientific Reports*, 8(1):3622, 2018.
- [69] K. Gowda, H. Riecke, and M. Silber. Transitions between patterned states in vegetation models for semiarid ecosystems. *Physical Review E*, 89(2):022701, 2014.
- [70] V. Grimm and S. F. Railsback. Pattern-oriented modelling: a ‘multi-scope’ for predictive systems ecology. *Philosophical Transactions of the Royal Society B*, 367(1586):298–310, 2012.
- [71] V. Grimm, E. Revilla, U. Berger, F. Jeltsch, W. M. Mooij, S. F. Railsback, H.-H. Thulke, J. Weiner, T. Wiegand, and D. L. DeAngelis. Pattern-oriented modeling of agent-based complex systems: lessons from ecology. *Science*, 310(5750):987–991, 2005.
- [72] J. Grodecki and G. Dial. Block adjustment of high-resolution satellite images described by rational polynomials. *Photogrammetric Engineering & Remote Sensing*, 69(1):59–68, 2003.
- [73] J. Guckenheimer and C. Kuehn. Homoclinic orbits of the FitzHugh–Nagumo equation: bifurcations in the full system. *SIAM Journal on Applied Dynamical Systems*, 9(1):138–153, 2010.
- [74] J. Hansen, R. Ruedy, J. Glascoe, and M. Sato. Giss analysis of surface temperature change. *Journal of Geophysical Research: Atmospheres*, 104(D24):30997–31022, 1999.
- [75] J. Hansen, R. Ruedy, M. Sato, and K. Lo. Global surface temperature change. *Reviews of Geophysics*, 48(4), 2010.
- [76] M. Haragus and A. Scheel. Almost planar waves in anisotropic media. *Communications in Partial Differential Equations*, 31(5):791–815, 2006.
- [77] M. Haragus and A. Scheel. Corner defects in almost planar interface propagation. *Annales de l'Institut Henri Poincaré (C) Non Linear Analysis*, 23(3):283–329, 2006.

- [78] A. Hastings and D. B. Wysham. Regime shifts in ecological systems can occur with no warning. *Ecology Letters*, 13:464–472, 2010.
- [79] S. P. Hastings. On the existence of homoclinic and periodic orbits for the FitzHugh–Nagumo equations. *Quarterly Journal of Mathematics*, 27(1):123–134, 1976.
- [80] G. Hek. Geometric singular perturbation theory in biological practice. *Journal of mathematical biology*, 60(3):347–386, 2010.
- [81] C. F. Hemming. Vegetation arcs in Somaliland. *Journal of Ecology*, 53(1):57–67, 1965.
- [82] C. S. Holling. Resilience and stability of ecological systems. *Annual review of ecology and systematics*, 4(1):1–23, 1973.
- [83] M. Holzer, A. Doelman, and T. J. Kaper. Existence and stability of traveling pulses in a reaction–diffusion–mechanics system. *Journal of Nonlinear Science*, 23(1):129–177, 2013.
- [84] H. Hupkes and B. Sandstede. Stability of pulse solutions for the discrete FitzHugh–Nagumo system. *Transactions of the American Mathematical Society*, 365(1):251–301, 2013.
- [85] D. Iron and M. J. Ward. The dynamics of multispikes solutions to the one-dimensional Gierer–Meinhardt model. *SIAM Journal on Applied Mathematics*, 62(6):1924–1951, 2002.
- [86] C. K. Jones. Geometric singular perturbation theory. In *Dynamical systems*, pages 44–118. Springer, 1995.
- [87] C. K. R. T. Jones, T. J. Kaper, and N. Kopell. Tracking invariant manifolds up to exponentially small errors. *SIAM Journal on Mathematical Analysis*, 27(2):558–577, 1996.
- [88] F. Joos and R. Spahni. Rates of change in natural and anthropogenic radiative forcing over the past 20,000 years. *Proceedings of the National Academy of Sciences*, 105(5):1425–1430, 2008.
- [89] T. J. Kaper. Systems theory for singular perturbation problems. *Analyzing multiscale phenomena using singular perturbation methods: American Mathematical Society short course, January 5–6, 1998, Baltimore, Maryland*, 56(56):85, 1999.
- [90] T. Kapitula. Multidimensional stability of planar travelling waves. *Transactions of the American Mathematical Society*, 349(1):257–269, 1997.
- [91] T. Kapitula and K. Promislow. *Spectral and dynamical stability of nonlinear waves*, volume 185 of *Applied Mathematical Sciences*. Springer, New York, 2013.
- [92] J. O. Kaplan, K. M. Krumhardt, E. C. Ellis, W. F. Ruddiman, C. Lemmen, and K. K. Goldewijk. Holocene carbon emissions as a result of anthropogenic land cover change. *The Holocene*, 21(5):775–791, 2011.
- [93] S. Kéfi, M. Rietkerk, C. L. Alados, Y. Pueyo, V. P. Papanastasis, A. ElAich, and P. C. de Ruiter. Spatial vegetation patterns and imminent desertification in mediterranean arid ecosystems. *Nature*, 449(7159):213, 2007.
- [94] T. H. Keitt. Spectral representation of neutral landscapes. *Landscape Ecology*, 15(5):479–494, 2000.
- [95] C. A. Klausmeier. Regular and irregular patterns in semiarid vegetation. *Science*, 284(5421):1826–1828, 1999.

- [96] K. Klein Goldewijk, A. Beusen, G. van Drecht, and M. de Vos. The HYDE 3.1 spatially explicit database of human-induced global land-use change over the past 12,000 years. *Global Ecology and Biogeography*, 20(1):73–86, 2011.
- [97] J. N. Klironomos, M. F. Allen, M. C. Rillig, J. Piotrowski, S. Makvandi-Nejad, B. E. Wolfe, and J. R. Powell. Abrupt rise in atmospheric CO<sub>2</sub> overestimates community response in a model plant–soil system. *Nature*, 433(7026):621, 2005.
- [98] A. Koch and H. Meinhardt. Biological pattern formation: from basic mechanisms to complex structures. *Reviews of modern physics*, 66(4):1481, 1994.
- [99] T. Kolokolnikov, M. J. Ward, and J. Wei. The existence and stability of spike equilibria in the one-dimensional Gray–Scott model on a finite domain. *Applied Mathematics Letters*, 18(8):951 – 956, 2005.
- [100] T. Kolokolnikov, M. J. Ward, and J. Wei. The existence and stability of spike equilibria in the one-dimensional Gray–Scott model: the low feed-rate regime. *Studies in Applied Mathematics*, 115(1):21–71, 2005.
- [101] T. Kolokolnikov, M. J. Ward, and J. Wei. The existence and stability of spike equilibria in the one-dimensional Gray–Scott model: the pulse-splitting regime. *Physica D: Nonlinear Phenomena*, 202(3–4):258 – 293, 2005.
- [102] T. Kolokolnikov, M. J. Ward, and J. Wei. Pulse-splitting for some reaction-diffusion systems in one-space dimension. *Studies in Applied Mathematics*, 114(2):115–165, 2005.
- [103] T. Kolokolnikov, M. J. Ward, and J. Wei. Slow translational instabilities of spike patterns in the one-dimensional Gray–Scott model. *Interfaces and Free Boundaries*, 8(2):185–222, 2006.
- [104] M. Krupa and P. Szmolyan. Extending geometric singular perturbation theory to nonhyperbolic points—fold and canard points in two dimensions. *SIAM Journal on Mathematical Analysis*, 33(2):286–314, 2001.
- [105] C. Kuehn. *Multiple time scale dynamics*, volume 191 of *Applied Mathematical Sciences*. Springer, Cham, 2015.
- [106] L. Larsen, C. Thomas, M. Eppinga, and T. Coulthard. Exploratory modeling: extracting causality from complexity. *Eos, Transactions American Geophysical Union*, 95(32):285–286, 2014.
- [107] L. G. Larsen, M. B. Eppinga, P. Passalacqua, W. M. Getz, K. A. Rose, and M. Liang. Appropriate complexity landscape modeling. *Earth-science reviews*, 160:111–130, 2016.
- [108] W. K. Lauenroth and P. B. Adler. Demography of perennial grassland plants: survival, life expectancy and life span. *Journal of Ecology*, 96(5):1023–1032, 2008.
- [109] K. J. Lee, W. McCormick, Q. Ouyang, and H. L. Swinney. Pattern formation by interacting chemical fronts. *Science*, 261(5118):192–194, 1993.
- [110] S. A. Levin. The problem of pattern and scale in ecology: the Robert H. MacArthur award lecture. *Ecology*, 73(6):1943–1967, 1992.
- [111] W. A. Macfadyen. Soil and vegetation in British Somaliland. *Nature*, 165:121, 1950.
- [112] W. A. Macfadyen. Vegetation patterns in the semi-desert plains of British Somaliland. *The Geographical Journal*, 116(4/6):199–211, 1950.
- [113] P. K. Maini. Applications of mathematical modelling to biological pattern formation. In *Coherent structures in complex systems*, pages 205–217. Springer, 2001.

- [114] R. M. May. Thresholds and breakpoints in ecosystems with a multiplicity of stable states. *Nature*, 269(5628):471–477, 1977.
- [115] H. Meinhardt. Models of biological pattern formation: from elementary steps to the organization of embryonic axes. *Current topics in developmental biology*, 81:1–63, 2008.
- [116] S. Mermoz, T. Le Toan, L. Villard, M. Réjou-Méchain, and J. Seifert-Granzin. Biomass assessment in the Cameroon savanna using ALOS PALSAR data. *Remote sensing of environment*, 155:109–119, 2014.
- [117] E. Meron. *Nonlinear Physics of Ecosystems*. CRC Press, 2015.
- [118] Millennium Ecosystem Assessment. *Ecosystems and human well-being: a framework for assessment*. Island Press, Washington, DC, USA, 2003.
- [119] C. Montana, J. Lopez-Portillo, and A. Mauchamp. The response of two woody species to the conditions created by a shifting ecotone in an arid ecosystem. *The Journal of Ecology*, pages 789–798, 1990.
- [120] I. Moyles, W. Tse, and M. Ward. Explicitly solvable nonlocal eigenvalue problems and the stability of localized stripes in reaction-diffusion systems. *Studies in Applied Mathematics*, 136(1):89–136, 2016.
- [121] W.-M. Ni. Diffusion, cross-diffusion, and their spike-layer steady states. *Notices of the AMS*, 45(1):9–18, 1998.
- [122] Y. Nishiura, Y. Oyama, K. I. Ueda, et al. Dynamics of traveling pulses in heterogeneous media of jump type. *Hokkaido mathematical journal*, 36(1):207–242, 2007.
- [123] Y. Nishiura, T. Teramoto, X. Yuan, and K. I. Ueda. Dynamics of traveling pulses in heterogeneous media. *Chaos: An interdisciplinary journal of nonlinear science*, 17(3):037104, 2007.
- [124] I. Noy-Meir. Stability of grazing systems: an application of predator-prey graphs. *The Journal of Ecology*, pages 459–481, 1975.
- [125] N. Otsu. A threshold selection method from gray-level histograms. *IEEE transactions on systems, man, and cybernetics*, 9(1):62–66, 1979.
- [126] K. J. Palmer. Exponential dichotomies and transversal homoclinic points. *Journal of Differential Equations*, 55(2):225–256, 1984.
- [127] J. E. Pearson. Complex patterns in a simple system. *Science*, 261(5118):189–192, 1993.
- [128] G. G. Penny, K. E. Daniels, and S. E. Thompson. Local properties of patterned vegetation: quantifying endogenous and exogenous effects. *Philosophical Transactions of the Royal Society A*, 371(2004):20120359, 2013.
- [129] I. Prigogine and G. Nicolis. *Self-organization in non-equilibrium systems: from dissipative structures to order through fluctuations*. New York: Wiley, 1977.
- [130] K. Promislow. A renormalization method for modulational stability of quasi-steady patterns in dispersive systems. *SIAM Journal on Mathematical Analysis*, 33(6):1455–1482, 2002.
- [131] B. Purinton and B. Bookhagen. Validation of digital elevation models (DEMs) and comparison of geomorphic metrics on the southern Central Andean Plateau. *Earth Surface Dynamics*, 5(2):211, 2017.

- [132] J. D. Rademacher. First and second order semistrong interaction in reaction-diffusion systems. *SIAM Journal on Applied Dynamical Systems*, 12(1):175–203, 2013.
- [133] J. D. Rademacher, B. Sandstede, and A. Scheel. Computing absolute and essential spectra using continuation. *Physica D: Nonlinear Phenomena*, 229(2):166–183, 2007.
- [134] J. D. Rademacher and A. Scheel. Instabilities of wave trains and Turing patterns in large domains. *International Journal of Bifurcation and Chaos*, 17(08):2679–2691, 2007.
- [135] E. Renshaw and E. Ford. The description of spatial pattern using two-dimensional spectral analysis. *Vegetatio*, 56(2):75–85, 1984.
- [136] M. Rietkerk, M. C. Boerlijst, F. van Langevelde, R. HilleRisLambers, J. van de Koppel, L. Kumar, H. H. T. Prins, and A. M. de Roos. Self-organization of vegetation in arid ecosystems. *The American Naturalist*, 160(4):524–530, 2002.
- [137] M. Rietkerk, S. C. Dekker, P. C. de Ruiter, and J. van de Koppel. Self-organized patchiness and catastrophic shifts in ecosystems. *Science*, 305(5692):1926–1929, 2004.
- [138] M. Rietkerk and J. van de Koppel. Regular pattern formation in real ecosystems. *Trends in ecology & evolution*, 23(3):169–175, 2008.
- [139] M. Rietkerk, F. van den Bosch, and J. van de Koppel. Site-specific properties and irreversible vegetation changes in semi-arid grazing systems. *Oikos*, pages 241–252, 1997.
- [140] J. Rottmann-Matthes. Stability of parabolic-hyperbolic traveling waves. *Dynamics of Partial Differential Equations*, 9(1):29–62, 2012.
- [141] V. Rottschäfer, J. Tzou, and M. Ward. Transition to blow-up in a reaction–diffusion model with localized spike solutions. *European Journal of Applied Mathematics*, 28(6):1015–1055, 2017.
- [142] B. Sandstede. Stability of travelling waves. *Handbook of dynamical systems*, 2:983–1055, 2002.
- [143] S. Schechter. Exchange lemmas. II. General exchange lemma. *Journal Differential Equations*, 245(2):411–441, 2008.
- [144] M. Scheffer, J. Bascompte, W. A. Brock, V. Brovkin, S. R. Carpenter, V. Dakos, H. Held, E. H. van Nes, M. Rietkerk, and G. Sugihara. Early-warning signals for critical transitions. *Nature*, 461(7260):53, 2009.
- [145] M. Scheffer, S. Carpenter, J. A. Foley, C. Folke, and B. Walker. Catastrophic shifts in ecosystems. *Nature*, 413(6856):591, 2001.
- [146] M. Scheffer, E. van Nes, M. Holmgren, and T. Hughes. Pulse driven loss of top-down control: The critical-rate hypothesis. *Ecosystems*, 11(2):226–237, 2008.
- [147] J. Schmidt, I. S. Evans, and J. Brinkmann. Comparison of polynomial models for land surface curvature calculation. *International Journal of Geographical Information Science*, 17(8):797–814, 2003.
- [148] L. Sewalt and A. Doelman. Spatially periodic multipulse patterns in a generalized Klausmeier–Gray–Scott model. *SIAM Journal on Applied Dynamical Systems*, 16(2):1113–1163, 2017.
- [149] J. A. Sherratt. Pattern solutions of the Klausmeier model for banded vegetation in semi-arid environments II: patterns with the largest possible propagation speeds. *Proceedings of the Royal Society A*, 467:3272–3294, 2011.



- 
- [150] J. A. Sherratt. History-dependent patterns of whole ecosystems. *Ecological Complexity*, 14:8–20, 2013.
- [151] J. A. Sherratt. Pattern solutions of the Klausmeier model for banded vegetation in semiarid environments IV: slowly moving patterns and their stability. *SIAM Journal on Applied Mathematics*, 73(1):330–350, 2013.
- [152] J. A. Sherratt. Pattern solutions of the Klausmeier model for banded vegetation in semiarid environments V: the transition from patterns to desert. *SIAM Journal on Applied Mathematics*, 73(4):1347–1367, 2013.
- [153] J. A. Sherratt. Using wavelength and slope to infer the historical origin of semiarid vegetation bands. *Proceedings of the National Academy of Sciences*, 112(14):4202–4207, 2015.
- [154] J. A. Sherratt and G. J. Lord. Nonlinear dynamics and pattern bifurcations in a model for vegetation stripes in semi-arid environments. *Theoretical population biology*, 71(1):1–11, 2007.
- [155] E. Siero, A. Doelman, M. Eppinga, J. D. Rademacher, M. Rietkerk, and K. Siteur. Striped pattern selection by advective reaction-diffusion systems: resilience of banded vegetation on slopes. *Chaos: An Interdisciplinary Journal of Nonlinear Science*, 25(3):036411, 2015.
- [156] K. Siteur. *Off the beaten track. How ecosystems fail to respond to environmental change*. PhD thesis, Utrecht University, The Netherlands, 2016.
- [157] K. Siteur, M. B. Eppinga, A. Doelman, E. Siero, and M. Rietkerk. Ecosystems off track: rate-induced critical transitions in ecological models. *Oikos*, 125(12):1689–1699, 2016.
- [158] K. Siteur, E. Siero, M. B. Eppinga, J. D. Rademacher, A. Doelman, and M. Rietkerk. Beyond Turing: the response of patterned ecosystems to environmental change. *Ecological Complexity*, 20:81–96, 2014.
- [159] C. Soto-Treviño. A geometric method for periodic orbits in singularly-perturbed systems. In *Multiple-time-scale dynamical systems*, volume 122 of *IMA Vol. Math. Appl.*, pages 141–202. Springer, New York, 2001.
- [160] W. Sun, M. J. Ward, and R. Russell. The slow dynamics of two-spike solutions for the Gray-Scott and Gierer–Meinhardt systems: competition and oscillatory instabilities. *SIAM Journal on Applied Dynamical Systems*, 4(4):904–953, 2005.
- [161] T. Tadono, H. Nagai, H. Ishida, F. Oda, S. Naito, K. Minakawa, and H. Iwamoto. Generation of the 30 m-mesh global digital surface model by ALOS PRISM. *International Archives of the Photogrammetry, Remote Sensing & Spatial Information Sciences*, 41, 2016.
- [162] J. Takaku, T. Tadono, K. Tsutsui, and M. Ichikawa. Validation of ‘AW3D’ global DSM generated from ALOS prism. *ISPRS Annals of Photogrammetry, Remote Sensing & Spatial Information Sciences*, 3(4), 2016.
- [163] B. Tietjen and F. Jeltsch. Semi-arid grazing systems and climate change: a survey of present modelling potential and future needs. *Journal of Applied Ecology*, 44(2):425–434, 2007.
- [164] A. Tikhonov. On the dependence of the solutions of differential equations on a small parameter. *Matematicheskii sbornik*, 64(2):193–204, 1948.

- [165] A. M. Turing. The chemical basis of morphogenesis. *Philosophical Transactions of the Royal Society of London B*, 237(641):37–72, 1952.
- [166] J. C. Tzou, M. J. Ward, and T. Kolokolnikov. Slowly varying control parameters, delayed bifurcations, and the stability of spikes in reaction–diffusion systems. *Physica D: Nonlinear Phenomena*, 290:24–43, 2015.
- [167] United Nations Convention to Combat Desertification. *The Global Land Outlook*. 2017.
- [168] I. G. Usoskin. A history of solar activity over millennia. *Living Reviews in Solar Physics*, 14(1):3, Mar 2017.
- [169] J. van de Koppel and C. Mullan Crain. Scale dependent inhibition drives regular tussock spacing in a freshwater marsh. *The American Naturalist*, 168(5):E136–E147, 2006. PMID: 17080356.
- [170] S. van der Stelt, A. Doelman, G. Hek, and J. D. M. Rademacher. Rise and fall of periodic patterns for a generalized Klausmeier–Gray–Scott model. *Journal of Nonlinear Science*, 23(1):39–95, 2013.
- [171] P. van Heijster, A. Doelman, T. J. Kaper, Y. Nishiura, and K. I. Ueda. Pinned fronts in heterogeneous media of jump type. *Nonlinearity*, 24(1):127, 2010.
- [172] P. van Heijster, A. Doelman, T. J. Kaper, and K. Promislow. Front interactions in a three-component system. *SIAM Journal on Applied Dynamical Systems*, 9(2):292–332, 2010.
- [173] W. van Saarloos, M. van Hecke, P. C. Hohenberg, et al. Amplitude equations for pattern forming systems. *Fundamental Problems in Statistical Mechanics*, 8:245–278, 1994.
- [174] F. Veerman. Breathing pulses in singularly perturbed reaction-diffusion systems. *Nonlinearity*, 28(7):2211, 2015.
- [175] F. Veerman and A. Doelman. Pulses in a Gierer–Meinhardt equation with a slow nonlinearity. *SIAM Journal on Applied Dynamical Systems*, 12(1):28–60, 2013.
- [176] J. von Hardenberg, E. Meron, M. Shachak, and Y. Zarmi. Diversity of vegetation patterns and desertification. *Physical Review Letters*, 87(19):198101, 2001.
- [177] G.-R. Walther, E. Post, P. Convey, A. Menzel, C. Parmesan, T. J. Beebee, J.-M. Fromentin, O. Hoegh-Guldberg, and F. Bairlein. Ecological responses to recent climate change. *Nature*, 416(6879):389, 2002.
- [178] J. Wei and M. Winter. *Mathematical aspects of pattern formation in biological systems*, volume 189. Springer Science & Business Media, 2013.
- [179] J. Wei and M. Winter. Stable spike clusters for the one-dimensional Gierer–Meinhardt system. *European Journal of Applied Mathematics*, 28(4):576–635, 2017.
- [180] J. Wei, M. Winter, and W. Yang. Stable spike clusters for the precursor Gierer–Meinhardt system in  $\mathbb{R}^2$ . *Calculus of Variations and Partial Differential Equations*, 56(5):142, 2017.
- [181] L. White. Brousse tigrée patterns in southern Niger. *The Journal of Ecology*, pages 549–553, 1970.
- [182] R. G. Wright and G. M. van Dyne. Environmental factors influencing semidesert grassland perennial grass demography. *The Southwestern Naturalist*, pages 259–273, 1976.

- [183] J. Xin. Front propagation in heterogeneous media. *SIAM review*, 42(2):161–230, 2000.
- [184] X. Yuan, T. Teramoto, and Y. Nishiura. Heterogeneity-induced defect bifurcation and pulse dynamics for a three-component reaction-diffusion system. *Physical Review E*, 75(3):036220, 2007.

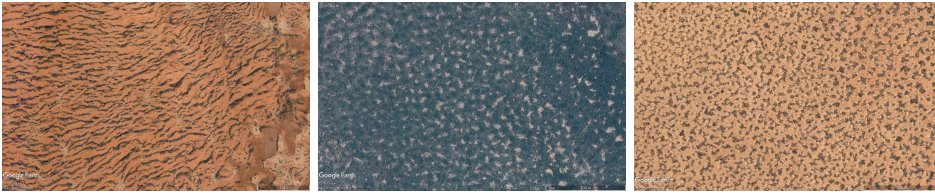
## Samenvatting

Verspreid over de hele wereld zijn er vele, grote gebieden waar jaarlijks de hoeveelheid vegetatie afneemt. Omdat – ook binnen een gebied – de begroeiing op sommige plekken eerder verdwijnt dan op andere, leidt dit tot patronen in de vegetatie. In eerste instantie kunnen dit ‘gaten’ in de vegetatie zijn, maar ook bijvoorbeeld bandpatronen en doolhofpatronen zijn waargenomen (zie figuur SV voor een aantal voorbeelden). Uiteindelijk zorgt een aanhoudende afname dat vruchtbare grond verandert tot lege, onbegroeiende en onvruchtbare stukken land. Dit aftakelingsproces, het zogenoemde verwoestijningsproces, heeft vaak desastreuze gevolgen voor de lokale bevolking die voor hun voedselvoorziening afhankelijk is van vee en gewassen, waar vruchtbare grond noodzakelijk voor is. Het voorkomen van dergelijke, veelal onomkeerbare verwoestijning is dus erg belangrijk. Een goed begrip van de mechanismen achter dit proces is hiervoor essentieel.

Om deze mechanismen beter te begrijpen, zijn er in de loop van de tijd vele verschillende wiskundige modellen opgesteld, variërend in de mate van realisme en complexiteit. Het bestuderen van deze modellen geeft inzichten in het gedrag van de werkelijke gebieden, wat dan weer bijdraagt aan het begrip van het verwoestijningsproces. In dit proefschrift is een aantal verschillende modellen bestudeerd met behulp van geavanceerde wiskunde. Deze modellen zijn hierin telkens zo simpel mogelijk gekozen, zodat er makkelijk mee gewerkt kan worden en nieuwe effecten beter inzichtelijk zijn. Tegelijk geeft bestudering van simpele modellen vaak een goede intuïtie voor het gedrag van geavanceerdere, meer realistische modellen en natuurlijk voor het werkelijke gedrag.

Deze theoretisch verkregen intuïtie moet vervolgens wel weer getest en vergeleken worden met de werkelijkheid. In hoofdstuk 2 speelt deze vergelijking de hoofdrol. Hierin is gekeken naar het typische gedrag van de wiskundige modellen en is dat op een gestructureerde manier vergeleken met satellietmetingen aan vegetatiepatronen in Somalië. Deze vergelijking verifieert veel intuïtie uit eerdere theoretische studies. In het bijzonder is er ‘multistabiliteit’ gevonden: in de bestudeerde gebieden is niet één specifiek patroon overheersend, maar is er juist een scala aan patronen mogelijk. Hierdoor kunnen dergelijke ecosystemen bij veranderingen aan het klimaat vrij gemakkelijk overgaan van het ene patroon in het andere – met relatief weinig consequenties voor de hoeveelheid vegetatie in het ecosysteem. Dit betekent dat deze gebieden – door de aanwezigheid van vegetatiepatronen – veel robuuster en veerkrachtiger zijn dan tot dusver bekend was en dus ook dat ze minder snel dan gedacht ineen zullen storten tot een kale, onvruchtbare woestijn.

Hoewel uit onderzoek dus bekend is dat vegetatiepatronen zorgen voor een veerkrachtiger ecosysteem, is niet precies bekend hoe. Hiervoor is meer kennis over de



(a) Bandpatroon in Somalia      (b) Gatenpatroon in Niger      (c) Doolhofpatroon in Sudan

**Figure SV** – Google Earth satelietbeelden van verschillende soorten vegetatiepatronen. (a) Bandpatroon in Somalië ( $8^{\circ}5'N$ ;  $47^{\circ}27'E$ ); (b) Gatenpatroon in Niger ( $12^{\circ}22'N$ ;  $2^{\circ}24'E$ ); (c) Doolhofpatroon in Sudan ( $11^{\circ}8'N$ ;  $27^{\circ}50'E$ ).

precieze stappen van het verwoestijningsproces nodig. Daarom is in hoofdstuk 3 van dit proefschrift gekeken naar het gedrag en de verdwijning van vegetatiepatronen. Deze studie heeft laten zien dat vegetatie een sterke voorkeur heeft voor regelmatigheid; over de tijd worden vegetatiepatronen steeds regelmatiger. Juist hierdoor kan de vegetatie grotere veranderingen aan het klimaat opvangen voordat een deel van de begroeiing verdwijnt. Er is ook gekeken naar welk deel dan verdwijnt en dit blijkt sterk afhankelijk van de regelmatigheid van het vegetatiepatroon: onregelmatige patronen verliezen vaker kleine stukken vegetatie, terwijl regelmatigere patronen af en toe in één keer grote stukken verliezen.

Uit metingen aan vegetatiepatronen (waaronder die in hoofdstuk 2) zijn verder enkele tekortkomingen ontdekt in de standaardmodellen. Zo voorspellen de modellen dat vegetatie zich langzaam heuvelopwaarts verplaatst, terwijl dit in werkelijkheid niet altijd gebeurt; er zijn observaties van omhooglopende vegetatiepatronen, maar ook van naar beneden lopende vegetatie en zelfs van stilstaande patronen. Om ook dit te vatten in modellen is het nodig om de precieze topografie van een gebied te modelleren. In hoofdstukken 3 en 4 wordt een simpel model op deze manier uitgebreid. Deze uitbreiding zorgt er onder andere voor dat zowel een heuvelopwaartse als een heuvelafwaartse beweging van vegetatiepatronen waargenomen kan worden (sterk afhankelijk van de precieze vorm van het terrein). Verder wordt in hoofdstuk 4 de basis gelegd voor een wiskundige bestudering van deze uitgebreide modellen – door de aanwezigheid van een ingewikkelde topografie kan dit namelijk niet meer met de gebruikelijke methoden.

Tot slot is ook bekend dat niet alle type patronen overal voorkomen. Zo vormt vegetatie zich doorgaans alleen tot ‘banden’ op relatief steile<sup>1</sup> hellingen. Uit modelmatig werk is al eerder een zelfde conclusie getrokken. De vraag is dan ook waarom dit het geval is. In hoofdstuk 5 wordt deze vraag deels beantwoord. Hier wordt wiskundig bewezen dat vegetatiebanden kunnen ontstaan als de heuvels in het model steil genoeg zijn. In combinatie met eerder werk dat laat zien dat ze juist niet kunnen ontstaan op te vlakke ondergronden, toont dit dat deze observaties overeenkomen met het theoretisch begrip van deze modellen.

<sup>1</sup>De bestudeerde gebieden zijn doorgaans niet bepaald steil in absolute zin; hellingen zijn typisch rond 0% tot 1%.

## Curriculum Vitae

Robbin Bastiaansen was born on the 21<sup>st</sup> of March 1991. From 2002 to 2009 he attended the Norbertuscollege in Roosendaal and received his gymnasium diploma (profiles ‘Natuur & Gezondheid’ and ‘Natuur & Techniek’). Starting from 2009 he enrolled at Leiden university and followed both a bachelor program in Mathematics and one in Physics; he completed both cum laude in 2013 with a bachelor thesis on ‘Bending and buckling in elastic patterned sheets’ under joint supervision by prof. dr. Martin van Hecke and dr. Vivi Rottschäfer. In the same year he started two master studies, one in Theoretical Physics and one in Applied Mathematics. He finished his degree in Applied Mathematics cum laude in 2015 with a master thesis titled ‘Pattern formation in animal populations’ under the supervision of dr. Vivi Rottschäfer. That year he also discontinued his studies in Theoretical Physics in favour of a Ph.D. research position at the Mathematical Institute of Leiden University under the guidance of prof. dr. Arjen Doelman, prof. dr. ir. Max Rietkerk and dr. Martina Chirilus-Bruckner. The results of this project are partly presented as the contents of this thesis.

Besides his studies, he has been active in many different roles, including the following. In 2011–2012 he was vice president of the study association De Leidsche Flesch. From 2010 to 2014 he worked as ‘student ambassador’ to provide information to and to organize activities for prospective (mathematics) students. In 2013 he was member of the student council for the faculty of sciences. In 2011 and 2012 he organized the first two Leiden Education Debates. In 2013 he organized the Dutch-Flemish mathematics Olympiad LIMO for students. In 2017 he organized the NDNS+ PhD Days. Since 2017 he has been co-organizer of Leiden’s informal Analysis seminar.

